

Strain-tuning of the electronic, optical, and vibrational properties of two-dimensional crystals F

Cite as: Appl. Phys. Rev. **8**, 021318 (2021); <https://doi.org/10.1063/5.0037852>

Submitted: 16 November 2020 . Accepted: 26 February 2021 . Published Online: 03 June 2021

 E. Blundo,  E. Cappelluti,  M. Felici,  G. Pettinari, and  A. Polimeni

COLLECTIONS

F This paper was selected as Featured



View Online



Export Citation



CrossMark



Applied Physics
Reviews

Try to keep up.

APR's Impact Factor is trending up.
Is your next paper ready? **Submit it now!**

2019 JOURNAL IMPACT FACTOR

017.034
65



Strain-tuning of the electronic, optical, and vibrational properties of two-dimensional crystals

Cite as: Appl. Phys. Rev. **8**, 021318 (2021); doi: [10.1063/5.0037852](https://doi.org/10.1063/5.0037852)

Submitted: 16 November 2020 · Accepted: 26 February 2021 ·

Published Online: 3 June 2021



E. Blundo,¹  E. Cappelluti,²  M. Felici,¹  G. Pettinari,³  and A. Polimeni^{1,a)} 

AFFILIATIONS

¹Physics Department, Sapienza Università di Roma, 00185 Rome, Italy

²Istituto di Struttura della Materia-CNR (ISM-CNR), Sede di Trieste, 34149 Trieste, Italy

³Institute for Photonics and Nanotechnologies, National Research Council, 00156 Rome, Italy

^{a)} Author to whom correspondence should be addressed: antonio.polimeni@roma1.infn.it

ABSTRACT

The variegated family of two-dimensional (2D) crystals has developed rapidly since the isolation of its forerunner: Graphene. Their plane-confined nature is typically associated with exceptional and peculiar electronic, optical, magnetic, and mechanical properties, heightening the interest of fundamental science and showing promise for applications. Methods for tuning their properties on demand have been pursued, among which the application of mechanical stresses, allowed by the incredible mechanical robustness and flexibility of these atomically thin materials. Great experimental and theoretical efforts have been focused on the development of straining protocols and on the evaluation of their impact on the peculiar properties of 2D crystals, revealing a novel, alluring physics. The relevance held by strain for 2D materials is introduced in Sec. I. Sections II and III present the multiplicity of methods developed to induce strain, highlighting the peculiarities, effectiveness, and drawbacks of each technique. Strain has largely widened the 2D material phase space in a quasi-seamless manner, leading to new and rich scenarios, which are discussed in Secs. IV–VI of this work. The effects of strain on the electronic, optical, vibrational, and mechanical properties of 2D crystals are discussed, as well as the possibility to exploit strain gradients for single-photon emission, non-linear optics, or valley/spintronics. Quantitative surveys of the relevant parameters governing these phenomena are provided. This review seeks to provide a comprehensive state-of-the-art overview of the straining methods and strain-induced effects, and to shed light on possible future paths. The aims and developments, the tools and strategies, and the achievements and challenges of this research field are widely presented and discussed.

© 2021 Author(s). All article content, except where otherwise noted, is licensed under a Creative Commons Attribution (CC BY) license (<http://creativecommons.org/licenses/by/4.0/>). <https://doi.org/10.1063/5.0037852>

TABLE OF CONTENTS

I. INTRODUCTION	2	4. Stretching devices	10
A. Importance and impact of strain	2	D. Blistering	11
B. Review motivation	2	E. Hydrostatic pressure	15
C. Review organization	3	III. CONTROLLED STRAIN FROM MECHANICAL DEFORMATIONS	16
II. METHODS FOR STRAINING 2D CRYSTALS	3	A. Uniform strains	16
A. Deposition on dissimilar substrates	3	B. Non-uniform strains	17
B. Growth-based techniques	5	IV. PHYSICAL EFFECTS	19
C. Devices: Bending, bulging, indenting and stretching	7	A. Band structure and electronic properties	19
1. Bending devices	7	1. Graphene	20
2. Bulging devices	8	2. Semiconducting transition-metal dichalcogenides MX ₂	21
3. Indenting devices	9	Band-structure properties	21

Exciton physics	24
The funnel effect in non-uniform strain gradients	25
3. Black phosphorus	26
B. Optical properties	27
1. Transition-metal dichalcogenides	27
2. Post-transition-metal chalcogenides	31
3. Black phosphorus	31
C. Single-photon emitters	32
D. Vibrational properties	35
1. Transition-metal dichalcogenides	40
2. Graphene	43
3. h-BN	46
4. Post-TMCs	46
5. Black Phosphorus	46
E. Nonlinear optical phenomena: Second and third harmonic generation	47
1. SHG	49
2. THG	52
F. Inhomogeneous strain and gauge fields	53
G. Strain tuning of valley/spintronics effects	54
V. ELASTO-MECHANICAL PROPERTIES	57
VI. CONCLUSIONS AND PERSPECTIVES	61

I. INTRODUCTION

The dawn of few-layer-thick crystals occurred in an intriguing context, which can be traced back to several decades ago. Due to the fascinating phenomena potentially associated with quasi two-dimensional (2D) systems, the condensed matter physics community has looked at these materials with great interest since the first half of the 20th century, much before the discovery of stable 2D crystals. In 1959, Richard Feynman gave an influential lecture entitled “There’s Plenty of Room at the Bottom,”¹ wherein he envisioned a scientific breakthrough in the field of physics with his questions: “*What could we do with layered structures with just the right layers? What would the properties of materials be if we could really arrange the atoms the way we want them?*” However, the theories developed by Peierls and Landau in the 1930s turned down the possible existence of truly 2D crystals in stable form due to a divergent contribution of thermal fluctuations.^{2,3} The latter should induce atom displacements comparable to the interatomic distances at any finite temperature and thus render atomically thin systems unstable.⁴ The argument was later supported by Mermin⁵ and by an omnibus of experimental observations.⁶ The possibility to explore a truly 2D world seemed, therefore, denied.

In a paper published in 1972,⁷ however, thin layers of NbSe₂ were obtained in order to study the superconducting-resistive transition temperature as the crystal thickness was reduced. Interestingly, the author affirms that “*because of the weak bonding between adjacent Se layers, the crystals are easily cleaved*” and “*thin crystals are obtained by sticking a crystal onto the substrate and peeling it away until a very thin crystal remains on the substrate,*” obtaining flakes as thin as 6 layers. The same technique had already been used, in Ref. 8, to obtain thin crystals of MoS₂—a material which, like NbSe₂, belongs to the class of transition metal dichalcogenides (TMDs). Still, notwithstanding these slow advancements, the research field aimed at the investigation of quasi 2D systems mostly laid dormant until the incipit of the

third millennium, when it received a tremendous boost with the ground-breaking discovery of graphene. Most interestingly, graphene—a monolayer of carbon atoms tightly packed into a 2D honeycomb lattice—was first isolated in 2004 by Novoselov and Geim neither with specific devices nor via ultra-complicated techniques, but via the simple—though brilliant—use of scotch tape to “peel away” single layers of graphite.⁹ The isolation and stability of a single layer of carbon atoms, thought to be impossible until then, opened the doors of Flatland¹⁰ to condensed-matter physicists. Since then, the ranks of truly 2D systems have grown rapidly, as many other materials have been found to be characterized by a layered structure akin to graphite, with different layers bound together by weak van der Waals (vdW) forces. Among them, graphene features a semimetallic nature and is characterized by exceptionally high carrier mobilities; hexagonal boron nitride (h-BN) is an extremely good insulator and dielectric with a large bandgap; black phosphorus (BP) has some interesting properties that arise from its inherent in-plane anisotropy—and, as a consequence, from its anisotropic band structure; the family of TMDs is richly varied, as it comprises superconducting materials with charge density waves and Weyl semimetal properties, as well as several semiconducting materials, with bandgaps ranging from the visible to the near infrared spectral region. In the single-layer limit, semiconducting TMDs are characterized by an extremely efficient light emission, which makes them ideal candidates for the realization of innovative, flexible, optoelectronic devices. Finally, post transition-metal chalcogenides have recently attracted interest as 2D semiconductors, for their high carriers’ mobilities and their potentiality for hydrogen storage.

A. Importance and impact of strain

Aside from the possibility of exploring the effects of lower dimensionality on the properties of atomically thin crystals, the existence of these crystals in stable form opens new avenues to materials engineering. Indeed, the inherent all-surface nature of these systems entails a higher sensitivity to external perturbations,^{11,12} which can in turn be exploited to modify the material properties. Among all possible external perturbations, the incredible mechanical flexibility and robustness^{13–15} of 2D crystals have offered the possibility to subject them to high mechanical deformations, engendering strains larger than 10%. Such strains are able to induce major modifications in the electronic, optical, magnetic, transport, and chemical properties of 2D materials, leading to the observation of a plethora of intriguing phenomena—ripe with new physics and novel opportunities.

B. Review motivation

In the past decade, great attention has been devoted to the development of methods to mechanically deform 2D crystals, easily realizing strain fields much larger than those generally attainable in conventional bulk semiconductors and quantum wells.^{11,16} These studies have revealed how strain can induce major changes in the electronic structure of 2D crystals, originating intriguing novel phenomena and rendering these materials extremely promising and apt for flexible electronics.^{11,12,16} Furthermore, single atomic layers with diverse chemical composition and optoelectronic characteristics can be stacked together to create heterostructures, which can be elastically deformed to create a wide number of novel layered materials with as

yet unexplored physical properties.^{17,18} Research in this field has been hot and has paved the way toward the creation of planar electronic devices with ultralow-power consumption, flexible electronics, sensors, and components for energy scavenging and storage.¹¹

Within such a flourishing research context, new discoveries have been seamlessly unveiled in recent years, and still new targets are currently being reached. In this wide panorama, a comprehensive work on the effect of strain can help current research in having an aware view over the past and present achievements, and a perspective view toward the future.

Some previous reviews focused on some specific aspects related to the strain engineering of 2D materials. For instance, Amorim *et al.*¹⁹ thoroughly discussed the effect of strain on the electronic properties of graphene; Si *et al.*²⁰ provided an insight into the strain engineering of graphene; Roldán *et al.*²¹ discussed the effect of strain on the optoelectronic properties of TMDs and other semiconducting 2D materials; Dai *et al.*²² discussed the methods to induce micro-scale local deformations and their relevance for the understanding of the elastic and adhesive properties of layered materials; Deng *et al.*²³ focused on the strain engineering of 2D materials beyond graphene, presenting some possible methods to induce strain and the effect of strain on various properties of 2D materials; finally, very recently Sanchez *et al.*²⁴ wrote a review focused on 2D material bubbles, a system where the built-in strain plays a crucial role.

Compared to these previous works, here we try to give the readers a broader view of how strain modifies and tunes the properties of the variegated family of 2D crystals. All the most employed techniques to strain atomically thin materials are discussed in detail, including deposition- and growth-based methods, the application of hydrostatic pressures, the use of devices to bend, bulge, indent, and stretch 2D membranes, and the formation of nano- and microblisters or bubbles. The role of strain in modifying the electronic, optical, and vibrational properties of these materials is then accounted for, as well as the possibility to exploit mechanical deformations to create controlled quantum emitters, to have tunable non-linear optics sources, to achieve control over the spin and valley properties of the crystals, to generate gauge fields engendering novel and intriguing effects, and much more besides. The possibility to exploit mechanical deformation to obtain precious information on the elasto-mechanical properties of these materials is also discussed.

To summarize, this review aims at discussing—in an as much as possible comprehensive manner—the possible strategies for straining 2D materials, the main achievements in this field, and the promising scenarios opened by the unique opportunity to deform these materials on demand.

C. Review organization

The ability to control the properties of deformed 2D materials relies on the development of controllable techniques to stretch or compress the crystal matrix, either at the macro-, micro-, or nanoscale. In Sec. II, we will discuss a variety of strategies developed over the past decades to strain atomically thin materials. Each method will be separately described and the pluses and minuses of each technique will be highlighted.

Indeed, any mechanical deformation entails a certain strain distribution, the knowledge of which can be important for a full understanding of the strain-induced physical effects. This aspect will be

discussed in Sec. III, where we will create a link between the methods described in Sec. II and the strain tensor, whenever possible. We will, in particular, show how different techniques give rise to different strain magnitudes, spatial distributions, and strain anisotropy.

The physical effects induced by strain will be thoroughly investigated in Sec. IV, by focusing on different 2D materials and on a variety of different aspects, including the electronic, optical, and vibrational properties, the possibility to exploit strain to generate quantum emitters, the effect of strain on nonlinear optical phenomena (such as second and third harmonic generation), the possibility to generate pseudo-gauge fields and their relevance, and the ability to modulate the valley- and spintronic properties of several 2D materials via strain. We will also show how some strain-related effects—such as those on the opto-electronic properties of the crystal—can vary remarkably for different classes of 2D materials, while the effect on other properties—such as the vibrational ones—share some common trends.

Finally, in Sec. V, we will show how mechanical deformations represent a unique platform to investigate the elasto-mechanical and adhesive properties of 2D materials and we will discuss the main experimental techniques developed for their investigation and review the results obtained in this field.

II. METHODS FOR STRAINING 2D CRYSTALS

Researchers have developed a large variety of methods to induce strain in 2D crystals. In this section, we categorize the different approaches and describe how the underlying mechanical deformation leads to a characteristic strain value. Tables I and II summarize the highest strain values reached by the different methods in different materials.

A. Deposition on dissimilar substrates

Given the inherent flexibility of 2D crystals, deposition on patterned substrates is a natural choice for stressing them. Single or multiple layers can indeed conform to the shape of the patterned substrate underneath, resulting in a localized layer deformation.^{25–33} This method was used by several groups to create restricted regions of a TMD crystal subjected to strain fields, as depicted in Fig. 1. For the deposition process, a mono- (or few-) layer 2D crystal attached to poly(methyl methacrylate) (PMMA) or polydimethylsiloxane (PDMS) is transferred on top of lithographically patterned substrates, typically made of Si/SiO₂—either bare³² or covered by dielectric or metallic coatings—^{25,28,29} or ZnO nanorod array,³⁰ or Au nanocones,³¹ or more recently of GaP nanoantennas.³⁴ The transfer can be either dry^{26,28,29} or assisted by a wet solvent ensuring a nearly perfect adhesion of the layer to the patterned substrate,^{27,30–32} as shown in Fig. 1(a). Figure 1(b) shows the exemplary case of a MoS₂ monolayer nicely adhering to ZnO nanorods. Figure 1(c) shows the result of the wet transfer process of a chemical vapor deposition (CVD)-grown MoS₂ monolayer leading to a large-scale array of indented MoS₂ regions. The insets show a zoomed-in view of the array, where wrinkled highly strained regions of the monolayer are formed on top and at the edges of a single indenter. The maximum value of strain ϵ is reached on top of the indenters, where the strain is biaxial for symmetry reasons and is anisotropic elsewhere.³⁵ ϵ values equal to 0.6%,^{29,30} 1.0%,³⁶ and 1.35%³¹ were derived by measuring the photoluminescence (PL) peak energy associated with the bandgap exciton or the Raman mode shifts (as it will be discussed in more detail in Sec. IV). Figure 2 shows the

TABLE I. Typical uniaxial strain values achieved by different devices. For each work, the maximum strain achieved is displayed.

Ref.	Material	Strain	Max. value (%)
Growth			
48	MoS ₂	Uniaxial	3.0
Bending devices^a			
52	Graphene	Uniaxial	0.5
58	Graphene	Uniaxial	0.6
94	Graphene	Uniaxial	0.7
61	Graphene	Uniaxial	1.3
95	h-BN	Uniaxial	0.45
52	MoS ₂	Uniaxial	0.5
56	MoS ₂ /WS ₂	Uniaxial	0.7
55	WSe ₂	Uniaxial	3.6
54	WS ₂ , MoS ₂ , MoS ₂ /WS ₂	Uniaxial	0.6
64	MoSe ₂ , WSe ₂ , WS ₂ , MoS ₂	Uniaxial	1.5
51	MoS ₂	Uniaxial	0.8
53	WSe ₂	Uniaxial	2.0
66	MoS ₂	Uniaxial	2.4
96	MoS ₂	Uniaxial	0.4
62	MoS ₂	Uniaxial	1.9
65	MoS ₂	Uniaxial	1.5
65	WSe ₂	Uniaxial	1.7
65	WS ₂	Uniaxial	5.7
97	ReSe ₂	Uniaxial	-1.1
98	InSe	Uniaxial	-0.62; +1.06
57	InSe	Uniaxial	1.15
99	InSe	Uniaxial	1.2
100	GaSe	Uniaxial	0.7
60	BP	Uniaxial	-0.3; +0.8
101	BP	Uniaxial	0.85
102	BP	Uniaxial	0.9
103	BP	Uniaxial	< ±5%
Stretching devices^a			
91	MoS ₂	Uniaxial	0.5
90	WS ₂	Uniaxial	0.2
89	Graphene	Uniaxial	1.6
86	Graphene	Uniaxial	-0.15; +0.8

^aThe strain values displayed here refer to the strains in the bending/stretching direction.

AFM image of a strained MoS₂ monolayer sample on patterned Au nanopillars³⁶ and the strain distribution obtained from scanning micro-Raman spectroscopy indicating that the maximum strain is indeed reached on top of the indenting pillars, in agreement with the theoretical predictions.³⁵ One of the main applications of this approach is related to the creation of potential minima in which charge carriers localize, thus forming confined excitons. These latter exhibit atomic-like properties and behave as single-photon emitters

TABLE II. Typical biaxial strain values achieved by different devices. For each work, the maximum strain achieved is displayed.

Ref.	Material	Strain	Max. value (%)
Growth			
49	WS ₂ /WSe ₂	Biaxial	1.4
50	WS ₂	Biaxial	-0.14; +0.94
Patterned substrates			
30	MoS ₂	Biaxial	0.6
36	MoS ₂	Biaxial	1.0
27	MoS ₂	Biaxial	0.5
29	WSe ₂	Biaxial	0.6
31	MoS ₂	Biaxial	1.35
32	MoS ₂	Biaxial	2.4
Stretching devices			
92	MoS ₂	Biaxial	0.64
87	MoS ₂	Biaxial	-0.2
104	h-BN	Biaxial	-0.13
105	InSe	Biaxial	0.13
106	InSe	Biaxial	-0.22; +0.23
Indenting devices			
107	graphene	Biaxial	12-13
79	h-BN	Biaxial	6-7
15	MoS ₂	Biaxial	5-6
81	WSe ₂	Biaxial	3.7
76	MoTe ₂	Biaxial	5
77	BP	Biaxial	4.6
108	Bi ₂ Se ₃	Biaxial	4
109	Bi ₂ Te ₃	Biaxial	1-2
Bulging devices			
68	MoS ₂	Biaxial	5.6
Blistering			
110	MoS ₂	Biaxial	~2
111	MoS ₂	Biaxial	2.1
112	MoS ₂	Biaxial	1.8
112	MoSe ₂	Biaxial	2.3
112	MoTe ₂	Biaxial	2.0
112	WS ₂	Biaxial	2.0
112	WSe ₂	Biaxial	1.6
112	WTe ₂	Biaxial	1.2
113	MoS ₂	Biaxial	7.4
Blistering+indenting			
114	MoS ₂	Biaxial	~7-8

(SPEs),²⁶⁻²⁹ as discussed in more detail in Sec. IV C. SPEs in 2D TMDs were already observed in seemingly strain-free monolayers^{37,38} due to randomly positioned defects in the 2D layer. The method depicted in Figs. 1 and 2 allows instead a precise spatial control of the SPE (made of TMDs, GaSe, or h-BN) location that is pivotal for

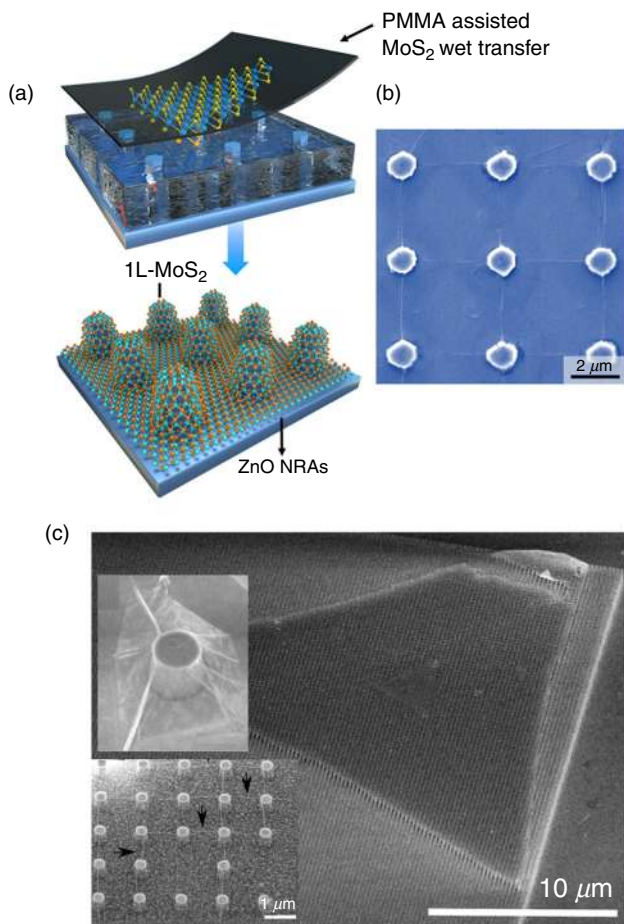


FIG. 1. (a) Sketch of the wet deposition procedure of a CVD-grown MoS₂ monolayer on a patterned substrate made of ZnO nanorod arrays (NRAs). The capillary force generated during the solvent evaporation forces the monolayer to conform to the patterned substrate. (b) Scanning electron microscope image of the resulting deposition process. (a) and (b) Reprinted with permission from Liu *et al.*, ACS Nano **13**, 9057 (2019). Copyright 2019 American Chemical Society.³⁰ (c) Scanning electron microscope images at different magnifications of a MoS₂ monolayer deposited on an array of SiO₂ pillars. The top left inset makes it appreciable the formation of wrinkles around a single pillar (diameter equal to 565 nm and height equal to 420 nm). Reprinted with permission from Chaste *et al.*, ACS Nano **12**, 3235 (2018), Copyright 2018 American Chemical Society.³²

coupling the emitters to plasmonic structures^{38–41} or photonic devices.^{34,38,42–44} As a matter of fact, localized strain fields can attract electron and holes toward those defects with the lowest energy thanks to the local strain-induced decrease in the underlying bandgap value, as schematically shown in Fig. 3. Figure 4 shows an effective and simple method to couple strain-induced WSe₂ SPEs to a waveguide.⁴⁵ Deposition of the monolayer on the waveguide ridges [see panel (a)] creates strain in the former and hence localized sources of photons [see panel (b)], which couple naturally to the waveguide as depicted in panel (c).

Very interestingly, a similar combination of defects and strain is promising for enhancing the catalyzing properties of MoS₂ monolayers.^{31,36} It was reported that S vacancies are activation centers for

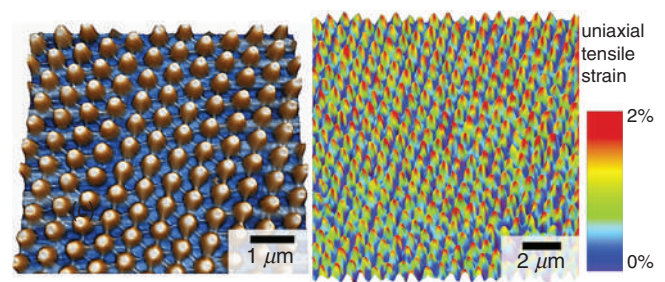


FIG. 2. Left panel: Atomic force microscopy image of an array of a strained MoS₂ monolayer adhering to Au nanopillars with diameter of 350 nm and height of 80 nm. Right panel: Corresponding map strain derived from micro-Raman measurements. Reprinted with permission from Li *et al.*, J. Am. Chem. Soc. **138**, 5123 (2016). Copyright 2016 American Chemical Society.³⁶

the hydrogen evolution reaction (HER) on the basal plane of MoS₂. In addition, the HER kinetics of S vacancies can be accelerated by tensile elastic strain obtained by a patterned substrate as the one shown in Fig. 2. Finally, Table II reports the highest biaxial strain values reached by growth on patterned substrates.

B. Growth-based techniques

At the early stages of epitaxial techniques—such as molecular beam epitaxy and CVD—lattice mismatch was a first important hurdle toward the achievement of a full flexibility in the combination of substrates and deposited layers as well as in the choice of different

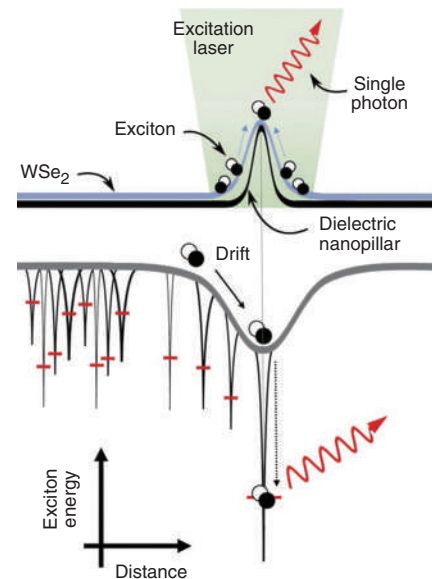


FIG. 3. Schematic view of the exciton potential profile close to a nanopillar. Strain generates an energy local minimum on which defect-related levels are superimposed. Carriers diffuse toward those localization centers featuring minimum energy. Reprinted with permission from Branny *et al.*, Nat. Commun. **8**, 15053 (2017). Copyright 2017 Author(s), licensed under a Creative Commons Attribution 4.0 International License.²⁹

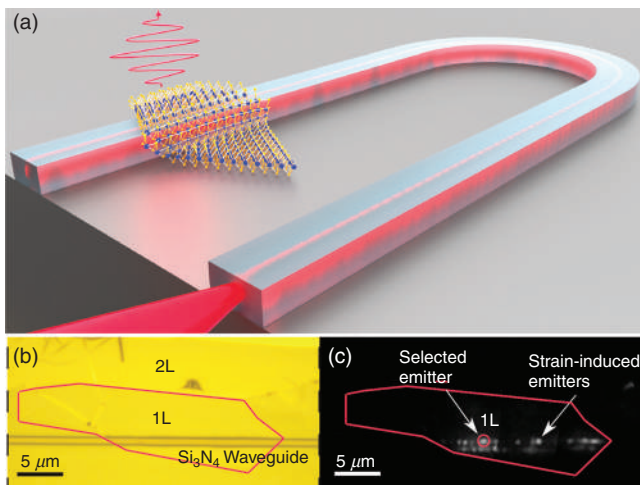


FIG. 4. (a) Illustration of a WSe₂ monolayer nesting on the edges of a Si₃N₄ waveguide acting simultaneously as a generator of single-photon sources and guide to the emitted photons. (b) Microscope image of the Si₃N₄ sketched in panel (a). The monolayer is marked in red (1L). (c) PL with defocused excitation shows strain-localized emitters along the waveguide edges. Adapted with permission from Errando-Herranz *et al.*, [arXiv:2002.07657](https://arxiv.org/abs/2002.07657) (2020). Copyright 2020.⁴⁵

lattices alternating in a stacked configuration. Consequently, the synthesis of strained layers (e.g., InGaAs/GaAs and Si/Ge) was limited to a maximum thickness of the epitaxial overlayers. However, this issue turned out to be an opportunity to exploit strain as a driving force toward the creation of novel nanostructures. A most remarkable example is represented by self-assembled quantum dots that form at the interface between two crystals whose lattice constants differ by few percent.⁴⁶

Direct growth of 2D crystals on pre-patterned substrates is a possible means to induce strain on the grown material over a large scale, which is suitable for applications. For this to happen, it is necessary that the deposited layer adheres to the substrate beneath. This approach was exploited in the CVD growth of bilayer MoS₂ on patterned sapphire substrates aiming at the fabrication of photodetectors with enhanced performances.⁴⁷ Figure 5 shows the growth scheme [panels (a)–(b)] in which a MoS₂ bilayer nicely conforms to the cone-shaped sapphire substrate, as apparent from the transmission electron microscopy images in panels (b) and (c). The thermal expansion mismatch between the bilayer and the substrate gives rise, during the sample cooldown, to a biaxial compressive strain. Although of small extent, that strain, combined with the electric field distribution, was sufficient to favor the collection of carriers toward the regions of minimum strain close to the photodetector electrodes, thus enhancing the device sensitivity to light absorption, as illustrated in panels (d) and (e) of Fig. 5. A similar approach was presented for CVD-grown MoS₂ on trenced SiO₂ substrates.⁴⁸ In that work, the anisotropic growth mode of many-layer MoS₂ gave rise to frequency-shifted and anisotropic vibrational modes consistent with a tensile strain of about 3%.

A more effective means to transfer controllable amounts of strain on 2D crystals can be achieved by a sophisticated method based on lateral CVD growth of vdW crystal superlattices.⁴⁹ As depicted in

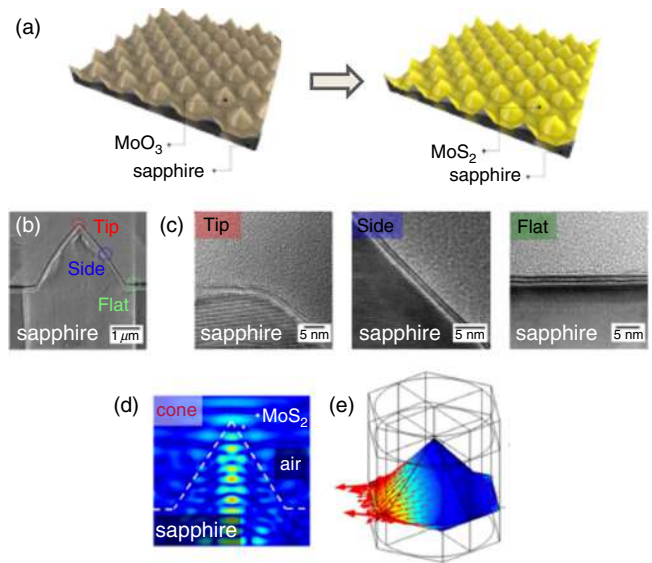


FIG. 5. (a) Schematic of the growth process of a MoS₂ bilayer obtained by sulfurizing MoO₃, which was first deposited as the seed material on top of a periodically patterned sapphire substrate. (b) Transmission electron microscopy (TEM) image of a cone-shaped patterned sapphire substrate with MoS₂ bilayers. (c) TEM images of three locations in panel (b) highlighting the uniform cover along the different surfaces of the patterned substrate. (d) Electric field distribution, localized mainly in the cone region. (e) Photon-generated electron density. Reprinted with permission from Wang *et al.*, *ACS Nano* **11**, 8768 (2017). Copyright 2017 American Chemical Society.⁴⁷

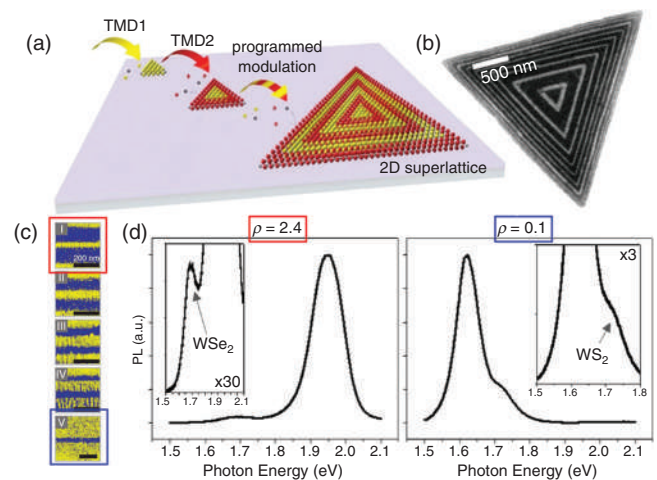


FIG. 6. (a) Sketch of the laterally modulated metal-organic chemical vapor deposition of TMD monolayers (specifically, TMD1 = WS₂ and TMD2 = WSe₂). (b) Scanning electron microscopy (SEM) image of a WS₂/WSe₂ lateral superlattice. (c) SEM images of different superlattices with different values of ρ equal to the ratio of the WS₂ thickness to the WSe₂ thickness. (d) PL spectra of the superlattices highlighted by colored rectangles in panel (c). Reprinted with permission from Xie *et al.*, *Science* **359**, 1131 (2018). Copyright 2018 American Association for the Advancement of Science.⁴⁹

Fig. 6(a), it is possible to alternate TMD monolayers featuring different composition (e.g., WS_2 and WSe_2) in the growth plane. This can be achieved by a carefully controlled release and timing of the precursors during metal-organic CVD growth. The scanning electron microscopy (SEM) image in panel (b) witnesses the sharp interfaces obtained with this technique. By changing the thickness of the WS_2 and WSe_2 layers in the superlattice, it is then possible to make the thicker layer determine the lattice constant of the thinner one, provided that coherent growth is maintained (namely, the ML lattice constant parallel to the heterointerface does not vary). Different configurations, corresponding to a different relative thickness of WS_2 and WSe_2 , are illustrated in panel (c) of Fig. 6. Eventually, the strain exerted at the WS_2/WSe_2 interface modifies progressively the bandgap of each ML as shown in panel (d), where the bandgap exciton resonance of WS_2 redshifts as the interfacial tensile strain increases (corresponding up to 1.4% isotropic biaxial tensile strain).

Alternatively, a controlled mechanical stress on the *planar* growth of 2D materials can be applied by exploiting the mismatch between the thermal coefficient expansion of the 2D crystal and of the substrate on which growth occurs. Depending on the difference between those coefficients, a tensile or a compressive biaxial strain is exerted on the grown material.⁵⁰ In this way, large regions of a 2D material can be subjected to relatively large biaxial strains. Figure 7 shows the specific case of a WSe_2 monolayer deposited on various substrates (SiO_2 , $\epsilon = 0.94\%$; AlN , $\epsilon = 0.32\%$; Al_2O_3 , $\epsilon \sim 0\%$; SrTiO_3 , $\epsilon = -0.14\%$). The maximum strain values reached by the growth-based techniques can be found in Tables I and II.

C. Devices: Bending, bulging, indenting and stretching

Growth and deposition on patterned substrates are methods that satisfy the scalability and controllability conditions required for any industrial application.¹¹ However, they lack the possibility to modify the applied strain dynamically and, thus, to investigate how the physical properties of a 2D crystal react to a continuously varying perturbation. The all-surface nature of 2D materials makes them particularly responsive to mechanical deformations and various methods have been developed during the last few years. In all methods, one of the main points to be considered is the effective stress that can be actually transferred from the deforming device to the 2D layer. Next, we will discuss various devices that have been developed to address the effects of strain on 2D materials.

1. Bending devices

In a typical bending device, a 2D crystal (either in the monolayer or multilayer form) is deposited on a flexible substrate. This latter is usually made of polymeric material to which 2D crystals adhere. This allows for a transfer of uniaxial strain to the sample upon substrate bending.^{51–57} Alternatively, the thin layer can be deposited on a cantilever, which is bent to transfer uniaxial strain up to about $\epsilon = 0.6\%$.^{52,58}

Figure 8 illustrates the main characteristics of a bending device, where 2D crystals are transferred on a plastic substrate (such as polyethylene terephthalate, known as PET, and poly-methyl methacrylate, or PMMA) enabling a high degree of mechanical flexibility. In particular, panel (a) shows a four-point bending apparatus⁵⁵ and panel (b)

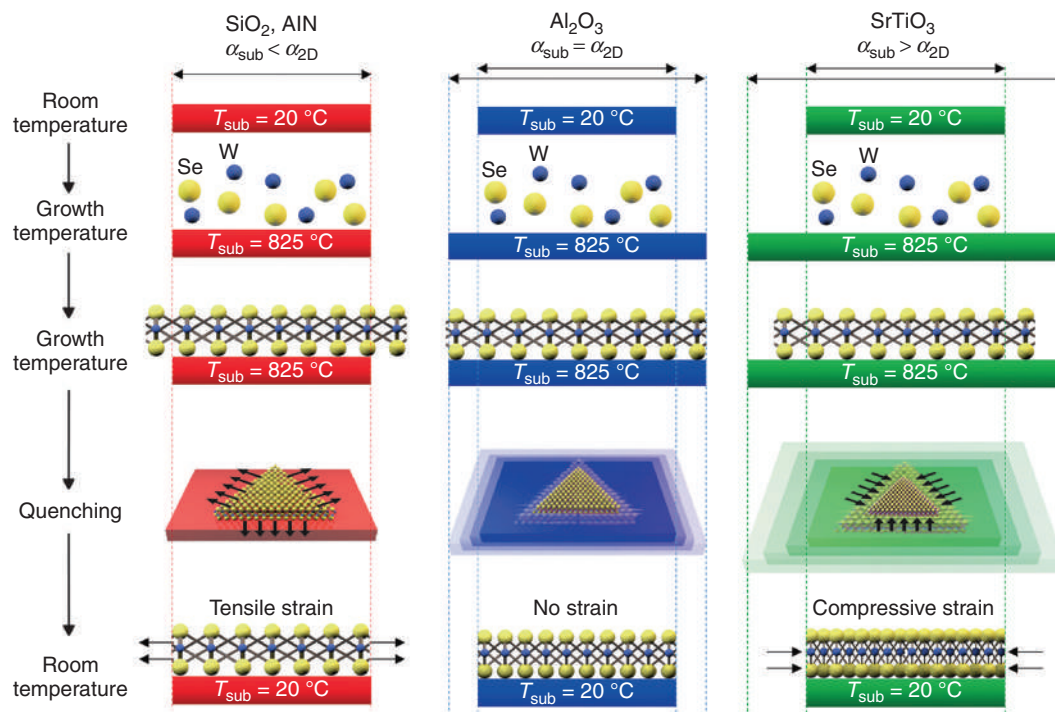


FIG. 7. CVD growth of a monolayer on substrates featuring different thermal coefficient (α_{sub}) with respect to that of the WSe_2 flake ($\alpha_{2\text{D}}$). Depending on the relative magnitude of the coefficients, a tensile strain (left), no strain (center) or a compressive strain (right) may be exerted on the 2D flake. Reprinted with permission from Ahn *et al.*, Nat. Commun. **8**, 608 (2017). Copyright 2017 Author(s), licensed under a Creative Commons Attribution 4.0 International License.⁵⁰

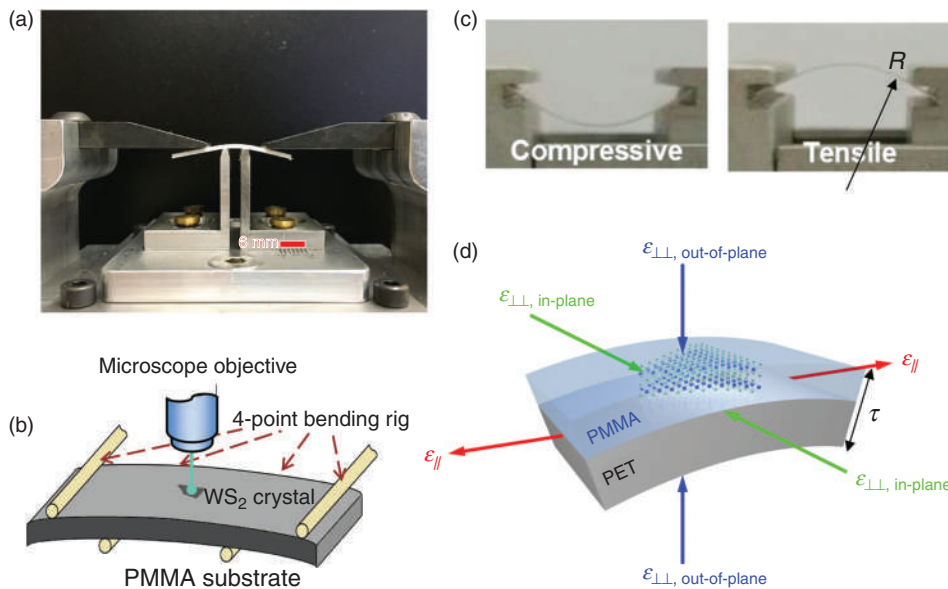


FIG. 8. (a) Picture of a four-point bending device,⁵⁵ whose working principle is illustrated in panel (b).⁵⁹ (c) Alternative device that uses a PET substrate that can be bent upward or downward^{56,60} to induce different kinds of uniaxial strain. R indicates the curvature radius imposed to the PET substrate. (d) Sketch of a bent 2D crystal indicating the different components of the strain tensor; τ is the thickness of the substrate. (a) and (d) Reprinted with permission from Wu *et al.*, *Nano Lett.* **18**, 2351 (2018). Copyright 2018 American Chemical Society.⁵⁵ (b) Reprinted with permission from Wang *et al.*, *2D Mater.* **7**, 045022 (2020). Copyright 2020 Author(s), licensed under a Creative Commons Attribution 4.0 International License. (c) Reprinted with permission from Pak *et al.*, *Nano Lett.* **17**, 5634 (2017). Copyright 2017 American Chemical Society.

displays a sketch of the working principle of the device and its implementation with an optical objective for inspection and optical measurements. In panel (c), it is shown as a compressive or tensile strain that can be applied to the deposited crystal depending on the direction of the bending force.^{56,60} Bending setups permit the application of uniaxial strain with high reproducibility and possibility to apply stress in a controllable manner.^{61,62} More sophisticated designs allow us also to exert a biaxial strain as done for graphene.⁶³ The main drawback of this method is due to the sliding occurring between the deposited layers and the substrate or even between different layers in the case of heterostructures or multilayer samples. In some cases, this may result in an incomplete strain transfer. As a matter of fact, uniaxial strain values typically below 2% were reported, see Table I. Higher uniaxial strain values (up to 3.6%) can be attained by encapsulating the 2D crystal with polymers that prevent layer slippage.^{53,55,64,65} In another case, titanium clamps were employed to that purpose.⁶⁶ In bending devices, the uniaxial strain value is evaluated as

$$\varepsilon = \frac{\tau}{2R}, \quad (1)$$

where τ and R are the thickness and curvature radius of the flexible polymeric film on which the samples are deposited, see definition of R and τ in Figs. 8(c) and 8(d), respectively. In Sec. IV, we review the strain gauge values of the optical gap energy and Raman mode frequencies observed by bending devices. It is also worth mentioning that this approach was employed to smooth out the negative effects of random local mechanical deformations in graphene. This led to an increase in the carrier mobility, observed by bending the substrate on which the device was deposited.⁶⁷

2. Bulging devices

A more efficient means to induce strain on 2D crystals is to apply stress not only along a single direction—as in the case of most

bending devices—but along two directions, thus nearly doubling the attainable elastic deformation. This can be accomplished by bulging devices, which exploit the pressure difference established across the two sides of a membrane. A sketch of the bulging process is presented in Fig. 9(a). An array of cylindrical micro-holes is first etched in a SiO₂/Si substrate (the figure shows just one micro-hole for simplicity reasons). Typically, the micro-holes have a diameter of a few micrometers, are few hundreds nm deep, and are sealed by a sheet of a 2D crystal; e.g., single- or multilayered graphene, h-BN, or TMDs. Afterwards, the sample is placed in a pressurization chamber containing N₂, Ar, He or H₂ up to about $p_{int}=1000$ atm.^{68–71} After an amount of time that can vary between several hours⁷¹ and many days,⁷² the pressure inside the holes equals that of the pressurization chamber. The gas is thought to fill the holes by permeating through the interface between the 2D membrane and the SiO₂/Si substrate.⁷¹ Once the sample is brought out of the chamber, the pressure difference with the ambient (i.e., $p_{ext}=1$ atm) causes a bulging of the membrane (it is also possible to induce a downward bulging if $\Delta p = p_{int} - p_{ext} < 0$, which is obtained by placing the sample in a vacuum chamber to reach $p_{int}=0$ and by pressurizing the same chamber by N₂).⁶⁸ Figure 9(b) depicts the final result for a graphene bilayer, showing how the bulged membrane can then be characterized by scanning probe microscopy and micro-Raman.⁷⁰ The stress exerted by Δp leads to a tensile strain, which is isotropic biaxial right at the center of the bulged membrane, where it reaches its maximum value. It then becomes anisotropic toward the edges. A thorough characterization of the strain tensor will be discussed in the following. This straining technique is particularly appealing since it allows us to achieve biaxial strains as high as 5.6% at the center of the deformed membrane.⁶⁸ The possibility to create deformations with the desired amount of strain makes this method interesting for a variety of reasons. Indeed, it can be exploited to study how the vibrational and optoelectronic properties of the 2D material change as a function of strain,⁶⁸ but it also provides a platform to study the elastic and

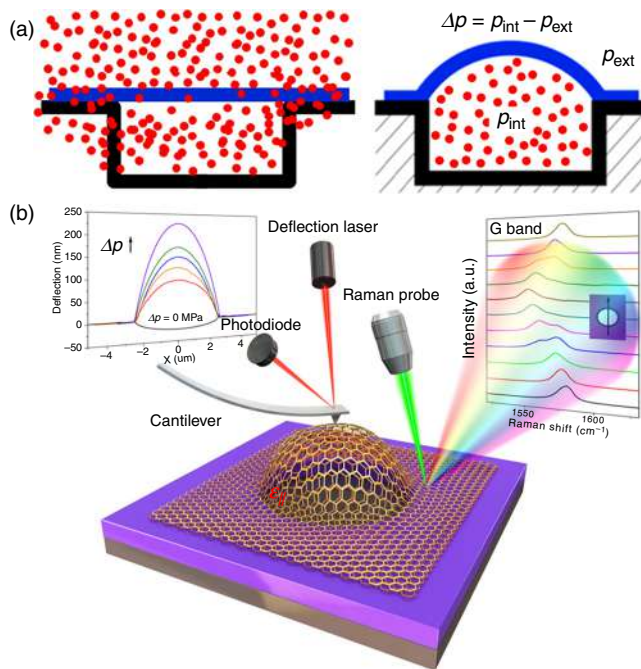


FIG. 9. (a) Two-step bulging process of a 2D membrane: left, deposition of a 2D membrane on a micro-hole created in a substrate and subsequent pressurization by a gas at p_{int} ; right, swelling of the membrane once the sample is brought to ambient pressure p_{amb} , so that a pressure difference is created. (b) Sketch of bulged bilayer graphene obtained by the method outlined in panel (a). AFM profiles measured in a real device are shown in the top-left inset. Depending on the value of $\Delta p = p_{int} - p_{ext}$, a given amount of tensile strain is transferred to the membrane, which can be characterized, e.g., by scanning probe and micro-Raman microscopies, as shown in the top-right inset. (b) Reprinted with permission from Wang *et al.*, Phys. Rev. Lett. **119**, 036101 (2017), Copyright 2017 American Physical Society.⁷⁰

adhesive properties of layered materials showing, for instance, how strain can lead to a reduction in the friction on a 2D material for increasing strain.⁷³ Finally, bulging devices based on holes with different shapes—such as triangular ones—were also recently used.⁷⁴

A bulging device alternative to that depicted in Fig. 9 is shown in Fig. 10 and referred to as “blown-bubble” bulging technique.⁷⁵ A

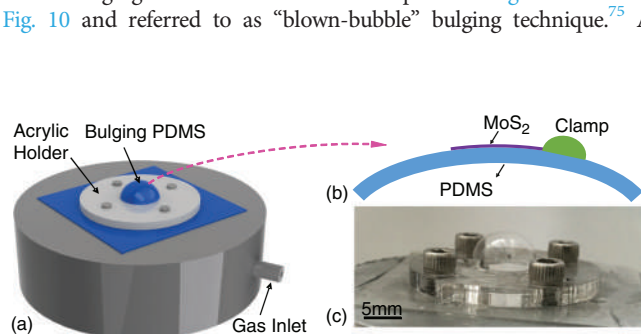


FIG. 10. (a) Sketch of the blown-bubble method to strain a MoS₂ flake clamped on the PDMS layer, see panel (b). By inflating this latter through the gas inlet, strain is transferred to the 2D crystal. (c) Photograph of the real device. Adapted with permission from Yang *et al.*, Nano Lett. **17**, 4568 (2017), Copyright 2017 American Chemical Society.⁷⁵

MoS₂ monolayer is exfoliated on a PDMS flexible substrate, which is subsequently fixed to an inflation chamber, as shown in Fig. 10. The monolayer is then clamped on the PDMS by silicone and afterwards N₂ gas is introduced in the chamber up to a 1.3 atm. In this manner, the strain applied to the PDMS can be transferred to the MoS₂ monolayer resulting in an isotropic biaxial tensile strain, reaching values up to 1.2%. For higher pressure values, sliding between the 2D crystal and the substrates occurs and strain turns anisotropic and non-linearly related to the strain applied to the PDMS layer. In any event, this method provides a fast and reliable means to strain-tune the mechanical and, hence, electronic properties of MoS₂ thin layers.⁷⁵

3. Indenting devices

These devices are typically fabricated by transferring a 2D crystal on lithographically-defined apertures in a substrate (SiO₂/Si is the most used choice). As shown in Fig. 11, the membrane can be suspended between two arms or lie on circular apertures. In both instances, a stress is applied by an AFM tip with relatively large curvature radius (of the order of few tens of nm). The locally applied stress results in a biaxial tensile strain, whose extent can be controlled by the indentation process, namely by the amount of deflection of the membrane, δ_{mem} , that equals the difference between the displacement of the sample and the deflection of the AFM tip: $\delta_{mem} = z_{piezo} - \delta_{probe}$ [see Figs. 12(a) and 12(b)]. As the AFM tip is moved downward [see Fig. 12(a)], δ_{mem} changes, and therefore, the applied load F is modified according to

$$F = a \cdot \delta_{mem} + b \cdot \delta_{mem}^3, \quad (2)$$

where the first and second terms prevail at small and large deformations, respectively. a and b are coefficients that depend on the geometrical shape of the membrane (e.g., circular or rectangular) and on its thickness. Importantly, a and b embed information on the relevant elastic characteristics of the 2D crystal, described by the in-plane Young's modulus, the Poisson's ratio, and the tension of the membrane before indentation is applied. The explicit expressions for those coefficients can be found, for instance, in Refs. 76–79 and will be

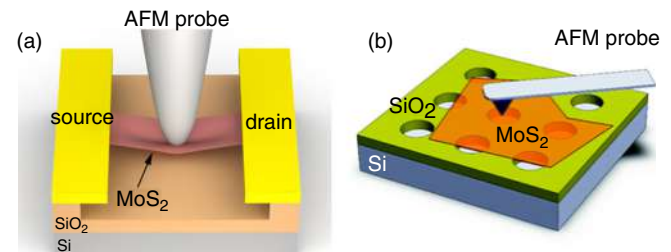


FIG. 11. (a) Sketch of an indenting experiment, where a 2D crystal is held between contacts to probe the transport properties of the material as a function of the stress exerted by an AFM tip. Reprinted with permission from Manzeli *et al.*, Nano Lett. **15**, 5330 (2015). Copyright 2015 American Chemical Society.⁸⁰ (b) In this picture, the 2D crystal is deposited on a hole-patterned Si/SiO₂ substrate and load-distance measurements are carried out. Reprinted with permission from Bertolazzi *et al.*, ACS Nano **5**, 9703 (2011), Copyright 2011 American Chemical Society.¹⁵

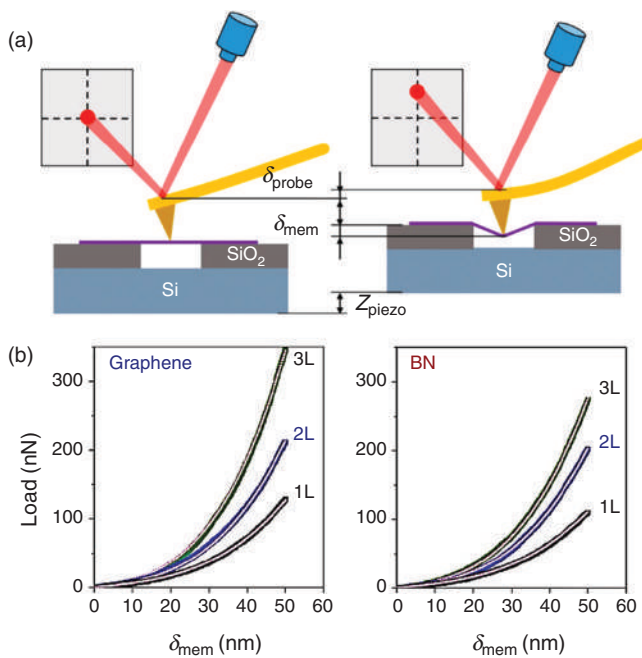


FIG. 12. (a) Sketch of a nanoindentation experiment. The indentation depth δ_{mem} is determined by $Z_{\text{piezo}} - \delta_{\text{probe}}$, where Z_{piezo} is the moving distance of the sample stage and δ_{probe} is the deflection of the AFM tip detected by a laser reflection system. Reprinted with permission from Sun *et al.*, *Nano Lett.* **19**, 761 (2019). Copyright 2019 American Chemical Society.⁷⁶ (b) Load-displacement curves and the corresponding fittings for mono- to three layers of graphene and BN. The fittings allow us to determine the mechanical properties of the 2D crystals. Reprinted with permission from A. Falin *et al.*, *Nat. Commun.* **8**, 15815 (2017), Copyright 2017 Author(s), licensed under a Creative Commons Attribution 4.0 International License.⁷⁹

discussed in more detail in Sec. V of this review, concerning the elastomechanical properties of 2D materials. By measuring the load-displacement curve of a membrane, then, it is possible to extract precious information on the elastic properties of a large variety of layered materials. As an example, Fig. 12(b) shows the case of graphene and BN samples with different thickness,⁷⁹ where sliding phenomena between adjacent single layers could be investigated. Indentation experiments were mostly employed to probe the mechanical properties of van der Waals crystals, and we will thoroughly discuss this possibility and the results obtained in this field in Sec. V. Here, instead, it is worth mentioning that in some cases, indentation experiments were used to study the effect of strain on atomically thin membranes. For instance, Manzeli *et al.*⁸⁰ demonstrated the emergence of a piezoresistive effect in indented MoS_2 crystals; Moon *et al.*⁸¹ exploited indentation with a nanoscale tip to induce strain gradients to study exciton funneling in WSe_2 monolayers; and Benimetskiy *et al.*⁸² exploited indentation to study the local bandgap change of strained MoSe_2 -MLs. Furthermore, interesting effects were also reported by indenting 2D materials deposited on polymeric substrates rather than on suspended ones. For instance, Rosenberger *et al.*⁸³ deposited a WSe_2 -ML over a polymer and demonstrated how, upon applying a sufficient mechanical stress using an AFM tip, the WSe_2 /polymer composite deforms, resulting in the formation of highly localized strain fields with good

control. A sketch of the process and the possibility to locally increase the luminescence on controlled spots—by exploiting strain gradients—is demonstrated in Figs. 13(a) and 13(b). Interestingly, this method offers the possibility to create single-photon emitters in the indented areas. Another interesting example was provided by Liu *et al.*,⁸⁴ who used a heated nanotip on a MoS_2 /polymer structure. By applying a suitable combination of indentation force and tip temperature, they were able to induce a well-controlled and permanent local deformation of the 2D material/polymer system, as shown in Fig. 13(c).

4. Stretching devices

In the case of stretching devices, strain is transferred to the 2D crystal via application of stress to the substrate or by exploiting the mismatch existing between the thermal and/or mechanical properties of the deposited membrane and its substrate. At variance with bending devices, stretching devices operate in a planar and, usually, more compact experimental geometry. Stress can also be applied simultaneously along two different directions, so that a relatively large total strain can be eventually introduced in the samples. Figure 14(a) shows a mechanical straining device coupled to a confocal microscopy system.⁸⁵ Panel (b) exemplifies the tensor components in the case of a h-BN bilayer deposited on PDMS. It is worth highlighting the presence of an out-of-plane strain component, which arises as a consequence of the in-plane deformation. Stress can also be applied biaxially using a piezoelectric (PZ) crystal on which the 2D sample is positioned. Application of an electric field perpendicular to the PZ substrate generates a biaxial in-plane strain $\epsilon_{//}$ as depicted in Fig. 14(c). With this method, both

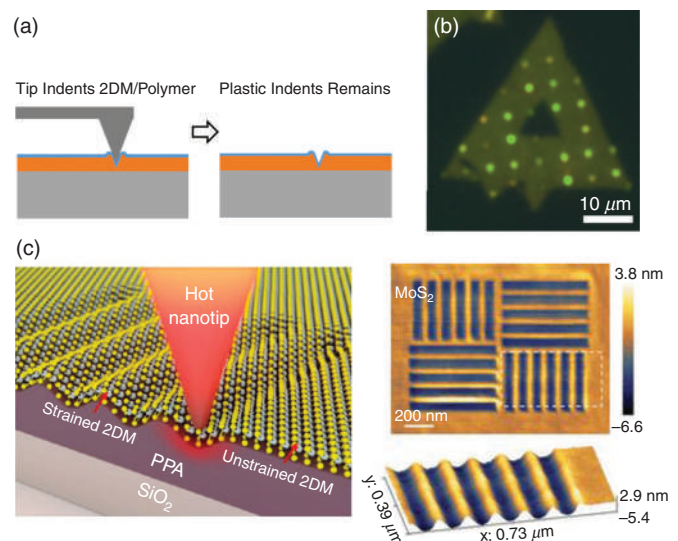


FIG. 13. (a) Sketch of a WSe_2 /polymer structure used in indenting experiments. The AFM tip indents the system (left) and applies sufficient load to plastically deform the polymer (right). (b) Fluorescence image of a WSe_2 /PMMA sample after a grid of AFM indentations were made. (a) and (b) Reprinted with permission from Rosenberger *et al.*, *ACS Nano* **13**, 904 (2019). Copyright 2019 American Chemical Society.⁸³ (c) Left: Conceptual illustration of the thermomechanical nanoindentation process for strain nanopatterning of 2D materials. Right: AFM topography of written MoS_2 ripple nanostructures (top) and three-dimensional representation of the area within the white dashed rectangle (bottom). Reprinted with permission from Liu *et al.*, *Nano Lett.* **20**, 8250 (2020), Copyright 2020 American Chemical Society.⁸⁴

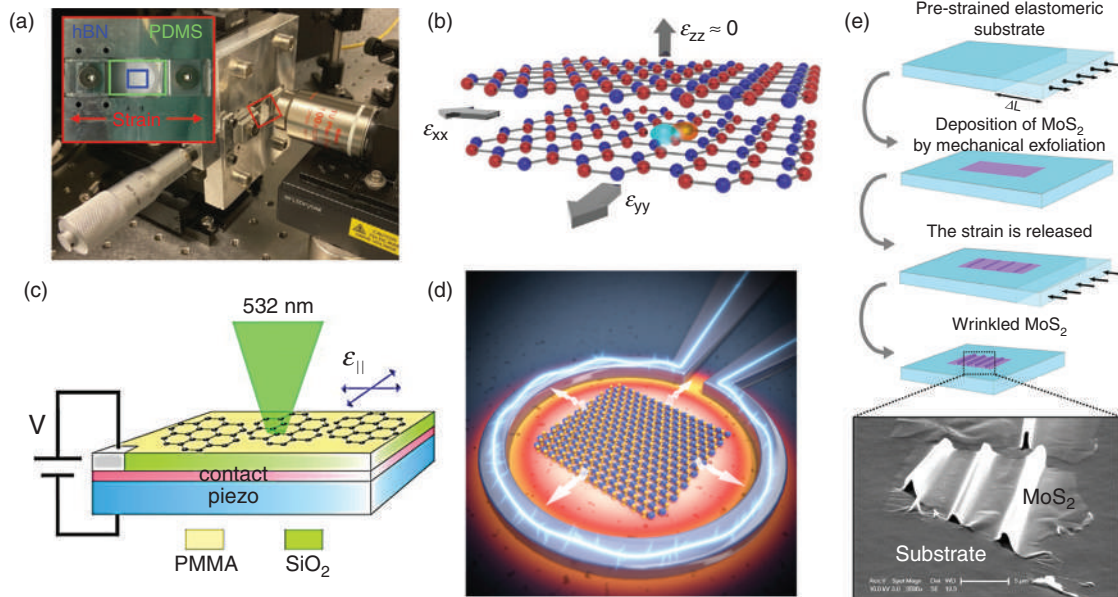


FIG. 14. (a) Apparatus used for stretching h-BN. The red box highlights the PDMS slab on which an h-BN flake was transferred. The inset displays a close-up view of the red boxed region outlining the PDMS slab and h-BN film. (b) Sketch of the various strain tensor components acting on an h-BN bilayer. (a) and (b) Reprinted with permission from Mendelson *et al.*, *Adv. Mater.* **32**, 1908316 (2020), Copyright 2020 Wiley-VCH Verlag GmbH & Co. KGaA, Weinheim.⁸⁵ (c) Sketch of an electro-mechanical device used to apply in-plane biaxial strain to the graphene. A bias voltage V applied to the piezoelectric substrate results in an out-of-plane electric field causing an in-plane strain $\epsilon_{||}$. Reprinted with permission from Ding *et al.*, *Nano Lett.* **10**, 3453 (2010), Copyright 2010 American Chemical Society.⁸⁶ (d) Sketch of a micro-heater device that exploits the mismatch between the large thermal expansion coefficient of polypropylene (the substrate on which the 2D crystal is deposited) and that of the 2D crystal. A metallic ring-shaped micro-heater is used to change the temperature of the substrate leading to a biaxial expansion in the 2D flakes. Reprinted with permission from Ryu *et al.*, *Nano Lett.* **20**, 5339 (2020). Copyright 2020 American Chemical Society.⁹² (e) Fabrication process of wrinkled MoS₂ monolayers. An elastomeric substrate is stretched prior deposition of MoS₂. The strain is released afterward, producing wrinkled MoS₂ flakes. Reprinted with permission from Castellanos-Gomez *et al.*, *Nano Lett.* **13**, 5361 (2013). Copyright 2013 American Chemical Society.⁹³

tensile and compressive strains could be applied to graphene⁸⁶ and TMDs.^{87,88} In-plane stretching of PDMS and PET substrates was also successfully employed to induce a sizable uniaxial tensile strain to graphene⁸⁹ and to investigate the efficiency of strain transfer from the substrates to the sample.^{90,91} In-plane biaxial strains can be achieved also thanks to the different thermal expansion coefficient of the 2D material and of its substrate,⁹² similarly to what is shown in Fig. 7 for the CVD-growth-based method. Figure 14(d) depicts a microheater actuator able to transfer a biaxial strain of about 0.6% to a MoS₂ flake. Likewise, this method can also be used to modulate strain by exploiting the different mechanical properties between the substrate and the deposited 2D layer. Figure 14(e) demonstrates how the stretching method can be exploited to induce local deformation of the membrane at the nano-/microscale, such as wrinkles. In fact, upon the release of the pretension accumulated in the gel-like elastomeric substrate, wrinkles can form due to the different elastic parameters of the substrate and of the 2D layer.⁹³ In such a way, an inhomogeneous strain distribution is achieved, which reaches a maximum uniaxial strain on the wrinkle top. In stretching (and bending) devices (see Figs. 8, 10, and 14), the main issue is the capability to determine the actual strain transferred to the 2D crystal. Slippage, the unidirectional character of the applied stress, and the non-perfect adhesion between the sample and its supporting substrate (where mechanical stress is directly applied) are some of the main mechanisms that may prevent the attainment of large strains. This drawback is surpassed by some of the

bulging devices presented before (see Fig. 9), where stress is directly transferred to the 2D crystal by the expansion of a gaseous medium. However, the need of a cumbersome inflating apparatus and the low time durability of gas bulges limit the use of this system in many instances. In Sec. IID, we discuss blistering of 2D materials as an efficacious method to achieve large and durable strain values without the need of external means.

The maximum strain values for each device can be found in Tables I and II.

D. Blistering

The process of placing/growing/depositing one or few 2D layers on a substrate or on a different 2D crystal is the first, crucial step in the preparation of 2D materials and heterostructures. Of course, this step always entails the risk of forming non-planar features—such as *blisters*, *bubbles*, *wrinkles* and *buckles*—on the sample surface, due, e.g., to the trapping of contaminants underneath a deposited flake, or to the imperfect adhesion of the 2D layers to the substrate.²⁴ These non-planar features are naturally accompanied by large lattice distortions, which are, in turn, responsible for the emergence of sizeable strain gradients. As a result, these features rapidly started to gain attention as potential test-beds for the investigation of the effects of strain on the optical and electronic properties of 2D materials. In a seminal 2010 paper, Levy and co-workers¹¹⁵ experimentally verified an earlier

theoretical prediction¹¹⁶ by measuring giant (~ 300 T), strain-induced pseudo-magnetic fields in the nanobubbles formed on the surface of graphene grown on Pt, as we will discuss in more detail in Sec. IV F. The generation of similar pseudo-magnetic fields is also expected to occur in strained TMD materials,¹¹⁷ which should lead to the observation of peculiar phenomena in their carrier dynamics, such as valley polarization¹¹⁸ and dissipation-less transport via the quantum spin Hall effect.¹¹⁹

In the attempt to harness these effects for the realization of innovative applications and devices, several methods for triggering the formation—and, eventually, for controlling the position—of strained features in 2D crystals were promptly developed. As mentioned before, the formation of nanobubbles was first observed at the interface between graphene and a metallic substrate in several situations: (i) either forming upon cooling down the sample after the graphene growth process, as a result of the differing thermal expansion coefficients of graphene and the metallic substrate;¹¹⁵ (ii) or following controlled irradiation by Ar^+ ions;¹²⁰ (iii) or by the intercalation of noble gas atoms in graphene deposited on Ni and subsequent annealing treatments, so that while graphene in direct contact with the Ni surface decomposes, some floating regions encase the noble gas aggregates forming graphene nanosized blisters.¹²¹ Many other diverse methods to form nano- and micro-bubbles were then developed. A first class of techniques directly acts on the conditions under which the flakes are deposited, for example, by applying a high pressure to the viscoelastic stamp used to place the flake on the substrate (the so-called “cold stamping” technique). Upon deposition, the abrupt release of the pressure acting on the flake leads to the formation of a large density of nanobubbles on the sample.¹²² This is particularly interesting in light of the recent observation that localized excitons in TMD MLs can deliver single photons with high brightness,^{123,124} and that the properties of these photon sources can be accurately controlled using strain.⁸⁸ Despite the physical origin of TMD quantum emitters (QEs) still being under debate, several works have demonstrated that their appearance is tightly connected to local strain gradients.^{125–128} These gradients favor exciton funneling¹²⁹ from strain-free, high-energy regions

toward strain-induced local energy minima, where single, localized exciton levels can be efficiently populated. Indeed, the strained blisters and nanobubbles created by cold stamping¹²² in a WSe_2 crystal have recently shown the ability to emit single photons (see Fig. 15), confirming their potential for nanophotonic devices based on 2D materials.

A second class of strained non-planar features, typically larger in size ($\geq 1 \mu\text{m}$) and characterized by a smooth, continuous strain distribution, is obtained as a by-product of the “wet-transfer” technique, first described in Ref. 130. With this method, 2D monolayers are first exfoliated on a poly(methyl methacrylate) PMMA membrane, which is then placed face down on the substrate of choice (the precision in the positioning of the 2D layer is ensured by the use of a micromanipulator). After dissolving the PMMA, the attractive vdW forces between the monolayer and the substrate squeeze out the trapped contaminants (mostly water and hydrocarbons), leading to the formation of μm and sub- μm bubbles and leaving the remaining interface atomically sharp and uncontaminated. This process, known as “self-cleansing,” can be accelerated and optimized by annealing the sample for a few minutes at moderate temperatures. Khestanova *et al.*¹³¹ verified that an annealing at 150°C for ~ 30 min is sufficient for the bubbles to reach their equilibrium shape and size. As formalized in several theoretical works on the mechanics of these structures—such as Yue *et al.*¹³²—indeed, the bubble’s shape and aspect ratio (i.e., the ratio between the maximum height and footprint radius, h_m/R) result from balancing the elastic properties of the monolayer (its Young’s modulus, E_{2D}) with its interaction with the substrate (the adhesion energy γ). More specifically, by minimizing the total energy of the system one finds that

$$h_m/R \propto \left(\frac{\gamma}{E_{2D}} \right)^{1/4}. \quad (3)$$

Therefore, the bubble’s aspect ratio is only a function of the 2D crystal/substrate pairing, irrespective of each bubble’s size. Given that, as discussed in the following, the maximal strain present in a dome/

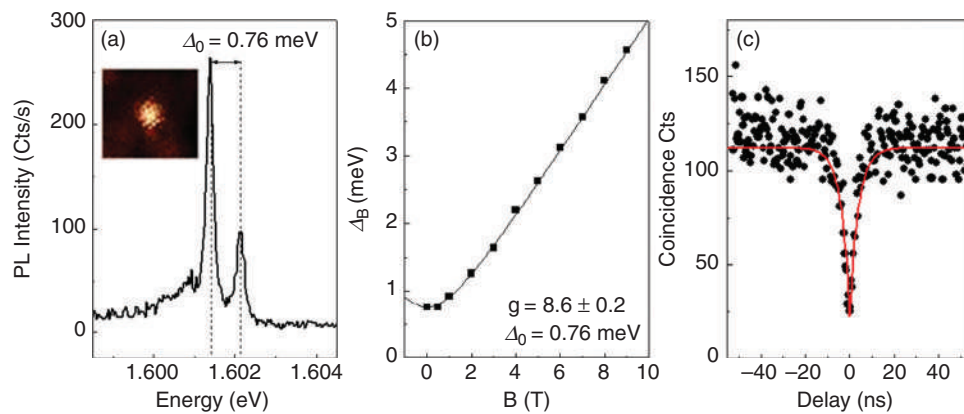


FIG. 15. Magnetic field dependence and antibunching behavior of a typical PL line associated with a nanoemitter obtained by cold stamping. (a) High-resolution micro-PL spectrum of the nanoemitter. The inset is the 2D spatial micro-PL scan of the emitter. The two peaks of the doublet are the zero-field fine-structure splitting components. (b) Magnetic field dependence of the Zeeman splitting ($B \leq 9$ T) in Faraday geometry. (c) Second-order autocorrelation function $g^{(2)}(\tau)$ of the PL line shown in (a) under nonresonant CW excitation, showing pronounced photon antibunching [$g^{(2)}(0) = 0.2$; the photon recovery time is 3.8 ns]. No bunching behavior is visible up to delay times of $1 \mu\text{s}$, indicating that the quantum emitter is not affected by blinking. Reprinted with permission from Shepard *et al.*, 2D Mater. 4, 021019 (2017). Copyright 2017 IOP Publishing Ltd.¹²²

bubble structure is proportional to the square of its aspect ratio. Hence, the strain distribution within a bubble—and, thus, its PL emission—is also expected to be universal for every bubble formed on a specific 2D material/substrate combination. Such uniformity, paired with the smooth variation of the strain tensor across the dome's surface, makes these bubbles ideal “guinea pigs” for the investigation of the effects of strain on the properties of 2D materials. In Ref. 110, for example, the energy of the PL emission from all the bubbles created on a flake was indeed found to be very uniform, and to agree rather well with the strain-induced bandgap reduction expected for a given monolayer/substrate pairing (see Fig. 16).

It is worth mentioning that similar, contaminant-filled bubbles can also be obtained via the modified exfoliation technique described in Ref. 133: Recently, the formation of bubbles with $>10\ \mu\text{m}$ radius was reported in few-layer flakes obtained with this method.¹¹¹ The sheer size of these bubbles allows for the observation of pronounced oscillations in the PL signal acquired as the laser is scanned across the bubble (see Fig. 17), due to the interference between the photons emitted upwards and those emitted downwards, which are then reflected by the substrate. Moreover, the PL spectra of these bubbles reveal the presence of several peaks—absent in the spectra acquired on the flat part of the 2D flake—associated with direct-gap and indirect-gap (phonon-assisted) transitions. As also suggested by density-functional theory (DFT) calculations, the emergence of these peaks may be ascribed to the effects of strain on the band structure of the multilayer, as well as to the weakening of the interlayer interaction within the curved bubble structure.

The non-planar features that form due to the trapping of contaminants present several advantages, such as their size, uniformity, and durability (lifetimes of more than 1 yr have been reported, see, e.g., Ref. 111). However, their formation is both inherently stochastic—and, thus, hard to control—and dependent on the presence of undesired, extraneous substances on the substrate. A cleaner

alternative, which also offers the possibility to control the size, position, and shape of the fabricated structures, is represented by *hydrogen-filled* bubbles (or *domes*), obtained by irradiating the sample with ionized H.^{112,134} In TMD materials, indeed, the exposure of bulk (3D) flakes to a low-energy ($\sim 20\ \text{eV}$) H^+ flux results in the formation of very stable (up to 3 yr), 1 ML-thick micro- and nanodomes on the sample surface (see Fig. 18).

As sketched in Fig. 19, indeed, TMDs are permeable to protons, but not to H_2 molecules.¹³⁵ As a result, protons penetrate through the top basal plane, becoming confined in the first interlayer region. Therein, the production of H_2 takes place—according to the hydrogen-evolution-reaction $2\text{H}^+ + 2\text{e}^- \rightarrow \text{H}_2$ —and hydrogen molecules remain trapped underneath the top monolayer. The local exfoliation of the uppermost monolayer associated with the formation of each TMD nanodome results in an indirect-to-direct bandgap transition (see Sec. IV A) and, thus, in efficient light emission at room temperature and beyond (up to at least $510\ \text{K}$)¹¹².

In addition, the large sizes reached by these features (see, e.g., Fig. 18), displaying domes with diameters of several micrometers, make it possible to map the domes' properties with conventional optical techniques, such as micro-PL and micro-Raman. By performing such mappings, then, it is possible to continuously trace the evolution of the properties of the curved 2D material as a function of the strain gradient present across the dome. As we will discuss in more detail in Sec. IV A, this enabled the first experimental observation of the direct-to-indirect transition theoretically predicted to occur in TMD MLs under tensile strain.¹³⁴

Furthermore, the size and position of the fabricated domes can be precisely controlled by covering the sample surface with an H-opaque mask, patterned with holes defined by electron-beam lithography (see Fig. 20). Notably, in such patterned samples, it is also possible to tune the amount of strain in the domes, by carefully balancing the hole size and the H dose employed.¹¹³ As previously discussed, indeed,

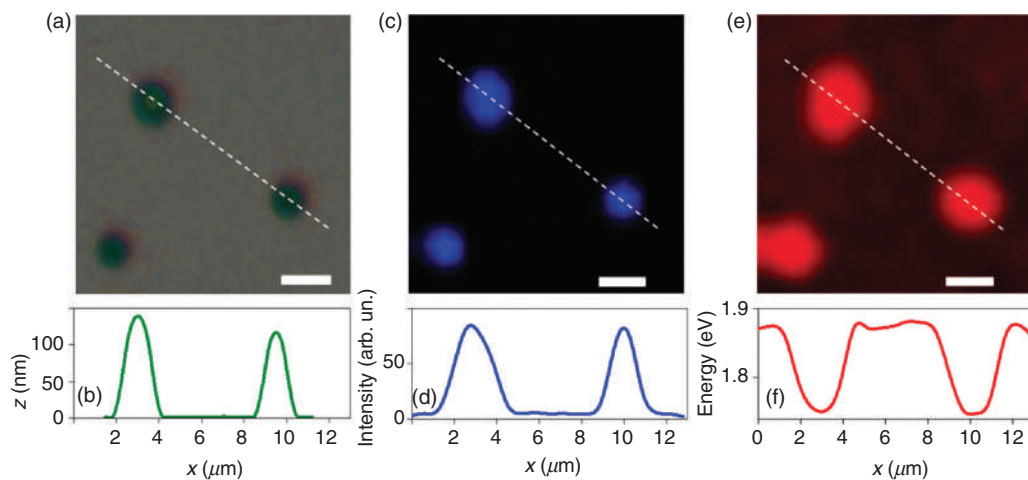


FIG. 16. (a) Optical micrograph of three bubbles formed in a MoS₂ monolayer deposited on a graphite substrate. The scale bar equal to $2\ \mu\text{m}$ in all panels. (b) AFM profile measured along the white dashed line in (a). (c) Map of the PL intensity in the same region displayed in (a) (the PL signal is integrated in the 1.4 eV to 1.95 eV range). (d) PL intensity profile measured along the white dashed line in (c). (e) Map of the PL peak energy measured in the same region displayed in (a) and (c). The dark color corresponds to the energy of unstrained MoS₂ ($E = 1.88\ \text{eV}$), while red stands for $E = 1.74\ \text{eV}$, the energy expected on top of a strained MoS₂/graphite bubble. (f) PL peak energy profile measured along the white dashed line in (e). Reprinted with permission from Tyurnina *et al.*, ACS Photonics 6, 516 (2019). Copyright 2019 American Chemical Society.¹¹⁰

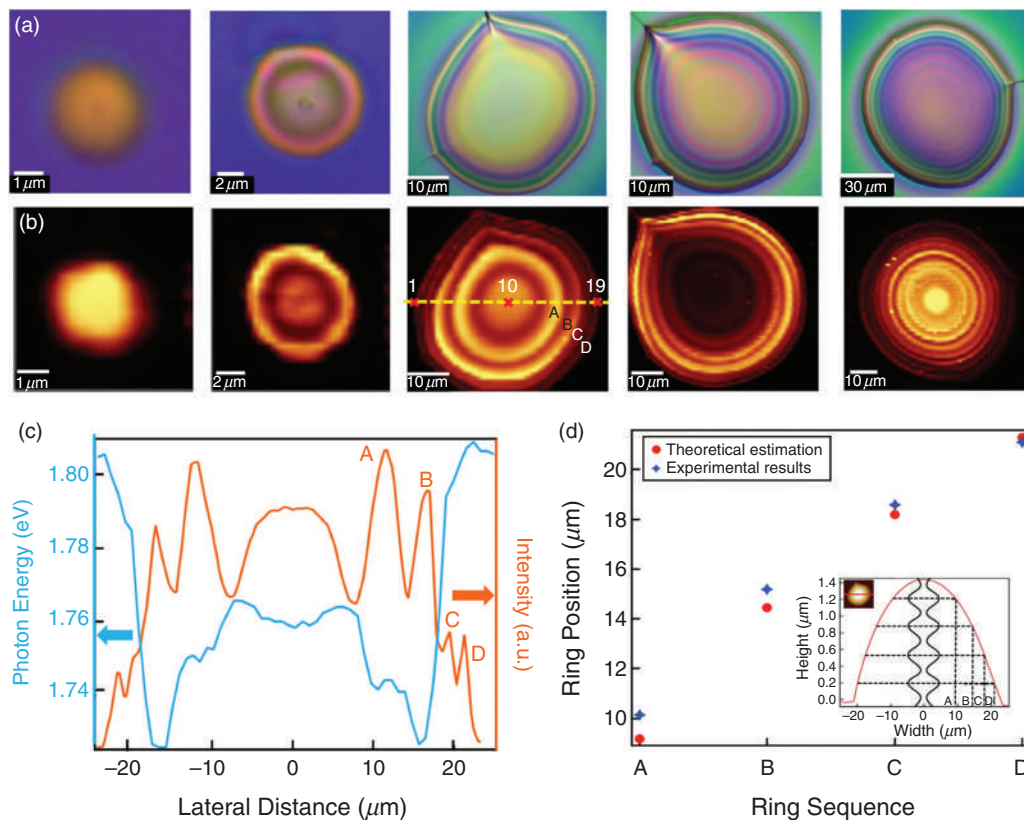


FIG. 17. Interference effects in multilayer MoS₂ bubbles. (a) and (b) are, respectively, optical images and PL mapping images of five different multilayer MoS₂ bubbles. PL intensity mapping images are integrated at 1.75 eV (integration energy window: 0.1 eV). (c) Oscillations of the PL intensity and PL peak position as observed in the MoS₂ bubble shown in the center in (b). (d) Calculated position of interference maxima in the bubble in (c). The inset in (d) is the height profile of the bubble. Adapted with permission from Luo *et al.*, Phys. Rev. Materials 4, 074006 (2020). Copyright 2020 American Physical Society.¹¹¹

the height-to-radius ratio of a bubble/dome (and, thus, the strain distribution on the dome's surface) depends on the interplay between the elastic properties of the dome's "peel," the adhesion forces between the topmost layer and the rest of the flake (supplemented by the additional forces exerted by the H-opaque mask, in the case of patterned samples), and the tendency to expand of the trapped gas, which results in the application of a constant pressure on the dome's walls. By forcing a dome containing a given number of H₂ molecules to grow into a hole with a radius much smaller than its equilibrium radius, then, it is indeed possible to greatly exceed the "natural" height-to-radius ratio of the domes. The domes shown in panel (d) of Fig. 20 for example—grown in holes with size $S = 1 \mu\text{m}$ —sport a h_m/R ratio as high as 0.3, much higher than the value observed in random MoS₂ domes (0.16). In light of the direct dependence of the maximal strain present in a dome on h_m/R (see above), this leads to the possibility of reaching up to $\sim 7\%$ biaxial strain at the dome's summit, close to the rupture limit.

The formation of H-filled bubbles is seemingly possible in many 2D crystals, although the optimal approach to their fabrication may vary from material to material. H-ion irradiation systematically creates ML-thick domes in at least six TMD materials (WS₂, WSe₂, WTe₂, MoS₂, MoSe₂, and MoTe₂¹¹²), whereas in hexagonal boron nitride (h-BN), multilayer bubbles were successfully formed by a H-plasma treatment.¹³⁶ In graphite/graphene, on the

other hand, low-energy H ions preferentially bind to the C atoms toward the formation of graphane,^{137–139} so that these methods do not yield any bubbles, unless much higher proton energies ($\sim 0.5 \text{ MeV}$) are employed.¹⁴⁰ However, even in this case, the resulting structures are not filled with H₂ molecules, but rather with the products of the interaction between the highly energetic protons and the SiO₂ substrate. Curiously, the formation of H-filled, position- and shape-controlled graphene nanobubbles was recently obtained with an innovative approach, almost diametrically opposed to H irradiation. After growing graphene on a H-terminated Ge surface, indeed, Jia and coworkers¹⁴¹ were able to obtain a controlled release of H from the substrate, by scanning the (graphene-covered) sample surface with a voltage-biased AFM tip. The desorbed H atoms then evolve into H₂ molecules, which—once again—remain trapped underneath the impenetrable 2D layer. The superior maneuverability of the AFM tip allows for controlling each nanobubble's position with a precision of a few nm, whereas the dependence of the H desorption rate on the applied bias voltage provides a fine-tuning knob for the nanobubble's height. A few examples of the patterns attainable with this approach are displayed in Fig. 21. As apparent in Table II, blistering too may lead to high strain values with the advantage of a quite long stability of the deformed membrane.

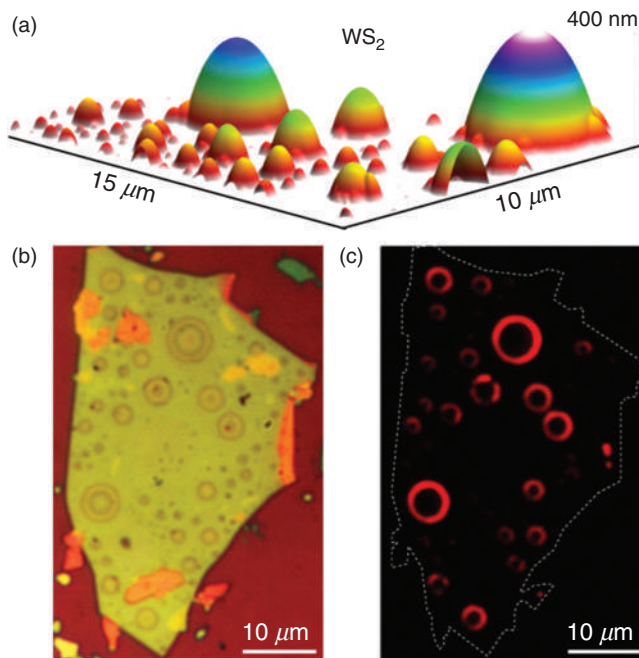


FIG. 18. (a) 3D AFM image of a bulk WS_2 flake irradiated with hydrogen ions (dose $d_H = 4 \times 10^{16} \text{ H}^+/\text{cm}^2$), showing the formation of many domes across the sample's surface. (b) Optical image of a WS_2 flake, where many relatively large domes formed after proton irradiation ($d_H = 5 \times 10^{16} \text{ H}^+/\text{cm}^2$). (c) Laser-excited red luminescence coming from the same flake shown in (b). Reprinted with permission from Blundo *et al.*, *Phys. Rev. Research* **2**, 012024 (2020). Copyright 2020 Author(s), licensed under a Creative Commons Attribution 4.0 International License.¹³⁴

E. Hydrostatic pressure

The methods discussed so far are characterized by a large non-isotropic character of the applied stress. A method to induce large, ideally isotropic, modifications of the interatomic distances in solids is provided by the application of hydrostatic pressure P .¹⁴² The latter causes an equal compression of the crystal along all the three spatial directions and can be handily treated by theoretical methods, which very often exploit P -based studies as a model benchmark. Hydrostatic pressure can be achieved by clamp cells (that permit an excellent control of the pressure up to few GPa¹⁴³) and, more frequently, by diamond anvil cells (DACs), where P values as high as hundreds of GPa can be reached.¹⁴⁴ In DACs, two oppositely aligned beveled diamond anvils are pushed against a sample immersed into a pressure-transmitting medium, usually made of, e.g., a noble gas or silicone oil or a methanol-ethanol mixture to allow optical and transport measurements [see Fig. 22(a)]. DACs can also be used as a means to induce an out-of-plane compression of 2D materials,¹⁴⁵ contrary to most of the approaches based on in-plane tension described before. In the present context, it is of particular interest the use of hydrostatic pressure to induce a semiconductor to metal transition at a critical value P_t in bulk van der Waals crystals, like MoS_2 ($P_t \approx 20 \text{ GPa}$),^{146–148} WSe_2 ($P_t \approx 30\text{--}60 \text{ GPa}$),¹⁴⁹ MoSe_2 ($P_t \approx 26 \text{ GPa}$),¹⁵⁰ GaSe ($P_t \approx 30 \text{ GPa}$),¹⁵¹ ReSe_2 ($P_t \approx 35 \text{ GPa}$),¹⁵² and SnSe_2 ($P_t \approx 15 \text{ GPa}$).¹⁵³ The metallization was ascribed to the increasing chalcogenide atom interactions in MoS_2 ¹⁴⁶ and MoSe_2 ¹⁵⁰ associated with the pressure-

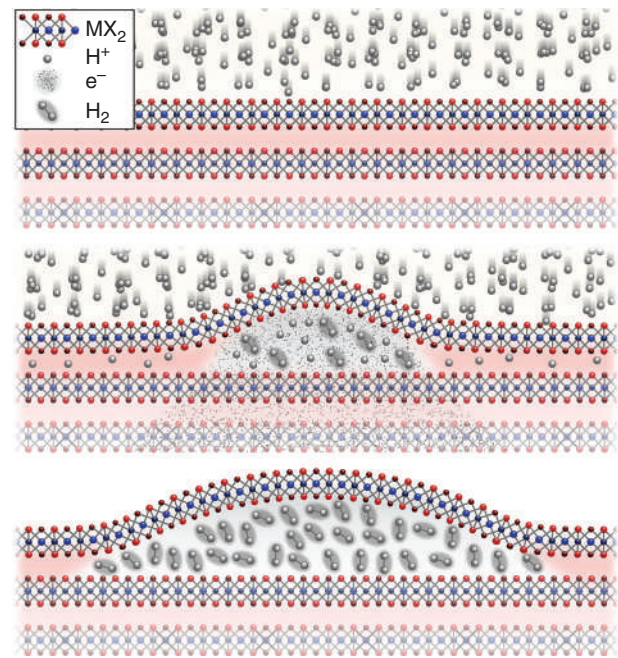


FIG. 19. Sketch of the process leading to the formation of monolayer-thick domes following H^+ irradiation (see main text). Reprinted with permission from Tedeschi *et al.*, *Adv. Mater.* **31**, 1903795 (2019). Copyright 2019 Wiley-VCH Verlag GmbH & Co. KGaA, Weinheim.¹¹²

induced reduction of the intralayer distance. Instead, a P -induced isostructural phase transition from $2H_c$ to $2H_a$ was deemed as the cause of the crystal metallization in WSe_2 ¹⁴⁹ and MoS_2 .¹⁴⁷ Structural phase transitions were also found to accompany the metallic character of the material above a given P in InSe ¹⁵⁴ and GaSe ,¹⁵¹ while no evidence of a similar phenomenon was reported at the semiconductor-to-metal crossover for SeSe_2 ¹⁵³ and ReSe_2 .¹⁵²

A more complicated situation may occur when the crystal thickness approaches the monolayer limit. In that case, the very small lateral surface of the monolayer might lead to a less effective force transmission as compared to that established on the top surface; see Fig. 22(b). Consequently, a deviation of the overall stress from pure hydrostatic could happen.¹⁵⁵ This can be avoided by encapsulation of the monolayer by h-BN ¹⁵⁵ that increases the 2D material effective thickness. Alternatively, monolayers are deposited directly on the diamond anvil surface^{156–159} rather than on Si/SiO_2 substrates. Indeed, these latter were found to add extra strain, thus unbalancing the ideal hydrostatic condition and introducing intralayer distortions apparent as a splitting and softening of the Raman modes.^{159,160} It is worth mentioning that DACs allow reaching strain values that can remarkably exceed those that a 2D crystal subjected to an in-plane stress can withstand before fracturing occurs, typically $\sim 10\text{--}20\%$, see Table II and Ref. 161. Compressive in-plane strains as large as $>30\%$ were deduced for applied pressures of about 30 GPa in WS_2 ¹⁶² and MoS_2 .^{158,162} Such large strains would enable the semiconductor-to-metal transition in TMD monolayers that, e.g., are predicted to occur at 86 GPa in WS_2 ¹⁶² and 68 GPa in MoS_2 ^{158,162} with an in-plane strain of about 50% in both instances.

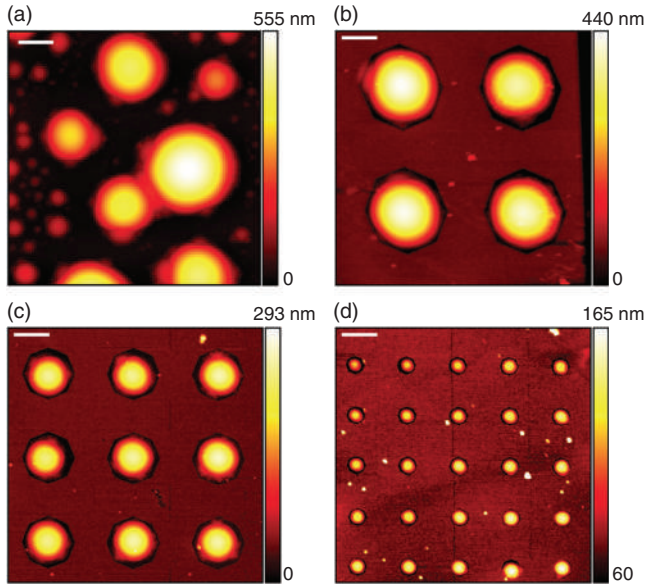


FIG. 20. Formation of random and patterned arrays of MoS₂ domes. (a) AFM image of a 15 × 15 μm² area of a H-irradiated MoS₂ flake. Many domes with different dimensions (the largest dome has a footprint diameter $D = 6.03$ μm) formed on the flake surface following the irradiation process. The aspect ratio for these domes varies between about 0.14 and 0.18. (b)–(d) Same as (a), for MoS₂ flakes patterned with an 80 nm-thick mask with openings of size (b) $S = 5$ μm, (c) 3 μm, and (d) 1 μm. The diameter of the domes is in this case determined by the size of the opening, and higher aspect ratios with respect to the random domes are obtained, as discussed in the main text. The scale bars correspond to 2 μm, while the origin of the z-axis is set at the flake surface. Reprinted with permission from Blundo *et al.*, *Adv. Mater. Interfaces* **7**, 2000621 (2020). Copyright 2020 Wiley-VCH Verlag GmbH & Co. KGaA, Weinheim.¹¹³

III. CONTROLLED STRAIN FROM MECHANICAL DEFORMATIONS

Leaving aside the intrinsic generation of local strains from the local breaking of the crystal structure (vacancies, dislocations, edges, corrugations, etc.), the techniques described in Sec. II share the common aim of engineering a designed strain profile by means of controlled mechanical deformations. However, such a task can be accomplished in a successful way only when the characterization of the morphological properties (heights/radii of bubbles, bending angles, patterning of the substrate, etc.), can be translated in a compelling way in the tailored profile of the strain tensor. In most cases, the applied mechanical deformation acts on the scale of micrometers or tenths/hundredths of nanometers, i.e., much larger than the interatomic scales of the crystal structure. Within this context, the theory of elasticity and membranes^{163,164} provides a powerful way to determine the strain tensor—eventually also on the local scale—from the knowledge of the morphological profile of the two-dimensional compound.

As a benchmark example, in order to highlight the basic physical concepts governing the strain, we consider a two-dimensional sheet with infinitesimally small thickness t and assume that the sheet is initially flat in the absence of mechanical deformations. Thus, we consider an out-of-plane deformation profile $h(x, y)$, with h much smaller

than the characteristic length over which h itself varies. The strain tensor $\bar{\epsilon}(x, y)$ can be thus evaluated as¹⁶⁴

$$\epsilon_{ij}(x, y) = \frac{1}{2} \left[\frac{\partial u_j(x, y)}{\partial r_i} + \frac{\partial u_i(x, y)}{\partial r_j} + \frac{\partial h(x, y)}{\partial r_i} \frac{\partial h(x, y)}{\partial r_j} \right], \quad (4)$$

where $i = x, y$ and $r_x = x, r_y = y$. A key role is played here by the displacement vector $\vec{u}(x, y)$, which is not an independent quantity, but it is ruled itself by the out-of-plane displacement $h(x, y)$ as a consequence of energy minimization. The previous description applies well for a wide variety of cases, e.g., bending, bulging, wrinkling upon release of an elastic substrate, indenting, deposition on pillars, blistering, and inflated bubbles. However, the specific determination of the profile $h(x, y)$ depends on the specific case, on material-dependent parameters (e.g., bending energy, effective membrane thickness, etc.), and on external conditions (e.g., adhesive energy needed to detach the membrane from the substrate, external and internal pressure of the bubbles, temperature, etc.). Generally, the knowledge of the out-of-plane profile $h(x, y)$ is determined by experimental techniques (most frequently, by scanning probe microscopy) or by computational/analytical considerations. On the ground of such input, the displacement vector $\vec{u}(x, y)$ can be obtained by minimizing the classic elastic energy $E[\vec{u}, h]$ with respect to $\vec{u}(x, y)$. The elastic energy is given by

$$E[\vec{u}, h] = \frac{1}{2} \lambda \int d\mathbf{r} (\epsilon_{xx} + \epsilon_{yy})^2 + \mu \int d\mathbf{r} (\epsilon_{xx}^2 + \epsilon_{yy}^2 + 2\epsilon_{xy}\epsilon_{yx}), \quad (5)$$

where λ and μ are the Lamé elastic coefficients and where the strain elements are related to the mechanical deformation via Eq. (4). The same equation can be equivalently expressed in terms of the Poisson's ratio (ν) and the 2D Young's modulus (E_{2D}) of the material, given that for a 2D membrane $\lambda = \nu E_{2D}/(1 - \nu^2)$ and $\mu = E_{2D}/(2 + 2\nu)$. Upon minimization with respect to u_x , we obtain, for instance,

$$\begin{aligned} & -(\lambda + 2\mu)\partial_x^2 u_x - \lambda\partial_x\partial_y u_y - \mu\partial_y^2 u_x - \mu\partial_x\partial_y u_y \\ & -(\lambda + 2\mu)(\partial_x h)(\partial_x^2 h) - \lambda(\partial_y h)(\partial_x\partial_y h) - \mu(\partial_x h)(\partial_y^2 h) \\ & -\mu(\partial_y\partial_x h)(\partial_y h) = 0, \end{aligned} \quad (6)$$

where the implicit notation $\partial_i = \partial/\partial r_i$, $\partial_i^2 = \partial^2/\partial r_i^2$ has been employed. A similar equation holds true while minimizing with respect to u_y , upon exchange of the labels $x \leftrightarrow y$. It should also be noted that the same equations can be obtained by imposing force equilibrium conditions.¹⁶⁵

Equation (6)—together with boundary conditions—can be used to evaluate the lattice displacements provided that the height profile is known, and afterwards the strain tensor, by computational means (such as finite-element-based tools)^{112,113,165–167} or, when affordable, by means of analytical approaches.^{35,115,131,132,165,168}

We will now discuss the strain distribution in some specific cases, where strain is applied using the methods described in Sec. III. In general, we can define two major families: that of *uniform strains* and that of *non-uniform strains*.

A. Uniform strains

Uniform strains are achieved whenever the method employed to deform the membrane acts on the device length scale rather than on

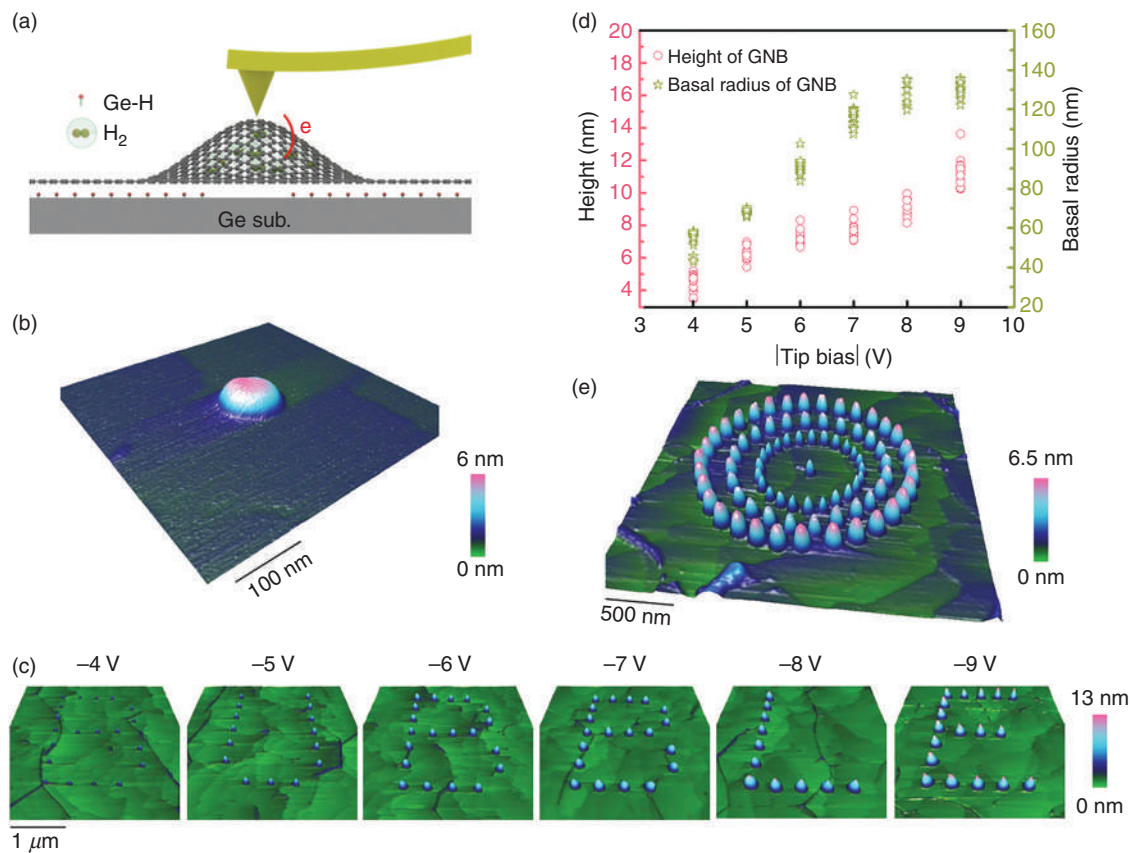


FIG. 21. Graphene nanobubbles (GNBs) obtained by AFM tip (see main text). (a) Sketch of the fabrication process. (b) A single GNB, obtained with an AFM tip with a bias voltage of -5 V. (c) “Bubble” pattern of GNBs, created with bias voltages ranging from -4 V to -9 V scanning in contact mode. (d) Height and basal radius of the fabricated GNBs [extracted from the AFM images in (c)] as a function of the tip bias. (e) Corral pattern of GNBs, created with the AFM tip working in ramp mode. The tip voltages applied to create GNBs located in the inner, middle, and outer loops are -6 , -7 , and -8 V, respectively. Reprinted with permission from Jia *et al.*, *Nat. Commun.* **10**, 046801 (2019). Copyright 2019 Author(s), licensed under a Creative Commons Attribution 4.0 International.¹⁴¹

the scale of the 2D material. This is obviously the case of stretching devices, where the entire substrate expands or contracts. This is also the case of growth techniques, whenever the 2D material is grown on a flat substrate (as in Fig. 7). Finally, uniform strains are also achieved in bending devices, since the whole substrate is bent. In this case, the strain magnitude in the bending direction ε can be easily quantified analytically according to Eq. (1), as also shown in Fig. 23(a). It should be noticed that this quantity accounts only for the deformation in the bending direction and not for the total strain acting on the 2D membrane. The membrane will in fact compress in the perpendicular direction by $\nu\varepsilon$, so that the total strain will be given by $\varepsilon_{\text{tot}} = (1 - \nu)\varepsilon$. Indeed, it is questionable whether it is more correct to use the Poisson’s ratio of the 2D material or that of the substrate, and the matter is complicated since there might not be a unique solution to this problem, rather depending on the specific device. We will focus in more detail on this issue when discussing how strain affects the vibrational properties of 2D materials, since a comparison between DFT calculations and experimental results can help us in understanding which is the best choice of the Poisson’s ratio. For the present moment,

we recall that the Poisson’s ratios of the substrates commonly used in the devices are typically in the range of 0.3 to 0.4, while the Poisson’s ratios of 2D materials—estimated via DFT calculations^{169–171}—are listed in Table III.

The uniform nature of the strain distribution achieved in bending devices is confirmed by optical measurements such as those displayed in Fig. 23(b), showing a homogeneous redshift of the photoluminescence peak all throughout a bent MoSe_2 monolayer.

In all the cases mentioned here, the strain can be typically estimated numerically, provided that there is good adhesion between the 2D material and the substrate and sliding effects are negligible.

B. Non-uniform strains

Non-uniform strains are achieved whenever the 2D membrane is mechanically deformed at the micro–nano scale. This happens in growth techniques where pre-patterned substrates are used (as in Fig. 5) or where superlattices are grown (as in Fig. 6). Indeed, the same happens if the 2D material is deposited on a patterned substrate (such

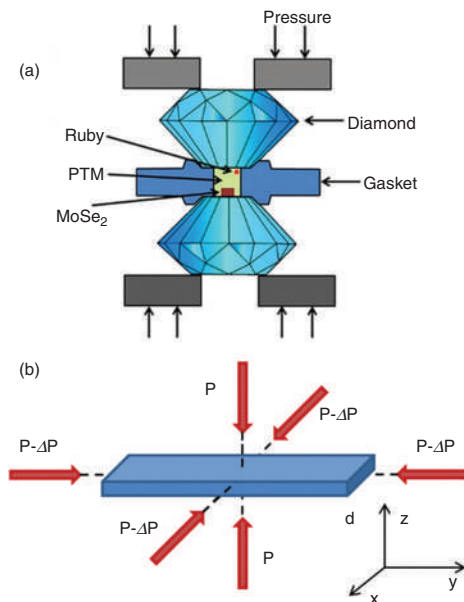


FIG. 22. (a) Sketch of a diamond anvil cell (DAC). The sample, indicated as MoSe₂, is inserted between two diamond anvils and immersed in a pressure transmission medium (PTM) enclosed by a gasket. A ruby crystal is included in the PTM. The *P*-induced wavelength shift of the ruby crystal is used to monitor the pressure acting inside the DAC. Reprinted with permission from Fu *et al.*, *J. Phys. Chem. Lett.* **8**, 3556 (2017). Copyright 2017 American Chemical Society.¹⁵⁷ (b) Schematic representation of the stress components acting on a crystal with a very small thickness compared to its surface. ΔP indicates the increasing deviation from the hydrostatic situation ($\Delta P = 0$) occurring as the sample thickness approaches the single atomic layer thickness. Reprinted with permission from Franciscó-Lopez *et al.*, *Pap. Phys.* **11**, 110005 (2019). Copyright 2019 Author(s), licensed under a Creative Commons Attribution 4.0 International License.¹⁵⁵

as on nanocones, pillars, etc., see Figs. 1, 2, and 3). Non-uniform strains are indeed also achieved by indenting the membrane (as in Fig. 11) or whenever the 2D membrane is bent locally, at the nano-/micro-scale, such as in the case of wrinkles [see Fig. 14(e)] or bulges/blisters/bubbles (see Figs. 16–21). In all these situations, it is generally difficult to calculate the strain distribution analytically, and numerical methods generally need to be employed.

Analytical methods have proved particularly useful in the case of inflated bubbles or nano-tents (obtained by deposition on pillars) that present, to a good degree of approximation, a circular symmetry.^{35,131,132,165,168} In such systems, Hencky and Fichter's analytical model^{68,165,174} predicts that the strain is maximum at the summit of the bulge, and in that point, it is proportional to the square of the aspect ratio of the structure

$$\varepsilon_m = f(\nu) \cdot (h_m/R)^2, \quad (7)$$

where *f* is a function just of the Poisson's ratio of the 2D material, ν , while *R* and *h_m* are the bulge footprint radius and maximum height, respectively. A set of Poisson's ratios is provided in Table III, while for 2D materials *f*(ν) typically takes values in between 0.72 and 0.74. The values of *f* for several TMDs can be found in Ref. 112. Generally, the summit is the only point where the strain is isotropic, while it tends to

become strongly anisotropic as soon as the considered point moves toward the edge of the bulge. Therefore, while Eq. (7) provides a simple analytical expression at the summit, it is generally non-trivial to evaluate the strain distribution across the whole deformed region. Given the spherical symmetry of the systems considered here, it is convenient to introduce a polar coordinate system,^{112,165} where the strain tensor components can be defined as shown in Fig. 23(c). Figure 23 highlights the radial (ε_r) and circumferential (ε_θ) components that add up to give an in-plane strain $\varepsilon_{\text{tot}} = \varepsilon_r + \varepsilon_\theta$.^{112,134} Theoretical calculations highlight the isotropic response of the band structure of semiconducting 2D materials, such as TMDs, to strain¹⁷⁵ independently of the considered direction, therefore, the total in-plane strain is the relevant quantity to be considered when studying the optical response of the strained system. However, an out-of-plane compressive strain (ε_z) is also expected. The in-plane and out-of-plane strains are related by: $\varepsilon_z = -(D_{13}/D_{33})\varepsilon_{\text{tot}}$, where *D*₁₃ and *D*₃₃ are the pertinent components of the elasticity matrix.¹⁷⁶ The matrix elements for most 2D materials can be found either in Ref. 112 or Refs. 169–171. The whole strain distribution can be calculated analytically^{35,132,165,168} under specific assumptions on the height profile and on in-plane displacement vector or strain components, though the necessity to start from specific assumptions limits the accuracy of the analytical solutions.¹⁶⁵ Therefore, for a more accurate solution, numerical calculations are generally employed.^{112,113,165,166,177,178} These latter allow on the one side to simulate the height profile, showing excellent agreement with the experimental data^{112,113} [see top left inset of Fig. 23(c)]; on the other side, they allow us to calculate the strain distribution, as displayed in Fig. 23(d). The calculations reveal how fully isotropic and fully anisotropic strains are obtained in the two limiting cases at the bulge center and edge: At the center, the in-plane tensile strain is equibiaxial with $\varepsilon_r = \varepsilon_\theta = \varepsilon_m$, the maximum strain ε_m being given by Eq. (7); at the edges, the strain is purely uniaxial ($\varepsilon_r = 0$ and $\varepsilon_\theta \neq 0$), respectively. The strain values at a generic distance *r* from the center vary between these two limits. Optical measurements performed on 2D-material bubbles confirm the exactness of the numerical solution, as we will discuss in Sec. IV B.

It should be noticed that numerical calculations can generally be employed to derive the strain tensor components not only for spherically symmetric structures, but also for general anisotropic deformations at the micro-/nanoscale, as discussed in Ref. 166.

Note that at this stage, both in the case of the uniform and non-uniform cases discussed above, the spatial dependence of the strain tensor $\vec{\varepsilon}(x, y)$ is dictated only by the mechanical properties, and it is quite general for any class of materials, provided that few elastic parameters are known, such as the Lamé's coefficients or the Poisson's ratio, the bending rigidity, and the sample thickness. The next step, i.e., the quantification of the effects of strain on the electronic/optical properties, is a more delicate issue, which is strongly material-dependent since it is ruled by the electronic structure, the crystal orientation, etc.

As a general rule, such a task is addressed in the literature at different levels of approximations. (i) At the most basic (but often very effective) level, exploiting the fact that in some of the most employed experimental configurations (such as in the bending setups) mechanical deformations occur at scales much larger than the crystal structure characteristic lengths, the strain is implicitly assumed to be homogeneous. Within this context, the strain effects on the physical properties

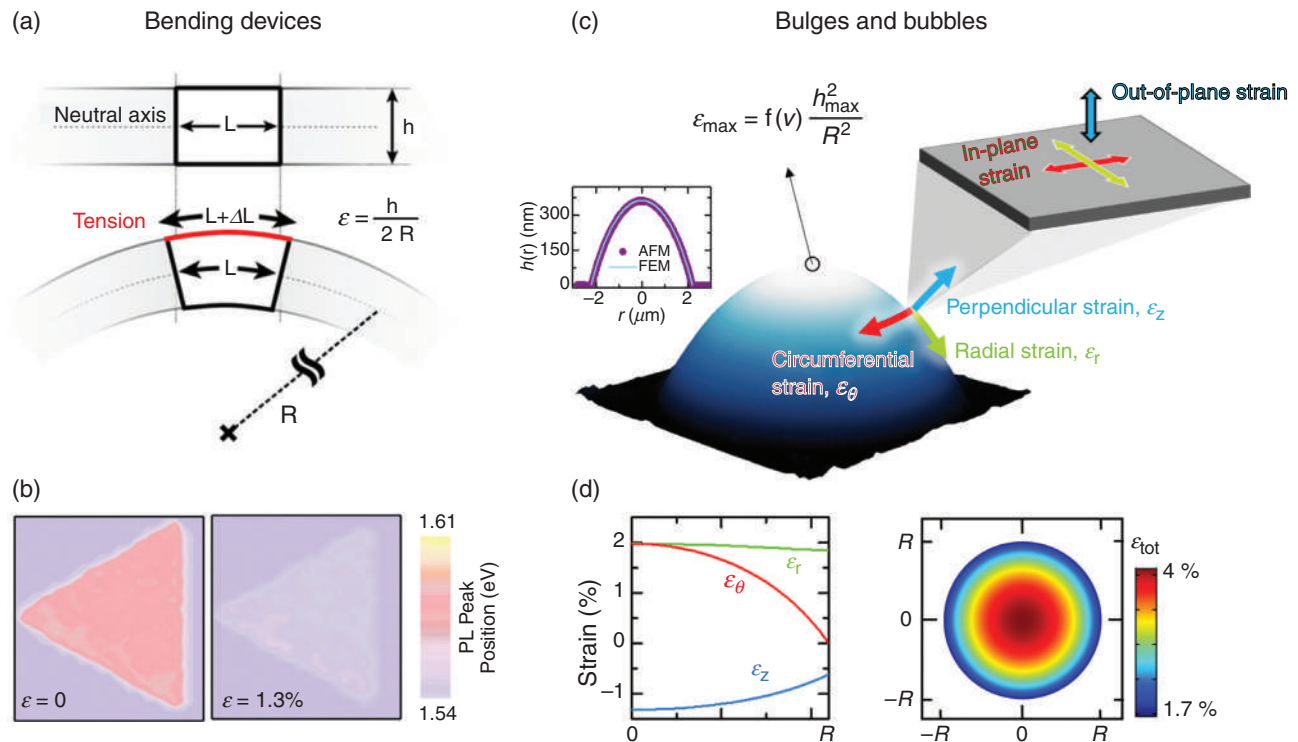


FIG. 23. (a) Sketch of the deformation applied to a flexible substrate in a bending device. Bending results in a tensile strain on top of the device, quantified by the equation displayed. Adapted with permission from Schmidt *et al.*, 2D Materials 3, 021011 (2016). Copyright 2016 IOP Publishing Ltd.²⁹⁰ (b) Photoluminescence (PL) mapping of an unstrained MoSe₂-ML grown by CVD (left) and of the same ML under 1.3% of strain applied via a bending device (right). A homogeneous PL peak shift is observed, demonstrating a uniform strain distribution. Reprinted with permission from Liang *et al.*, Nano Lett. 17, 7539 (2017). Copyright 2017 American Chemical Society.²⁹² (c) AFM image of a TMD monolayer dome—obtained by the hydrogen-induced blistering method¹¹² described in Sec. II D—as representative of the bulging and blistering methods. The maximum strain is achieved at the summit and is given by Hencky's equation, displayed in the same panel. Across the surface of the bulge, the strain tensor components can be defined in a spherical coordinate system, as illustrated. Inset: Comparison between the height profile measured by AFM and calculated via FEM numerical calculations, for a MoS₂ bubble. (d) Strain tensor components (left) and total in-plane strain ($\epsilon_{\text{tot}} = \epsilon_r + \epsilon_\theta$) calculated numerically for the MoS₂ bubble shown in the inset of panel (c). The inset of panel (c) and panel (d) were adapted with permission from Blundo *et al.*, Adv. Mater. Interfaces 7, 2000621 (2020). Copyright 2020 Wiley-VCH Verlag GmbH & Co. KGaA, Weinheim.¹¹³

are interpreted using concepts based on a homogeneous description, such as a well-defined band structure, *Ab-initio* calculations provide a useful guide in this framework, wherein such properties can be evaluated in a computationally efficient way by applying homogeneous strain on the single unit cell. (ii) At a higher (semi-classical) level of approximation, the same physical concepts based on a uniform strain are still employed, but the strain magnitude is assumed to be spatially modulated by $\vec{\epsilon}(x, y)$. In this perspective, a local band structure is defined, which depends locally on the amount of strain. Such level of analysis has been shown to be particularly useful in describing the strain-dependent funnel effect,¹²⁹ where an electron-hole excitation can migrate coherently or split in different directions according to the strain profile of the conduction and valence band. (iii) At an even higher level of analysis, the spatial modulation of the strain tensor $\vec{\epsilon}(x, y)$ is fundamental not only to locally determine the strain magnitude, but also because it yields a finite in-plane strain *gradient*, which gives rise to effective gauge fields and to a pseudo-electromagnetic electric field.^{19,115,179,180} In this case, the emergence of a novel physics is governed by the *derivative* of the strain tensor. (iv) Finally, in the most extreme cases, as for instance in argon-filled graphene

nanobubbles, the size of the strain modulation can be of the same order of the crystal structure. In this case, concepts such as a well-defined band structure are questionable, and confinement effects crucially enter in play.

The strain-induced physics related to the scenarios (i) and (ii) for some of the most relevant two-dimensional materials (graphene, transition-metal dichalcogenides) is discussed in Sec. IV A, whereas the more complex physics associated with inhomogeneous strain (iii) and its interplay with other degrees of freedom (spin, valley, etc.) will be addressed in Sec. IV G.

IV. PHYSICAL EFFECTS

A. Band structure and electronic properties

A controlled engineering of the band structure is one of the key goals for the field of “straintronics,” which aims at tailoring the physical properties of flexible two-dimensional materials by means of mechanical deformations. The underlying band structure indeed rules not only the most direct electronic features related to quasiparticle properties (transport, magnetism, different kinds of scattering rates

TABLE III. Poisson's ratio ν for the most common 2D materials. Unless otherwise specified, these values were deduced from The Materials Project.^{169,170}

Material	Poisson's ratio (ν)
Graphene	0.176
h-BN	0.223
MoS ₂	0.250
MoSe ₂	0.233
MoTe ₂	0.245
WS ₂	0.219
WSe ₂	0.196
WTe ₂	0.176 ^a
1T-VS ₂	0.18
β -InSe	0.291
γ -InSe	0.264
β -GaSe	0.241
Bi ₂ Se ₃	0.266
Bi ₂ Te ₃	0.244
BP	0.23 (bulk), -0.93 (ML) ^b

^aThis value was derived from the elastic matrix elements calculated in Ref. 171.

^bWhile a positive value of ν has been reported for bulk BP in some works,^{169–172} a negative value has been calculated for single layers of BP.¹⁷³

depending on the electronic density of states, etc.), but also the particle-hole excitations governing optical and dielectric features, as well as the strength of the particle–particle coupling responsible for a possible superconducting pairing.

Given the variety of different band structures present in 2D materials, the aims of strain engineering are different according to the peculiar characteristics of the electronic properties of each material. In monolayer graphene, for instance, the low-energy electronic dispersion is described by Dirac cones, which touch at the Fermi level at the K and K' points. Due to the absence of a bandgap, the aim of external strains is the possible opening of a controlled gap, and, at a second instance, the manipulation of the Dirac properties (e.g., anisotropy induced by uniaxial strain). TMDs, on the other hand, present an intrinsic gap whose magnitude and nature (direct vs indirect) depend significantly on the number of layers and on external fields (e.g., applied electric fields). In this context, strain engineering aims at providing a powerful and reversible way to manipulate such bandgap features, eventually inducing also metal-insulator transitions.

Given the layered and two-dimensional nature of the materials under consideration, the majority of theoretical and experimental works have focused on the application of in-plane strains (biaxial or uniaxial strain). More recently, the analysis of the out-of-plane strain (meant as compression between different layers in multilayered systems, or as vertical compression of the unit cell atoms in single-layer systems) has spawned a new research direction, also aimed at the investigation of the effects of the presence of a *strain gradient* along different layers. A comprehensive understanding of the distinct roles played by these different effects of strain is fundamental, since in realistic strain setups—involving for instance bending, folding, and conformal growth on substrates—these effects often occur concomitantly, all acting at the same time and possibly interfering with each other.

1. Graphene

Ideally flat (suspended) graphene, because of its bipartite lattice and its symmetries, is well known to be a semimetal with two linear Dirac cones being established at the K and K' corners of the Brillouin zone (see Fig. 24).¹⁸¹ The Dirac velocity v of such cones is dictated by the interatomic hopping processes (e.g., $t_0 \approx 3$ eV for nearest neighbor hopping), which rules also the electronic density of states (DOS) $N(\mu) \propto |\mu|/v^2$ at finite chemical potential μ . Experimental estimates of v can be achieved for instance by means of scanning tunneling microscopy (STM)¹⁸² or by measuring magnetic oscillations in transport and/or thermodynamical properties.¹⁸³

Homogeneous biaxial strain preserves of course all the symmetry of unstrained graphene, leading to a mere redefinition of the Brillouin zone.¹⁸⁴ The only physical effect of strain would be thus a relative change in the value of v and in the associated physical observables. In realistic strain setups, however, strain effects are often concomitant with other environment manipulations (e.g., interplay with the substrate), which will affect the Dirac velocity, as well. Detecting biaxial strain disentangled by other additional effects appears thus unrealistic. More promising and interesting is a controlled tuning of the physical properties of graphene by means of uniaxial strain. Since a generic uniaxial strain does not lift the symmetries responsible for the Dirac physics, the semimetal nature of graphene is preserved even in the presence of uniaxial strain,¹⁸⁵ which however leads to a *shift* of the Dirac point away from the K and K' corners.^{186–189} Such shift is accompanied by an *anisotropy* of the Dirac velocity in the directions parallel and perpendicular to the applied strain.^{188,190,191} Eventually, for very large strains (~ 23 – 28%), the Dirac cones at K and K' can merge, resulting in a gap in the band structure.^{186–189} Such large-strain magnitudes are however at the limit of the lattice stability and are not yet achievable nowadays.^{189,192}

More promising, in the perspective of inducing a controlled bandgap, is the band structure of bilayer graphene, which is also a semimetal but is characterized by two touching upper and lower *parabolic* bands at the K and K' points, rather than linear Dirac cones. In this case, a sizeable bandgap can be opened—and tuned in a suitable way—in a field-effect geometry, by applying a bias electric field that breaks the degeneracy of the upper and lower

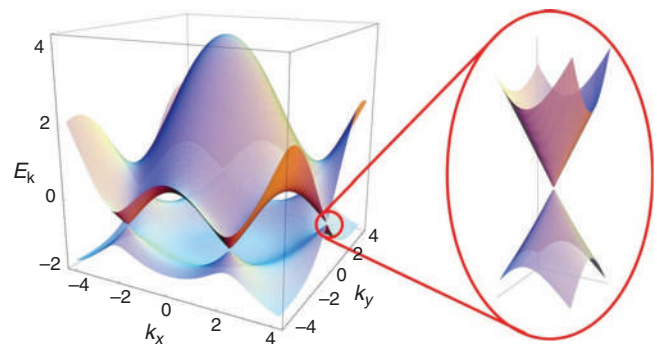


FIG. 24. Band structure of monolayer graphene displaying Dirac cones at K and K' points. Reprinted with permission from Castro Neto *et al.*, *Rev. Mod. Phys.* **81**, 109 (2009). Copyright 2009 American Physical Society.¹⁸⁴

graphene planes.^{193,194} A similar effect can be achieved by means of layer-dependent strain, which has shown the ability to open a gap and even, under biased conditions, to give rise to a “skewed double-well” band structure, resulting in physical effects typical of finite-DOS semimetals.^{195,196}

2. Semiconducting transition-metal dichalcogenides MX_2

Band-structure properties. Semiconducting transition-metal dichalcogenides MX_2 ($M = \text{Mo}, \text{W}, X = \text{S}, \text{Se}$) differ drastically from graphene since they present a gapped band structure, with the gap magnitude varying with the number of layers. In the most studied material, MoS_2 , the bandgap varies from 1.90 eV in the monolayer system to 1.29 eV in the bulk (infinite-layer) case (Fig. 25). Quite interestingly, also the bandgap nature (direct- vs indirect-gap) can be tuned with the number of layers N , where monolayer compounds typically show a direct gap, and systems with $N \geq 2$ present an indirect gap,^{197–200} as highlighted in Fig. 25. The possibility of tuning, in a relatively easy way, the direct/indirect character of the gap is due to the presence, in monolayer systems, of secondary band edges in both the valence and conduction bands, with an energy almost degenerate with the primary band edges.

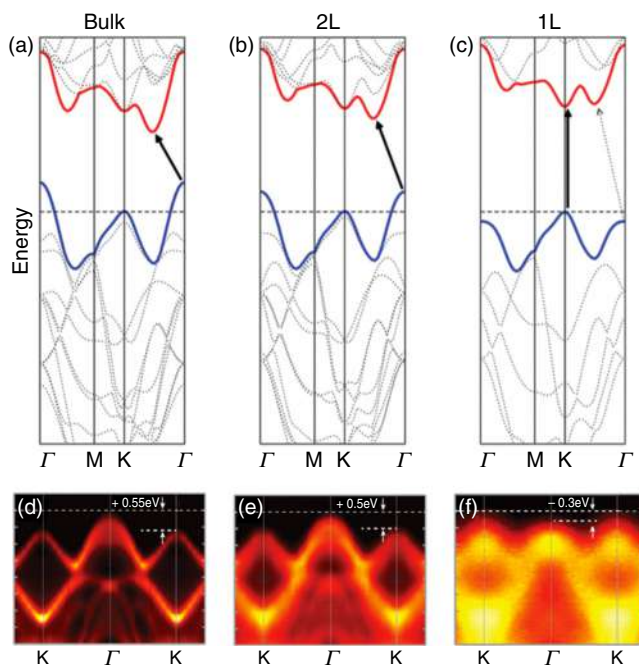


FIG. 25. Evolution of the band structure without spin-orbit coupling (a)–(c) and experimental valence band (VB) measured via angle-resolved photoemission experiments (d)–(f) of MoS_2 as a function of the number of layers N . From left to right: $N = \infty, 2, 1$. The figure highlights how the VB maximum shifts from the Γ point to the K point when achieving the single-layer limit. Panels (a)–(c) were reprinted with permission from Splendiani *et al.*, *Nano Lett.* **10**, 1271 (2010). Copyright 2010 American Chemical Society.¹⁹⁹ Panels (d)–(f) were reprinted with permission from Yuan *et al.*, *Nano Lett.* **16**, 4738 (2016). Copyright 2016 American Chemical Society.²⁰⁰

Single-layer TMD compounds are typically characterized by a direct gap at the K point (see Fig. 25), whereas a secondary band edge slightly higher in energy is present in the conduction band at the Q_{CB} point (Q is midway between Γ and K, in some works it is equivalently referred to as the Λ point), as well as a secondary band edge in the valence band at the Γ_{VB} point. Also noticeable is the spin-orbit splitting of the valence band edge at the K point, as highlighted in the case of WSe_2 in Fig. 26 (see red and magenta dots). Such a splitting is mainly governed by the atomic spin-orbit coupling of the metal atom, and it will therefore result to be stronger for heavier atoms (W rather than Mo; Se rather than S). The spin splitting has direct consequences on the optical transitions, since it gives rise to the so-called A and B excitons, involving the conduction band minimum at K and the upper (for the A exciton) and lower (for the B exciton) spin-split valence band at the K point. Also noticeable is the region of *band nesting*, between the Γ and Q points, characterized by almost-parallel conduction and valence bands.^{201–205} Band nesting gives rise to a high joint density of states for the particle-hole excitations, and it is thought to be responsible for the so-called C exciton.

In multilayer compounds, the interlayer coupling leaves the band structure almost unchanged at the K point, whereas it is mostly effective at the Q and Γ point, producing a sizable split of the energy levels in the bilayer case which will evolve in a finite z -dispersion in the bulk (large-multilayer) limit.

Such striking differences of TMDs with respect to graphene can be related to the different atomic structure. Single-layer graphene can indeed be described by a truly monoatomically thin sheet, whereas single-layer MoS_2 is built up by a plane of metal atoms M sandwiched in between two planes of chalcogen atoms X [see Fig. 27(a)]. Although the relevant low-energy bands are mostly governed by the orbitals of the metal atoms, the interlayer hopping, and eventually the direct/indirect character of the bandgap, are mainly ruled by the outer

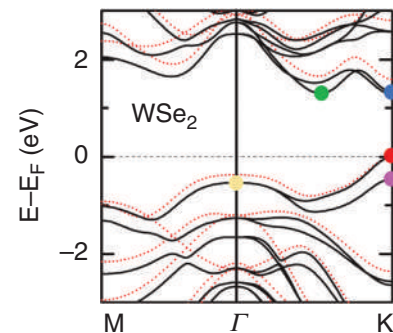


FIG. 26. Band-structure of monolayer WSe_2 with (black solid line) and without (pink dashed line) spin-orbit coupling. The relevant band edges are here marked with colored dots: Primary conduction band at K point (blue dot); secondary conduction band edge at an intermediate point between Γ and K, referred to either as the Q point or as the Λ point (green dot); primary valence band edge at the K point (red dot); secondary band edge at the Γ point (yellow dot). The lowest energy spin-split valence state at the K point is also marked (magenta dot). The two edges at the K point in the valence band (red and magenta dots) would be degenerate in the absence of spin-orbit coupling. The spin-orbit interaction leads to an effective splitting and to an almost complete spin polarization of these two states. Reprinted with permission from Zhu *et al.*, *Phys. Rev. B* **84**, 153402 (2011). Copyright 2011 American Physical Society.⁴³¹

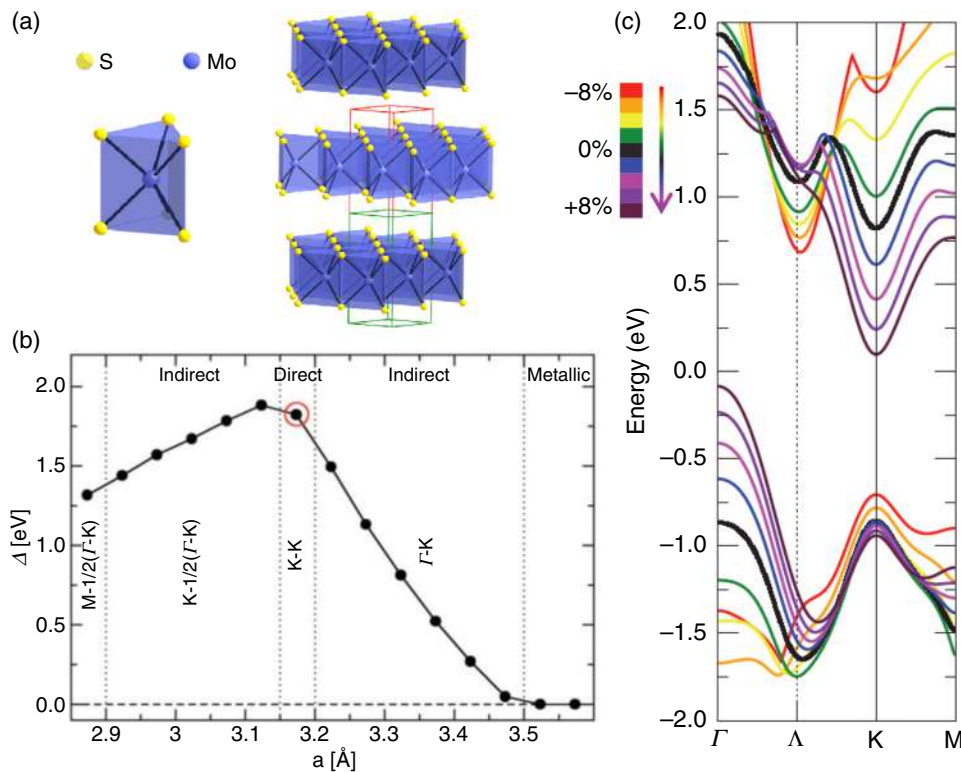


FIG. 27. (a) Crystal structure of MoS₂. Left: unit cell of monolayer MoS₂. Right: multilayer MoS₂ obtained as stacking of single-layer units. Adapted with permission from Cappelluti *et al.*, Phys. Rev. B **88**, 075409 (2013). Copyright 2013 American Physical Society.²⁰⁶ (b) Evolution of the size and character (direct vs indirect) bandgap in monolayer MoS₂ subjected to an equibiaxial strain, here parametrized in terms of the in-plane lattice constant. The unstrained case is marked by a red circle. Reprinted with permission from Ghorbani-Asl *et al.*, Phys. Rev. B **87**, 235434 (2013). Copyright 2013 American Physical Society.²¹¹ (c) Change of highest valence band and lowest conduction band of MoS₂ under compressive (minus sign), null, or tensile (plus sign) equibiaxial strains. The calculations were performed from -8% to $+8\%$, in steps of 2% (see colorbar displayed on the left). Adapted with permission from Chang *et al.*, Phys. Rev. B **88**, 195420 (2013). Copyright 2013 American Physical Society.²¹³

chalcogen-atom planes.²⁰⁶ The hybridization between metal and chalcogen atoms appears thus to play a fundamental role, since it is directly responsible for the magnitude and the direct/indirect character of the bandgap. It is clear that in this situation, in-plane strains as well as out-of-plane strains can have crucial effects, since strain modulates the interatomic distances, and hence, the hopping processes responsible for the properties of the band structure.²¹

The high sensitivity of the band structure to the presence of strain in 2D crystals was clearly outlined already in a series of early studies, wherein the effects of a uniform (uniaxial and biaxial) in-plane strain in monolayer TMD compounds were first theoretically investigated.^{175,207–217} In all cases, it was shown that the bandgap character, generally direct in unstrained TMD monolayers, becomes indirect above a relatively low threshold, $\sim 1\text{--}3\%$ for both tensile and compressive strain. For tensile strain, this is due to a reordering of the critical points in the valence band, while for compressive strain to a reordering in the conduction band, as clearly shown in Fig. 27(b) in the case of MoS₂. Such evolution of the bandgap character descends directly from the different effects of strain on the different band edges, displayed in Fig. 27(c) for MoS₂ MLs. As a general rule, tensile/compressive strain leads to a reduction/increase in the direct bandgap energy at the K point, with a shift rate in the range $\sim 50\text{--}100$ meV/% (where the rate is referred to as the total in-plane strain, ε_{tot}). The precise value depends on the number of layers, on the specific MX₂ material, for some materials on whether strain is uniaxial or biaxial, etc. Such bandgap tuning can be efficiently characterized—e.g., via photoluminescence or reflectance measurements—by tracing the peak energy of the A exciton, a

quantity which is known to move together with the direct bandgap (given an almost strain-independent binding energy for the A exciton), as discussed later. The evolution of the B exciton has also been shown to follow closely that of the A exciton, in agreement with the idea of a pure, weakly strain-dependent, spin-orbit-induced splitting.

Strain has a much stronger effect on the Q_{CB} point (equivalently referred to also as the Λ_{CB} point) in the conduction band and on the Γ_{VB} point of the valence band, as can be clearly noticed in Fig. 27(c). More in detail, *tensile* strain affects the band structure by shifting upwards the valence band edge at the Γ_{VB} point at a higher rate with respect to the K_{VB} point, resulting in the establishment of an *indirect* $\Gamma_{\text{VB}}\text{--}K_{\text{VB}}$ gap above a strain threshold of $\sim 2\%$ [see Figs. 27(b) and 27(c)]. On the other hand, one of the crucial effects of a *compressive* strain is the lowering of the conduction band edge at Q_{CB} (or equivalently Λ_{CB}), while the K point shifts upward, resulting in an indirect Q_{CB}– K_{VB} gap [see Figs. 27(b) and 27(c); in panel (b), the Q/ Λ point is indicated as $1/2(\Gamma\text{--}K)$]. In both the tensile and compressive strain cases, a further increase in the strain up to $\varepsilon_{\text{tot}} > 10\text{--}15\%$ is predicted to result in an insulator-to-metal transition.^{158,162,207,211}

This general qualitative behavior holds for all TMDs, with quantitative differences depending on the compound, as shown in Fig. 28, where the calculated trends with strain for the most relevant optical transitions are shown. The shaded regions in panels (b)–(d) highlight the bandgap crossover values at which a transition from a direct regime to an indirect regime occurs. The crossover strain varies depending on the compound. Indeed, this accounts for a remarkable possibility to tune the electronic

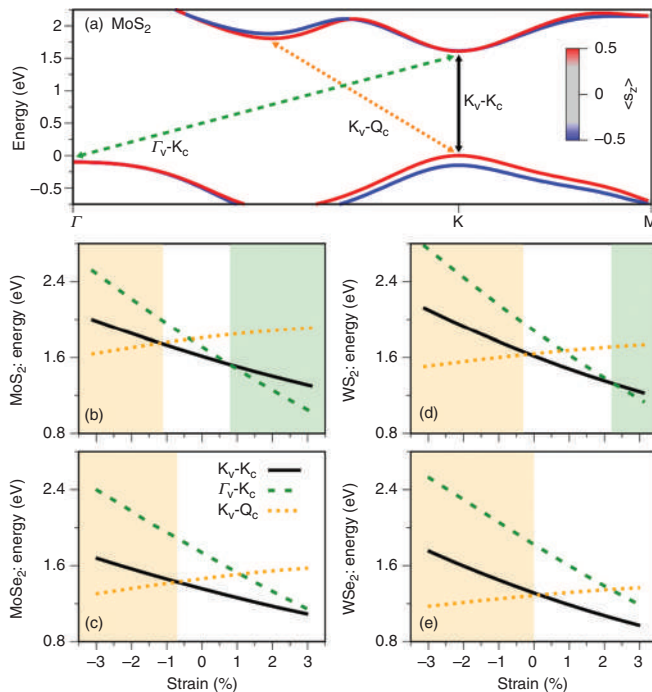


FIG. 28. (a) Band structure of MoS₂ at zero strain, highlighting the important optical transitions mostly affected by strain. The transitions are identified by the reciprocal space point (K, Q, Γ) and by the energy band (subindices v and c stand for the valence and conduction bands, respectively). Evolution of the transition energies depicted in (a) as a function of strain for (b) MoS₂, (c) MoSe₂, (d) WS₂, and (e) WSe₂ MLs. The shaded regions indicate indirect bandgap regimes (K-Q for negative, i.e., compressive strain, and Γ -K for positive, i.e., tensile strain). Reprinted with permission from Zollner *et al.*, Phys. Rev. B **100**, 195126 (2019). Copyright 2019 American Physical Society.²²³

properties of single-layer TMDs, holding relevance for the realization of devices, where strain could be exploited on demand according to the specific needs.

Several experiments confirmed the predicted bandgap reduction (increase) upon the application of in-plane tensile (compressive) strains, mostly via optical measurements—as discussed in the following—and more rarely, via direct inspection, e.g., via scanning tunneling spectroscopy (STS). STS measurements are indeed less easily accessible, but offer the unique opportunity to measure at the same time the local strain and the electronic bandgap.^{218–221} Most interestingly, clear experimental evidence of the expected direct-to-indirect transitions were recently reported. More specifically, the transition from a K_{CB} - K_{VB} direct bandgap regime to a Q_{CB} - K_{VB} indirect bandgap regime upon compressive strain was observed optically in MoS₂ via hydrostatic pressure experiments, for instance in Ref. 222, as better detailed in the following. An even clearer experimental evidence was obtained for the crossover from a K_{CB} - K_{VB} direct bandgap to a K_{CB} - Γ_{VB} indirect bandgap upon the application of tensile strains in WS₂, MoS₂, and WSe₂ MLs.^{32,134,218} In particular, in Refs. 32 and 134, the presence of both the direct and indirect transitions could be observed in the spectra via PL measurements, thus probing the excitons rather than directly probing the band

structure, as detailed later. On the other hand, Shin *et al.*²¹⁸ performed STS experiments in MoS₂ flakes subjected to local strains induced by the corrugated substrate, and obtained direct evidence of the K_{VB} to Γ_{VB} VB maximum crossover, as illustrated in Fig. 29. While the trends observed experimentally qualitatively agree with the theoretical trends and optical experiments, a striking difference is observed quantitatively. In fact, the STS experiments of Ref. 218 provide shift rates of ~ 270 meV/% for the direct transition and of ~ 515 meV/% for the indirect transition. While the ratio between the indirect-transition-rate and the direct-transition-rate is ~ 1.9 —in good agreement with theory^{212,213,223}—the absolute value of the shift rates is a factor of 4 to 5 larger than the theoretically predicted shift rates and than those measured optically. Similarly, high shift rates of about 400 to 500 meV were found by STS in other works, by Trainer *et al.*²¹⁹ in MoS₂ MLs deposited on curved structures, and by Zhang *et al.*²²⁰ in MoS₂ MLs at heterojunction interfaces, where lattice-misfit strains are present. The reason for this quantitative difference with theory and optical experiments is still to be understood. One possible reason could be traced to the fact that in the mentioned works, the strain was varying at the few-nm scale, rather than being homogeneous.

Although the possibility of using strain to switch the bandgap character of monolayer TMD systems from direct to indirect is of significant fundamental interest, the reverse task, namely the possibility of changing in a controlled way the bandgap character from *indirect* to *direct*, would arguably represent an even bigger achievement, due to its potential importance for optoelectronic applications. The opportunity of using strain to achieve this goal is seemingly provided by monolayer WSe₂, where—because of the extremely large spin-orbit coupling—in

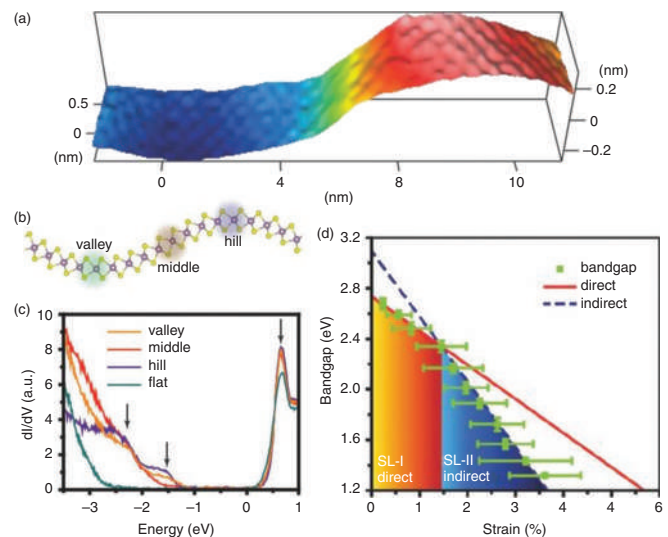


FIG. 29. (a) 3D scanning tunneling microscopy (STM) image of a locally bent MoS₂ region, showing sulfur-induced protrusions. (b) Sketch of the MoS₂ bent region shown in panel (a), defining three different regions: valley, middle, hill. (c) STS spectra acquired in the three regions indicated in panel (b) and on a flat, unstrained area of the MoS₂-ML flake. (d) Bandgap energy determined via STS measurements as a function of the corresponding local strain. Reprinted with permission from Shin *et al.*, Adv. Mater. **28**, 9378 (2016). Copyright 2016 Wiley-VCH Verlag GmbH & Co. KGaA, Weinheim.²¹⁸

some theoretical works, the bandgap in the absence of strain was found (at odds with other monolayer TMDs) to be indirect with a $Q_{CB}-K_{VB}$ character. In such situations, tensile strain shifts upwards of the Q_{CB} band edge, thus restoring a direct gap at the K_{CB} point.²²⁴ A similar situation has been encountered as well in multilayer WSe_2 , wherein a strain-induced indirect-to-direct bandgap transition was also observed experimentally in PL experiments.^{50,53}

In the above discussion, we have focused on the effects of *in-plane* strains on the band structure of TMDs. Most of the experimental setups are designed for generating an in-plane strain, although an out-of-plane strain is always intrinsically involved, either because of the bending/curvature in the third dimension, or due to the unavoidable Poisson effect. In most cases, the presence of an out-of-plane strain component is merely viewed as a further complication, and it is often overlooked in the interpretation of experimental data and in theoretical simulations. On the other hand, the possibility of a controlled tuning of the electronic properties of MoS_2 by means of out-of-plane strain was demonstrated a few years ago in Ref. 225. Therein, a direct-to-indirect bandgap transition was assessed as a result of the compression of the sample “thickness,” i.e., of the vertical sulphur–sulphur distance. This task can be obviously achieved in a feasible way only in single-layer TMDs, since in multilayer crystals, most of the applied vertical compression will result in a reduction of the *inter-layer* distance (distance between MX_2 sandwiches) rather than in the shortening of the *intra-layer* $M-X$ or $X-X$ bond lengths. Moreover, it should be emphasized that the semiclassical concepts of a vertical intralayer $X-X$ distance, as a static thermodynamic parameter, can be highly questionable in these materials since it is strongly governed by the phonon lattice quantum vibrations. In single-layer as well as in multilayer systems, such quantum lattice fluctuations are large enough that different band structure “snapshots” are probed, with different direct and indirect bandgap character.²²⁶ The effects of the quantum lattice fluctuations should thus be consistently taken into account in a compelling description of the band structure of these materials.

Exciton physics. The strain tuning of the bandgap results in an effective dependence on strain of the transport properties as well as of the optical excitonic properties.^{207,211,212,217,227–230} The latter are more usually investigated experimentally, due to the noninvasive and relatively controllable—up to scales of few hundreds of nm—nature of optical techniques. In fact, direct investigation of the effect of strain on the electronic properties could only be otherwise achieved by angle-resolved photoemission experiments, requiring high beam energies that may damage the 2D material and not compatible with almost all the straining techniques, or by STS experiments. The latter, as shown before, allow one to directly measure both the strain gradient and its effect on the electronic bandgap. As a drawback, such experiments are not easy to handle and could be exploited only for a minority of straining methods. Optical methods result therefore to be a good compromise. However, in semiconducting 2D materials—which are characterized by high binding energies—the optical spectra are dominated by excitons rather than by band-to-band transitions up to room temperature and above. This differs from what typically happens in conventional semiconductors and nanostructures, where the contribution of uncorrelated single-particle transitions may be evidenced by temperature-,²³¹ polarization-,²³² and magnetic field-dependent²³³

absorption and photoluminescence measurements, like in InP nanowires.²³⁴ Of course, the relative strength of the external perturbation has to be gauged to the exciton binding energy to interpret correctly the optical spectra and thus derive fundamental band structure parameters, such as in the case of the carrier effective mass in magneto-optical experiments.²³⁵ Figure 30 compares the exciton binding energy vs the bandgap of two classes of materials: bulk (or 3D) semiconductors and 2D materials. In the latter case, the exciton binding energy exceeds the same quantity in 3D crystals between one and more than two orders of magnitude. Such a strong electron-hole interaction is due to the strongly diminished dielectric screening caused by the absence of a bulk medium and by the large confinement that obliges the charge carriers to stay at a smaller distance.^{236,237}

As mentioned above, the optical spectra of TMDs are typically dominated by the A exciton, resulting from the $K_{CB}-K_{VB}$ transition, as schematized in Fig. 31(a). The corresponding binding energy was characterized in several TMD compounds and with different techniques, resulting in values spreading between 0.2 and 0.7 eV.²³⁷ Slightly larger binding energies are expected for the B exciton, involving the lower split CB at K/K' [shown in Fig. 31(a) and having opposite spin with respect to the band involved in the A exciton formation] and the lower spin-split VB, at much lower energy than the upper band [not shown in Fig. 31(a), it typically lies few hundreds of meV below the upper band²⁰⁰]. Indeed, very similar effective masses are found for the split CBs, while the effective mass in the lower VB is found to be larger than that in the upper band ($m_K^{VB,upper} \sim 1.3 \cdot m_K^{VB,lower}$),²⁴⁰ so that a larger binding energy is expected for the B exciton. An even larger binding energy is expected for indirect transitions. In particular, it has been calculated that in the CB, the effective mass at the Q_{CB} point should be larger than at the K_{CB} point ($m_Q^{CB} \sim 2.0 \cdot m_K^{CB}$).²⁴¹ An even larger difference was found—both theoretically and experimentally—in the VB, where the effective mass at Γ_{VB} is remarkably larger than that at K_{VB} ($m_{\Gamma}^{VB} \sim 5.1 \cdot m_K^{VB}$).²⁴⁰ Such a difference in the binding energy of different excitons results in a smaller energy difference between indirect and direct transitions in the exciton picture with

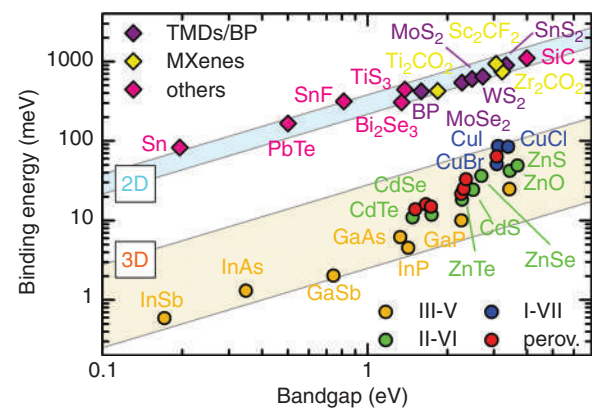


FIG. 30. Exciton binding energy vs bandgap of the most common conventional 3D semiconductors (from https://www.tf.uni-kiel.de/matwis/amat/semi_en/kap_5/advanced/t5_1_3.html and Ref. 238 for GaP) and perovskites (measured experimentally in Ref. 239), and those calculated theoretically for several 2D materials in Ref. 236. The cyan and sand yellow shaded regions highlight the ranges of exciton binding energies of 2D and 3D semiconductors, respectively.

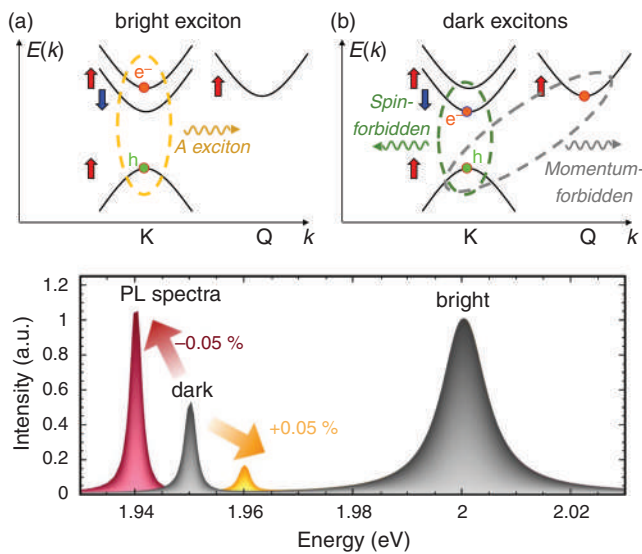


FIG. 31. (a) and (b) Sketch of the lowest energy bright (a) and dark (b) exciton transitions. The colored arrows indicate spin-up (red) and spin-down (blue) states. Dark excitons can be either spin-forbidden dark excitons (dark green) or momentum-forbidden dark excitons (gray). (c) Calculated PL spectrum, showing the effect of strain on the momentum-forbidden dark exciton and revealing its extremely high sensitivity to strain. (c) Reprinted with permission from Feierabend *et al.*, *Phys. Rev. B* **99**, 195454 (2019). Copyright 2019 American Physical Society.²⁴¹

respect to the single-particle picture. This might also lead to a different ordering of the transitions in cases where the difference in binding energies exceeds the electronic band difference, so that the electronic gap is still direct while the exciton one is already indirect.

Within this framework, strain has been shown not to alter the effective masses remarkably, thus leaving the binding energies almost unvaried; in turn, almost the same shift rate is expected for the excitonic and electronic transitions.²²³ The excitons are thus expected to follow the same behavior expected for the electronic structure, though the direct-to-indirect exciton crossovers are expected to happen at lower strain values than the electronic ones.

Strain can also lead to intriguing effects in some compounds. For instance, TMDs are well known for the opportunity to give rise to the formation of *dark excitons*, which can be either spin-forbidden dark excitons—where electrons and holes have opposite spin—or momentum-forbidden dark excitons—where electrons and holes are located in different valleys, as schematized in Fig. 31(b). Such excitons cannot be generally accessed by light due to the required spin-flip or large momentum transfer. Mechanisms to activate such exciton states are thus required to observe them, such as high magnetic fields or surface plasmons for spin-forbidden states, or the interaction with phonons or disorder (or any other momentum-generating mechanism) for the momentum-forbidden ones.²⁴¹ Indeed, spin-forbidden states typically involve electrons and holes with different spin at the K point of both CB and VB, and are thus expected to shift with strain analogously to the A and B excitons. To the contrary, momentum-forbidden excitons involve electrons and holes with the same spin, but located at the K_{VB} and Q_{CB} points. Such excitons are especially interesting in tungsten-based materials, where they typically lie at lower energy than the bright A exciton due to the larger binding energy.

Furthermore, since the Q_{CB} point shifts oppositely to the K_{CB} point with strain, such excitons are expected to shift farther or closer to the bright exciton depending on whether tensile or compressive strains are applied. Theoretical calculations show how the dark-bright exciton energy separation ($\Delta E^{\text{dark-bright}}$) changes at a very high rate with strain, so that extremely low strains are sufficient to give remarkable variations, as shown in Fig. 31(c). The relative intensity of the dark and bright states is also expected to be highly sensitive to strain, since it is expected²⁴¹ to be proportional to $\exp\left(-\frac{\Delta E^{\text{dark-bright}}}{k_B T}\right)$.

Therefore, dark excitons might in principle be extremely sensitive probes of strain in TMDs, though the actual study of dark excitons is strongly hindered by the fact that the same mechanisms that could activate such states could also lead to a broadening of the excitons, thus making it challenging to observe the dark states.

The funnel effect in non-uniform strain gradients. It should be furthermore stressed that the modeling of realistic setups in terms of strain effects on the band structure can be in principle questionable, since most of the theoretical concepts used for the interpretation of the experimental data have been enforced assuming homogeneous strains. In most of the cases, the magnitude and the spatial variations of the applied strain are very weak, so that strain can be safely assumed to be homogeneous. The band structure description can be also useful in an intermediate regime, where the spatial modulations of the strain tensor are very large with respect to the crystal structure periodicity. In this context, a semiclassical picture can still be employed, where a well-defined band structure description is assumed to be valid at a *local* scale, probing the effects of a non uniform strain that can be modeled as *uniform* over a short range. The possibility of tuning the electronic and optical properties of two-dimensional materials at the local scale via strain has been demonstrated in a variety of different contexts, where micrometer- or sub-micron-sized local deformations were achieved or modeled.^{48,80,81,112,134,242–250} This is the case, for instance, of Ref. 93, where exciton shifts with strain were observed at the hundreds of nm scale in wrinkled MoS_2 (see Fig. 32). Similar results were obtained with other techniques and in other materials.^{48,80,81,112,134,243,245,247,248}

In the specific case of semiconducting transition-metal dichalcogenides, the space modulation of the valence/conduction band edge with strain has been shown to give rise to a *funnel effect*, namely the migration of electron-hole excitations toward local spots where the bandgap is minimum (see, e.g., Fig. 3).^{129,134} The funnel effect has actually shown to be relevant in several conditions,^{81,93,112,134,245–248} and it looks quite promising since it can be tailored by means of external tunable conditions. Indeed, the possibility to control the funnel effect to redirect photogenerated electron-hole excitations toward one or more specific, reconfigurable, locations has exciting perspectives for, e.g., photon harvesting. The funnel effect has also been shown to give rise to changes in the spectral weight from neutral to charged excitons, i.e., to favor the formation of trions.⁷⁴ This can be explained by considering that impurities or intrinsic doping cause the presence of free electrons which are typically distributed uniformly over the flakes; the presence of strain gradients makes the free electrons drift and accumulate, giving rise to local free-electron-density increases and therein favoring excitons to form lower-energy-bound complexes with the accumulated free carriers.²⁵¹ Therefore, funneling induces an

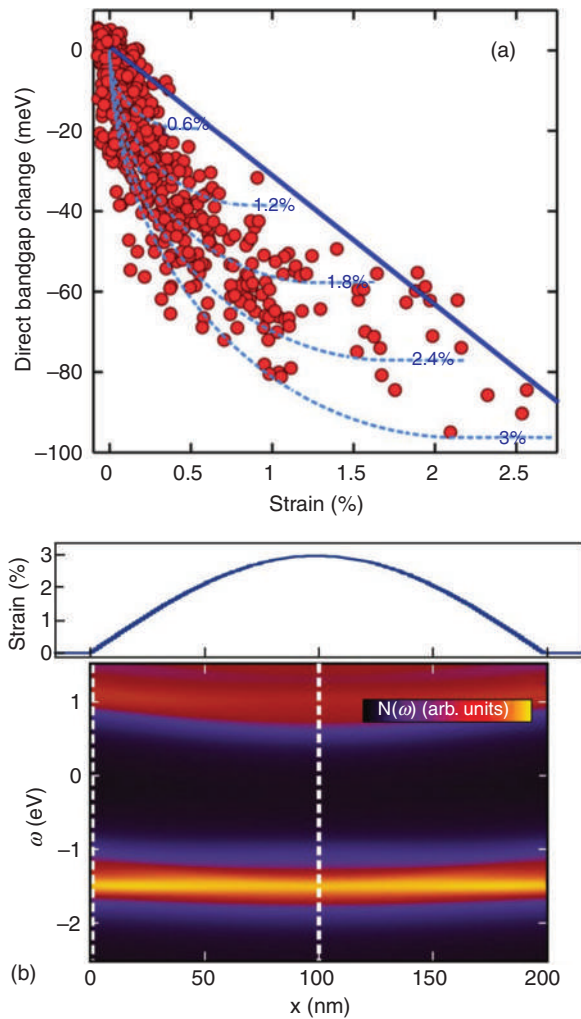


FIG. 32. (a) Local bandgap energy Δ_i measured by photoluminescence vs the magnitude of the local strain ε_i , measured by phonon Raman spectroscopy. The data were collected on several spots on several multilayer wrinkled MoS₂ samples. The correlation between Δ_i vs ε_i shows the possibility of tuning the bandgap at the local scale by governing the local strain. The non-linear behavior between these two quantities is accounted for the funnel effect. (b) Theoretical simulation of a strained wrinkle using a tight-binding model. The upper panel shows the strain profile and the lower panel the local electronic density of states, strictly following the strain profile. Reprinted with permission from Castellanos-Gomez *et al.*, *Nano Lett.* **13**, 5361 (2013). Copyright 2013 American Chemical Society.⁹³

exciton-to-trion conversion. Finally, it should be stressed that the funnel effect can also play an important role in particular cases, where the spatial variation of the strain is sharp enough; in such circumstances, strain-induced bound states can be also established, on top of the continuum spectrum of the band structure.^{252,253}

3. Black phosphorus

Among all the layered materials that can be exfoliated/grown at the atomic-thickness level, BP is probably the most promising with

respect to bandgap engineering. This peculiar semiconductor, indeed, is characterized by the largest bandgap variation as a function of the number of layers,^{254,255} ranging from ~ 0.3 – 0.35 eV in the bulk limit²⁵⁶ to ~ 1.45 – 2 eV for single-layer systems.^{257–259} Quite remarkably, the bandgap retains its direct character, regardless of the number of layers. The large spread characterizing the reported values of the bandgap (especially in the monolayer limit) depends on the different experimental techniques employed to measure the gap, and it might be related to the presence of sizable excitonic effects, which in BP are expected to be as relevant as in single-layer TMDs, given their common two-dimensional nature and direct-bandgap character,²⁵⁷ as also shown in Fig. 30. Unlike graphene and TMDs, BP does not have hexagonal/triangular symmetry and is not flat, but it presents a puckered structure (Fig. 33) with an intrinsically anisotropic structure that reverberates in its electronic and optical properties.^{260,261} On the experimental side, the characterization and assessment of the physical properties of few-layer BP are hampered by its strong tendency to degrade in the presence of oxygen and water. On these grounds, *ab initio* theoretical calculations have provided a valid support and guide for understanding the underlying physics.²⁶² For instance, the shrinking of the bandgap size for an increasing number of layers can

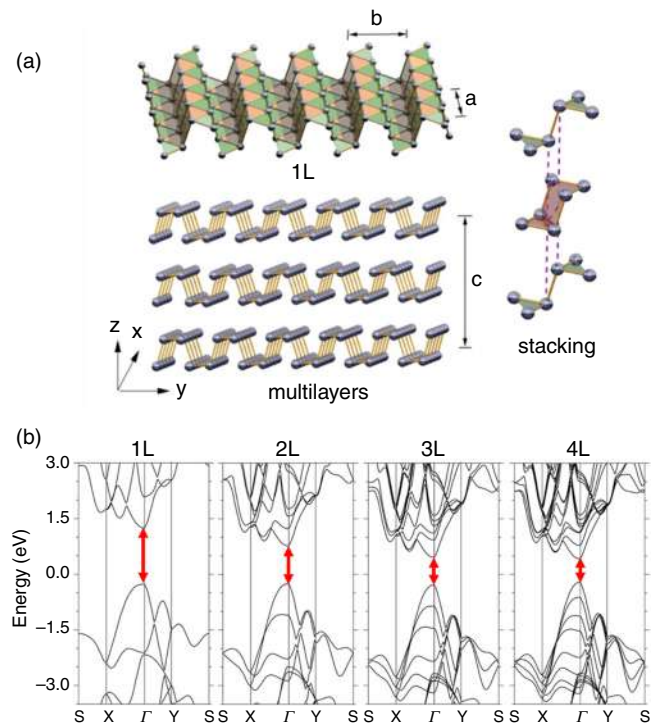


FIG. 33. (a) Lattice structure of single-layer (left) and of stacked multilayer (bottom) BP. Reprinted with permission from Cai *et al.*, *Adv. Func. Mat.* **25**, 2230 (2015). Copyright 2015 Wiley-VCH Verlag GmbH & Co. KGaA, Weinheim.²⁶⁰ (b) Evolution of the band structure of BP with the number of layers. The bandgap has a direct character for any number of layers and it is here represented by the optical transition at the Γ , highlighted by the red arrows. Adapted with permission from Cai *et al.*, *Sci. Rep.* **4**, 6677 (2014). Copyright 2014 Author(s), licensed under a Creative Commons Attribution-NonCommercial-ShareAlike 4.0 International License.²⁶¹

be rationalized, similarly as in TMDs, in terms of quantum confinement,^{263,264} wherein the reduced hopping between adjacent layers constrains the electronic dispersion. Moreover, due to the underlying anisotropy of the crystal, the band structure is also highly anisotropic; in particular, effective masses are much higher (flatter bands) perpendicular to the puckers [zigzag axis, Γ -X in Fig. 33(b)] than along the parallel direction [armchair axis, Γ -Y in Fig. 33(b)].^{256,263–268} Most importantly, *ab initio* calculations revealed a high sensitivity of the electronic and optical properties to strain.^{103,106,267,269–274} Such strong sensitivity can be ascribed to the corrugated structure, in which—in contrast to, e.g., graphene—it is much easier to stretch/compress the in-plane lattice parameters, if the atomic positions can be re-optimized by adjusting the lattice parameter in the out-of-plane direction. Strain has also been predicted to drive BP toward a direct–indirect bandgap transition and eventually to a semiconductor–metal transition, depending on the direction of the applied strain.^{269,270} Quite promising, in view of device applications and photon harvesting, is the prediction, in the presence of a strain gradient, of an *inverse* funnel effect, more precisely of the spatial separation of particle-hole excitations along one specific direction, as shown in Fig. 34.²⁴⁷

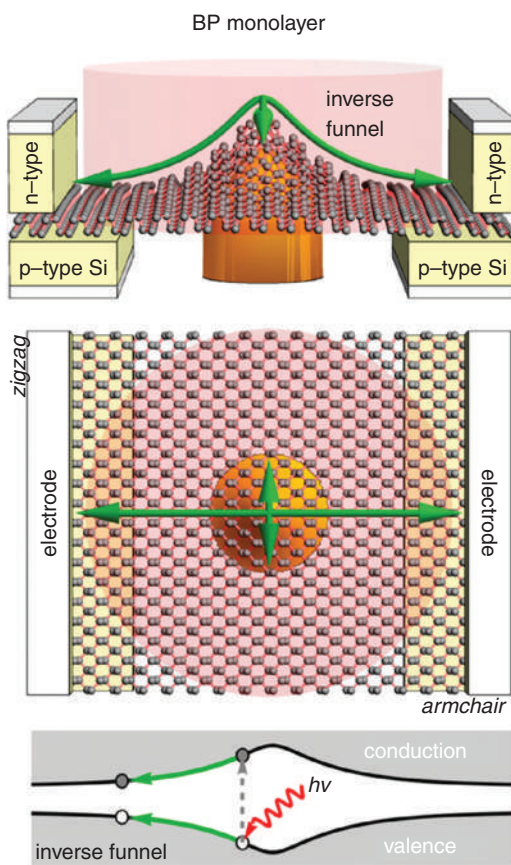


FIG. 34. In BP, the strain profile induced by an indenter creates a highly anisotropic inverse funnel effect that pushes excitons away from the indentation point, along the armchair direction. Reprinted with permission from San-Jose *et al.*, Phys. Rev. X **6**, 031046 (2016). Copyright 2016 Author(s), licensed under a Creative Commons Attribution 3.0 License.²⁴⁷

B. Optical properties

Optical measurements, such as absorption, reflectance and photoluminescence (PL), are nondestructive techniques for the investigation of the electronic states of solids, and are well suited for 2D materials and nanostructures. Absorption and reflectance, in particular, are methods of choice for the investigation of above-the-gap states, whereas PL is especially suitable for probing the states below the bandgap and near the band edges. As such, PL can address with high sensitivity the characteristics of single-photon emitters and the presence of impurities and defects in the material, providing an insightful spectroscopic “bar-code” of each system. In addition, optical measurements are also most apt to investigate the changes induced on the electronic states of nanostructures subjected to external perturbations, such as temperature, electric, and magnetic fields and, of course, mechanical deformations resulting in the insurgence of strain fields. Usually, strain fields are characterized by a certain degree of anisotropy—intentional or not—that dovetails nicely with the capability to discriminate between different polarization states inherent to optical techniques.

Indeed, optical measurements are chiefly relevant for studying the properties of strained 2D crystals in the case of semiconducting materials. Given the high inherent flexibility of 2D membranes and, in turn, their high potentiality for flexible devices, it is indeed of crucial importance to understand how mechanical deformations affect the absorption/emission properties of the material. As discussed in Sec. IV A, the general trend is that tensile in-plane strains lead to a bandgap reduction, while compressive in-plane strains to a bandgap increase. In both cases, a linear response to strain is found for all the high symmetry points of the Brillouin zone.^{175,213,223} This generally results in a linear redshift (blueshift) of the exciton transitions under tensile (compressive) in-plane strain, which is quantified by the *shift rate* (also referred to as *gauge factor*) Δ (typically measured in meV/%). On the one hand, Δ represents a quantitative figure to assess the degree of tunability of the optical properties provided by strain for a specific 2D crystal. On the other hand, the shift rate can be straightforwardly compared with band structure calculations, wherein strain can be easily introduced through a relatively simple variation of the atomic and crystal plane distances.

In the following, we discuss some examples of the consequences of strain on the extended electronic states of 2D crystals. A detailed account of the role played by strain in the (controlled) formation of single-photon sources in 2D crystals will be discussed in Sec. IV C.

1. Transition-metal dichalcogenides

Figure 35 shows a PL study performed on a single WS₂ monolayer dome produced with the method sketched in Fig. 19(a).¹¹² The AFM image of the dome is shown in panel (b). The micro-PL spectra displayed in panel (a) were recorded by scanning the laser from the edge (bottom-most spectrum) to the center (top-most spectrum) of the dome. Indeed, a dramatic line shape variation is observed with increasing in-plane strain $\epsilon_{\text{tot}} = \epsilon_r + \epsilon_\theta$ as the laser moves along the dome’s diameter. In particular, at the edge, the PL spectrum is dominated by the A exciton (that involves the transition K_{CB} - K_{VB} between an electron and a hole at the K point in the conduction and valence band, respectively; see Figs. 25 and 27). The A exciton is however redshifted with respect to the unstrained-ML value, due to a non-null

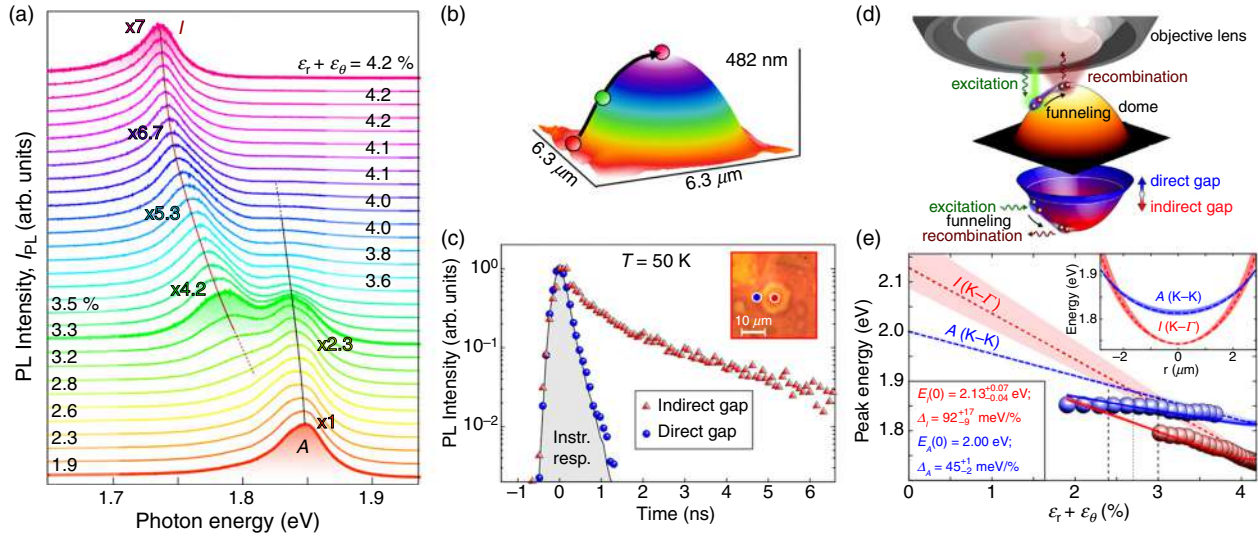


FIG. 35. (a) Normalized PL spectra of a WS₂ dome, whose AFM image is shown in panel (b). Each spectrum corresponds to steps of about 200 nm from the edge to the apex of the dome along the radius highlighted in panel (b). Some selected spectra are labeled with the values of the in-plane strain. The intensity factors are also displayed for some spectra. (c) The main part of the panel shows the temporal evolution of the micro-PL signal relative to the direct A and indirect I exciton transition recorded respectively at the edge (blue circle in the inset) and center (red circle in the inset) of the dome whose optical image is shown as inset. These measurements were recorded at 50 K in order to reduce the influence of non-radiative recombination channels. (d) Sketch of a micro-PL experiment (excitation+recombination) on a single WS₂ dome (whose AFM image is shown in shaded orange). The exciton funneling over the dome strain distribution is depicted. The blue-red paraboloid provides a correspondence between the dome AFM image and the exciton energy, highlighting the direct-to-indirect transition region. (e) Dependence of the energy of the direct (blue dots) and indirect (red dots) exciton transitions on the in-plane strain tensor, for the same dome of panels (a) and (b). The solid blue/red lines (relative to the direct/indirect exciton) are fits based on Eq. (8), while also taking funneling into account. These fits entail linear dependencies of the exciton energies on the in-plane strain, which are displayed as dashed lines; the shaded areas enveloping each curve account for the uncertainty of the fitting procedure. In turn, these linear dependencies yield the evolution of the direct and indirect exciton energy across the dome plotted in the inset. Reprinted with permission from Blundo *et al.*, Phys. Rev. Res. **2**, 012024(R) (2020). Copyright 2020 Author(s), licensed under a Creative Commons Attribution 4.0 International License.¹³⁴

strain already at the edge of the bulge [see strain distribution in Fig. 23(d)]. While moving toward the dome's summit, the total strain increases and for $\epsilon_{\text{tot}} \gtrsim 3\%$ a new band, named I, appears at an energy lower than that of the A exciton. The I band eventually takes over the spectrum at the dome's center. Indeed, the appearance of this new band while increasing strain can be attributable to the occurrence of a strain-induced direct-to-indirect bandgap transition¹³⁴ (the VB maximum shifting from K to Γ), as we discussed in Sec. IV A 2 based on the predictions of theoretical works. This is also suggested by the decrease in intensity observed for increasing strain [see intensity factors quoted in Fig. 35(a)]. To support this hypothesis, time-resolved PL measurements were performed on the bubbles, as shown in panel (c). Such measurements clearly indicate that, while the decay time of the A exciton is instrument-limited (<250 ps), consistently with other reports,^{275,276} the I exciton band shows a much longer temporal decay (~ 3 ns). This finding points to an indirect character of the I transition with an electron at K_{CB} and a hole at Γ_{VB} [see Figs. 27(b) and 27(c) and Fig. 28]. An analysis of the exciton energy shifts across the dome surface is expected to provide the strain-induced shift rates of the A and I excitons. Given the isotropic response to strain of TMDs,¹⁷⁵ one would expect the peak energies to vary linearly with the total strain, as

$$E_{A,I}(\epsilon_{\text{tot}}) = E_{A,I}(0) - \Delta_{A,I}\epsilon_{\text{tot}}. \quad (8)$$

However, due to the nanoscale seamless variation of strain in the dome, funneling phenomena [see Fig. 35(d)] indeed occur and need to

be taken into account.^{129,134} This eventually leads to the trends displayed in Fig. 35(c), where a fit performed including the funnel effect allows us to infer the shift rates and extrapolation energies of the A and I excitons. The obtained shift rates are displayed in Table IV, where also the gauge factors obtained with different straining techniques are shown. An analogous strain-induced bandgap crossover to that discussed for WS₂ was observed also in MoS₂ and WSe₂ domes.¹³⁴

Evidence of a direct-to-indirect transition was also found in the case of a MoS₂ monolayer deposited on a SiO₂ pillar,³² as shown in Fig. 36. Wrinkles are clearly seen in panel (a) in correspondence with the pillar apex, where a maximum strain is reached. Panel (b) of Fig. 36 shows the PL spectra recorded on different points of the tent-like structure, as detailed in the figure caption. A prominent effect of the high tensile strain is the observation of a change in the PL line shape. Indeed, a new band, indicated as I, takes over the A transition. The authors attribute the I band to the k -space indirect transition involving holes at the Γ point of the valence band.³² A 2.4% biaxial tensile strain is eventually deduced at the pillar apex from the A exciton energy shift. This is in relatively good agreement with the transition strain value $\epsilon_{\text{tot}} = (1.8 \pm 0.7)\%$ reported in Ref. 134 for MoS₂.

To expand our brief survey on the most common optical characterization techniques used for 2D materials, we will also show the results obtained via absorption measurements. Absorption is probably best suited for probing the density of extended electronic states of a

TABLE IV. Redshift rates of direct excitons (A, B, C, D), trions ($T=A^-$), and indirect excitons (I) in WS_2 . Notice that the shift rate is calculated via Eq. (9), and hence with respect to the total in-plane strain ϵ_{tot} . Therefore, the values displayed here may differ from those reported in the corresponding work, where the shift rate is often calculated with respect to the bending/stretching strain or to the biaxial strain [see discussion after Eq. (9)].

Mater.	#L	Ref.	System	Measurement	Δ (meV/%)					
					A	T	B	C	D	I
WS_2	1L	Blundo <i>et al.</i> ¹³⁴	Bubble	PL	45_{-2}^{+1}	/	/	/	/	92_{-9}^{+17}
		Tedeschi <i>et al.</i> ¹¹²	Bubble	PL	~ 52	/	/	/	/	/
	Y. Wang <i>et al.</i> ²⁸⁵	Stretching (uniax., mech.)	PL	15.1	/	/	/	/	24.9	
	F. Wang <i>et al.</i> ⁵⁹		Bending	75.2 ± 1.8	115.1 ± 6.3	/	/	/	/	
	Mennel <i>et al.</i> ²⁸⁶	Bending	PL	78.4 ± 4.9	/	/	/	/	/	
	Liang <i>et al.</i> ²⁸⁷	Bending	PL	128	/	/	/	/	/	
	Niehues <i>et al.</i> ⁶⁴	Bending	PL	64	/	/	/	/	/	
	Niehues <i>et al.</i> ⁶⁴	Bending	Absorption	70	/	/	/	/	/	
	Li <i>et al.</i> ⁶⁵	Bending ^a	PL	55	/	/	/	/	/	
	X. He <i>et al.</i> ⁵⁴	Bending	PL	59	55	/	/	/	/	
	Carrascoso <i>et al.</i> ²⁸⁸	Bending	Reflectance	56.3 ± 2.8	/	/	/	/	/	
	Frisenda <i>et al.</i> ²⁸⁹	Stretching (biaxial, thermal)	Reflectance	47	/	/	/	/	/	
	2L	Carrascoso <i>et al.</i> ²⁸⁸	Bending	Reflectance	39.8 ± 3.5	/	49.3 ± 9.2	/	/	/
	3L	Carrascoso <i>et al.</i> ²⁸⁸	Bending	Reflectance	50.8 ± 4.9	/	59.4 ± 9.1	/	/	/

^aIn this case, the 2D material was polymer encapsulated.

material. Contrary to PL, which is dominated by relaxation phenomena, absorption can provide information on the behavior under strain of higher energy critical points of the first Brillouin zone. This is shown in Fig. 37 for a WSe_2 monolayer subjected to uniaxial tensile strain, obtained via a bending device. Indeed, the spectra shown in panel (a) demonstrate a redshift with increasing tensile strain for all the observed transitions [see panel (b)]. This redshift features a linear dependence on strain, as shown in panel (c), where the shift rate is calculated with respect to the strain in the bending direction ϵ [see Fig. 23(a)].

The experimental results discussed here confirm the general trends predicted by DFT calculations (see, e.g., Fig. 28), showing a red-shifting behavior for increasing tensile strain. Furthermore, recent

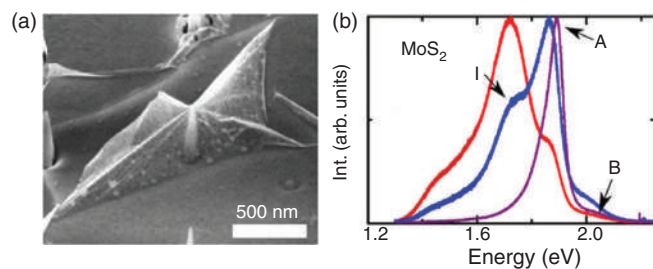


FIG. 36. (a) Scanning electron microscopy image of a SiO_2 pillar (height about 560 nm) on which a MoS_2 monolayer was deposited. The 2D layer is clearly seen in the picture along with membrane wrinkling. (b) Photoluminescence spectra recorded on different points of the tent-like structure displayed in (a). Purple line: reference point (strain-free); blue line: position close to the tent apex; red line: apex. A and B are the exciton resonances related to the spin-orbit split K point of the valence band and the K point of the conduction band. I is the indirect exciton transition $K_{CB}-\Gamma_{VB}$. Reprinted with permission from Chaste *et al.*, ACS Nano **12**, 3235 (2018). Copyright 2018 American Chemical Society.³²

experiments^{32,134} confirmed also that a direct-to-indirect transition can be induced with relatively small strains in WS_2 and MoS_2 , while higher strains are needed in WSe_2 and possibly even higher strains in $MoSe_2$ in agreement with theory. The same qualitative redshifting trend discussed for TMD MLs holds also in the case of multilayers, since also in this case, tensile (compressive) strain leads to a bandgap reduction (increase). It should be noticed, however, that while in MLs strain drives the system toward an indirect regime, which in turns leads to a reduction in the emission efficiency, TMD multilayers are already indirect-gap materials at null strain. In this case, strain can instead lead to an opposite effect, leading to a strain-induced indirect-to-direct exciton transition, and thus in an optical efficiency improvement. This was shown experimentally, for instance, in the case of WSe_2 multilayers by Desai *et al.*⁵³

Finally, a direct-to-indirect bandgap transition involving a reordering of the extrema in the conduction band can be triggered by hydrostatic pressure P . P induces a compression of the lattice volume by exerting an equal force along all the spatial directions of the crystal. The effect of a uniaxial compressive strain on the electronic properties of TMD monolayers was discussed in Sec. IV A 2. Here, we consider the effect of isotropic compressive strains induced by the DAC method (see Sec. II E) in the same material system. In TMD monolayers, P leads to a bandgap increase that manifests as a blueshift of the PL peak accompanied by a sizable decrease in the emission intensity, as shown in Fig. 38 for a WS_2 monolayer. Usually, it is observed that the PL peak energy slows down as soon as P reaches few GPa and it varies little for further increase in P .^{159,162} Qualitatively similar findings were reported in MoS_2 ,^{158,162,222,277} $MoSe_2$,¹⁵⁷ and WSe_2 .²⁷⁸ However, in Ref. 222, the energy of the PL peak reaches a maximum and exhibits a red-shift afterwards, as shown in Fig. 39. It should be noted, though, that the very different P regime, where a plateau in the PL peak energy is reached in Refs. 158, 162, 222, and 277 is likely due to the use in

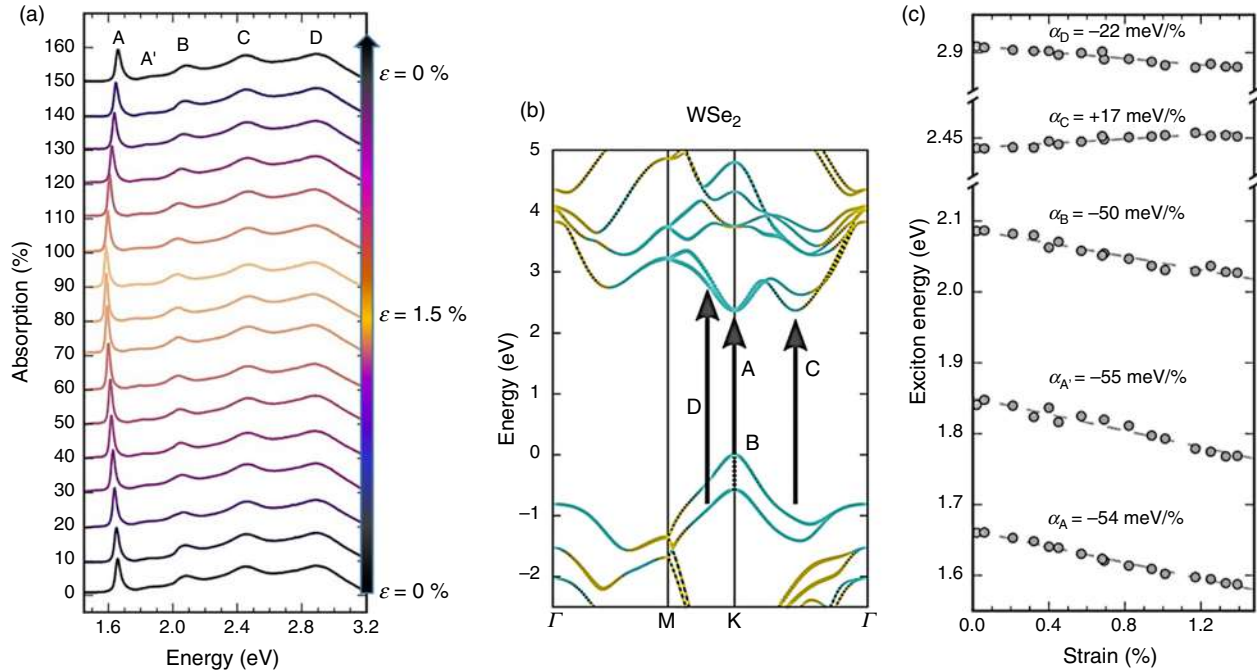


FIG. 37. (a) Absorption spectra of a WSe₂ monolayer acquired while increasing and decreasing the uniaxial tensile strain generated by a bending device. (b) LDA-DFT band structure of WSe₂. The arrows indicate the transitions observed in the absorption spectra. The A (A' is the A exciton first excited state) and B excitons are the direct transitions located at the K point split due to spin-orbit coupling. The C exciton involves several transitions (band nesting) along the K-Γ direction. The D exciton is due to transitions along the K-M direction. (c) Strain-induced shift of the different transitions observed in the absorption spectra. The shift rate with respect to the bending strain of each transition is also quoted. Reprinted with permission from Schimdt *et al.*, 2D Mater. 3, 021011 (2016). Copyright 2016 The Institute of Physics.²⁵⁰

Ref. 222 of a monolayer sample deposited on a Si/SiO₂ substrate. This latter may have provided an extra, yet non-hydrostatic, compressive strain that adds to that set in the anvil cell, as outlined in Refs. 155,156,159 In any event, the *P*-induced effects described above were attributed to a change of the conduction band minimum from K_{CB} to Λ_{CB} [or Q_{CB}, see Fig. 27(c)].^{156,157,162,278–280} Basically, upon a *P* increase, the K_{CB} energy increases slower than the Λ_{CB} energy decreases, until the two extrema cross and Λ_{CB} becomes the CB minimum; see panels (b) and (c) of Fig. 38, showing the band structure and density of states of a WS₂ monolayer at null *P* and at a value of *P* just after the K_{CB}-Λ_{CB} crossover occurred, respectively. The reason for the different behavior of the critical points involved (i.e., their different rate and sign of energy variation with *P*) was nicely accounted for in Ref. 279 in terms of the increasing internal angle of the S-Mo-S bond under pressure. A further increase of *P* eventually transforms a WS₂ monolayer from a semiconductor to a metal [Fig. 38(c)].

Finally, it is worth mentioning that TMDs in the bulk form exhibit the transition to the metal phase at much lower *P* values. For instance, in MoS₂ this transition was observed at about 20 GPa,^{146–148} while theoretical estimations predict that MoS₂ monolayer becomes a metal for *P* equal to 68 GPa.¹⁵⁸ This is attributed to the important role that interlayer orbital hybridization plays in the transition to the metallic phase of multilayered MoS₂.^{146,279} Of course, the interlayer contribution ceases in the monolayer, where higher *P*s are necessary to induce the metal phase via intralayer orbital hybridization.^{156,158}

To conclude this section—where we have discussed the main achievements obtained by the study of the effect of strain on the optical properties of TMDs—we will now provide a quantitative survey of the results obtained with different experimental techniques and via different straining devices. In particular, in Tables IV–VII, we give the reader an overview of the shift rates measured experimentally for WS₂, WSe₂, MoS₂, and MoSe₂, in both single-layer TMDs and multilayer TMDs. In order to consider the same quantity independently of the fabrication method, we display the redshift rates calculated as

$$\Delta_X = -\frac{\partial E_X}{\partial \varepsilon_{\text{tot}}}. \quad (9)$$

X representing a generic optical transition, and where $\varepsilon_{\text{tot}} = \varepsilon_r + \varepsilon_\theta$ for bulging devices and bubbles [see Figs. 23(c) and 23(d)], $\varepsilon_{\text{tot}} = (1 - \nu) \cdot \varepsilon_{\text{bend./stretch.}}$ for bending/stretching devices where uniaxial strains are applied (the Poisson's ratios ν of Table III are used), and $\varepsilon_{\text{tot}} = 2 \cdot \varepsilon_{\text{stretch.}}^{\text{biaxial}}$ if equibiaxial strains ($\varepsilon_{\text{stretch.}}^{\text{biaxial}}$) are induced using stretching devices.

It can be noticed that, for a given 2D material, the obtained values feature a remarkable variation. This can be ascribed to a non-perfect adhesion between the material and the substrate used in some of the straining devices, or to the variable inherent quality and cleanness of the 2D material, which could change based on the experimental conditions and environment employed to isolate the 2D sheet, or to non-perfect strain calibrations of the employed devices. The drawback of

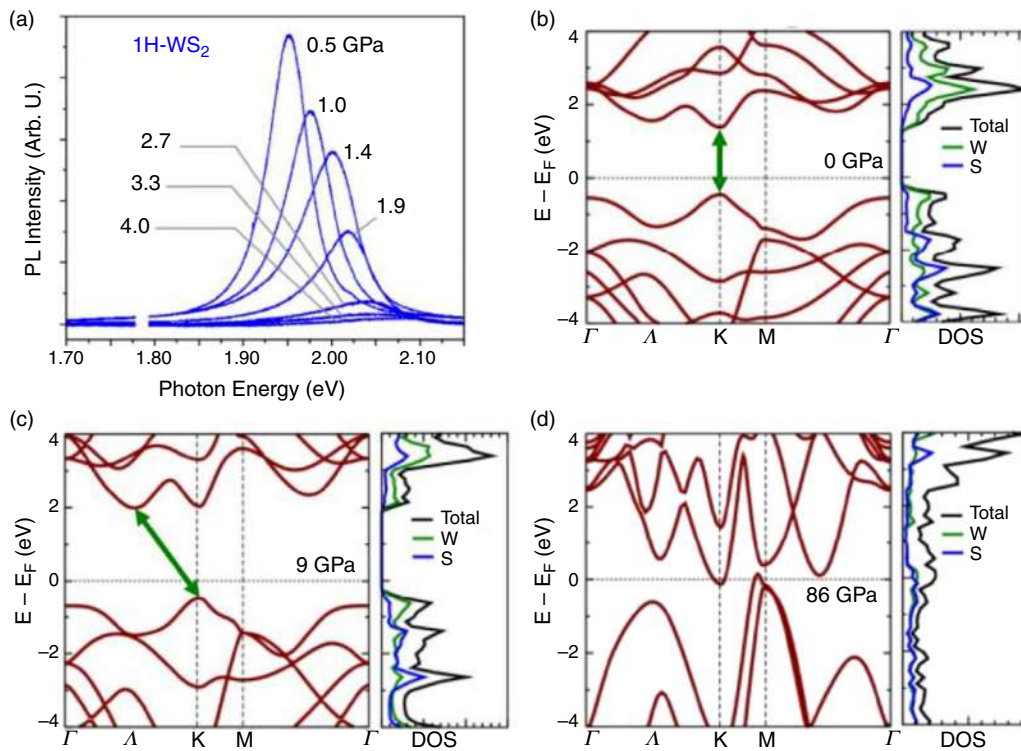


FIG. 38. (a) Room-temperature PL spectra of a WS₂ monolayer at different hydrostatic pressures. (b) Band structure and density of states with the contribution from different atomic elements at ambient pressure. (c) The same at a pressure for which the WS₂ monolayer bandgap becomes indirect. (d) As before at the metallization pressure. Green arrows indicate the bandgaps. Reprinted with permission from Kim *et al.*, 2D Mater. **5**, 015008 (2018). Copyright 2018 The Institute of Physics.¹⁶²

this high variability is that the exciton peak energy cannot represent a precise tool to be used for estimating strain in situations where the mechanical deformation is hardly quantifiable.

2. Post-transition-metal chalcogenides

Post-transition-metal chalcogenides (post-TMCs) are semiconducting materials that have heightened significant attention in light of their high carrier mobilities²⁸¹ and their potentiality for hydrogen storage.²⁸² Among them, InSe has raised particular interest. Its bandgap varies over a wide range of values as the thickness of the flakes decreases,⁵⁷ as shown in Fig. 40(a). More specifically, as the thickness decreases from bulk to three layers, the PL intensity reduces dramatically and the emission peak blueshifts from ~ 1.25 to ~ 1.7 eV. The exciton transitions observed in PL experiments can in this case be ascribed to direct optical transitions at the Γ point of the Brillouin zone, as shown in Fig. 40(b). In fact, while decreasing the flake thickness from the bulk to few layers, the conduction band minimum remains at the Γ_{CB} point and shifts to high energy; in contrast, the valence band maximum moves away from Γ_{VB} toward the K_{CB} points, and the VB takes the form of an inverted “Mexican hat.”²⁸³ The size of the hat increases while reducing the thickness, i.e., the VB maximum shifts farther from Γ_{VB} and, in the monolayer limit, it lies at about 30% of the Γ_{VB} - K_{VB} wavevector. Thus, a direct-to-indirect bandgap crossover occurs gradually with decreasing the thickness,²⁸³ as also demonstrated by the decrease in PL intensity [see panel (a)].

Similarly to TMDs, a bandgap reduction is induced when 2D post-TMCs are subjected to tensile strain, as shown in Fig. 40(c) for a 5L-InSe flake strained via a bending apparatus. Despite the different energy at null strain, analogous results are obtained independently of the layer thickness and similar shift rates are found for the A exciton in flakes with thicknesses between 4L and 8L, as demonstrated in Fig. 40(d) and displayed in Table VIII.

For thick enough samples, such as in the case of the bulk, the B exciton transition at ~ 2.4 eV also can be observed [see sketch in panel (b)]. The latter is found to feature a shift rate definitely smaller than that of the A exciton⁵⁷ (see Table VIII), due to the different orbitals involved in the VB.

The phenomenology discussed here for InSe similarly holds also for GaSe, whose PL energy varies from about 2 eV in the bulk to about 3 eV in the ML, and whose PL intensity decreases noticeably with decreasing the flake thickness, suggesting a direct-to-indirect transition to occur.²⁸⁴ The effect of strain on GaSe thin flakes has not been investigated in detail, yet, though studies on ~ 50 nm-thick samples showed PL redshifts comparable to that of InSe¹⁰⁰ (see Table VIII).

3. Black phosphorus

Even though PL is a powerful, yet easily accessible, technique for the investigation of the electronic properties of low-dimensional systems, there are instances in which it is more convenient to take an alternative approach. For example, reflectance is especially practical in

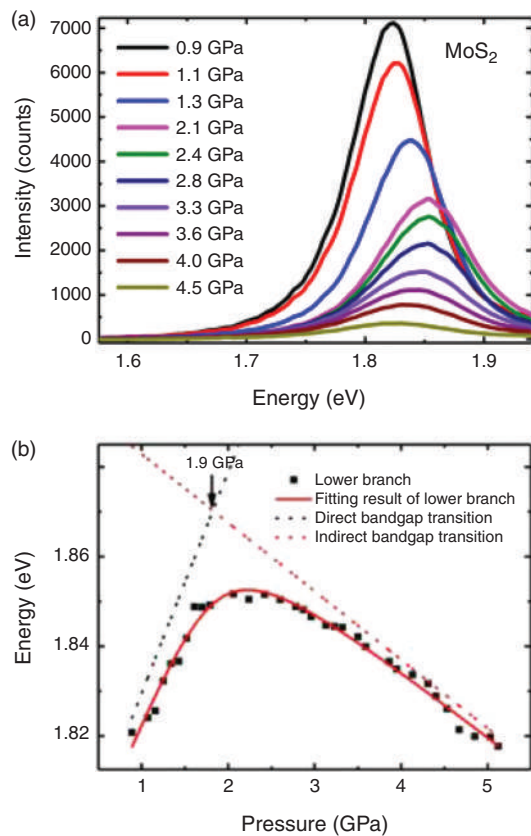


FIG. 39. (a) Room-temperature PL spectra of a MoS₂ monolayer at different hydrostatic pressures. (b) Evolution of the energy of the PL peak vs pressure. The black dots represent peak energies of monolayer MoS₂ under various pressures; the red solid line represents the fitting result based on a two-band (direct and indirect) anti-crossing model; and black and red dotted lines represent the direct and indirect transition under various pressures extracted from the fitting, respectively. Reprinted with permission Zu *et al.*, *Sci. Adv.* **3**, e1700162 (2017). Copyright 2017 Author(s), licensed under a Creative Commons Attribution 4.0 License.²²²

wavelength regions in which PL measurements are not feasible, due to the lack of low-noise, efficient light detectors. This is the case of thick BP, whose bandgap energy falls in the infrared region, as shown in Fig. 33(b). Figure 41(a) shows IR reflectance measurements performed on a 20 nm-thick layer of BP subjected to both compressive and tensile strains applied along different crystallographic directions⁶⁰ using a device similar to the one shown in Fig. 8. Figure 41(b) shows the strain dependence of the bandgap on strain for two samples featuring two different shift rates, depending on the straining crystallographic direction considered [$\Delta = (99 \pm 4)$ meV/% in the armchair direction and $\Delta = (109 \pm 2)$ meV/% in the zigzag direction].

C. Single-photon emitters

Along with the interest warranted by their peculiar intrinsic optical properties, gapped 2D materials such as TMDs and h-BN²⁹³ also garnered additional attention owing to their ability to host high-quality, single-photon emitters. In a series of papers that came out, nearly simultaneously, in June 2015^{123,124,294,295} four research groups

reported the observation of narrow (full width at half maximum, FWHM, ~ 100 μ eV) emission lines coming from localized centers in monolayer WSe₂. Second-order autocorrelation measurements performed on these sharp lines presented clear evidence of photon antibunching, indisputably proving their single-photon-emitter nature.²⁹⁶ Later, these localized levels also showed evidence of cascaded photon emission²⁹⁷—a prerequisite for the generation of *entangled photon pairs*²⁹⁸—and the possibility to pump these levels electrically was demonstrated.²⁹⁹ In addition, in October 2015, room-temperature single-photon emission was reported in hexagonal boron nitride,³⁰⁰ further solidifying the status of 2D materials as promising systems for the development of non-classical light emitters, of great interest for quantum communications and quantum information applications.

As already noted in Sec. IID, strain was immediately identified as a key ingredient for the realization of such quantum-light sources, as strongly localized strain gradients—such as those generated by buckles and nanoblister (see Fig. 15)—clearly show the ability to generate single photons. As also supported by theoretical calculations,²⁵² indeed, the bandgap reduction induced by a $\sim 1\%$ tensile strain is expected to generate quantum-confined states, if the strain modulation occurs over a region with ≤ 10 nm radius. In addition—as briefly discussed in Sec. IIA—“smoother” strain gradients, such as those obtained by depositing TMD monolayers on patterned substrates (see Fig. 42 as well as Figs. 1 and 2 and Ref. 29), can also be exploited to “funnel” excitons toward predefined areas of the material, thus favoring the recombination from point defects localized in the strain-induced, lower-gap regions (see Fig. 3). These point defects, which are naturally abundant in 2D crystals, have also shown the ability to generate quantum light; for example, a recent paper by Mendelson *et al.* identified carbon-related impurities as the most likely origin for the emission of single photons in h-BN.³⁰¹ Furthermore, the position of these point defects can also be precisely controlled, as recently reported in Ref. 302. As summarized in Fig. 43, indeed, the site-selective exposure of a MoS₂ monolayer to a flux of helium ions results in the formation of large arrays of single-photon sources with narrowly distributed emission energies.

The ability to embed quantum emitters in 2D crystals—coupled with the tight relationship existing between strain and the properties of these emitters—naturally entails the possibility to exploit strain engineering to control the emission of single photons. Notably, this control can also be exerted dynamically, by applying reconfigurable strains either mechanically—as recently proposed for h-BN by Mendelson *et al.* (see Fig. 44 and Ref. 85)—or by exploiting piezoelectric substrates.⁸⁸ This is particularly important for nanoemitters whose position is controlled with the aid of patterned substrates, in light of the fairly large inhomogeneous broadening observed for these sources: a FWHM of ~ 33 meV was reported for deterministically ordered arrays of WSe₂ nanoemitters,²⁹ possibly due to the inability to control the exact placement of the optically active defects within the strain gradient defined by the patterned substrate. The achievement of a high level of control over the properties of the photons generated by these site-controlled nanoemitters is potentially crucial for their applications to nanophotonics, as the possibility to independently and dynamically tune, e.g., their energy and polarization would allow them to greatly improve their coupling with optical microcavities. In addition, the ability to precisely match the energy of two remote quantum emitters would enable their interfacing via Hong-Ou-Mandel quantum

TABLE V. Redshift rates of direct excitons (A, B, C, D), trions ($T=A^-$), and indirect excitons (I) in WSe_2 . Notice that the shift rate is calculated via Eq. (9), and hence with respect to the total in-plane strain ϵ_{tot} . Therefore, the values displayed here may differ from those reported in the corresponding works, where the shift rate is often calculated with respect to the bending/stretching strain or to the biaxial strain [see discussion after Eq. (9)].

Mater.	#L	Ref.	System	Measurement	Δ (meV/%)					
					A	T	B	C	D	I
WSe_2	1L	Tedeschi <i>et al.</i> ¹¹²	Bubble	PL	~ 63	/	/	/	/	/
		Mennel <i>et al.</i> ²⁸⁶	Bending	PL	65.9 ± 3.9	/	/	/	/	/
		Niehues <i>et al.</i> ⁶⁴	Bending	PL	61	/	/	/	/	/
		Niehues <i>et al.</i> ⁶⁴	Bending	Absorption	61	/	/	/	/	/
		Li <i>et al.</i> ⁶⁵	Bending ^a	PL	136	/	/	/	/	/
		Li <i>et al.</i> ⁶⁵	Bending ^b	PL	66	/	/	/	/	/
		Carrascoso <i>et al.</i> ²⁸⁸	Bending	Reflectance	71.5 ± 5.2	/	51.6 ± 4.5	/	/	/
	2L	Frisenda <i>et al.</i> ²⁸⁹	Stretching (biaxial, thermal)	Reflectance	32	/	22	/	/	/
		Schmidt <i>et al.</i> ²⁹⁰		Bending	Absorption	67	68	62	21	27
	3L	Schmidt <i>et al.</i> ²⁹⁰	Bending	Absorption	67	68	62	21	27	/
		Carrascoso <i>et al.</i> ²⁸⁸	Bending	Reflectance	63.1 ± 7.6	/	76.4 ± 7.2	/	/	/
		Carrascoso <i>et al.</i> ²⁸⁸	Bending	Reflectance	35.2 ± 6.3	/	19.9 ± 3.0	/	/	/

^aIn this case, the 2D material was polymer encapsulated.

^bDifferently from the previous case, here the WSe_2 sheet was grown by CVD.

TABLE VI. Redshift rate of direct excitons (A, B, C, D), trions ($T=A^-$), and indirect excitons (I) in MoS_2 . Notice that the shift rate is calculated via Eq. (9), and hence with respect to the total in-plane strain ϵ_{tot} . Therefore, the values displayed here may differ from those reported in the corresponding works, where the shift rate is often calculated with respect to the bending/stretching strain or to the biaxial strain [see discussion after Eq. (9)].

Mater.	#L	Ref.	System	Measurement	Δ (meV/%)					
					A	T	B	C	D	I
MoS_2	1L	Blundo <i>et al.</i> ¹³⁴	Bubble	PL	37^{+3}_{-1}	/	/	/	/	93
		Tedeschi <i>et al.</i> ¹¹²	Bubble	PL	~ 50	/	/	/	/	/
		Lloyd <i>et al.</i> ⁶⁸	Bulge center	PL	50 ± 3	50 ± 3	50 ± 3	/	/	/
		Yang <i>et al.</i> ⁷⁵	Bulging device	PL ^a	$21 \pm 2; 9.3$	/	/	/	/	/
		Conley <i>et al.</i> ⁶⁶	Bending	PL	60 ± 9	/	/	/	/	/
		K. He <i>et al.</i> ⁵²	Bending	Absorption	85 ± 7	/	91 ± 7	/	/	/
		Zhu <i>et al.</i> ⁵¹	Bending	PL	64	/	/	/	/	/
		Liang <i>et al.</i> ²⁸⁷	Bending	PL	53	/	/	/	/	/
		Niehues <i>et al.</i> ⁶⁴	Bending	PL	37	/	/	/	/	/
		Niehues <i>et al.</i> ^{64,291}	Bending	Absorption ^b	$56 \pm 3; 56 \pm 3$	/	$51 \pm 5; 57 \pm 5$	/	/	/
		Li <i>et al.</i> ⁶⁵	Bending	PL	81	/	/	/	/	/
		Li <i>et al.</i> ⁶⁵	Bending ^c	PL	167	/	/	/	/	/
		He <i>et al.</i> ⁵⁴	Bending	PL	75	/	/	/	/	/
	John <i>et al.</i> ⁹⁶	Bending	PL	104 ± 5	/	/	/	/	/	
	Carrascoso <i>et al.</i> ²⁸⁸	Bending	Reflectance ^d	52.5 ± 7.9	/	41.1 ± 8.3	/	/	/	
	Frisenda <i>et al.</i> ²⁸⁹	Stretching (biaxial, thermal)	Reflectance	26	/	25	/	/	/	
	Lloyd <i>et al.</i> ⁶⁸		Bulge center	PL	46	/	~ 59	/	/	72
	2L	Yang <i>et al.</i> ⁷⁵	Bulging device	PL	13.7	/	/	/	/	44.6
		He <i>et al.</i> ⁵²	Bending	Absorption	95 ± 7	/	89 ± 7	/	/	/
		He <i>et al.</i> ⁵²	Bending	PL	64 ± 7	/	/	/	/	103 ± 7
Zhu <i>et al.</i> ⁵¹		Bending	PL	61	/	/	/	/	115	
Conley <i>et al.</i> ⁶⁶		Bending	PL	71 ± 13	/	/	/	/	172 ± 27	

TABLE VI. (Continued.)

Mater.	#L	Ref.	System	Measurement	Δ (meV/%)					
					A	T	B	C	D	I
		John <i>et al.</i> ⁹⁶	Bending	PL	45 ± 4	/	/	/	/	207 ± 15
		Carrascoso <i>et al.</i> ²⁸⁸	Bending	Reflectance	51.3 ± 4.0	/	55.9 ± 2.8	/	/	/
	3L	Lloyd <i>et al.</i> ⁶⁸	Bulge center	PL	37	/	~ 54	/	/	55
		Yang <i>et al.</i> ⁷⁵	Bulging device	PL	15 ± 2	/	/	/	/	7 ± 1
		Carrascoso <i>et al.</i> ²⁸⁸	Bending	Reflectance	50.7 ± 1.3	/	48.7 ± 1.1	/	/	/

^aThe shift rates from two different devices were displayed in this work.

^bIn Ref. 291, two different flakes were studied, one mechanically exfoliated (first value) and one grown by CVD (second value).

^cIn this case, the 2D material was polymer encapsulated.

^dThe authors reported the shift rates from 15 different devices. Here, we calculated and reported the average and standard deviation of the 15 rates.

interference—a breakthrough that would pave the way toward the implementation of quantum emitters based on 2D materials in quantum information science and technology.

Further, it is worth noting that strain engineering may also prove instrumental to the realization of TMD-based emitters of entangled photon pairs. As it is well known, indeed, entangled-photons sources based on semiconductor quantum dots (QDs) typically rely on the emissions associated with the biexciton (XX)-exciton (X) cascade.²⁹⁸ While for an ideal source the photons generated during this process are expected to be perfectly entangled,³⁰³ the structural asymmetries unavoidably present in real systems usually lead to the emergence of a finite fine-structure splitting (FSS) in the intermediate X state. In semiconductor QDs, a FSS of just a few μeV is typically sufficient to irredeemably prevent the achievement of a high degree of entanglement, by providing “which path” information for the cascading photons. Recently, the application of anisotropic, reconfigurable in-plane stresses by micromachined piezoelectric actuators was demonstrated to be a viable option for restoring the degeneracy of the X state in semiconductor QDs,³⁰⁴ while also allowing for the tuning of the photon energy over a few meV. The potential pairing of these actuators to 2D materials—possibly coupled with an external electric field, which

was recently reported to effectively suppress the FSS in WSe_2 -based nanoemitters³⁰⁵—provides a clear path toward the realization of energy-tunable sources of optimally entangled photons based on 2D materials.

Finally, 2D materials also offer an intriguing alternative route to the creation of quantum light sources, associated with the possibility to easily create heterostructures by stacking two different 2D crystals one on top of the other. When this is done, interlayer excitons (IXs, where electrons and holes are spatially located in the two different TMDs) may form.³⁰⁶ IXs exhibit a highly enhanced lifetime (exceeding tens of nanoseconds) with respect to their intralayer counterpart in monolayers. In turn, this property makes IXs interesting for the observation of quantum many-body effects (such as exciton condensation) and practical for their spatial transport and for their energy tuning owing to the relatively large wavefunction extent. Like for intralayer excitons, IXs can also be spatially restricted by a strain field. Indeed, the formation of localized IX complexes in highly strained MoSe_2 - WSe_2 heterostructures (following deposition over pillars) was recently observed,³⁰⁷ as depicted in panel (a) of Fig. 45. Figure 45(b) shows the appearance of narrow PL lines at an energy lower than that of the free IX in the region of high strain. The localized IXs feature an excitation

TABLE VII. Redshift rate of direct excitons (A, B, C, D), trions ($T=A^-$), and indirect excitons (I) in MoSe_2 . Notice that the shift rate is calculated via Eq. (9), and hence with respect to the total in-plane strain ϵ_{tot} . Therefore, the values displayed here may differ from those reported in the corresponding works, where the shift rate is often calculated with respect to the bending/stretching strain or to the biaxial strain [see discussion after Eq. (9)].

Mater.	#L	Ref.	System	Measurement	Δ (meV/%)						
					A	T	B	C	D	I	
MoSe_2	1L	Tedeschi <i>et al.</i> ¹¹²	Bubble	PL	~ 44	/	/	/	/	/	
		Mennel <i>et al.</i> ²⁸⁶	Bending	PL	75.5 ± 7.6	/	/	/	/	/	
		Liang <i>et al.</i> ²⁹²	Bending	PL	50.3	/	/	/	/	/	
		Niehues <i>et al.</i> ⁶⁴	Bending	PL	50	/	/	/	/	/	
		Niehues <i>et al.</i> ⁶⁴	Bending	Absorption	44	/	/	/	/	/	
		Island <i>et al.</i> ²⁸⁶	bending	PL	35 ± 3	/	/	/	/	/	
		Carrascoso <i>et al.</i> ²⁸⁸	Bending	Reflectance	53.8 ± 4.0	/	28.9 ± 1.6	/	/	/	
		Frisenda <i>et al.</i> ²⁸⁹	Stretching (biaxial, thermal)	Reflectance	17	/	15	/	/	/	
		2L	Carrascoso <i>et al.</i> ²⁸⁸	Bending	Reflectance	36.6 ± 1.3	/	25.2 ± 9.4	/	/	/
		3L	Carrascoso <i>et al.</i> ²⁸⁸	Bending	Reflectance	26.6 ± 2.7	/	34.4 ± 2.3	/	/	/

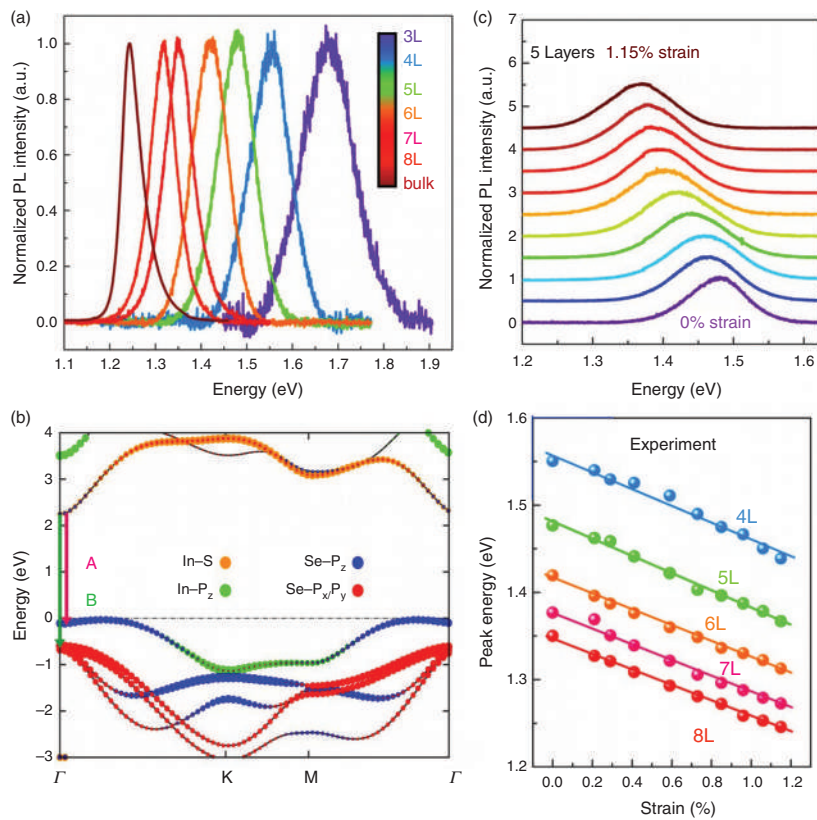


FIG. 40. (a) Normalized room-temperature PL spectra of bulk and 3- to 8-layer InSe. (b) Band structure of monolayer InSe, highlighting the contribution of the different orbitals. The size of the dots gives the weight of the corresponding orbital components. The A and B transitions at the Γ point are indicated. (c) Normalized PL spectra of the A exciton of strained 5-layer InSe. (d) The PL peak energies of InSe as a function of the uniaxial bending strain for different layer thicknesses. Solid lines are linear fits. Adapted with permission from Song *et al.*, ACS Appl. Mater. Interfaces **10**, 3994 (2018). Copyright 2018 American Chemical Society.⁵⁷

power dependence distinctive of multi-particle complexes. Furthermore, by stacking two materials having the same or similar lattice constants, it is possible to observe the emergence of a moiré interference pattern, whose specific geometry depends on the twist angle between the two layers. The underlying periodicity of the moiré may result in the formation of a superlattice of trapping potentials³⁰⁸ that can confine excitons.^{309,310} Very recently—as summarized in Fig. 46—Baek *et al.* reported evidence of single-photon emission from the moiré-trapped excitons formed in a MoSe₂/WSe₂ heterobilayer sample.³¹¹ Magneto-optical spectroscopy confirmed the attribution of the observed transitions to moiré excitons. Moreover, owing to the large permanent dipole of IXs, it was also possible to achieve a large (40 meV) direct current (DC) Stark tuning of the emission energy. This last observation hints at the possibility to use moiré excitons for the realization of energy-tunable single-photon sources, particularly suited for the integration with optical microcavities.

D. Vibrational properties

As we saw in Secs. IV A–IV B, the ability to control strain paves the way to the fine-tuning of the band structure of 2D crystals, and, thus, of their electronic and optical properties. In order to fully unleash the potential of strain engineering for tailoring new functionalities in 2D materials, however, the development of methods to effectively induce controlled lattice deformations must be complemented by the availability of efficient tools for measuring strain independently. Indeed, the effective amount of strain induced in a 2D compound can

be quite different from the nominal one and/or from theoretical expectations, due to different extrinsic effects such as slippage, substrate adhesion, etc.

Besides being coupled with the electronic degrees of freedom, strain also significantly affects the lattice dynamics. In conventional solids, as a general rule, lattice stretching (tensile strain) induces a softening of the phonon modes, whereas lattice shrinking (compressive strain) leads to a corresponding phonon hardening. Few exceptions to such trend can be found, as in ZrW₂O₈,^{312–314} and, most noticeably, for some acoustic modes in graphene.³¹⁵ Monitoring the phonon spectral properties in the presence of induced strains thus provides a powerful tool for characterizing the amount of strain effectively present in the system, as well as its degree of anisotropy. With respect to these goals, Raman spectroscopy has been established as the technique of choice for investigating phonons in 2D crystals, while also providing a powerful and noninvasive means for determining accurately the number of layers, the amount of disorder, and the charge doping present in a given material.^{316–320} Moreover, micro-Raman measurements allow us to collect this information at a sub- μm scale. Raman spectroscopy is a two-photon process related to the derivatives of the polarizability. At the first-order (single-phonon), it essentially probes lattice modes with zero momentum ($\mathbf{q} = 0$), in the center of the Brillouin zone (Γ point), so that only a few phonon modes with selected symmetry are Raman active. At a high order level, it can also probe coupled phonon excitations with opposite momenta ($\mathbf{q}, -\mathbf{q}$), or edge-zone modes triggered by defect scattering. Such processes have resulted to be particularly relevant in graphene, where, for instance, the spectral properties

TABLE VIII. Redshift rate of excitons for the post-transition-metal chalcogenides (post-TMCs) InSe and GaSe. Here, the *A* and *B* excitons involve direct optical transitions at the Γ point of the Brillouin zone.⁵⁷ Notice that the shift rate is calculated via Eq. (9), and hence with respect to the total in-plane strain ϵ_{tot} . Therefore, the values displayed here may differ from those reported in the corresponding works, where the shift rate is often calculated with respect to the bending/stretching strain or to the biaxial strain [see discussion after Eq. (9)].

Mater.	#L	Ref.	System	Measurement	Δ (meV/%)	
					A	B
γ -InSe	4L	Song <i>et al.</i> ⁵⁷	Bending	PL	~ 135	/
	5L	Song <i>et al.</i> ⁵⁷	Bending	PL	~ 135	/
		Li <i>et al.</i> ^{98a}	Bending	PL	~ 208	/
		Zhao <i>et al.</i> ¹⁰⁵	Thermal expansion biaxial	PL	98 ± 10	/
	6L	Song <i>et al.</i> ⁵⁷	Bending	PL	~ 124	/
		Li <i>et al.</i> ^{98,a}	Bending, compressive	PL	~ 190	/
	7L	Song <i>et al.</i> ⁵⁷	Bending	PL	~ 122	/
		Li <i>et al.</i> ^{98,a}	Bending	PL	~ 209	/
	8L	Song <i>et al.</i> ⁵⁷	Bending	PL	~ 120	/
	9L	Li <i>et al.</i> ^{98,a}	Bending, compressive	PL	~ 167	/
	11L	Li <i>et al.</i> ^{98,a}	Bending	PL	~ 179	/
	12L	Li <i>et al.</i> ^{98,a}	Bending, compressive	PL	~ 181	/
	15L	Li <i>et al.</i> ^{98,a}	Bending	PL	~ 137	/
	17L	Li <i>et al.</i> ^{98,a}	Bending, compressive	PL	~ 136	/
	25L	Li <i>et al.</i> ^{98,a}	Bending	PL	~ 120	/
	bulky	Song <i>et al.</i> ⁵⁷	Bending	PL	160	58
		Li <i>et al.</i> ^{98,a}	Bending	PL	~ 110	/
		Zhao <i>et al.</i> ^{105,b}	Thermal expansion biaxial	PL	32 ± 3	/
GaSe	bulky	Zhou <i>et al.</i> ¹⁰⁰	Stretching, uniaxial	PL	~ 90	/

^aThe authors of this work mentioned the flake thickness in nm. We thus estimated the number of layers by assuming a thickness $t = 0.8$ nm for each layer and taking the closer integer number. In the bulky case, the thickness is about 44 L.

^bThe flake thickness was about 30 L.

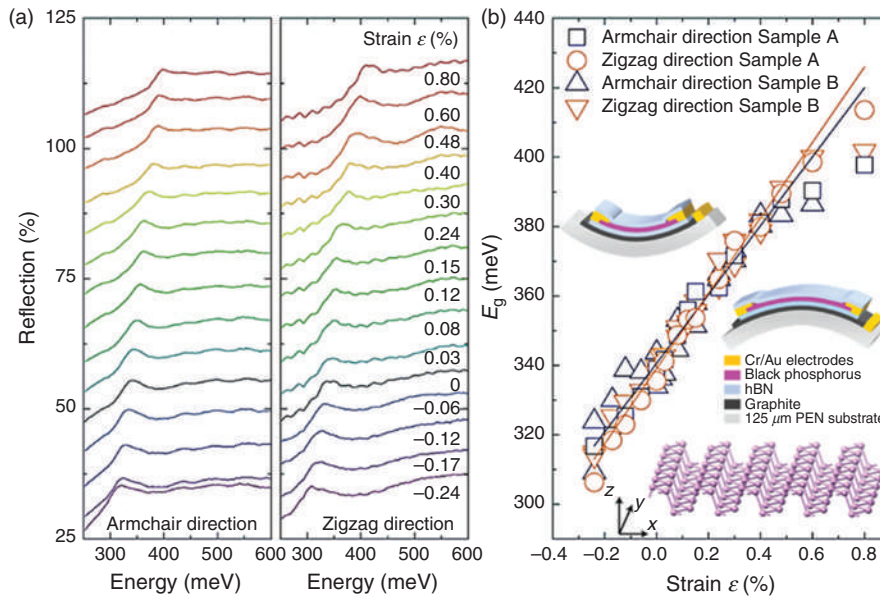


FIG. 41. (a) Reflectance spectra on a 20 nm-thick layer of BP as a function of the uniaxial bending strain applied along the armchair direction (or *x*) and zigzag (or *y*). The strain was applied by a bending device depicted in the insets of panel (b). (b) Band gap dependence on strain for two different samples (A: 20 nm-thick, and B: 50 nm-thick), for strains in both the armchair and zigzag direction. Reprinted with permission from Zhang *et al.*, Nano Lett. 17, 6097 (2017). Copyright 2017 American Chemical Society.⁶⁰

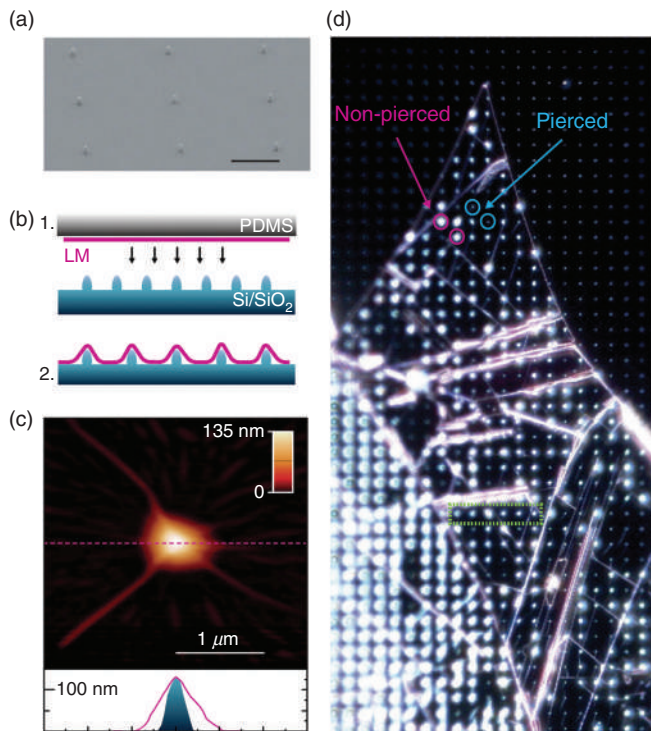


FIG. 42. Fabrication and characterization of site-controlled single-photon emitter arrays. (a) SEM image of SiO₂ substrate patterned with a nanopillar array fabricated by electron beam lithography. Black scale bar, 2 μm. (b) Illustration of the fabrication method: (1) mechanical exfoliation of monolayer (ML) on PDMS (polydimethylsiloxane) and all-dry viscoelastic deposition on patterned substrate; (2) ML deposited on patterned substrate. (c, top) AFM scan of a WSe₂ ML on a nanopillar. (bottom) AFM height profile of a bare nanopillar (blue-shaded region) and of the flake deposited over it (pink line), measured along the dashed pink line cut in the top panel. The color-scale bar represents the height in nm; the white scale bar corresponds to 1 μm. (d) Dark-field optical microscopy image (real color) of a WSe₂ ML deposited on a substrate patterned with a nanopillar array (130 nm high, 4 μm separation). The full image corresponds to a 170 μm by 210 μm area. The blue circles indicate two pierced nanopillars, while the pink circles indicate two non-pierced nanopillars. Reprinted with permission from Palacios-Berraquero *et al.*, Nat. Commun. **8**, 15093 (2017). Copyright 2017 Author(s), licensed under a Creative Commons Attribution 4.0 International License.²⁶

of the 2D peak have been used to characterize the number of layers and the amount of doping.

The most common means for evaluating the amount of strain in 2D materials is provided by a quantitative analysis of the energy peak position of the Raman phonon modes.

In general, the different long-wavelength phonon branches in a given crystal correspond to different symmetries of vibration of the atoms in the unit cell and are characterized by irreducible representations of the space group of the crystal lattice. Hence, in the infinite-wavelength approximation for the Raman phonons, the crystal point group can be used in classifying the phonon symmetries.³²¹ The correspondence between irreducible representations and Raman modes permits the determination of the Raman tensor of each mode and, in turn, to define its peculiar properties.³²² For instance, this allows us to say if a mode is single or doubly

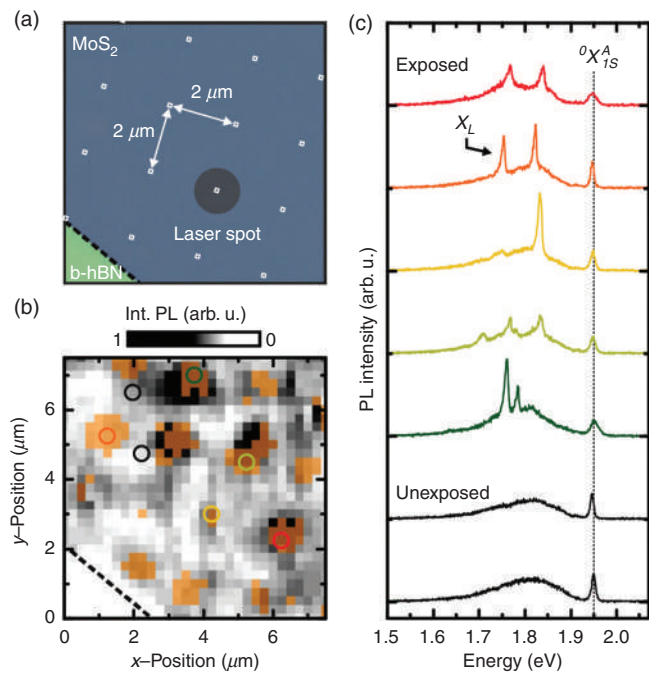


FIG. 43. Site-selective generation of defect emission by helium ion (He⁺) exposure. (a) Optical micrograph of a monolayer MoS₂/h-BN van der Waals heterostructure prior to He⁺ exposure and full encapsulation in h-BN. Before encapsulation multiple 100 nm x 100 nm areas, arranged in an array with 2 μm pitch, are exposed with a dose $\sigma = 2.2 \cdot 10^{12} \text{ cm}^{-2}$. (b) Corresponding spatially resolved and spectrally integrated PL mapping (grayscale) at 10 K. Spectra are integrated over a 10 meV range around a $\Delta E = 193 \text{ meV}$ detuning with respect to the MoS₂ free exciton, where most emissions from localized states are observed. The spatial occurrence of emitters in the ΔE_L range $\sim 100\text{--}220 \text{ meV}$ is highlighted in orange. (c) Selected spectra taken from (b) are shown. All spectra display the emission associated with the MoS₂ free exciton, while only irradiated areas reveal emissions from localized states. The latter is absent in unexposed areas [black spectra and corresponding circles in (b)]. Reprinted with permission from Klein *et al.*, Nat. Commun. **10**, 2755 (2019). Copyright 2019 Author(s), licensed under a Creative Commons Attribution 4.0 International License.³⁰²

degenerate. This is particularly relevant because anisotropic strains in 2D materials break the degeneracies thus inducing mode splittings. These splittings can be exploited for a full characterization of the applied strain, and, in particular, to determine the strain direction, together with its magnitude.

Let us consider, for completeness, the most general case of an anisotropic in-plane strain. Such a strain can be described by a longitudinal ϵ_l component along the main strain direction, and a ϵ_t component along the transverse one. In this circumstance, a (two-degenerate) in-plane Raman mode with frequency ω_E will split by symmetry in two modes, with frequencies ω_E^+ and ω_E^- . It is convenient to define an average frequency

$$\omega_E^{\text{av}} = \frac{\omega_E^+ + \omega_E^-}{2}, \quad (10)$$

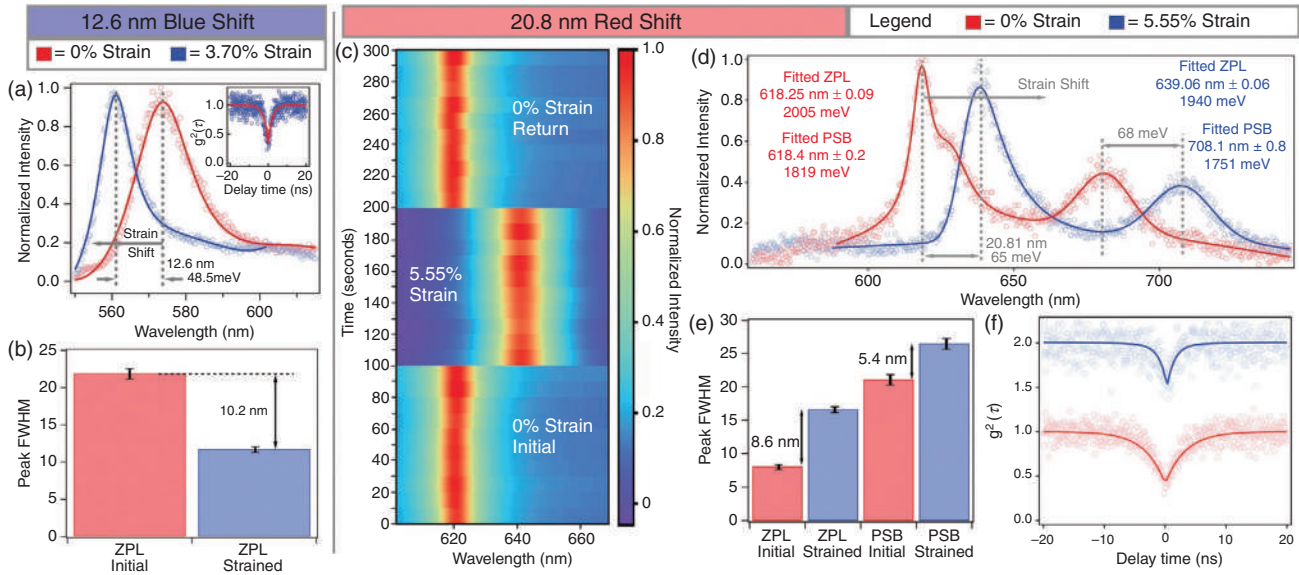


FIG. 44. Large strain-induced energy shifts for h-BN-based SPEs. In (a)–(e), red corresponds to unstrained SPEs, while blue corresponds to shifted emission lines. (a) A tensile strain of 3.70% is applied to a SPE with initial emission wavelength of 573.40 ± 0.08 nm (red trace), inducing a blue-shift of 12.6 nm, to 560.82 ± 0.04 nm (blue trace). The raw data for each measurement (circles) are fitted with Lorentzian functions, shown as a solid trace. The inset displays the $g^2(\tau)$ function measured for 0% strain, confirming the quantum nature of the emission. (b) The FWHM of both peaks is plotted, showing a ≈ 9.0 nm decrease in the associated linewidth of the emitter from 21.9 ± 0.8 nm (0% strain) to 12.9 ± 0.5 nm (3.7% strain). (c) Time-resolved micro-PL intensity for a SPE with 0% strain (bottom), 5.55% strain (middle), and returning to 0% strain (top). Each panel displays 10 consecutive spectral acquisitions of 10 s each, demonstrating negligible spectral diffusion during the measurement, and the reversibility of the strain-induced redshift. There is a time offset between the three measurements, and each is normalized individually. (d) Spectra of a SPE with 0% strain (red trace), characterized by a ZPL centered at 618.25 ± 0.09 nm, and with 5.55% strain (blue trace), characterized by a ZPL centered at 639.06 ± 0.06 nm, showing a redshift of ≈ 20.8 nm. The raw data for each measurement (circles) are fitted with Lorentzian functions, shown as solid traces. (e) Bar graph plotting the FWHM of the ZPL and PSB peaks at 0% and 5.55% strain, respectively. Both the ZPL and the PSB are significantly broadened upon straining. (f) $g^2(\tau)$ histogram collected for unstrained and strained SPEs, showing a decrease in ≈ 2.5 ns for the extracted excited state lifetime of the emitter upon straining. Reprinted with permission from Mendelson *et al.*, *Adv. Mater.* **32**, 1908316 (2020). Copyright 2020 Wiley-VCH Verlag GmbH & Co. KGaA, Weinheim.⁸⁵

and the mode splitting

$$\sigma_E = \omega_E^+ - \omega_E^- \quad (11)$$

It is understood that both quantities depend on the magnitude and structure of the strain tensor $\vec{\varepsilon}$, so that $\omega_E^{\text{av}} = \omega_E^{\text{av}}(\vec{\varepsilon})$, and $\sigma_E = \sigma_E(\vec{\varepsilon})$.

The frequency shift (softening or hardening) upon strain of the two phonon modes ω_E^+ and ω_E^- can be captured by the frequency shift rate

$$\Delta_E = -\frac{\partial \omega_E^{\text{av}}}{\partial \varepsilon_{\text{tot}}}, \quad (12)$$

and by the splitting rate

$$\Sigma_E = \frac{\partial \sigma_E}{\partial \varepsilon_{\text{diff}}}, \quad (13)$$

where ε_{tot} and $\varepsilon_{\text{diff}}$ represent the sum and difference, respectively, of the in-plane components of the principal strain tensor, namely $\varepsilon_{\text{tot}} = \varepsilon_l + \varepsilon_t$, $\varepsilon_{\text{diff}} = \varepsilon_l - \varepsilon_t$.

It is furthermore convenient to introduce dimensionless quantities, as the phonon mode Grüneisen parameter

$$\gamma_E = \frac{\Delta_E}{\omega_E^0}, \quad (14)$$

and the shear deformation potential

$$\beta_E = \frac{\Sigma_E}{\omega_E^0}, \quad (15)$$

where ω_E^0 is the mode frequency in the absence of strain.

For biaxial strains, in the absence of in-plane symmetry-breaking, there is no mode splitting and the only relevant parameter is the shift rate (alternatively, the Grüneisen parameter).^{207,213,214,319} The same occurs, of course, for Raman modes involving out-of-plane displacements, as for instance for the A_{1g} modes in TMDs.

The above analysis has a more direct application in specific strain setups, as, for instance, in the particular cases:

- *bending or uniaxially stretching devices:* in bending setups, the main strain ε_l is achieved along the bending direction (see Fig. 8) and its magnitude can be described by Eq. (1). When referring to the strain applied to the membrane in bending setups, it is common use to refer to this longitudinal strain component $\varepsilon_l = \varepsilon$ —which can be easily quantified via Eq. (1)—rather than to the total strain. In fact, the longitudinal strain results as well in a deformation in the transverse direction given by $\varepsilon_t = -\nu\varepsilon$, where ν is the Poisson's ratio of the material or of the substrate, depending on the setup. In general, it is under debate which choice is the most correct. As discussed later, following the analysis of Ref. 62, in this work we employ the Poisson's ratio of the material. Hence, the total strain would be given by $\varepsilon_{\text{tot}} = (1 - \nu)\varepsilon$, and the shift rate and the splitting rate take the form

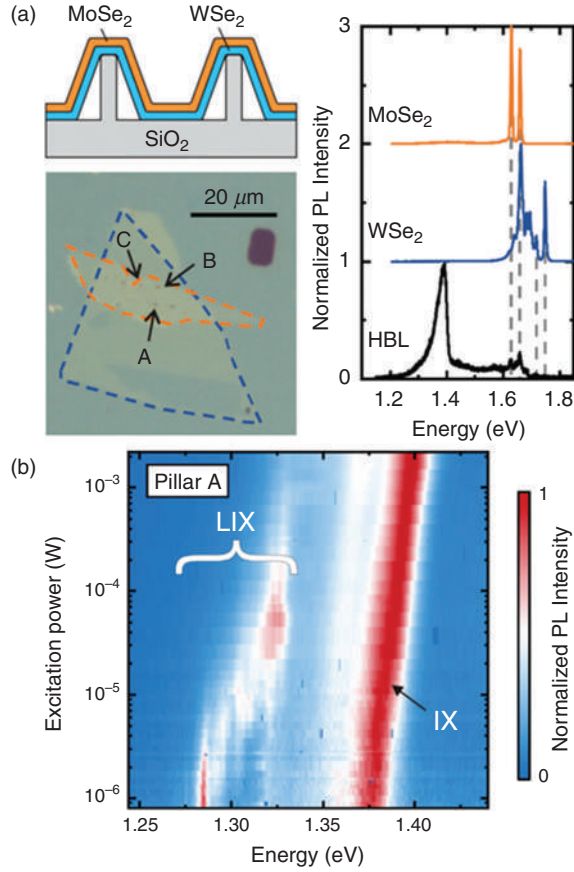


FIG. 45. Site-selective creation of strain-localized interlayer excitons. (a) Left top: Sketch of a MoSe₂-WSe₂ heterostructure deposited on a SiO₂ substrate patterned with pillars of the same material (height and diameter equal to 90 and 130 nm, respectively). The different layer composition is highlighted by different colors. Left bottom: Optical microscope image of the heterostructure displaying the borders of each layer and indicating the location of different pillars individuated by capital letters. Right: representative micro-PL spectra recorded at $T = 10$ K in the regions outside the pillars showing the emission of the single (non-interacting) layers and of the heterobilayer (HBL), where interlayer excitons (IXs) form. (b) Excitation power-dependent micro-PL spectra at $T = 10$ K recorded on top of a pillar. The presence of narrow lines attributable to localized interlayer excitons (LIXs) can be noticed at energies lower than that of the free IX. Reprinted with permission from Kremser *et al.*, NPJ 2D Mater. Appl. 4, 8 (2020). Copyright 2020 Author(s), licensed under a Creative Commons Attribution 4.0 International License.³⁰⁷

$$\Delta_E = -\frac{1}{1-\nu} \cdot \frac{\partial \omega_E^{\text{av}}(\varepsilon)}{\partial \varepsilon}, \quad (16)$$

$$\Sigma_E = \frac{1}{1+\nu} \cdot \frac{\partial \sigma_E(\varepsilon)}{\partial \varepsilon}, \quad (17)$$

with ν being given in Table III. The same holds also for uniaxially stretching devices.

- *spherical bulges and bubbles*: the principal strain tensor is given in polar coordinates, as shown in Fig. 23(d). In this case, the shift

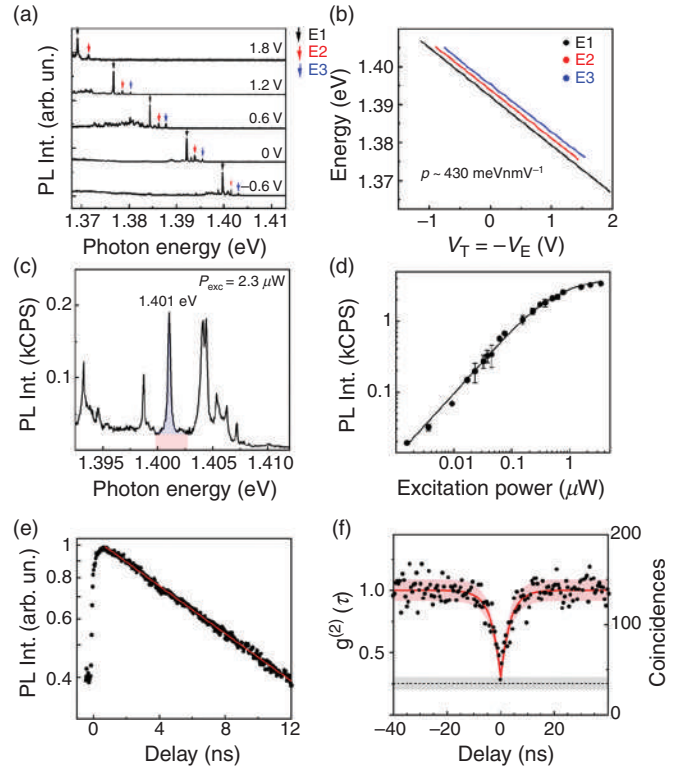


FIG. 46. (a) PL spectra of moiré excitons at different gate voltages. Three representative peaks are indicated as E1, E2, and E3. (b) Plot of the dependence of the emission energy on the gate voltage, for the E1, E2, and E3 peaks. A value of the electrical dipole moment of ≈ 420 meV·nm·V⁻¹ is determined by linear fits. (c) Representative PL spectrum of a moiré exciton. The peak at 1.401 eV is used for the power dependence, time-resolved PL, and second-order photon correlation measurements displayed in the following panels. The blue and red regions represent the estimated PL signal from the emitter and the background. (d) Integrated PL intensity of a single emitter at different excitation powers. (e) Time-resolved normalized PL intensity of the single emitter under 80-MHz pulsed excitation at 1.63 eV, with an average excitation power of 4 μ W. The red solid line shows a single exponential decay fit to the experimental data, revealing a lifetime of 12.1 ± 0.3 ns. (f) Second-order photon correlation statistics using 2.3 μ W CW excitation at 760 nm (black dots) show clear antibunching. The red solid line represents a fit of the experimental data, revealing a $g^{(2)}(0) = 0.28 \pm 0.03$. The red shadowed area represents the Poissonian interval error associated with the experimental determination of $g^{(2)}(\tau)$. The black dashed line represents the experimental limitation for $g^{(2)}(0)$ owing to the non-filtered emission background. The gray shadowed area shows the error interval in the determination of the limitation for $g^{(2)}(0)$. Reprinted with permission from Baek *et al.*, Sci. Adv. 6, eaba8526 (2020). Copyright 2020 Author(s), licensed under a Creative Commons Attribution License 4.0.³¹¹

and splitting rates can be expressed as functions of the radial coordinate r as

$$\Delta_E = -\frac{\partial \omega_E^{\text{av}}(r)}{\partial \varepsilon_{\text{tot}}(r)}, \quad (18)$$

$$\Sigma_E = \frac{\partial \sigma_E(r)}{\partial \varepsilon_{\text{diff}}(r)}, \quad (19)$$

where $\varepsilon_{\text{tot}}(r) = \varepsilon_r(r) + \varepsilon_\theta(r)$ and $\varepsilon_{\text{diff}}(r) = \varepsilon_r(r) - \varepsilon_\theta(r)$.

1. Transition-metal dichalcogenides

We will now discuss first the case of TMDs (MX_2), where the typical Raman phonons under investigation are the in-plane lattice displacements of the M atoms in counterphase with the X atoms in the outer planes; and the out-of-plane breathing of the X planes, in the X-M-X sandwich, leaving the metal plane at rest. The modes corresponding to in-plane vibrations are conventionally labeled as E_{2g}^1 , E_g^1 , and E' , in bulk, bilayer, and single-layer TMDs, while those corresponding to out-of-plane vibrations are labeled as A_{1g} , A_{1g}^2 , and A_1' , respectively (see sketches in Fig. 47).³¹⁹ The different labeling is due to the fact that the bulk TMD crystals are characterized by the D_{6h} point group, while even-few-layers TMDs from the D_{3d} group and odd-few-layer TMDs from the D_{3h} group. This results in slight differences in the Raman tensors, as we will point out in the following. For sake of compactness, following Ref. 68, we denote such Raman modes as E_{2g}^1 and A_{1g} independently of the number of layers. In the absence of symmetry breaking, the E_{2g}^1 modes are double-degenerate, corresponding to two equivalent directions in the plane (x and y).

A characteristic example of the frequency shift for both the E_{2g}^1 and A_{1g} modes of MoS_2 upon biaxial strain in a bulging device (for single-layer to few layers) is shown in Fig. 48. The spectra were acquired at the summit of the bulges, and the strain was quantified by Hencky's Model [see Eq. (7) and Fig. 23(c)], resulting in a shift rate described by Eq. (18). For both modes, a decrease in the shift rate is observed as the number of layers increases. Furthermore, the smallest shift rate upon strain of the A_{1g} mode with respect to the E_{2g}^1 modes is noticeable. The A_{1g} mode results to be, on the other hand, more sensitive to charge doping, so that the Raman phonon peaks of the E_{2g}^1 and A_{1g} modes can be used for monitoring doping and strain in the samples in an independent way. Indeed, a similar shift is observed also

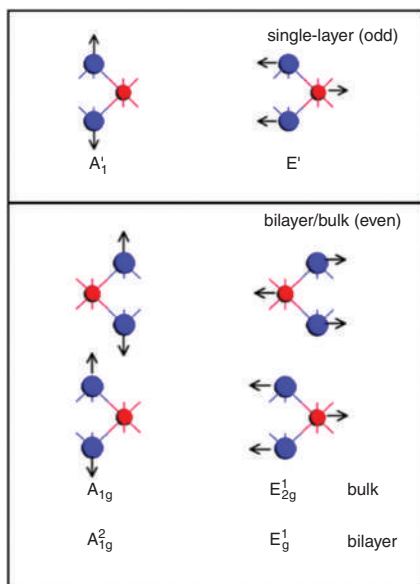


FIG. 47. Main Raman-active phonons in transition-metal dichalcogenides in the single layer case (top panel), representative of odd number of layers; and in bilayer and bulk systems (bottom panel), representative of systems with even number of layers. Reproduced with permission from Zhang *et al.*, Chem. Soc. Rev. **44**, 2757 (2015). Copyright 2015 Royal Society of Chemistry.³¹⁹

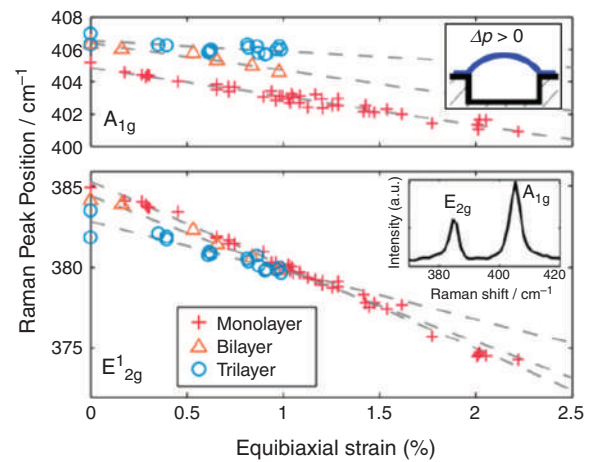


FIG. 48. E_{2g}^1 and A_{1g} Raman modes for unstrained MoS_2 (bottom inset) and peak positions as a function of equibiaxial strain obtained with a bulging device (see sketch in the top inset) for different membrane thicknesses. Reprinted with permission from Lloyd *et al.*, Nano Lett. **16**, 5836 (2016). Copyright 2016 American Chemical Society.⁶⁸

under uniaxial strain, but in this case, the E_{2g}^1 mode shows also a splitting related to the anisotropy introduced in the system. This can be nicely appreciated by performing Raman measurements along the diameter of a bulge/bubble, since the strain turns from equibiaxial at the center to purely uniaxial at the edge [see Fig. 23(d)]. In fact, as shown in Fig. 49, Raman measurements show a clear splitting at the edge—footprint of the anisotropic character of strain—while the two modes merge and further redshift while going toward the summit of the structure.³²³

The mode-splitting behavior upon the application of a uniaxial strain can be well appreciated in the exemplifying case of a MoS_2 -bilayer on a bending device in Fig. 50. This figure allows us to undertake a consideration on strain in the case of bending and stretching devices. As described in Sec. IV B [Eq. (8)], the excitons' shift rates depend on the total amount of strain to which the 2D membrane is subjected. The same holds for the Raman shift rates, as described earlier [Eqs. (12) and (14)]. In the literature, whenever bending devices were used to strain 2D materials, the excitons' rates and the phonon modes' rates have been usually calculated with respect to the strain applied in the bending direction ($\epsilon_l = \epsilon$)—quantified via Eq. (1)—rather than with respect to the total strain. The total strain is in fact given by $\epsilon_{\text{tot}} = (1 - \nu)\epsilon_l$. The same occurred when stretching devices applying strain in one specific direction were employed. The use of the applied strain rather than the total strain has led to some confusion since, for instance, the rates obtained with different methods have often been compared without taking this fact into account. On the other hand, however, it is essential to know the Poisson's ratio ν to quantify the total strain. This might be non-trivial since it is under debate whether it is more correct to employ the Poisson's ratio of the strained material or that of the substrate. In most of the works, either one of these two options was assumed. A compelling analysis was conducted in Ref. 62, where the experimental shift rates of the E_{2g}^1 modes were compared to the theoretical trends obtained by DFT calculations as a function of the Poisson's ratio. As shown in Fig. 50, the best

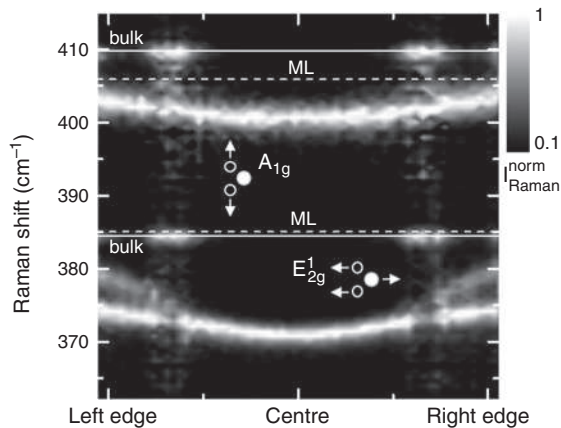


FIG. 49. (a) One-dimensional, room-temperature (RT), μ -Raman scan along the diameter of a MoS₂ dome (with diameter $D = 3.2 \mu\text{m}$) in the spectral region of the out-of-plane A_{1g} phonon mode and of the in-plane E_{2g}^1 mode (depicted as inset). The horizontal axis indicates the laser spot position with respect to the dome centre, whereas the vertical axis indicates the Raman shift with respect to the laser line. The Raman data were separately normalized in the two phonon ranges of the in-plane and out-of-plane modes, and the base-10 logarithm of the normalized intensity is shown in a false color scale (see color bar). The choice to display the normalized data is aimed at following the phonon-energy behaviors along the scan more clearly. The A_{1g} and E_{2g}^1 modes of bulk MoS₂ (at 408.6 and 383.5 cm^{-1} , respectively, highlighted by white solid lines) can be noticed (due to the presence of the bulk flake underneath). While the bulk frequencies are constant, the μ -Raman signal of the dome is clearly shifted at lower frequency with respect to the unstrained ML modes (whose frequencies are highlighted by the white dashed lines). Reprinted with permission from Blundo, Nuovo Cimento C **43**, 112 (2020). Copyright 2020 Author(s), licensed under a Creative Commons Attribution 4.0 International License.³²³

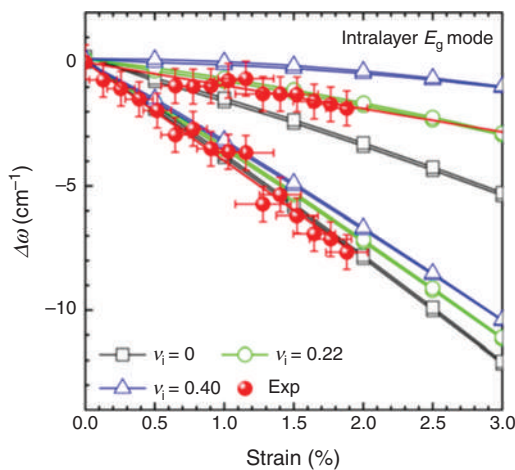


FIG. 50. Frequency of the intralayer split E_{2g}^1 phonon modes (red points) in bilayer MoS₂ as a function of increasing uniaxial strain. The strain is applied via a bending device. The solid lines represent the frequencies calculated via DFT calculations for different values of the Poisson's ratio. Reprinted with permission from Lee *et al.*, Nat. Commun. **8**, 1370 (2017). Copyright 2017 Author(s), licensed under a Creative Commons Attribution 4.0 International License.⁶²

agreement is obtained by using the Poisson's ratio of the 2D material. This suggests using the Poisson's ratios listed in Table III for the calculation of the shift and splitting rates. Indeed, the use of these Poisson's ratios rather than those of the substrate/polymer becomes more questionable in specific devices, where the 2D material is encapsulated.

A survey of the shift and splitting rates, and of the corresponding Grüneisen parameter and shear deformation potential, for the main Raman phonon modes in single-layer and few-layer transition-metal dichalcogenides is provided in Table IX, under different setup geometries. Since different notations were employed in the literature in the definition of the shift rates and of the Grüneisen parameter, we uniformed all the data according to the definitions of Eqs. (10)–(15), by using the Poisson's ratios of Table III.

Coming back to the physics behind the splitting shown in Fig. 50, the weaker and the stronger phonon softening of the two split modes under uniaxial strain can be rationalized in simple terms by considering that modes with lattice displacements along the strain direction are more sensitive to the strain (stronger softening) than those with lattice displacements along the perpendicular direction (smaller softening).³²⁹ Since at $\mathbf{q} = \mathbf{0}$ in the absence of strain the two E_{2g}^1 modes are degenerate, they can be always labeled according to the direction of the forthcoming strain. As a result, the eigenvectors of the split modes in the presence of uniaxial strain are naturally aligned along and perpendicular to the strain direction, *independently* of the crystallographic direction of the system. According to this argument, no information about the direction of the applied strain with respect to the crystal axes can be inferred from the pure measurement of the phonon frequencies.

Powerful information about the crystal orientation is however encoded in the analysis of the polarized Raman peak intensities in the presence of strain. In a typical setup, the intensity of the Raman peaks is measured as a function of the angle ϕ between the polarization of the incoming and outgoing photons, varying ϕ from 0° to 360°. In strain-free systems, with the full crystal symmetry, the intensity of the E_{2g}^1 mode ($I_{E_{2g}^1} = I_{E_{2g}^{1+}} + I_{E_{2g}^{1-}}$) shows no significant dependence on the angle ϕ , whereas the A_{1g} mode has a strongly modulated intensity upon ϕ (see Fig. 51).³³⁰ Notice that such polarization dependence of the intensities of the E_{2g}^1 and A_{1g} modes is quite general and it does not depend on the number of layers. However, it should be remarked that the isotropic polar dependence of the E_{2g}^1 mode strongly relies on the full symmetry of the unstrained crystal (or biaxially strained) and it is a result of the degeneracy of the two in-plane E_{2g}^1 modes. This is remarkably revealed in the presence of uniaxial strain where the two E_{2g}^1 modes are split and the intensity of each separate mode can be traced down as a function of the angle ϕ , as nicely shown in Ref. 62 for bilayer MoS₂. A typical Raman spectrum for bilayer MoS₂ is reproduced in Fig. 52(a), also showing the interlayer shear (S) and breathing (B) modes at low energies. The study of the angle dependence of the intensity of each mode in the presence of uniaxial strain—displayed in Fig. 52(b)—shows that the angle dependence of the A_{1g} intensity is barely affected by strain, whereas the E_{2g} modes split and the intensities of the E_{2g}^{1+} and E_{2g}^{1-} have an orthogonal behavior with ϕ .

TABLE IX. Shift rates, Grüneisen parameters, splitting rates and shear deformation potentials [see Eqs. (12)–(19)] estimated experimentally for TMDs under tensile strain. Notice that the shift/splitting rate is calculated with respect to the total in-plane strain ϵ_{tot} . Therefore, the values displayed here may differ from those reported in the corresponding works, where the rate is often calculated with respect to the bending/stretching strain or to the biaxial strain [see discussion of Eqs. (12)–(19)]. The E_{2g}^1 and A_{1g} Raman modes are here considered. The straining system is indicated, as well as the number of layers of the material. FL stands for few layers. Mech. stands for mechanical.

Mater.	#L	Ref.	System	$\Delta_{E_{2g}^1}$ (cm ⁻¹ /%)	$\gamma_{E_{2g}^1}$	$\Sigma_{E_{2g}^1}$ (cm ⁻¹ /%)	$\beta_{E_{2g}^1}$	$\Delta_{A_{1g}}$ (cm ⁻¹ /%)	$\gamma_{A_{1g}}$
MoS ₂	1L	Blundo <i>et al.</i> ¹¹³	Bubble center	2.2 ± 0.1	0.58 ± 0.03	/	/	0.80 ± 0.05	0.20 ± 0.01
		Tedeschi <i>et al.</i> ¹¹²	Bubble center	2.70 ± 0.51	0.70 ± 0.13	1.04 ± 0.51	0.27 ± 0.13	0.89 ± 0.36	0.22 ± 0.09
		Lloyd <i>et al.</i> ⁶⁸	Blister center	2.6	0.68	/	/	0.85	0.21
		Conley <i>et al.</i> ⁶⁶	Bending	3.7 ± 1.4	0.95 ± 0.36	2.80 ± 0.84	0.73 ± 0.22	~ 0	~ 0
		Y. Wang <i>et al.</i> ³²⁴	Bending	2.20 ± 0.42	0.57 ± 0.11	1.36 ± 0.25	0.35 ± 0.07	~ 0	~ 0
	Rice <i>et al.</i> ⁹⁴	Bending	2.8	0.73	/	/	0.53	0.13	
	2L	Lloyd <i>et al.</i> ⁶⁸	Blister center	2.1	0.55	/	/	0.65	0.16
		Lee <i>et al.</i> ⁶²	Bending	3.27 ± 0.30	0.85 ± 0.08	2.48 ± 0.18	0.64 ± 0.05	0.40 ± 0.13	0.10 ± 0.03
		Conley <i>et al.</i> ⁶⁶	Bending	3.7 ± 1.3	0.97 ± 0.34	2.88 ± 0.79	0.75 ± 0.20	~ 0	~ 0
	3L	Lloyd <i>et al.</i> ⁶⁸	Blister center	1.5	0.39	/	/	0.35	0.09
FL	Rice <i>et al.</i> ⁹⁴	Bending	2.27	0.59	/	/	0.53	0.13	
WS ₂	1L	Tedeschi <i>et al.</i> ¹¹²	Bubble center	2.08 ± 0.29	0.58 ± 0.08	/	/	1.13 ± 0.29	0.27 ± 0.07
		Dadgar <i>et al.</i> ³²⁵	Bending	1.7	0.46	1.0	0.28	0.38	0.09
		Wang <i>et al.</i> ³²⁶	Bending	2.62 ± 0.18	0.74 ± 0.05	/	/	0.74 ± 0.09	0.18 ± 0.02
		Wang <i>et al.</i> ²⁸⁵	Stretching (uniax., mech.)	0.75	0.21	0.71	0.20	1.41	0.34
	FL	F. Wang <i>et al.</i> ³²⁶	Bending	1.32 ± 0.23	0.37 ± 0.07	/	/	0.95 ± 0.06	0.23 ± 0.02
WSe ₂	1L	Dadgar <i>et al.</i> ³²⁵	Bending	0.35	0.44	0.98	0.38	0.50	0.20
	2L	Desai <i>et al.</i> ⁵³	Bending	~ 2.6	~ 1.1	~ 3.9	~ 1.6	/	/
MoTe ₂	FL	Karki <i>et al.</i> ³²⁷	Stretching (uniax., mech.)	0.33	0.14	/	/	/	/
1T-VS ₂	FL ^a	Wang <i>et al.</i> ³²⁸	Blister center	2.55	0.83	/	/	1.05	0.32

^aThree samples with thicknesses of about 10, 15, and 21 L were studied, and no thickness-dependent trends were observed.

Such dependence of the polarization can be rationalized by a close inspection of the Raman tensor \hat{R}^μ for each mode μ . The dependence of the intensity of each mode μ on the polarization of the incoming and outgoing photons can be expressed as

$$I^\mu = |\vec{e}_{\text{in}}^\dagger \cdot \hat{R}^\mu \cdot \vec{e}_{\text{out}}|^2. \quad (20)$$

The knowledge of the Raman tensors, which can be deduced based on symmetry arguments, thus allows us to predict the intensity behavior of each mode. Thus, in Table X, we display the Raman tensors concerning the most relevant Raman modes of several layered crystals, as derived from the crystal symmetries.

Let us consider the case of TMDs. Since in typical experiments the polarization of the incoming and outgoing photons lies in the x-y plane, we are actually interested in the x-y part of the Raman tensors. By looking at Table X, we notice that the 2×2 tensor we have for the A_{1g} and E_{2g}^1 modes is the same for both odd few layers, even few layers, and bulk,

$$\hat{R}_{x-y}^{A_{1g}} = \begin{pmatrix} a & 0 \\ 0 & a \end{pmatrix}, \quad (21)$$

$$\hat{R}_{x-y}^{E_{2g}^{1,x}} = \begin{pmatrix} 0 & c \\ c & 0 \end{pmatrix}, \quad (22)$$

$$\hat{R}_{x-y}^{E_{2g}^{1,y}} = \begin{pmatrix} c & 0 \\ 0 & -c \end{pmatrix}, \quad (23)$$

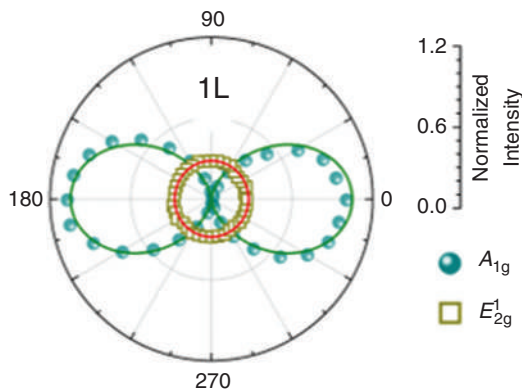


FIG. 51. Polar plot of the intensity of the E_{2g}^1 and A_{1g} modes in an unstrained MoS₂ ML as a function of the angle ϕ between the polarization of the incoming and outgoing photons. The solid lines are fits to the data. Adapted with permission from Kim *et al.*, J. Raman Spectrosc. 51, 774 (2020). Copyright 2020 John Wiley & Sons, Ltd.³³⁰

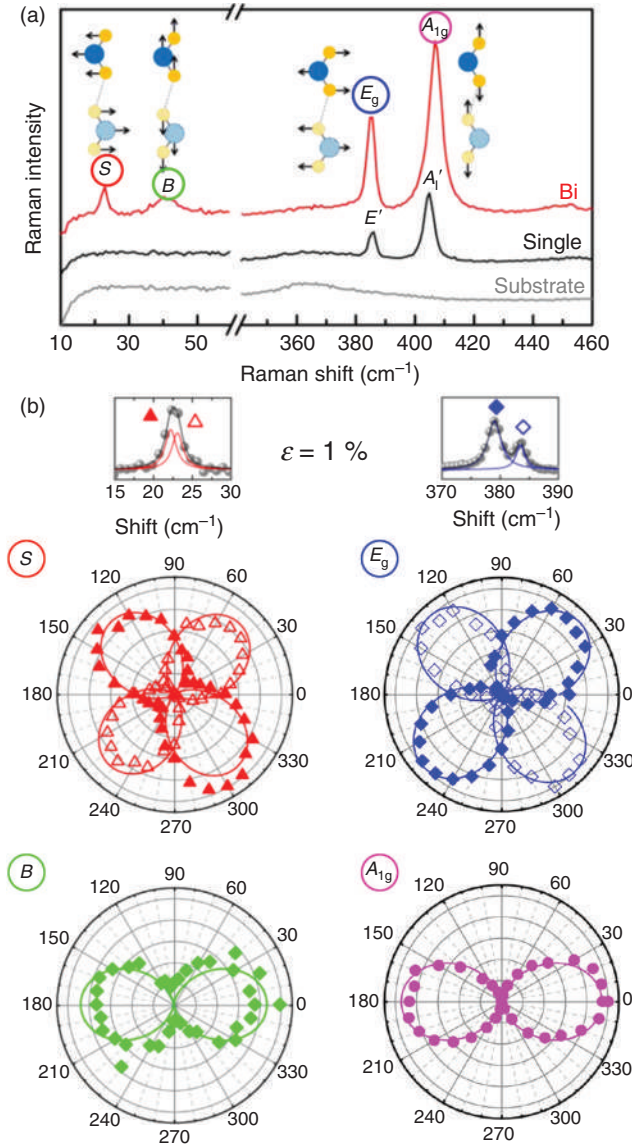


FIG. 52. (a) Raman spectrum of single-layer and bilayer MoS₂ on a substrate, in the absence of strain. Besides the intralayer modes E_{2g}^1 and A_{1g} , the interlayer shear (S) and breathing (B) modes can also be seen in the spectrum of the bilayer flake. The Raman spectrum of the substrate is also shown for sake of completeness. (b) Top: Spectra of the S and the E_{2g}^1 modes from a bilayer subjected to a uniaxial strain in the bending direction equal to 1%. A splitting of the modes can be seen, due to the anisotropic nature of strain. Bottom: Polar angle dependence of the intensities of the interlayer S and B modes and the intralayer A_{1g} and E_{2g}^1 modes upon the application of a strain in the bending direction: $\varepsilon = 1.28\%$. Adapted with permission from Lee *et al.*, Nat. Commun. 8, 1370 (2017). Copyright 2017 Authors, licensed under a Creative Commons Attribution 4.0 International License.⁶²

where x and y refer to the armchair or zigzag directions. Let us consider the general case in which strain is aligned along an arbitrary direction, at an angle θ with respect to the x axis. Since the atomic displacement vectors are parallel or perpendicular to the strain direction,

the out-of-plane mode will be unaffected by the change of basis, while the in-plane modes' tensors will be rotated resulting in

$$\begin{aligned} \hat{R}^{E_{2g}^{1,+}} &= \begin{pmatrix} \cos \theta & \sin \theta \\ -\sin \theta & \cos \theta \end{pmatrix} \cdot \begin{pmatrix} 0 & c \\ c & 0 \end{pmatrix} \\ &= \begin{pmatrix} c \cdot \sin \theta & c \cdot \cos \theta \\ c \cdot \cos \theta & -c \cdot \sin \theta \end{pmatrix}, \end{aligned} \quad (24)$$

$$\begin{aligned} \hat{R}^{E_{2g}^{1,-}} &= \begin{pmatrix} \cos \theta & \sin \theta \\ -\sin \theta & \cos \theta \end{pmatrix} \cdot \begin{pmatrix} c & 0 \\ 0 & -c \end{pmatrix} \\ &= \begin{pmatrix} c \cdot \cos \theta & -c \cdot \sin \theta \\ -c \cdot \sin \theta & -c \cdot \cos \theta \end{pmatrix}. \end{aligned} \quad (25)$$

During the experiments, the polarization of the incoming photon is typically kept fixed in an arbitrary direction, forming an angle ϕ_0 with respect to the x axis. We can thus set $\vec{e}_{\text{in}} = (\cos \phi_0, \sin \phi_0, 0)^T$. The angle ϕ between the polarization of the outgoing and incoming photon is then varied from 0° to 360° , so that we have: $\vec{e}_{\text{out}} = (\cos(\phi + \phi_0), \sin(\phi + \phi_0), 0)^T$. From Eqs. (24) and (25), we find that for TMDs,

$$\begin{aligned} I^{A_{1g}} &= a^2 \cos^2 \phi, \\ I^{E_{2g}^{1,+}} &= c^2 \cos^2(\phi + 2\phi_0 + \theta), \\ I^{E_{2g}^{1,-}} &= c^2 \sin^2(\phi + 2\phi_0 + \theta), \\ I^{E_{2g}^1} &= I^{E_{2g}^{1,+}} + I^{E_{2g}^{1,-}} = c^2. \end{aligned} \quad (26)$$

We observe that the A_{1g} mode dependence on ϕ is independent of the strain direction, while the total intensity of the E_{2g}^1 mode is constant independently of both ϕ and the strain axis. To the contrary, the intensities of the $E_{2g}^{1,\pm}$ modes feature a dependence both on ϕ and on the strain direction. If the polarization of the incoming photon is aligned along the strain axis ($\phi_0 = \theta$), we see that $I^{E_{2g}^{1,+}} = c^2 \cos^2(\phi + 3\theta)$ and $I^{E_{2g}^{1,-}} = c^2 \sin^2(\phi + 3\theta)$, thus in excellent agreement with the experimental results shown in Fig. 52. We see how the intensity behavior obtained by varying ϕ carries the relevant crystallographic information.

A similar analysis to that shown for a bilayer in Ref. 62 and shown in Fig. 52 was performed in single-layer systems.^{319,324,329} The investigation of the bilayer case in Ref. 62 further shows that similar selection rules apply as well for the interlayer B and S modes, with the B mode following essentially the same angle dependence on the polarization as the intralayer A_{1g} mode, and the (double-degenerate and split) interlayer shear modes S strictly mimicking the polar dependence of the intralayer E_{2g}^1 modes [see Fig. 52(b)].⁶²

2. Graphene

The efficiency of the Raman spectroscopy in characterizing the strength and properties of strain has been proven to be a powerful technique also in graphene, where the analysis is expected to be in principle even more straightforward since, in the single layer, only the double-degenerate optical mode E_{2g} at $\sim 1580 \text{ cm}^{-1}$ is Raman active (see sketch in Fig. 53). The Raman peak corresponding to the first-order E_{2g} phonon resonance is often denoted as G band in the literature.

TABLE X. Space group and Raman tensors for the most common layered materials and their 2D counterparts, including graphite/graphene, h-BN, TMDs in both the 2H and 1T phase, post-transition-metal chalcogenides (post-TMCs)—such as InSe and GaSe—in both the ϵ , β , and γ phases, and black phosphorus. a, b, \dots, e indicate constants depending on the system. The symmetry group and properties of the crystals were discussed in Refs. 319, 331–338. The Raman tensors were derived from Ref. 321.

Material(s)	Class, Group (System)	Raman tensors		
		A modes	E or B modes	E or B modes
<ul style="list-style-type: none"> • Graphite / Graphene • Even few layer h-BN • Bulk 2H TMDs • β Post TMC 	$6/mmm, D_{6h}$ (Hexagonal)	$A_{1g} : \begin{pmatrix} a & 0 & 0 \\ 0 & a & 0 \\ 0 & 0 & b \end{pmatrix}$	$E_{2g} : \begin{pmatrix} 0 & c & 0 \\ c & 0 & 0 \\ 0 & 0 & 0 \end{pmatrix}$	$E_{2g} : \begin{pmatrix} c & 0 & 0 \\ 0 & -c & 0 \\ 0 & 0 & 0 \end{pmatrix}$
<ul style="list-style-type: none"> • Odd few layer h-BN • Bulk h-BN • Odd few layer 2H TMDs • ϵ Post TMC 	$\bar{6}m2, D_{3h}$ (Hexagonal)	$A'_1 : \begin{pmatrix} a & 0 & 0 \\ 0 & a & 0 \\ 0 & 0 & b \end{pmatrix}$	$E'(x) : \begin{pmatrix} 0 & c & 0 \\ c & 0 & 0 \\ 0 & 0 & 0 \end{pmatrix}$	$E'(y) : \begin{pmatrix} c & 0 & 0 \\ 0 & -c & 0 \\ 0 & 0 & 0 \end{pmatrix}$
<ul style="list-style-type: none"> • Even few layer 2H TMDs • Odd and even layer 1T TMDs 	$\bar{3}m, D_{3d}$ (Trigonal)	$A_{1g} : \begin{pmatrix} a & 0 & 0 \\ 0 & a & 0 \\ 0 & 0 & b \end{pmatrix}$	$E_g : \begin{pmatrix} c & 0 & 0 \\ 0 & -c & d \\ 0 & d & 0 \end{pmatrix}$	$E_g : \begin{pmatrix} 0 & -c & -d \\ -c & 0 & 0 \\ -d & 0 & 0 \end{pmatrix}$
<ul style="list-style-type: none"> • γ Post TMC 	$3m, C_{3v}$ (Trigonal)	$A_1(z) : \begin{pmatrix} a & 0 & 0 \\ 0 & a & 0 \\ 0 & 0 & b \end{pmatrix}$	$E(y) : \begin{pmatrix} c & 0 & 0 \\ 0 & -c & d \\ 0 & d & 0 \end{pmatrix}$	$E(-x) : \begin{pmatrix} 0 & -c & -d \\ -c & 0 & 0 \\ -d & 0 & 0 \end{pmatrix}$
<ul style="list-style-type: none"> • Black phosphorus 	mmm, D_{2h} (Orthorhombic)	$A_g : \begin{pmatrix} a & 0 & 0 \\ 0 & b & 0 \\ 0 & 0 & c \end{pmatrix}$	$B_{2g} : \begin{pmatrix} 0 & 0 & d \\ 0 & 0 & 0 \\ d & 0 & 0 \end{pmatrix}$	$B_{3g} : \begin{pmatrix} 0 & 0 & 0 \\ 0 & 0 & e \\ 0 & e & 0 \end{pmatrix}$

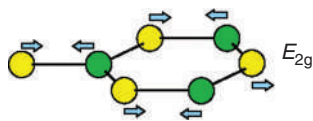


FIG. 53. Atomic lattice displacement of the E_{2g} phonon mode (also referred to as G mode) in single-layer graphene.

Bearing a close resemblance to the E_{2g} modes of TMDs, the G mode also undergoes a softening upon tensile biaxial strain and hardening upon compressive strain,^{61,86,89,339–347} as shown, for instance, in Fig. 54. Quite remarkably, a similar softening/hardening vs tensile/compressive strain is observed also for other higher-order phonon modes, labeled as $D, 2D, 2D'$.^{86,89,340–347} The origin for such phonon peaks is ascribed to diverse higher-order Raman processes. In particular, the double-resonance $2D$ peak involves the excitation of *two* phonons with opposite momentum ($\mathbf{q}, -\mathbf{q}$) very close to the zone edges K, K' .³⁴⁸ Since this Raman process does not require disorder, it is observed also in defect-free samples. In fact, an elevated intensity of the $2D$ peak with respect to the G peak is usually regarded as a footprint of high-quality samples. Also visible in Fig. 54 is the strain dependence of the Raman peaks $D, 2D'$, which also probe phonons at the zone edges K, K' , but they are assisted by a disorder-induced scattering. In this case, the letter D is meant to highlight they are defect-related peaks. The analysis of all these higher-order Raman peaks represents a powerful tool which is complementary to the study of the G (E_{2g}) peak. The latter in fact turns out to be sensitive to both strain and charge doping, so that in most of the realistic strained systems it is difficult to disentangle the energy shifts

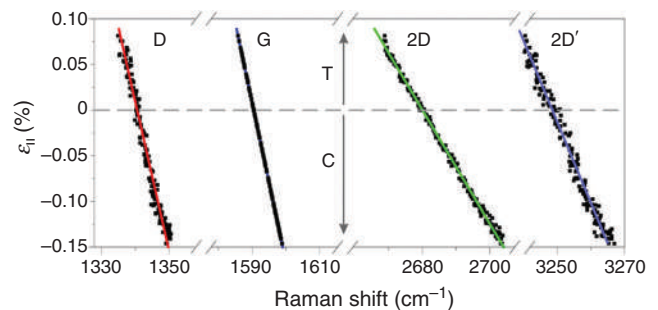


FIG. 54. Peak mode dependence on biaxial strain for the E_{2g} mode (or G mode) and for the higher-order phonon modes ($2D, D$, and D') in monolayer graphene. Strain is applied by stretched the 2D membrane by means of a piezoelectric substrate. Both softening and hardening effects are detected upon the application of tensile or compressive strain, respectively. Reprinted with permission from Ding *et al.*, *Nano Lett.* **10**, 3453 (2010). Copyright 2010 American Chemical Society.⁸⁶

induced by these two concomitant effects, hampering a compelling evaluation of the microscopic strain. The lower sensitivity to doping of these higher-order peaks thus provides a valuable reference to calibrate the effective strain. Within this context, so far, the crossed analysis of the strain dependence of the G band with the $2D$ peak,^{345,349,350} or with the $2D'$ peak⁵⁸ has been employed.

Finally, similar to TMDs, a uniaxial strain in graphene also leads to a splitting of the double-degenerate modes E_{2g} , which is experimentally observed [Figs. 55(a) and 55(b)] and can be employed to assess

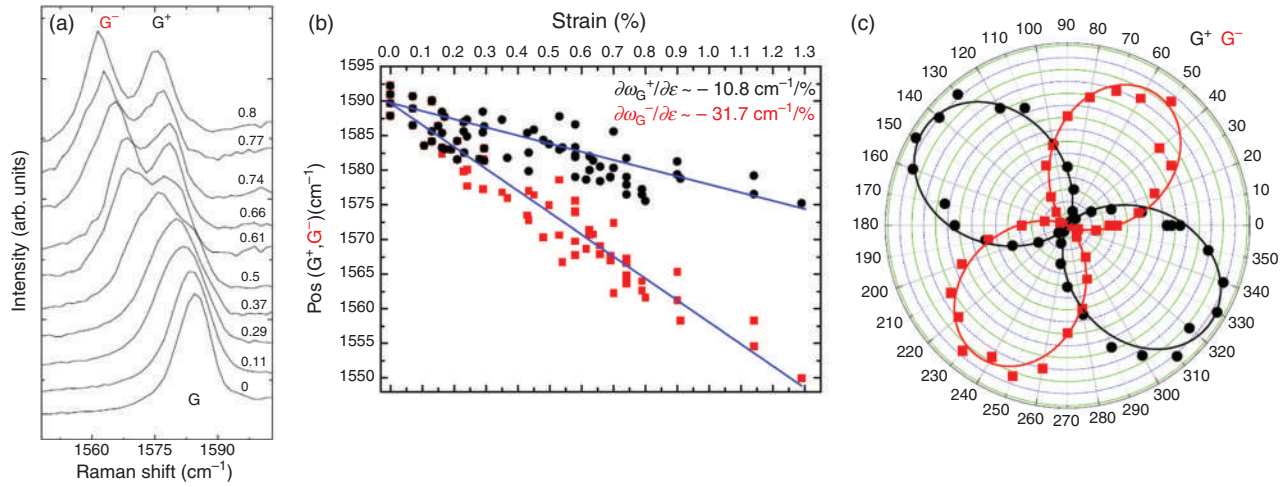


FIG. 55. (a) Raman spectra of graphene in the frequency range of the G phonon mode as a function of uniaxial strain (in a bending apparatus). The spectra are measured with incident light polarized along the strain direction, collecting the scattered light with no analyzer. The doubly degenerate G peak splits in two subbands G^+ and G^- . (b) Peak positions of the two split subbands as a function of the bending strain. The blue lines are main fits to the data. The slopes are indicated. (c) Polar plot of the G^+ and G^- peaks as a function of the angle between the incident light polarization and the strain axis θ . The measurements were performed for scattered light aligned with the strain direction and rotating the incident polarization with respect to the strain axis in steps of 10° . The polar data are fitted to $I_{G^-} \propto \sin^2(\theta + \theta_{\text{offset}})$ and $I_{G^+} \propto \cos^2(\theta + \theta_{\text{offset}})$. Reprinted with permission from Mohiuddin *et al.*, Phys. Rev. B **79**, 205433 (2009). Copyright 2009 American Physical Society.⁶¹

the anisotropy of the applied strain.^{61,340,341,343} Furthermore, a similar analysis of the Raman intensity of the split E_{2g} modes as a function of the polarization angle between incoming and outgoing photons in uniaxially strained graphene permits us to identify the crystal axis in graphene^{61,340,341,350} [see Fig. 55(c)], as in TMDs.

A collection of the experimental shift rates, Grüneisen parameters, splitting rates, and shear deformation potentials available in literature for the main phonon peaks of graphene is presented in Table XI. In Table XII, instead, we show for completeness the shift rates and Grüneisen parameters for the higher-order peaks normalized to those of the G peak.

TABLE XI. Shift rates, Grüneisen parameters, splitting rates, and shear deformation potentials [see Eqs. (12)–(19)] estimated experimentally for graphene under tensile strain. Notice that the shift/splitting rate is calculated with respect to the total in-plane strain ϵ_{tot} . Therefore, the values displayed here may differ from those reported in the corresponding works, where the rate is often calculated with respect to the bending/stretching strain or to the biaxial strain [see discussion of Eqs. (12)–(19)]. First-order Raman scattering (G peak) and double resonance Raman scattering (2D peak) processes are considered here. The straining system is indicated, as well as the number of layers of the material. mL stands for many layers. Mech. stands for mechanical.

Mater.	#L	Ref.	System	Δ_G (cm ⁻¹ /%)	γ_G	Σ_G (cm ⁻¹ /%)	β_G	Δ_{2D} (cm ⁻¹ /%)	γ_{2D}
Graphene	1L	Jiang <i>et al.</i> ⁸⁹	Stretching (uniax., mech.)	/	/	/	/	52.5	1.99
		Ni <i>et al.</i> ³⁴³	Stretching (uniax., mech.)	17.2 ± 0.8	1.09 ± 0.05	/	/	33.7 ± 1.0	1.25 ± 0.04
	Bending	Gong <i>et al.</i> ³⁴⁴	/	/	/	/	59.2 ± 3.0	2.24 ± 0.11	
		Gong <i>et al.</i> ³⁴⁴	/	/	/	/	70.0 ± 9.5	2.65 ± 0.36	
		Huang <i>et al.</i> ³⁴⁰	Bending	11.0 ± 3.5	0.69 ± 0.22	5.9 ± 2.4	0.37 ± 0.15	25.5 ± 5.1	0.95 ± 0.19
		Mohiuddin <i>et al.</i> ⁶¹	Bending	25.8	1.6	17.8	1.1	77.7	2.9
2L	Androulidakis <i>et al.</i> ³⁴⁷	Bending	24.0 ± 1.5	1.52 ± 0.09	13.9 ± 1.0	0.88 ± 0.07	59.0 ± 3.0	2.26 ± 0.12	
		Bending	/	/	/	/	47.2 ± 2.9	1.77 ± 0.11	
	Bending ^a	Gong <i>et al.</i> ³⁴⁴	/	/	/	/	65.4 ± 3.5	2.45 ± 0.13	
		Gong <i>et al.</i> ³⁴⁴	Bending ^a	/	/	/	/	56.6 ± 10.9	2.11 ± 0.41
3L	Ni <i>et al.</i> ³⁴³	Stretching (uniax., mech.)	14.7 ± 0.7	0.93 ± 0.05	/	/	26.6 ± 1.3	0.99 ± 0.05	
		Androulidakis <i>et al.</i> ³⁴⁷	Bending	15.1 ± 2.6	0.95 ± 0.17	10.0 ± 1.8	0.63 ± 0.12	34.7 ± 1.7	1.32 ± 0.06
	Bending	Gong <i>et al.</i> ³⁴⁴	/	/	/	/	39.3 ± 0.5	1.47 ± 0.02	
		Gong <i>et al.</i> ³⁴⁴	Bending ^a	/	/	/	/	45.4 ± 10.0	1.69 ± 0.37
mL	Gong <i>et al.</i> ³⁴⁴	Bending	/	/	/	/	45.4 ± 10.0	1.69 ± 0.37	
		Bending ^a	/	/	/	/	48.8 ± 17.2	1.81 ± 0.64	

^aIn this case, the flake was coated with an epoxy layer.

TABLE XII. Shift rates and Grüneisen parameters (see Table XI) estimated experimentally for the 2D peak and for the defect- and disorder-related peaks of graphene (D and 2D' peaks) under tensile strain. All the quantities are normalized to the G peak values.

Mater.	#L	Ref.	System	Δ_{2D}/Δ_G	γ_{2D}/γ_G	Δ_D/Δ_G	γ_D/γ_G	$\Delta_{2D'}/\Delta_G$	$\gamma_{2D'}/\gamma_G$
Graphene	1L	Ni <i>et al.</i> ³⁴³	Stretching (uniax., mech.)	1.96 ± 0.15	1.15 ± 0.09	/	/	/	/
		Ding <i>et al.</i> ⁸⁶	Stretching (biaxial, piezo)	2.80	1.66	1.07	1.28	1.96	0.96
	Zabel <i>et al.</i> ³⁴⁵	Bubble center	2.45 ± 0.37	1.44 ± 0.22	1.19 ± 0.23	1.40 ± 0.27	1.89 ± 0.28	0.92 ± 0.14	
	Huang <i>et al.</i> ³⁴⁰	Bending	2.3 ± 1.2	1.38 ± 0.71	/	/	/	/	
	Mohiuddin <i>et al.</i> ⁶¹	Bending	3.01	~ 1.8	/	/	1.65	~ 0.8	
	2L	Androulidakis <i>et al.</i> ³⁴⁷	Bending	2.46 ± 0.28	1.49 ± 0.17	/	/	/	/
	3L	Ni <i>et al.</i> ³⁴³	Stretching (uniax., mech.)	1.81 ± 0.17	1.06 ± 0.11	/	/	/	/
		Androulidakis <i>et al.</i> ³⁴⁷	Bending	2.31 ± 0.51	1.39 ± 0.31	/	/	/	/

3. h-BN

Analogously to graphene, at first order the Raman spectrum of h-BN is characterized by modes with E_{2g} symmetry (see Table X). In particular, the spectrum is dominated by an intralayer mode^{351,352} at $\sim 1370 \text{ cm}^{-1}$ and by an interlayer shear mode³⁵² at $\sim 50 \text{ cm}^{-1}$. The frequency of this shear mode is found to be highly sensitive to the number of layers, and can thus be used to identify the flake thickness. On the other hand, few studies on the effect of strain in h-BN showed how the intralayer mode is highly sensitive to mechanical deformations, with relatively high shift rates, as summarized in Table XIII.

4. Post-TMCs

Post-TMCs, such as InSe and GaSe, are mostly studied in their γ polytype. In this form, they belong to a symmetry group different from that of graphene, h-BN, or TMDs (see Table X). Nonetheless, the Raman tensors are still the A_1 —related to out-of-plane vibrations—and the E tensors—related to in-plane vibrations. Several modes with such symmetries are Raman active, as sketched in Fig. 56(a). In particular, as shown in Fig. 56(b), the Raman spectrum of InSe is characterized by the in-plane modes $E(\Gamma_3^3)/E(\Gamma_3^1)$ —TO at about 180 cm^{-1} and $E(\Gamma_3^3)$ —LO at about 205 cm^{-1} , and by the out-of-plane modes

$A_1(\Gamma_1^2)$ at about 110 cm^{-1} , $A_1(\Gamma_1^1)$ —LO at about 200 cm^{-1} , and $A_1(\Gamma_1^3)$ at about 225 cm^{-1} .^{98,99,282} Analogously to the other 2D materials discussed before, all these modes feature linear redshifts if tensile strains are applied, with relatively small shift rates comparable to those of TMDs. The shift rates and Grüneisen parameters for the Raman modes with E and A_1 symmetry are summarized in Tables XIV and XV, respectively. Interestingly, together with a shift in the peak frequency, for the LO modes, tensile strain can lead also to a signal enhancement, as can be clearly seen in Fig. 56(b). This behavior was explained in terms of intraband electron–phonon scattering channels, coupled with the fact that when uniaxial tensile strain is applied, the energy of the B transition shifts closer to that of the incident photon.⁹⁹

5. Black Phosphorus

BP is a 2D material with an intriguingly anisotropic structure, which reverberates in an anisotropic response of the vibrational modes to strain. The Raman spectrum of BP is characterized by three main modes, with either A_g (modes at about 362 and 468 cm^{-1}) or B_{2g} symmetry (mode at about 439 cm^{-1}) (see Table X and Fig. 57). The effect of strain on the Raman-active modes of BP was studied by subjecting thin crystals to either compressive (in a bending apparatus)^{353,354} or tensile

TABLE XIII. Shift rates, Grüneisen parameters, splitting rates, and shear deformation potentials [see Eqs. (12)–(19)] estimated experimentally for h-BN under tensile or compressive strain. Notice that the shift/splitting rate is calculated with respect to the total in-plane strain ϵ_{tot} . Therefore, the values displayed here may differ from those reported in the corresponding works, where the rate is often calculated with respect to the bending/stretching strain or to the biaxial strain [see discussion of Eqs. (12)–(19)]. The E_{2g} Raman mode is here considered. The straining system is indicated, as well as the number of layers of the material. mL stands for many layers ($>10L$).

Mater.	#L	Ref.	System	$\Delta_{E_{2g}} (\text{cm}^{-1}/\%)$	$\gamma_{E_{2g}}$	$\Sigma_{E_{2g}} (\text{cm}^{-1}/\%)$	$\beta_{E_{2g}}$
h-BN	1L	Cai <i>et al.</i> ¹⁰⁴	Thermal compression (biaxial)	11.5 ± 2.7	0.84 ± 0.20	/	/
	2L	Androulidakis <i>et al.</i> ⁹⁵	Bending	20.9 ± 11.4	1.53 ± 0.87	13.0 ± 7.5	0.95 ± 0.55
		Cai <i>et al.</i> ¹⁰⁴	Thermal compression (biaxial)	10.4 ± 3.1	0.76 ± 0.22	/	/
	3L	Androulidakis <i>et al.</i> ⁹⁵	Bending	20.2 ± 7.6	1.48 ± 0.55	13.1 ± 4.8	0.96 ± 0.35
		Androulidakis <i>et al.</i> ⁹⁵	Bending	21.4 ± 7.9	1.56 ± 0.58	14.7 ± 5.0	1.08 ± 0.37
		Cai <i>et al.</i> ¹⁰⁴	Thermal compression (biaxial)	8.5 ± 2.3	0.62 ± 0.17	/	/
	4L	Androulidakis <i>et al.</i> ⁹⁵	Bending	23.8 ± 11.7	1.74 ± 0.85	14.2 ± 7.4	1.03 ± 0.54
mL	Androulidakis <i>et al.</i> ⁹⁵	Bending	20.2 ± 7.6	1.48 ± 0.55	13.1 ± 4.8	0.96 ± 0.35	

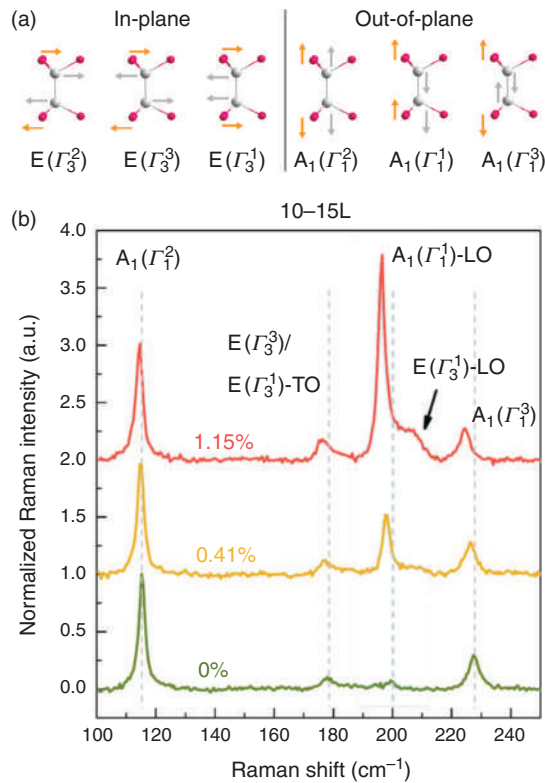


FIG. 56. (a) Lattice vibrations of all the first-order optical phonon modes of InSe. Mulliken symbols are used, while the corresponding Γ symbols are labeled in parentheses for comparison. (b) Raman spectra of InSe flakes with thickness of about 10 to 15 layers, as uniaxial tensile strain is applied in a bending apparatus. The values of strain in the bending directions corresponding to each spectrum are displayed. The assignment of the corresponding phonon mode for each Raman peak is marked. The vertical gray dashed lines indicate the positions of the respective Raman peaks in the absence of strain. Adapted with permission from Song *et al.*, Phys. Rev. B **99**, 195414 (2019). Copyright 2019 American Physical Society.⁹⁹

TABLE XIV. Shift rates and Grüneisen parameters [see Eqs. (12)–(19)] of the modes with E symmetry of InSe, estimated experimentally. Notice that the shift rate is calculated with respect to the total in-plane strain ϵ_{tot} . Therefore, the values displayed here may differ from those reported in the corresponding works, where the rate is often calculated with respect to the bending/stretching strain or to the biaxial strain [see discussion of Eqs. (12)–(19)]. The straining system is indicated, as well as the number of layers of the material.

Mater.	#L	Ref.	System	$\Delta_{E(\Gamma_3^2)/E(\Gamma_3^1)\text{-TO}}$ (cm ⁻¹ /%)	$\gamma_{E(\Gamma_3^2)/E(\Gamma_3^1)\text{-TO}}$	$\Delta_{E(\Gamma_3^1)\text{-LO}}$ (cm ⁻¹ /%)	$\gamma_{E(\Gamma_3^1)\text{-LO}}$
InSe	3L–6L	Song <i>et al.</i> ⁹⁹	Bending	2.0 ± 0.3	1.1 ± 0.2	/	/
	10L–15L	Song <i>et al.</i> ⁹⁹	Bending	2.0 ± 0.3	1.1 ± 0.2	2.7 ± 0.7	1.3 ± 0.3
		Li <i>et al.</i> ⁹⁸	Bending	~ 4.5	~ 2.5	/	/

TABLE XV. Shift rates and Grüneisen parameters [see Eqs. (12)–(19)] of the modes with A symmetry of InSe, estimated experimentally. Notice that the shift/splitting rate is calculated with respect to the total in-plane strain ϵ_{tot} . Therefore, the values displayed here may differ from those reported in the corresponding works, where the rate is often calculated with respect to the bending/stretching strain or to the biaxial strain [see discussion of Eqs. (12)–(19)]. The straining system is indicated, as well as the number of layers of the material.

Mater.	#L	Ref.	System	$\Delta_{A_1(\Gamma_1^2)}$ (cm ⁻¹ /%)	$\gamma_{A_1(\Gamma_1^2)}$	$\Delta_{A_1(\Gamma_1^1)\text{-LO}}$ (cm ⁻¹ /%)	$\gamma_{A_1(\Gamma_1^1)\text{-LO}}$	$\Delta_{A_1(\Gamma_1^3)}$ (cm ⁻¹ /%)	$\gamma_{A_1(\Gamma_1^3)}$
InSe	3L–6L	Song <i>et al.</i> ⁹⁹	Bending	1.1 ± 0.1	0.9 ± 0.1	3.7 ± 0.3	1.8 ± 0.1	3.3 ± 0.3	1.4 ± 0.1
	10L–15L	Song <i>et al.</i> ⁹⁹	Bending	1.1 ± 0.1	0.9 ± 0.1	3.4 ± 0.1	1.7 ± 0.1	3.4 ± 0.1	1.5 ± 0.1
		Li <i>et al.</i> ⁹⁸	Bending	/	/	~ 4.6	~ 2.3	~ 4.2	~ 1.8

strains (in bending^{101,353,354} or stretching³²⁷ setups). The results obtained in all these experiments are summarized in Table XVI. Rather large quantitative discrepancies are found by comparing the results of the different works, though some common trends can indeed be noticed. Generally, a redshift (blueshift) is observed upon the application of a tensile (compressive) strain, similarly to the other 2D materials, see Fig. 57(b). The experiments of Ref. 353 suggest that no remarkable differences are found by applying either tensile or compressive strains. Instead, bending experiments in Refs. 101 and 353 revealed how the Raman modes shift at a remarkably different rate depending on whether strain is applied in the armchair or zigzag direction. This is mostly attributable to the preferential directions along which the atomic displacements take place for each mode. For instance, for the B_{2g} mode, the displacement is mainly along the zigzag direction, and therefore this mode is highly sensitive to zigzag-aligned strains.¹⁰¹ Finally, it's worth mentioning that stretching experiments in Ref. 327 revealed how the shift is linear for small stretching strains (roughly below 0.5%), while a decrease in the shift is observed for larger strains for all the three modes. To the contrary, a linear behavior is observed in Ref. 101 up to bending strains of about 0.8%.

E. Nonlinear optical phenomena: Second and third harmonic generation

As discussed in Secs. IV A–IV B, semiconducting 2D materials feature a remarkable change in their opto-electronic properties when subjected to strain. These dramatic changes affect also the non-linear optical response of these crystals. In particular, the weak dielectric screening in thin TMDs enhances the Coulomb interaction between charge carriers and, in turn, the matrix elements of optical transitions, leading to a non-linear susceptibility orders of magnitude larger than in most nonlinear crystals.²⁸⁶ This results in a relatively strong second and third harmonic generation (SHG and THG, respectively). This means that the polarization can be expressed as $\mathbf{P} = \mathbf{P}^{(1)} + \mathbf{P}^{(2)} + \mathbf{P}^{(3)}$, where $\mathbf{P}^{(n)} = \epsilon \chi^{(n)} \mathbf{E}^n$, ϵ being the dielectric constant, \mathbf{E} the electric field, and $\chi^{(n)}$ tensors of rank $n + 1$ representing the n -th order susceptibility. Generally, in the presence of an

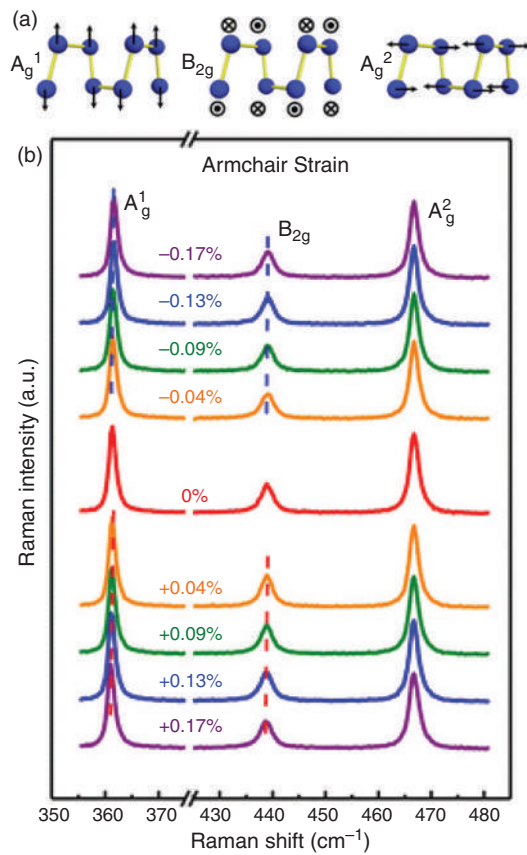


FIG. 57. (a) Sketch of the atomic vibrations of BP. (b) Raman spectrum of BP subjected to compressive, null, or tensile strain applied via a bending device. The strain values are indicated. Reprinted with permission from Du *et al.*, *Nano Lett.* **16**, 6701 (2016). Copyright 2016 American Chemical Society.³⁵³

optical field of the form $\mathbf{E} = Ee^{-i\omega t}$ (as under laser excitation at frequency ω), the presence of a non-vanishing second and third order susceptibility results in the generation of nonlinear contributions proportional to $\mathbf{E}^{(2)} \sim e^{-i2\omega t}$ and $\mathbf{E}^{(3)} \sim e^{-i3\omega t}$. A sketch of the SHG

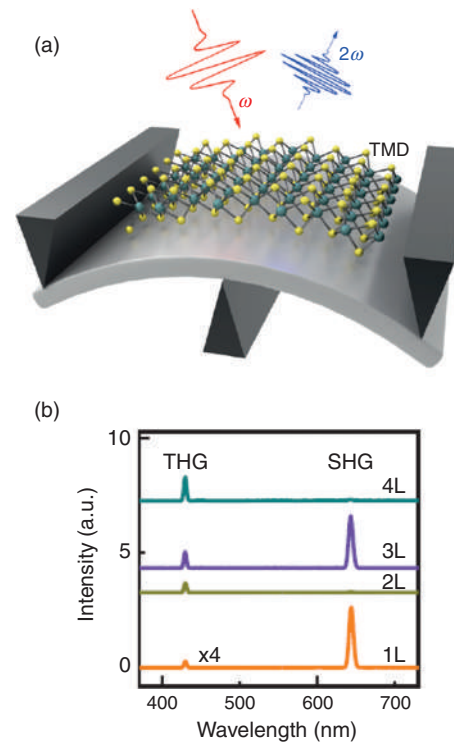


FIG. 58. (a) Sketch of the SHG process under excitation with an optical field of frequency ω , resulting in the emission of light of frequency 2ω . Reprinted with permission from Mennel *et al.*, *Nano Lett.* **20**, 4242 (2020). Copyright 2020 American Chemical Society.²⁰⁵ (b) SHG and THG signal revealed in few-layered WS_2 crystals. Reprinted with permission from Liang *et al.*, *Adv. Mater.* **31**, 1808160 (2019). Copyright 2019 Wiley-VCH Verlag GmbH & Co. KGaA, Weinheim.²⁸⁷

process in a strained 2D crystal is displayed in Fig. 58(a). From an experimental point of view, pulsed lasers emitting in the near-infrared range (between 800 and 1200 nm) are usually employed to stimulate the SHG or THG process. Such choice is grounded on the fact that the generated signals will be in the visible range (typically, in the blue range between 400 and 500 nm) and can thus be detected with

TABLE XVI. Shift of the Raman frequency obtained by bending or stretching BP. Due to the anisotropy in the properties of BP, in this case, the rate is calculated with respect to the strain in the bending/stretching direction rather than with respect to the total strain [see Eqs. (12)–(19)]. The straining system is indicated, as well as the number of layers of the material.

Mater.	System	Strain direction	Ref.	#L	Strain type	$-\partial\omega/\partial\epsilon_{\text{bend/stretch}} \text{ (cm}^{-1}\text{/\%)} $		
						A_g^1	B_{2g}	A_g^2
BP	Bending	Armchair	Li <i>et al.</i> ¹⁰¹	15L	Tensile	3.81 ± 0.15	1.85 ± 0.05	0.03 ± 0.05
			Du <i>et al.</i> ³⁵³	15L	Tensile	1.37	1.07	/
		Zigzag	Li <i>et al.</i> ¹⁰¹	15L	Compressive	1.78	0.88	/
			Du <i>et al.</i> ³⁵³	15L	Compressive	0.52 ± 0.06	10.92 ± 0.22	4.32 ± 0.11
	Stretching	Armchair	Karki <i>et al.</i> ³²⁷	15L	Tensile	0.56	5.46	2.73
				15L	Compressive	0.86	5.27	2.22
				2-3L	Tensile+compr.	0.86	0.63	0.21
				Few L	Tensile	3.4	5.3	5.5

Si-CCDs. The susceptibility tensor components reflect the symmetries of the crystal. This makes SHG negligible in all centrosymmetric 2D materials such as graphene and even-layered TMDs, while it is intense in non-centrosymmetric 2D materials such as odd-layered TMDs. On the contrary, the THG process is allowed also in centrosymmetric crystals, and thus it can be observed in both even- and odd-layered crystals. SHG and THG measurements on few layers of WS₂ are shown as an example in Fig. 58(b). Materials with strong SHG and THG are of interest for several potential applications, including nonlinear optical waveguides, frequency doubling for lasers, and optical imaging for disease diagnostics,³⁵⁵ etc. TMDs are thus virtually ideal candidates for applicative prospects due to their high nonlinear susceptibilities and the possibility to generate nonlinear optical phenomena on localized micrometer-size and sub-micron-size areas. For instance, SHG has been observed in buckled and wrinkled few-layered TMDs in Ref. 356 [see Figs. 59(a) and 59(b)], where it has been shown how these structures can lead to a strain-dependent SHG quenching or enhancement, which could be exploited for the development of optical devices. Furthermore, monolayer bubbles created by hydrogen-ion irradiation on bulk parent flakes act as efficient second-harmonic emitters due to their single-layer nature. Hence, ordered arrays of bubbles could thus conceivably act as site-controlled SHG “hot spots” ideal for the integration with specifically designed photonic crystal cavities,¹¹² as shown in Fig. 59(c). Indeed, both in the case of buckles, wrinkles, and bubbles, the SHG process concerns a mechanically deformed membrane and the knowledge of how the mechanical deformation affects the SHG would be important for

the integration into actual devices. In addition to the practical interest, SHG and THG have been proposed as a powerful tool to map the strain tensor in 2D materials, since they are highly symmetry dependent. In the following, we will discuss experimental results and theoretical analyses aimed at probing the SHG and THG dependence on strain.

1. SHG

To understand the SHG dependence on strain, elements of the point group theory should be considered.²⁹² In the absence of strain, non-centrosymmetric crystals are characterized by the threefold D_{3h} symmetry. Indeed, the same holds if the material is subjected to equibiaxial strain. In the case of uniaxial strain, instead, the symmetry changes. In particular, for uniaxial strain along high-symmetry directions (i.e., armchair or zigzag), the threefold C_3 axis disappears, and only one twofold C_2 axis along the armchair orientation survives. The crystalline symmetry is thus reduced from the D_{3h} to the C_{2v} point group. In the more general case, when strain is along random directions, the C_2 axis also disappears, and the symmetry is further reduced to the C_{1h} point group. This generally gives rise to asymmetries in the polarization-dependent SHG pattern. Two possible descriptions have been mostly used in the literature to describe the SHG intensity pattern. One possible description is to express the polarization-dependent SHG intensity in terms of the transition matrix element²⁹² as

$$I_{SHG} = |e_{2\omega}^T \vec{d} \cdot \vec{e}_\omega|^2, \quad (27)$$

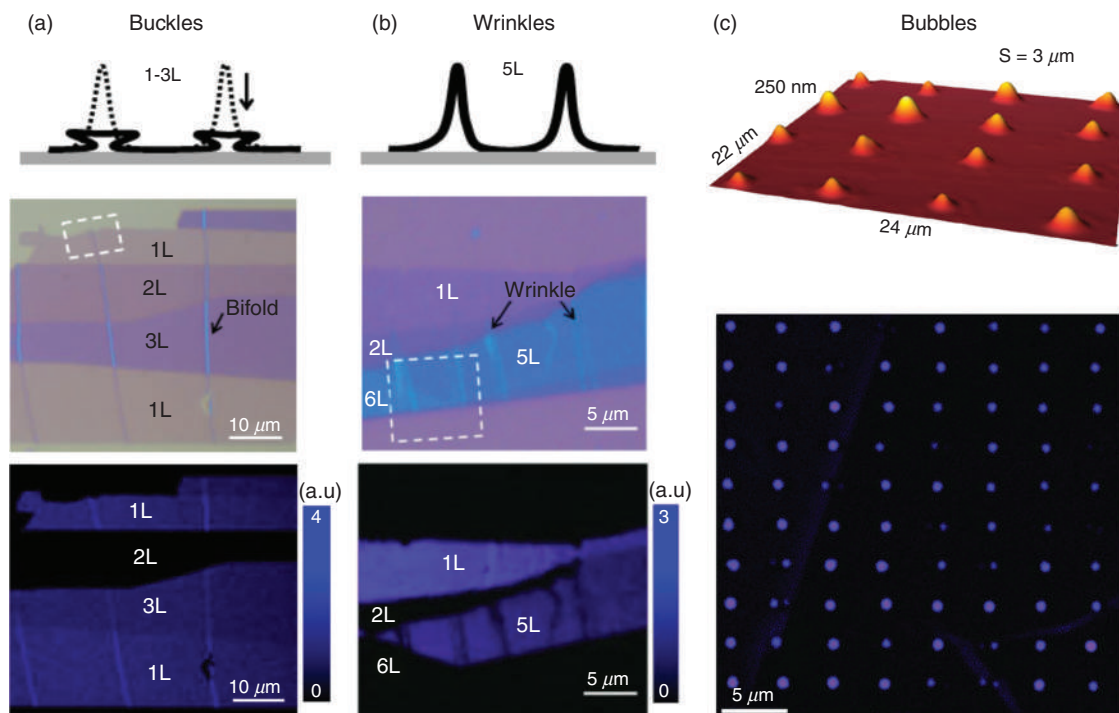


FIG. 59. (a) Top: Sketch of buckles; middle: optical image of a buckled thin WS₂ flake; bottom: SHG imaging of the same flakes of the panel in the middle. (b) Same in the case of wrinkles. (c) Top: AFM image of a square array (4 × 4) of WS₂ bubbles with diameter $S \sim 3 \mu\text{m}$. Bottom: SHG imaging of a rectangular array (8 × 10) of WS₂ bubbles. (a) and (b) Reprinted with permission from Khan *et al.*, ACS Nano 14, 15806 (2020). Copyright 2020 American Chemical Society.³⁵⁶ (c) Reprinted with permission from Tedeschi *et al.*, Adv. Mater. 31, 1903795 (2019). Copyright 2019 Wiley-VCH Verlag GmbH & Co. KGaA, Weinheim.¹¹²

where $\hat{e}_{2\omega}$ and \hat{e}_ω are the polarization orientations of the SHG electric field and incident electric field, respectively, and \vec{d} is the contracted notation for the nonlinear susceptibility 3×6 matrix defined as

$$d_{il} = \frac{1}{2} \chi_{ijk},$$

$$l \leftrightarrow jk : 1 \leftrightarrow 11, 2 \leftrightarrow 22, 3 \leftrightarrow 33,$$

$$4 \leftrightarrow 23, 32, 5 \leftrightarrow 31, 13, 6 \leftrightarrow 12, 21.$$
(28)

The symmetry-dependent \vec{d} matrices are given by

$$\vec{d}^{(D_{3h})} = \begin{bmatrix} 0 & 0 & 0 & 0 & 0 & \tilde{d} \\ \tilde{d} & -\tilde{d} & 0 & 0 & 0 & 0 \\ 0 & 0 & 0 & 0 & 0 & 0 \end{bmatrix},$$
(29)

$$\vec{d}^{(C_{2v})} = \begin{bmatrix} 0 & 0 & 0 & 0 & 0 & d_{16} \\ d_{21} & d_{22} & d_{23} & 0 & 0 & 0 \\ 0 & 0 & 0 & d_{34} & 0 & 0 \end{bmatrix},$$
(30)

$$\vec{d}^{(C_{1h})} = \begin{bmatrix} d_{11} & d_{12} & d_{13} & 0 & 0 & d_{16} \\ d_{21} & d_{22} & d_{23} & 0 & 0 & d_{26} \\ 0 & 0 & 0 & d_{34} & d_{35} & 0 \end{bmatrix}.$$
(31)

Generally, it is convenient to describe the SHG intensity in the cases where the SHG polarization is parallel (I_{\parallel}) or perpendicular (I_{\perp}) to that of the excitation laser. This common choice is due to the fact that the description is simplified in these two configurations. In the absence of strain or under equibiaxial strain,

$$I_{\parallel}^{(D_{3h})} = |\tilde{d} \cdot \cos(3\theta')|^2, \quad I_{\perp}^{(D_{3h})} = |\tilde{d} \cdot \sin(3\theta')|^2,$$
(32)

where θ' is the angle between the excitation laser-polarization and the armchair direction (i.e., $\hat{e}_\omega = [-\sin(\theta') \cos(\theta') \ 0]$), see Fig. 60(a). In

this case, the polarization pattern exhibits a sixfold symmetry for both the two states (\parallel or \perp), while the total intensity ($I = I_{\parallel}^{(D_{3h})} + I_{\perp}^{(D_{3h})}$) is constant. The θ -dependent patterns for I_{\parallel} , I_{\perp} , and for the total intensity I are displayed in Fig. 60 in the exemplifying case of a MoSe₂ ML (orange curves). In the presence of anisotropic strains whose preferential strain direction is oriented along the armchair or zigzag axis, one has that²⁹²

$$d_{22}^{(C_{2v})} = -\tilde{d}(1 + a \cdot \varepsilon),$$

$$d_{21}^{(C_{2v})} = \tilde{d}(1 + b \cdot \varepsilon),$$

$$d_{16}^{(C_{2v})} = \tilde{d}(1 + c \cdot \varepsilon),$$
(33)

where a , b , and c are material-dependent parameters and in principle, they might also depend on the strain direction (armchair or zigzag). In this case, the SHG intensities are given by²⁹²

$$I_{\parallel}^{(C_{2v})} = \tilde{d}^2 \cdot |\cos(3\theta') + \varepsilon_a(a \cdot \cos^3(\theta') - b \cdot \sin^2(\theta') \cos(\theta')) - 2c \cdot \sin^2(\theta') \cos(\theta')|^2,$$

$$I_{\perp}^{(C_{2v})} = \tilde{d}^2 \cdot |\sin(3\theta') + \varepsilon_a(a \cdot \sin(\theta') \cos^2(\theta') - b \cdot \sin^3(\theta')) + 2c \cdot \sin(\theta') \cos^2(\theta')|^2.$$
(34)

This introduces asymmetries in the sixfold SHG pattern, whose petals are no more all equivalent, as shown in Fig. 60. For strain along arbitrary directions, the $\vec{d}^{(C_{1h})}$ tensor should be used to describe the SHG pattern.

Analogous results to those obtained with this approach can be equivalently obtained by introducing a 5th rank photoelastic tensor p to describe the strain-induced changes in the nonlinear susceptibility.^{205,250,286,287} In this framework, it is convenient to consider the coordinate system in which the strain tensor is diagonal. In this system, the principal strain tensor is expressed as

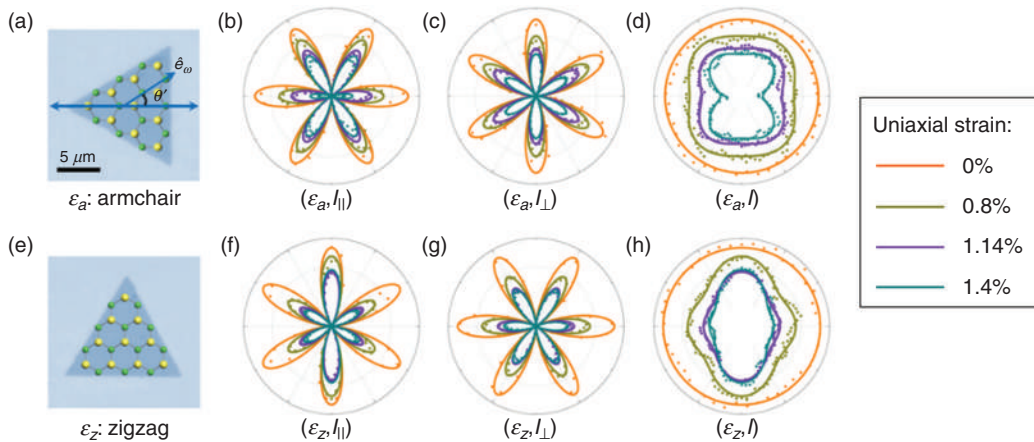


FIG. 60. Pattern evolution of the SHG intensity for a MoSe₂ ML under strain. (a) Optical image of the ML under strain along the crystalline armchair direction (ε_a), as indicated by the double-headed arrow. The ball and stick model shows the crystalline structure. The laser-polarization vector—forming an angle θ' with the armchair direction—is indicated by the single-headed arrow. (b)–(d) θ' -dependent SHG intensity pattern (for $\theta' \in [0^\circ : 360^\circ]$) for I_{\parallel} (b), I_{\perp} (c), and the total intensity I (d). The different colors represent different strain levels, as indicated in the legend. (e)–(h) The counterpart data under strain along the crystalline zigzag direction (ε_z). Dots are original data and lines are theoretical fits. Reprinted with permission from Liang et al., Nano Lett. 17, 7539 (2017). Copyright 2017 American Chemical Society.²⁹²

$$\xi = \begin{pmatrix} \varepsilon_{xx} - \nu\varepsilon_{yy} & 0 \\ 0 & \varepsilon_{yy} - \nu\varepsilon_{xx} \end{pmatrix}, \quad (35)$$

where ν is the Poisson's ratio of the material. The photoelastic tensor is then defined by the relationship

$$\chi_{ijk}^{(2)}(\varepsilon) = \chi_{ijk}^{(2)}(0) + p_{ijklm} \cdot \xi_{lm}. \quad (36)$$

The photoelastic tensor reflects the crystal symmetries, the symmetry of the strain tensor ($\xi_{lm} = \xi_{ml}$), and the symmetry of the SHG process ($\chi_{ijk}^{(2)} = \chi_{ikj}^{(2)}$). Under these conditions, it reduces to 12 nonzero elements²⁸⁶

$$\begin{aligned} p_{xxxx} &= p_1, & p_{xxyy} &= p_2, \\ p_{xyyy} &= -p_1, & p_{xyxx} &= -p_2, \\ p_{yyxy} &= p_{yyxx} = p_{yxyy} = p_{yxxy} &= -\frac{1}{2}(p_1 + p_2), \\ p_{yyyx} &= p_{yyxy} = p_{yxxy} = p_{xyxx} &= -\frac{1}{2}(p_1 - p_2). \end{aligned} \quad (37)$$

To interpret the SHG experiments, it's convenient to refer to the laboratory coordinates (X,Y). In bending setups, X typically indicates the bending direction. We can then define three different angles with respect to the X axis: the angle ψ with the horizontal direction of the coordinate system where the strain tensor is diagonal (which is typically left as a fitting parameter); the angle φ concerning the orientation of the armchair lattice direction; and the angle θ related to the laser-polarization direction [notice that $\theta = \theta' - \varphi$, where θ' is defined in Fig. 60(a)]. These leads to a SHG behavior given by²⁸⁶

$$I_{\parallel} \approx [A \cdot \cos(3\theta - 3\varphi) + B \cdot \cos(2\psi + \theta - 3\varphi)]^2 \quad (38)$$

in the case of collinear collection and excitation polarization. Here $A = (1 - \nu)(p_1 + p_2)(\varepsilon_{xx} + \varepsilon_{yy}) + 2\chi^{(2)}(0)$ and $B = (1 + \nu)(p_1 - p_2)(\varepsilon_{xx} - \varepsilon_{yy})$. The constant B is thus proportional to the difference of the principal in-plane strain components, and it is therefore non-null only for anisotropic strains. In this case, the sixfold symmetry is thus modified and anisotropy is introduced in the behavior of I_{\parallel} . This description is thus equivalent to Eq. (34).

While different works have led to analogous results concerning the effect of strain on the sixfold SHG pattern, there is still an open debate on the effect of strain on the total intensity. As a matter of fact, the understanding of the intensity behavior is non trivial due to several reasons: (i) substrate screening can drastically modify the excitonic effects and thus alter the strain-induced effects; (ii) strain modifies the band structure of TMDs. In particular, the frequency-doubled photon energy in SHG measurements is usually in the range of 400 to 500 nm and it thus falls in the region of the C exciton transition. The effect of strain on the fine structure of the C exciton can thus play an important role in determining the SHG intensity behavior, since on/off resonant conditions can be induced by strain. (iii) Band nesting phenomena lead to a resonant enhancement of the nonlinear susceptibility at specific frequencies, resulting in substantial material-dependent and energy-dependent change in the SHG response with strain.

As for the effect of the substrate on the SHG, its interplay with the stain-induced effects is still not well understood and further studies would be needed. Here, we will thus focus on the discussion of points (ii) and (iii). From a theoretical point of view, the relationship between excitonic effects and the SHG behavior has been investigated by Beach *et al.*³⁵⁷ via time-dependent DFT calculations of the polarization resulting from the interaction with a time-dependent electric field in

the dipole approximation. In order to calculate the nonlinear optical susceptibility, one can integrate numerically the equation of motion,

$$i\hbar\partial_t|v_{ik}\rangle = (H_{\mathbf{k}} + ie\mathcal{E}(t) \cdot \partial_{\mathbf{k}})|v_{ik}\rangle, \quad (39)$$

where $|v_{ik}\rangle$ are the time-evolving valence bands of the system, $H_{\mathbf{k}}$ is the Hamiltonian of the system, and the term $ie\mathcal{E}(t) \cdot \partial_{\mathbf{k}}$ determines the coupling of the system with the time-dependent external field $\mathcal{E}(t)$ in the dipole approximation. To keep into account the excitonic effects, the Hamiltonian can be expressed in terms of many-body contributions as

$$H_{\mathbf{k}} = H_{\mathbf{k}}^{KS} + \Delta H^{scissor} + V_h[\Delta\rho] + \Sigma_{SExc}, \quad (40)$$

where $H_{\mathbf{k}}^{KS}$ is the Kohn-Sham Hamiltonian; $\Delta H^{scissor}$ is a uniform scissor-shift correction, which is determined by the difference between the direct GW bandgap and the direct LDA bandgap; $V_h[\Delta\rho]$ is the time- and field-dependent Hartree potential; and Σ_{SExc} is the screened-exchange self-energy, which includes the Green's function description of the electron-hole interaction. Within this framework, Beach *et al.*³⁵⁷ have calculated the SHG response to strain for several TMDs as a function of the energy of the excitation laser. In Fig. 61(a), we display the results obtained in the case of uniaxial strain along the armchair direction, and of equibiaxial strain, in the exemplifying case of MoSe₂ and WS₂. Indeed, the strain response is generally both energy-dependent and material-dependent.

From an experimental point of view, only a few studies have been performed concerning the excitation-energy dependence of the strain-modified SHG. In Refs. 286 and 292, the authors performed SHG studies on several TMDs for fixed excitation energy equal to 1.51 eV. These works report a general reduction (for both uniaxial and biaxial strain) of the SHG intensity when applying strain to MoSe₂, as shown in Fig. 61(b). This is in agreement with the theoretical prediction for strain in the armchair direction and for biaxial strain, as shown in panel (a). But theory predicts instead an increase in the SHG intensity for strain in the zigzag direction,³⁵⁷ contrary to the experiment. Furthermore, in Ref. 286, the authors find a reduction of the SHG intensity for MoS₂ and WS₂ under biaxial strain, and an increase under uniaxial strain. Also in this case, these results agree with the theoretical calculations for strain in the armchair direction and for biaxial strain, but not with those concerning strain in the zigzag direction.³⁵⁷ Finally, the authors of Ref. 286 find a slight increase in the SHG of WSe₂ under biaxial strain and a constant behavior under uniaxial strain, in good agreement with theory. Excitation-wavelength-dependent studies were then performed on WS₂ folds and wrinkles in Ref. 356, as shown in Figs. 61(c) and 61(d). These studies show a general wavelength dependence of the SHG signal, which varies depending on the thickness of the flake and on the kind of applied strain (i.e., different results are obtained for folds and wrinkles). The excitation-energy dependence of the SHG is related to the electronic structure of these materials. In particular, besides the main exciton transitions (A and B), the higher energy exciton referred to as C exciton [see reflectance spectrum in Fig. 62(a)] plays an important role in SHG studies.³⁵⁸ Generally, an increase in the SHG intensity is observed for SHG energies resonant to the C exciton, as shown in Fig. 62(b). This exciton is the result of several optical transitions from the valence to the conduction band, and theoretical studies have been performed in Ref. 357 to unveil the fine structure of the C exciton. These studies have allowed us to establish a correspondence between maxima in the calculated SHG response and optical transitions at different k points of the

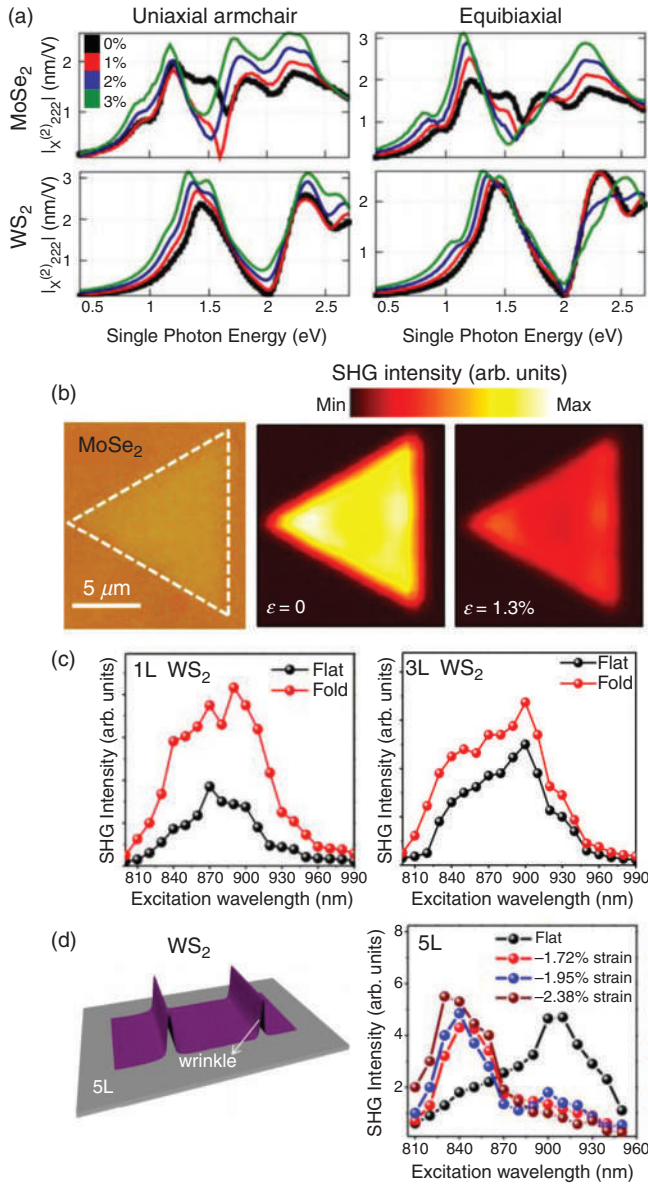


FIG. 61. (a) SHG spectrum of several TMDs (MoSe_2 and WS_2) theoretically calculated in the absence and presence of tensile strain. The different colors account for different strain values (see top-left legend). Adapted with permission from Beach *et al.*, Phys. Rev. B **101**, 155431 (2020). Copyright 2020 American Physical Society.³⁵⁷ (b) Left: Optical image of a MoSe_2 -ML grown by CVD. Middle: SHG intensity map of the same ML. Right: SHG intensity map of the same ML subjected to biaxial strain equal to 1.3%. Adapted with permission from Liang *et al.*, Nano Lett. **17**, 7539 (2017). Copyright 2017 American Chemical Society.²⁹² (c) SHG intensity of a flat WS_2 flake and of WS_2 folds, as a function of the excitation laser wavelength, for a 1L-thick flake (left) and of a 3L-thick flake (right). (d) Left: Sketch of a 5L-thick WS_2 wrinkle. Right: SHG intensity of a flat WS_2 flake and on WS_2 wrinkles corresponding to different strains, as a function of the excitation wavelength. (c) and (d) Reprinted with permission from Khan *et al.*, ACS Nano **14**, 15806 (2020). Copyright 2020 American Chemical Society.³⁵⁶

Brillouin zone, as shown in the case of WSe_2 in Figs. 62(c) and 62(d). Since the different critical points of the Brillouin zone feature a different behavior with strain, the SHG excitation-wavelength-behavior will change upon the introduction of strain in the system. Furthermore, the SHG modulation with strain will also be affected by band nesting phenomena. Band nesting appears when the valence and conduction bands run in parallel over an extended region in the Brillouin zone [as shown in Fig. 62(e)], enhancing the number of state pairs between which transitions at a given frequency Ω_R thereby become possible.²⁰⁵ In two dimensions, this results in singularities in the joint density of states (JDOS) at such frequencies Ω_R . This is particularly relevant for SHG since the non-linear susceptibility is proportional to the JDOS,

with $\chi^{(n)}(\omega) \propto \text{JDOS}(n\omega)$, (41)

$$\text{JDOS}(\Omega) \propto \sum_{C,V} \int_{\text{BZ}} \delta(E_C(\mathbf{k}) - E_V(\mathbf{k}) - \hbar\Omega) d\mathbf{k}, \quad (42)$$

where C and V stand for conduction and valence band, respectively, and $E_{C,V}$ is the related dispersion relation. Band nesting-induced singularities in the JDOS will thus result in a resonant enhancement of the 2nd order nonlinear susceptibility at frequency $\Omega_R = 2\omega_R$. Upon straining a TMD crystal, bond stretching reduces the energy difference between conduction and valence bands, reducing ω_R . On the other hand, the deformation of the bands also affects the JDOS, resulting in either a more pronounced or a less pronounced singularity depending on the material. Hence, while a redshift will be observed in the SHG response of all TMDs, the height and width of the SHG peak vs energy will vary in a different manner depending on the considered material. This effect is shown in Fig. 62(f) in the case of MoS_2 .

2. THG

The same discussion completed for SHG generally holds true also for THG. In this case, the photoelastic tensor p' will be a 6th-rank tensor, related to the 3rd order susceptibility by the formula

$$\chi_{ijk}^{(3)}(\varepsilon) = \chi_{ijk}^{(3)}(0) + p'_{ijklm} \cdot \zeta_{lm}, \quad (43)$$

where ζ is the strain tensor defined in Eq. (35). In the case of the D_{3h} symmetry typical of odd-layered TMDs, of the D_{3d} symmetry typical of even-layered TMDs, and of the C_{2v} of strained crystals, p' has 32 non-null elements which can, however, be expressed in terms of only 4 independent parameters. The general expression, holding both in the presence or absence of strain, is thus²⁸⁷

$$\begin{aligned} I_{\parallel} &= [\chi_{ijk}^{(3)}(0) + 3(1-\nu)(\varepsilon_{xx} + \varepsilon_{yy}) \cdot a + (1+\nu)(\varepsilon_{yy} - \varepsilon_{xx}) \\ &\quad \times (4b \cdot \cos(2\theta - 2\psi) + c \cdot \cos(6\phi + 2\theta + 2\psi))]^2, \\ I_{\perp} &= [(1+\nu)(\varepsilon_{yy} - \varepsilon_{xx})(2d \cdot \sin(2\theta - 2\psi) \\ &\quad + c \cdot \sin(6\phi + 2\theta + 2\psi))]^2, \end{aligned} \quad (44)$$

where a , b , c , and d are material-dependent parameters. The angles are defined with respect to the X axis of the laboratory coordinates, as in Eq. (38), i.e., ψ is the angle concerning the horizontal direction of the

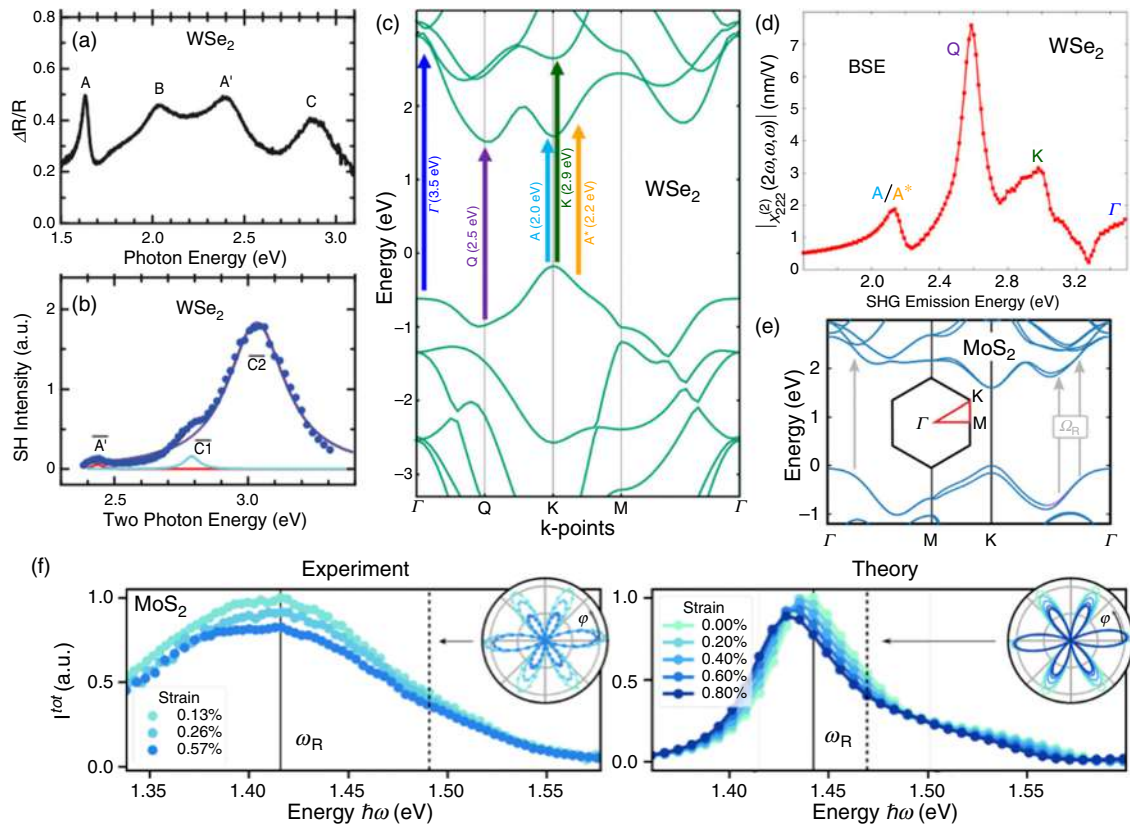


FIG. 62. (a) Differential reflectance spectrum of a WSe₂-ML on a SiO₂/Si(001) substrate. (b) SHG spectrum of the same WSe₂-ML. Blue dots: experimental spectra. Black lines: spectra fitted by a linear combination of Lorentz functions. (c) and (d) Comparison of optical transitions in the LDA band structure (c) with peaks in the theoretical SHG spectrum (d) for a WSe₂-ML. (e) Band structure of MoS₂ highlighting the band nesting region at frequency Ω_R . (f) Experimental (left) and theoretical (right) total SHG intensity for MoS₂ at measured and calculated bending strain values (see legend). Solid vertical lines mark the resonance frequency $\omega_R = \Omega_R/2$ at zero strain. The insets show one typical angular-resolved SHG signal at an energy where strain has a remarkable effect (marked by a dashed vertical line), with $\phi = 0$ fixed to the direction of strain. Different lattice orientations with respect to the direction of strain result in rotated and deformed angular-resolved patterns. (a) and (b) Reprinted with permission from Kikuchi *et al.*, Phys. Rev. B **100**, 075301 (2019). Copyright 2019 American Physical Society.³⁵⁸ (c) and (d) Reprinted with permission from Beach *et al.*, Phys. Rev. B **101**, 155431 (2020). Copyright 2020 American Physical Society.³⁵⁷ (e) and (f) Reprinted with permission from Mennel *et al.*, Nano Lett. **20**, 4242 (2020). Copyright 2020 American Chemical Society.²⁰⁵

coordinate system where the strain tensor is diagonal (which is typically left as a fitting parameter); the angle φ concerns the orientation of the armchair lattice direction [see Figs. 63(a) and 63(b)]; and the angle θ related to the laser-polarization direction. Hence, for THG in the absence of strain or for equibiaxial strain, I_{\perp} is null while I_{\parallel} is constant, as shown in Fig. 63 (orange data). When applying uniaxial strain, I_{\parallel} exhibits a twofold pattern and I_{\perp} exhibits a fourfold pattern. These patterns are symmetric if strain is oriented along high-symmetry directions, while it is asymmetric otherwise (see Fig. 63).

F. Inhomogeneous strain and gauge fields

Two-dimensional flexible materials are characterized by complex unit cells containing more than one atom. The most paradigmatic example is graphene where the unit cell is built by two carbon atoms belonging to two different (A and B) sublattices. Monolayer transition-metal dichalcogenides MX₂ involve three different atoms: the inner plane of metal M sandwiched between two symmetrical planes of chalcogen atoms X. Within this context, uniform (biaxial or uniaxial) strain mainly affects the hybridization energies (namely, the

hopping magnitudes in a tight-binding formalism) between different atoms. The geometrical atomic shift induced by the strain can be absorbed in a redefinition of the Bloch wave function, in the same way as a uniform time-independent scalar-vector potential can be reabsorbed in a *gauge* factor that has no physical observable. Non-uniform strains can on the other hand give rise to finite modulations of the magnitude/phase interatomic hopping. These modulations *cannot* be reabsorbed in a redefinition of a fictitious gauge, thus resulting in an effective pseudo-electromagnetic field which can be directly probed.

Within this framework, graphene is a textbook example since the sublattice degree of freedom can be mapped in a feasible way onto a pseudo-spin degree of freedom. Such correspondence allows us to apply concepts of a physical electromagnetic field to the case of strain-induced pseudo-electromagnetic fields. In particular, assuming the x -axis along the zigzag direction, we can define a pseudo-vector potential **A**

$$A_x(\mathbf{r}) = c[\varepsilon_{xx}(\mathbf{r}) - \varepsilon_{yy}(\mathbf{r})], \quad (45)$$

$$A_x(\mathbf{r}) = -2c\varepsilon_{xy}(\mathbf{r}), \quad (46)$$

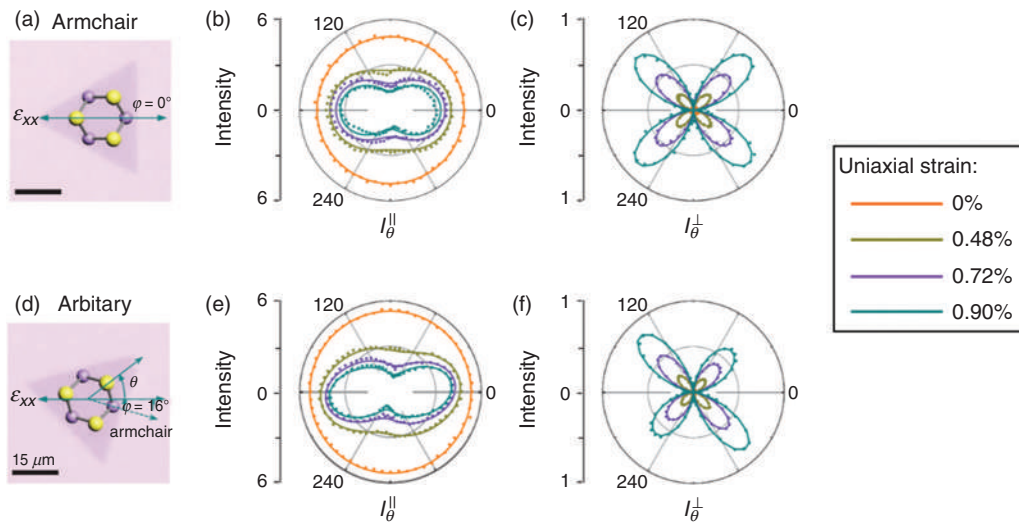


FIG. 63. Pattern evolution of the THG intensity for a WS₂ ML under uniaxial strain. (a) Optical images of the WS₂-ML and the corresponding crystal lattice structure by a ball-stick model. The uniaxial tensile strain ε_a is along the armchair direction. φ indicates the angle between the armchair direction and the straining direction X. (b) and (c) θ -dependent SHG intensity pattern (for $\theta \in [0^\circ : 360^\circ]$) for I_{\parallel} (b) and I_{\perp} , where θ indicates the angle between the laser-polarization direction and the straining direction X. (c). The different colors represent different strain levels, as indicated in the legend. Dots are original data and lines are theoretical fits. (d)–(f) Same as in (a)–(c) for another WS₂-ML with a general relative angle ($\varphi = 16^\circ$) to the armchair direction. Reprinted with permission from Liang *et al.*, *Adv. Mater.* **31**, 1808160 (2019). Copyright 2019 Wiley-VCH Verlag GmbH & Co. KGaA, Weinheim.²⁸⁷

where c is a material-dependent constant. The observable pseudo-electromagnetic fields are related to the *derivatives* of the pseudo-vector potential, showing that a non-uniform strain tensor is a necessary requirement for the onset of physical effects.

The most striking example of this scenario is the appearance of discretized pseudo-Landau levels induced by an inhomogeneous strain geometry that mimics the onset of a pure vertical magnetic field. Such peculiar conditions can be obtained in graphene in a triangular geometry, as the one discussed in Ref. 116 and shown in Fig. 64. The onset of a pseudo-magnetic field as large as the equivalent of 300 Tesla was thus established through the observation of discretized Landau pseudo-magnetic levels with the square-root-behavior of the energy spacing dictated in graphene by the linear Dirac dispersion, see Fig. 64. Another possible realization of a strain pattern giving rise to a pure constant pseudo-magnetic field is the so-called arc-shape geometry as discussed in Refs. 230, 359, and 360, see Fig. 64(b). Non-constant pseudomagnetic fields were also predicted under different strain configurations, such as uniform strains.³⁶¹ The concept of a pseudo-electromagnetic field arising from inhomogeneous strain has also been discussed for TMDs, where a simple mapping of the band structure in terms of a gapped Dirac model was suggested.¹¹⁹ Such mapping appears however too simplistic since it overlooks the crucial role of the hybridization between metal atoms and chalcogen atoms.^{206,362} A compelling analysis shows that strain effects cannot be cast in terms of a unique pseudo-vector potential. The complexity of the band structure gives rise indeed at least to *three* strain-induced gauge fields (five in the presence of spin-orbit coupling).²³⁰ Such fields do *not* commute with each other, so that the net effect of an inhomogeneous strain cannot be mapped onto a uniform pseudo-magnetic field, hampering the possibility of establishing well-defined, strain-induced Landau levels. The emergence of gauge fields induced by non-uniform strain can be

traced however in other physical effects, as the emergence of inhomogeneous inner-electric dipoles¹⁶⁸ in piezoelectric samples, such as monolayer TMDs, gapped graphene, and BN.^{168,363–365}

G. Strain tuning of valley/spintronics effects

Two-dimensional layered materials often display exciting properties also in regard to the so-called “valley”-tronics,^{366,367} namely the possibility to control in a different way, by means of external fields, the physical properties of two valleys in the band structure that would normally be degenerate. Since a lift of degeneracy is involved, such task is usually achieved by a breaking of symmetry of the crystal/electronic structures. In this field, the ultimate goal is represented by the achievement of the ability to control and manipulate the valley degree of freedom. In turn, this ability will be exploited for the development of new protocols to conveniently encode and read out information.

Graphene and TMDs are particularly appealing in this regard, since their band structure features two peculiar and degenerate band edges, or Dirac cones (valleys) at the K and K' points of the hexagonal Brillouin zone. Such degeneracy is inherited by the underlying triangular/hexagonal symmetry of the crystal structure.

Monolayer graphene is probably the most striking example. The hexagonal lattice structure contains two different sublattices (A and B) of carbon atoms, which are energetically equivalent but with different local environments. A and B carbon sublattices can be reproduced, or switched, by means of different symmetry operations (in-plane reflection, rotations, etc.). These crystal properties are reflected in the appearance of a degenerate band structure at K and K' points. It should be remarked, however, that although the K and K' points are energetically degenerate, they are *not* with respect to the inner degree of freedom represented by the two sublattices (pseudo-spin).¹⁸⁴ As a matter of fact, in single-layer graphene, the two degenerate Dirac cones

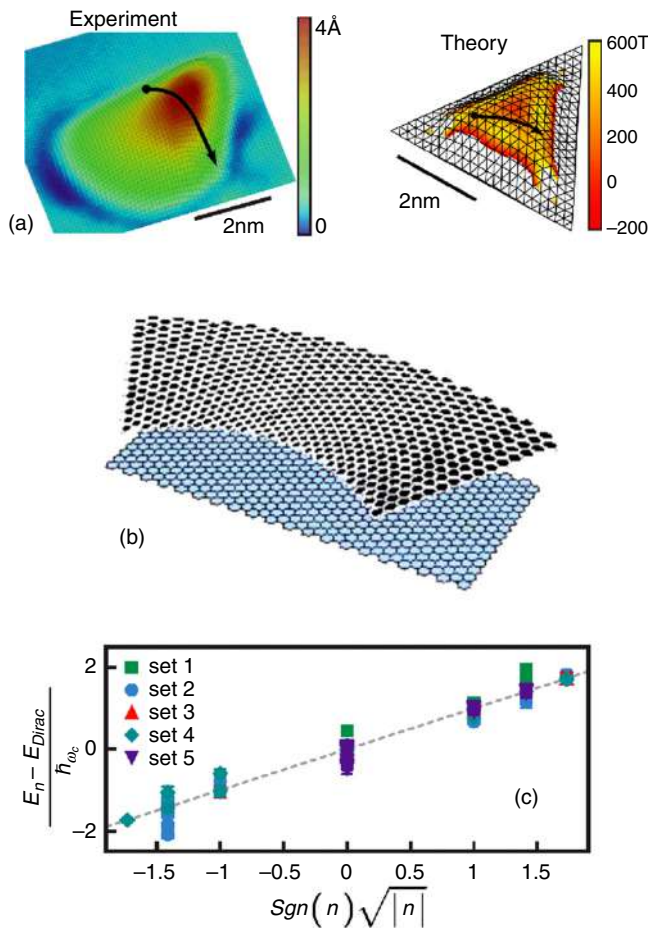


FIG. 64. (a) Left panel: triangular-shape dome of strained graphene formed on a platinum surface. Right panel: topographic modeling of the same dome with the corresponding magnitude (in color scale) of the pseudo-magnetic field. (b) Alternative arc-shape geometry giving rise to a pure magnetic field in graphene. The top black layer corresponds to the real arc-shaped lattice, whereas the underlying blue layer represents the uniform pseudo-magnetic field. (c) Energy values of the discrete pseudo-Landau levels E_n resulting from the strain geometry. The square-root behavior $E_n \propto \sqrt{|n|}$ is a direct evidence of the linear Dirac dispersion. (a) and (c) Reprinted with permission from Levy *et al.*, *Science* **329**, 544 (2010). Copyright 2010 American Association for the Advancement of Science.¹¹⁵ (b) Reprinted with permission from Guinea *et al.*, *Phys. Rev. B* **81**, 035408 (2010). Copyright 2010 American Physical Society.³⁵⁹

at the K and K' points present opposite *chirality*, i.e., an opposite (and complementary) dependence on the sublattice contents [Fig. 65(a)].

Different concepts have been designed where the transport or optical properties of different valleys can have an opposite effect so that, if one were able to read the information of a single valley, such information could be easily tuned and switched on/off. The challenge in this field is that the two valleys appear to be intrinsically equivalent from the transport point of view unless some external tool breaks the underlying relevant symmetry, in particular, the spatial inversion symmetry. Leaving aside sample edges in flakes or nanoribbons, in graphene a straightforward example in this regards is given by a possible

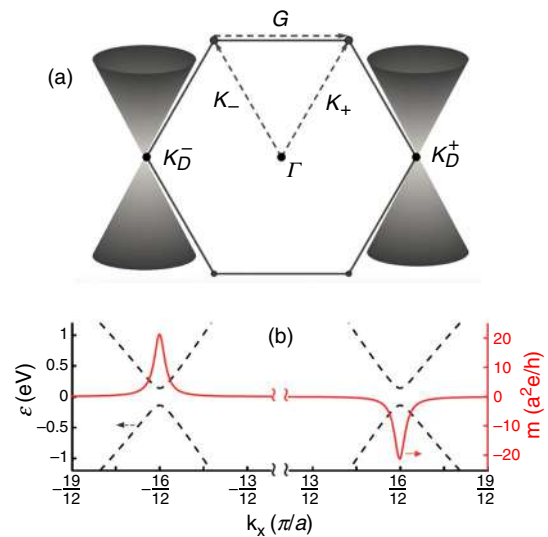


FIG. 65. (a) Hexagonal Brillouin zone of graphene displaying two inequivalent Dirac cones with different chirality at the K and K' points, here denoted as K_D^- and K_D^+ . Reprinted with permission from Andrade *et al.*, *Phys. Rev. B* **99**, 035411 (2019). Copyright 2019 American Physical Society.³⁶¹ (b) Berry curvature for the gapped Dirac model (equivalent to graphene with staggered potential on the A and B sublattices) along the line ($k_x, k_y = 0$), crossing the K and K' points. Reprinted with permission from Xiao *et al.*, *Phys. Rev. Lett.* **99**, 236809 (2007). Copyright 2007 American Physical Society.³⁶⁹

staggered potential between the A and B carbon sublattices, breaking the inversion symmetry and inducing an effective mass in the low-energy Dirac model. Such a symmetry breaking gives rise to a finite Berry curvature which acts as a staggered perpendicular magnetic field on the K and K', inducing a finite Hall effect with opposite signs in each valley [Fig. 65(b)].^{368–371} Alternatively, valley currents from the Berry curvature might arise in graphene as a result of the combined effect of the trigonal warping in the presence of valley-selective particle-hole excitations with proper polarized light [Fig. 66(a)].³⁷² In this context, it is important to stress the importance of the trigonal warping, which breaks the circular symmetry within each valley. Without trigonal warping, indeed the net current would be null in each valley.

Uniaxial strain can play a powerful role in the context of valleytronics since it provides a straightforward reduction of the global symmetries of the system. However, since it does not break the inversion symmetry, strain alone is not enough to induce, in the linear response theory, valley currents or valley-Hall effects, and it should be integrated with a further actor. An interesting suggestion was advanced in Ref. 373 where the shifts of the Dirac cones from the K (K') points and the strain-driven anisotropy of the Dirac velocities plays a similar role as warping in reducing the circular symmetry within each valley, giving rise, upon optical excitations with circularly polarized light, to a finite photo-induced current in each valley, of course with a different sign in each valley. Such context was further developed in Ref. 374 where it was shown that a finite nonlinear Hall-effect, related to the appearance of a finite Berry curvature dipole, can be induced in monolayer graphene by means of uniaxial strain and of a sublattice inequivalence as a consequence of the band dispersion warping.

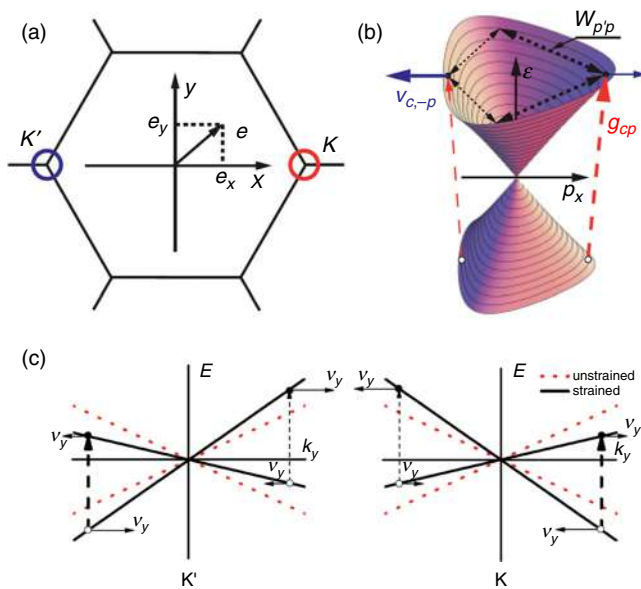


FIG. 66. (a) Brillouin zone of graphene. (b) Deformed Dirac cone in the presence of trigonal warping. Horizontal solid black lines represent Fermi velocities, vertical dashed red lines indicate optical transitions. The thickness of these lines denotes the magnitude of each quantity, pointing out the anisotropy induced by warping. (c) Sketch of K and K' Dirac cones in the presence of uniaxial strain. Dotted red (solid black) lines are here the Dirac cones in the absence (presence) of uniaxial strain; the vertical dashed lines represent optical transitions, whose thickness is also here proportional to the magnitude of probability that the transition occurs. Uniaxial strain plays here the same role as warping in generating a relevant anisotropy of the Dirac cones, reflected in a finite photo-induced valley current. (a) and (b) Reprinted with permission from Golub *et al.*, Phys. Rev. B **84**, 195408 (2011). Copyright 2011 American Physical Society.³⁷² (c) Reprinted with permission from Linnik, Phys. Rev. B **90**, 075406 (2014). Copyright 2014 American Physical Society.³⁷³

Alternatively to valley-selective optical excitations driven by circular polarized light, a valid support to the symmetry breaking of the uniaxial strain can be provided by magnetic barriers, as discussed for instance in Refs. 375–377. A valley-filtering effect is here governed by the appropriate matching of the Fermi surface of the strain area with the split Fermi surface of the unstrained area in the presence of a magnetic field. A typical example is shown in Fig. 67(a) where a cascade device along the x direction is depicted, encompassing a normal (N)/strained (S)/normal (N)/ferromagnetic (F)/normal (N) areas of graphene.³⁷⁶ The valley-spin filtering can be rationalized by means of a kinematical construction, as depicted in Fig. 67(b), where the iso-energy surfaces in each region are sketched. In the normal regions, charges with energy E fulfill the condition $k_x^2 + k_y^2 = E^2$. On the other hand, the isoenergy surfaces in the strained regions are displaced by $\pm \bar{k}_y$, where the sign \pm stands for different K (K') points and where \bar{k}_y is a momentum shift proportional to the strain-induced gauge potential A_S along y . Finally, the energy surfaces in the ferromagnetic region are given by two concentric circles corresponding to majority and minority spin. Due to the translational invariance along y , the energy E and the momentum k_y need to be conserved. This, however, can happen only under specific conditions. A striking representative is the case depicted as a horizontal orange line in Fig. 67(b). The electrons with such k_y momentum can propagate coherently along x only

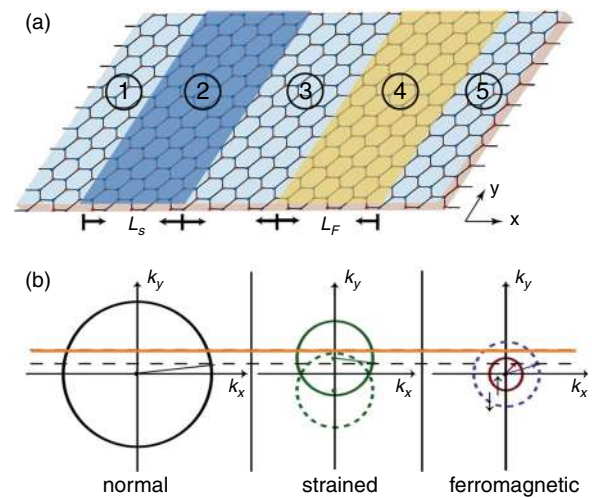


FIG. 67. (a) Sketch of a graphene-based device acting as a spin-valley filter. It includes along x a strained region and a ferromagnetic region. (b) Corresponding kinematical construction of the device in panel (a). Left: iso-energy surface of the normal region; middle: iso-energy surfaces in the strained regions, where the solid/dashed lines corresponds to the K/K' valleys respectively; right: iso-energy surfaces of the ferromagnetic region, where the dashed blue line represents the iso-energy surface of the majority (down) spin, and the solid wine line the iso-energy surface of the minority (up) spin. The orange horizontal line represents a perfect spin-valley filter for an electron with energy E and momentum k_y . (a) and (b) Reprinted with permission from Zhai and Yang, Appl. Phys. Lett. **98**, 062101 (2011). Copyright 2011 American Institute of Physics.³⁷⁶

passing through the K valley and with spin-up polarization. This provides an efficient spin-valley current filtering.³⁷⁶ The interplay between magnetism and a homogeneous uniaxial strain has been also proposed to be a suitable way to obtain a net valley polarization in graphene in a Corbino disk geometry.³⁷⁸

Tailored non-uniform strain has also been proposed in designing valley-dependent transport properties, where a crucial ingredient is the pseudo-magnetic field induced by the inhomogeneous strain (see Sec. IV F).^{379–382} In addition, the spin-orbit coupling has also been proposed as a main actor in designing spin-valley-dependent transport in the presence of strain and spin-orbit coupling.^{383–385} Given the weak intrinsic spin-orbit coupling of graphene, such task might appear unfavorable. On the other hand, precisely the weak spin-orbit interaction ensures long spin coherence which is a valuable feature in the field.

Favorable conditions for exploiting spin-valley degrees of freedom are also encountered naturally in semiconducting transition-metal dichalcogenides.^{386–388} Single-layer compounds are indeed non-centrosymmetric, allowing for a finite valley-dependent Berry curvature. The potential of transition-metal dichalcogenides is further enriched by the presence of a strong spin-orbit coupling driving a tight entanglement between spin and the valley degrees of freedom at the K and K' points of the Brillouin zone, corresponding to the bandgap edges (and to the optical gap in multilayer systems).^{386,387,389–392} Such strong entanglement permits using magnetic tools for manipulating the valley-dependent physical properties. A further entanglement is provided by the orbital content. The band edges at the K and K' point, both in the valence and conduction bands,

present indeed a well-defined angular momentum, which is opposite at K and K'. A precise valley-selective optical excitation is thus possible using circularly polarized light. In bilayer, bulk, or in transition-metal dichalcogenides with an even number of layers, the inversion symmetry is enforced, the Berry curvature vanishes, and many of these properties are not directly accessible. This can be also a favorable context since a finite electric field along the z-axis, breaking the symmetry, may lead to a finite valley-dependent Berry curvature and a strong-spin-valley-orbital entanglement can easily be restored in a tunable way.³⁹³

Barring a finite valley-dependent Berry curvature, single-layer transition-metal dichalcogenides share many similarities with gapped graphene. For instance, in Refs. 394 and 395, it was shown that a finite Berry curvature dipole, and hence a finite nonlinear-Hall effect, can be induced by a properly oriented uniaxial strain. In Refs. 396 and 397, Kerr rotation measurements were employed to experimentally pin down the valley magnetization—a close relative of a finite Berry curvature dipole—in uniaxially strained single-layer TMDs.

V. ELASTO-MECHANICAL PROPERTIES

Besides the physical effects following the presence of strain in a 2D membrane, mechanical deformations also offer an unprecedented platform to study the elasto-mechanical properties of layered materials. For instance, indentation experiments and mechanical modeling allowed the experimental estimation of the elastic modulus (or Young's modulus) of these materials. Several different approaches were then developed and used to this purpose, leading to the results summarized in Tables XVII–XVIII.

A typical method to obtain information on the elastic properties of a 2D membrane is via indentation experiments, such as those discussed in Sec. II C. Such experiments are typically performed by transferring the material on a holey substrate, as shown in Figs. 68(a)–68(c), and by indenting the material with an AFM tip, as previously shown in Figs. 11 and 12(a). This results in force-distance curves such as those in Figs. 12(b)–12(c) and described by Eq. (2), thus featuring a linear plus a cubic dependence on the indentation depth. Upon mechanical modeling—typically taking as a starting point Landau's theory of elasticity and the Föppl-von-Kármán equations^{418,419}—the linear and cubic constants [a and b, respectively, in Eq. (2)] can be expressed in terms of the relevant physical quantities of the system, and in particular, provide information on (i) the Young's modulus (Y) of the material and (ii) the pre-tension (T) of the membrane. In fact, in the most general formulation, Eq. (2) can be rewritten as⁷⁸

$$F(\delta_{\text{mem}}) = \left[\frac{4\pi Yt}{3(1-\nu^2)} \left(\frac{t}{R} \right)^2 + \pi T \right] \delta_{\text{mem}} + \frac{q^3 Yt}{R^2} \delta_{\text{mem}}^3, \quad (47)$$

where R is the radius of the hole, t is the membrane thickness, and q is a constant depending on the Poisson's ratio as $q = 1/(1.05 - 0.15\nu - 0.16\nu^2)$. It should be noticed that the 2D Young's modulus E_{2D} is related to the 3D Young's modulus Y via the equation $E_{2D} = Yt$. A statistical analysis of indentation measurements can thus allow us to quantify these two quantities (Y—or equivalently E_{2D} —and T), as shown in Figs. 68(d)–68(f). While the Young's modulus is an intrinsic quantity of the material, the pre-tension may originate from adhesion of the monolayer membrane to the sidewall of the

TABLE XVII. 3D (Y) and 2D (E_{2D}) Young's moduli of 2D materials measured by exploiting mechanical deformations. E_{2D} is calculated for a 1L-thick membrane as $E_{2D} = Yt$, taking $t = 1$ nm for Bi_2Se_3 , Bi_2Te_3 and mica, $t = 0.98$ nm for the MXene $\text{Ti}_3\text{C}_2\text{T}_x$, $t = 0.8$ nm for post-TMCs (InSe, GaS, GaSe, GaTe), $t = 0.625$ nm for TMDs, $t = 0.335$ nm for graphene, $t = 0.333$ nm for h-BN. The t of WN is not well known. The thickness of the heterostructures is taken as the sum of those of the constituent materials. Unless otherwise specified, the values were obtained via indentation experiments.

Mater.	Ref.	Y (GPa)	E_{2D} (N/m)
Graphene	Frank <i>et al.</i> ³⁹⁸	500	168
	Wang <i>et al.</i> ^{399,a}	939.5 ± 21.7	314.7 ± 7.3
	Lee <i>et al.</i> ¹⁰⁷	1010 ± 150	340 ± 50
	Liu <i>et al.</i> ⁴⁰⁰	1042 ± 36	349 ± 12
2H-MoS ₂	Cooper <i>et al.</i> ⁴⁰¹	210	131
	Di Giorgio <i>et al.</i> ^{114,b}	240 ± 58	150 ± 36
	Iguiñiz <i>et al.</i> ^{402,c}	246 ± 35	154 ± 22
	Bertolazzi <i>et al.</i> ¹⁵	270 ± 100	169 ± 63
	Li <i>et al.</i> ^{403,d}	265 ± 13	166 ± 8
	Liu <i>et al.</i> ⁴⁰⁰	274 ± 18	171 ± 11
	Wang <i>et al.</i> ^{399,a}	314.3 ± 8.4	196.4 ± 5.3
2H-WS ₂	Castellanos-Gomez <i>et al.</i> ⁷⁸	330 ± 70	206 ± 44
	Iguiñiz <i>et al.</i> ^{402,c}	236 ± 65	148 ± 41
MoS ₂ /WS ₂	Liu <i>et al.</i> ⁴⁰⁰	283 ± 19	177 ± 12
	Liu <i>et al.</i> ⁴⁰⁰	251 ± 25	314 ± 31
MoS ₂ /graph.	Liu <i>et al.</i> ⁴⁰⁰	486 ± 50	467 ± 48
2H-MoSe ₂	Yang <i>et al.</i> ⁴⁰⁴	177.2 ± 9.3	110.8 ± 5.8
2H-WSe ₂	Iguiñiz <i>et al.</i> ^{402,c}	163 ± 39	102 ± 24
	Zhang <i>et al.</i> ⁴⁰⁵	167.3 ± 6.7	104.6 ± 4.2
2H-MoTe ₂	Sun <i>et al.</i> ⁷⁶	110 ± 16	69 ± 10
1T-MoTe ₂	Sun <i>et al.</i> ⁷⁶	99 ± 15	62 ± 9
T _d -MoTe ₂	Sun <i>et al.</i> ⁷⁶	102 ± 16	64 ± 10
1T-WTe ₂	Lee <i>et al.</i> ^{406e}	~ 80	~ 50
1T-VS ₂	Wang <i>et al.</i> ³²⁸	44.4 ± 3.5	27.8 ± 2.2
h-BN	Wang <i>et al.</i> ^{399,a}	769.9 ± 12.9	256.4 ± 4.3
	Falin <i>et al.</i> ⁷⁹	865 ± 73	288 ± 24
γ -InSe	Zhao <i>et al.</i> ^{407,c}	23.1 ± 5.2	18.5 ± 4.2
	Li <i>et al.</i> ⁴⁰⁸	101 ± 18	81 ± 14
GaS	Chitara <i>et al.</i> ⁴⁰⁹	~ 60 -280	~ 50 -230
GaSe	Chitara <i>et al.</i> ⁴⁰⁹	~ 60 -100	~ 50 -80
GaTe	Chitara <i>et al.</i> ⁴⁰⁹	~ 20 -80	~ 15 -65
Bi ₂ Se ₃	Yan <i>et al.</i> ¹⁰⁸	10 - 37	10 - 37
Bi ₂ Te ₃	Guo <i>et al.</i> ¹⁰⁹	18.7 ± 7.0	18.7 ± 7.0
Mica	Castellanos-Gomez <i>et al.</i> ⁴¹⁰	202 ± 22	202 ± 22
	Wang <i>et al.</i> ⁴¹¹	390 ± 160	/
Ti ₃ C ₂ T _x	Lipatov <i>et al.</i> ⁴¹²	333 ± 30	326 ± 29

^aHere, the pressure behavior in bulging devices was studied: Interpreting the results in terms of the theory of elasticity,¹⁶⁵ it is possible to infer Y.

^bIn this work, the indentation was performed on micro-bubbles.

^cIn this work, the buckling metrology technique was used.

^dIn this work, the bimodal AFM technique was used.

^eIn this work, the nanoresonator technique was used.

TABLE XVIII. 3D (Y) and 2D (E_{2D}) Young's moduli of BP measured by exploiting mechanical deformations in both the armchair (AC) and zigzag (ZZ) directions. E_{2D} is calculated for a 1L-thick membrane as $E_{2D} = Yt$, taking $t = 0.85$ nm. Unless otherwise specified, the values were obtained via indentation experiments.

Ref.	Black phosphorus			
	Y (GPa)		E_{2D} (N/m)	
	AC	ZZ	AC	ZZ
Tao <i>et al.</i> ⁷⁷	27.2 ± 4.1	58.6 ± 11.7	23.1 ± 3.5	49.8 ± 9.9
Chen <i>et al.</i> ^{413,a}	27.4 ± 2.4	65.2 ± 4.5	23.3 ± 2.0	55.4 ± 3.8
Vaquero-Garzon <i>et al.</i> ^{414,b}	35.1 ± 6.3	93.3 ± 21.8	28.8 ± 5.4	79.3 ± 18.5
Wang <i>et al.</i> ^{415,c}	46.5	116.1	39.5	98.7
Moreno-Moreno <i>et al.</i> ⁴¹⁶	41 ± 15^d		35 ± 13^d	
Wang <i>et al.</i> ⁴¹⁷	80-280 ^{d,e}		70-240 ^{d,e}	

^aIn this work, the indentation was performed on a nanoribbon, and the whole angle dependence of the Young's modulus was determined.

^bIn this work, the buckling metrology technique was used.

^cIn this work, the nanoresonator technique was used.

^dA substrate with circular holes was used, so that the Young's modulus is not probed in a specific direction.

^eAn increasing value is measured while decreasing the flake thickness.

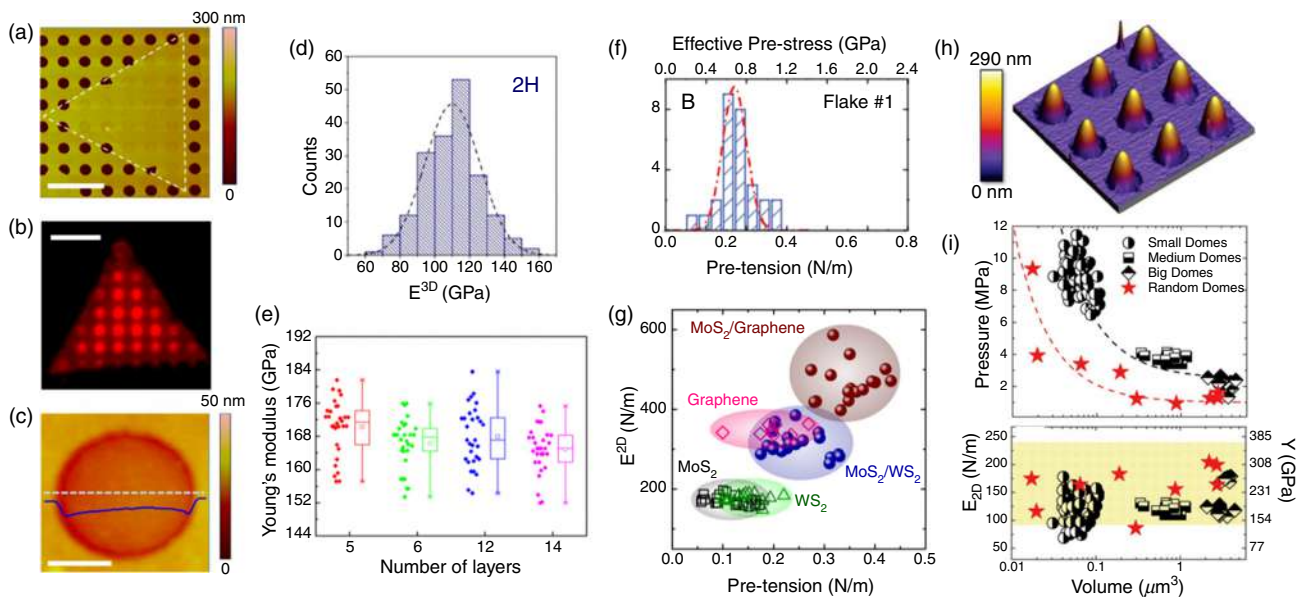


FIG. 68. (a) AFM topography of a triangle monolayer (obtained by CVD) transferred onto a holey substrate. Scale bar: $5 \mu\text{m}$. (b) Map of PL peak intensity from a triangle monolayer sitting on the holey substrate. Scale bar: $5 \mu\text{m}$. (c) Typical AFM topography of a MoS_2 monolayer over a hole. Scale bar: 500 nm . (d) Histograms of the elastic moduli measured in 2H- MoTe_2 . (e) Box chart of Young's moduli measured for WSe_2 membranes with different number of layers. (f) Histogram of film pretensions measured in a graphene ML. (g) Comparison of elastic properties of different 2D layers: Experimental data of 2D modulus and pretension for various 2D layers and heterostructures. (h) Tapping-mode AFM topography of a MoS_2 flake after hydrogenation, resulting in the formation of domes. The flake was previously coated with an HSQ mask to control the dome-formation process. The area is $15 \mu\text{m} \times 15 \mu\text{m}$ in lateral size. (i) Top: H_2 pressure values measured in H_2 -filled MoS_2 domes vs their volume for engineered (half-black scatters) and spontaneous (red stars) domes. Black and red dashed lines work as a guide for the eye. Bottom: Stretching modulus E_{2D} vs the domes' volume for engineered (half-black scatters) and spontaneous (red stars) domes. The yellow area highlights the range of E_{2D} values reported in literature for MoS_2 monolayer. (a)–(c) and panel (g) Reprinted with permission from Liu *et al.*, *Nano Lett.* **14**, 5097 (2014). Copyright 2014 American Chemical Society.⁴⁰⁰ (d) Reprinted with permission from Sun *et al.*, *Nano Lett.* **19**, 761 (2019). Copyright 2019 American Chemical Society.⁷⁶ (e) Reprinted with permission from Zhang *et al.*, *Appl. Phys. Lett.* **108**, 042104 (2016). Copyright 2016 American Institute of Physics.⁴⁰⁵ (f) Reprinted with permission from Lee *et al.*, *Science* **321**, 385 (2008). Copyright 2008 American Association for the Advancement of Science.¹⁰⁷ (h) and (i) Reprinted with permission from Di Giorgio *et al.*, *Adv. Mater. Interfaces* **7**, 2001024 (2020). Copyright 2020 Wiley-VCH Verlag GmbH & Co. KGaA, Weinheim.¹¹⁴

hole [see panel (c)] or may be affected by the bent nature of the membrane on the hole. Hence, the pre-tension of 2D layers depends both on their intrinsic mechanical properties and on the transfer process, and it is thus expected to feature a larger variation from flake to flake. A summary of the elastic moduli vs the pre-tension measured in MoS₂, WS₂, and graphene and in heterostructures made of MoS₂/WS₂ and MoS₂/graphene is shown in Fig. 68(g). Interestingly, the 2D moduli measured in the two heterostructures are both lower than the summed 2D moduli of the constituent layers (or, in other words, the 3D Young's modulus of the heterostructure is lower than the average of the 3D Young's moduli of the constituent layers). Instead, the heterostructures' pre-tensions are almost equal to the sum of the pre-tensions of the two materials. This indicates that the pre-tension is accumulated as the layers are stacked sequentially by the same transfer process.⁴⁰⁰

While indentation experiments are typically performed on samples deposited on circular holes, in some cases other geometries are employed, such as by suspending 2D-material stripes. This can be obtained by etching processes.⁷⁷ While this requires more complicated fabrication steps, the obtained device is particularly useful to study anisotropic materials where the Young's modulus is direction-dependent, such as in the case of BP. For a rectangular suspended stripe, Eq. (2) becomes⁷⁷

$$F(\delta_{\text{mem}}) = \left[\frac{\pi^4 w Y t^3}{6L^3} + \frac{T}{L} \right] \delta_{\text{mem}} + \frac{\pi^4 w Y t}{8L^3} \delta_{\text{mem}}^3, \quad (48)$$

where w and L are the width and length of the suspended part of the stripe, respectively. It is worth noticing that the same equation has also been used for suspended nanoribbons.⁴¹³

Finally, the indentation method has been recently extended to pressurized bulges and bubbles. In that case, Di Giorgio *et al.*¹¹⁴ showed how it is possible to get out a quantitative estimate of both the internal pressure of the blister p and the Young's modulus. This can be done by indenting the structures at their center and interpreting the results by using the solution of the Föppl-von-Kármán equation for pressurized, ultrathin elastic shells clamped to the edge of a circular hole of footprint radius R in the presence of external loading.⁴¹⁹ In particular, for small indentations, the force-distance curve will feature a linear behavior with slope k , which embeds information on the elastic properties of the material and on the difference between internal and external pressure Δp according to the following equations:¹¹⁴

$$E_{2D} = \log\left(\frac{R}{R_{\text{tip}}}\right) \frac{A_h^2 R^2 k}{2\pi A_\tau h_0^2}, \quad (49)$$

$$\Delta p = \log\left(\frac{R}{R_{\text{tip}}}\right) \cdot \frac{h_0 k}{(2\pi A_h A_\tau R^2)}, \quad (50)$$

where R and h_0 are the bulge footprint radius and height, respectively, R_{tip} is the AFM tip's radius, and where A_h and A_τ are constants depending on the Poisson's ratio.⁴¹⁹ Examples of indentation-based measurements of MoS₂ bubbles aimed at estimating the pressure and Young's modulus via Eqs. (49)–(50) are shown in Figs. 68(h) and 68(i). Both spontaneously formed bubbles and engineered bubbles formed with the approach described in Fig. 20 were studied and a higher internal pressure was found in the engineered structures, confirming how the patterning procedure represents an effective approach

to increase the built-in strain of the bubbles.¹¹³ Interestingly, for large indentation depths, the AFM may introduce an extra strain into the system, and total strains up to $\sim 15\%$ were achieved without causing the explosion of the bubbles.¹¹⁴

It should be remarked that—on the other side—the formation of the bubbles themselves is ruled by the minimization of the total energy, as discussed in Sec. III. In turn, this allows us to establish a correspondence between the aspect ratio of such structures (i.e., the ratio between the maximum height and footprint radius, which is a universal quantity^{112,131,132}), the elastic parameters of the membrane, and its adhesion energy, via Eq. (3).

This shows how mechanical deformations of 2D membranes represent an ideal system to obtain information on the fundamental elastic, adhesive, and mechanical properties of the material.

Over the past decade, indentation experiments have provided estimates of the elastic moduli for a wide variety of 2D materials and some heterostructures, which are summarized in Table XVII. The results obtained in the case of BP are instead displayed in Table XVIII, where the spatial anisotropy of the Young's modulus is highlighted by showing the noticeable difference in the values measured in the arm-chair and zigzag direction.

To conclude the discussion on indentation experiments, it should be mentioned that they can not only provide information on the elastic properties of the membrane, but also on its mechanical strength. In fact, extremely large deformations can be achieved with this method (see Table II), usually up to causing the 2D membrane to break. In such a way, it is possible to quantify the maximum stress the membrane is able to sustain. With this approach, typical breaking total strains were found to be $\epsilon_{\text{tot}}^{\text{break}} \sim 25\%$ for graphene,¹⁰⁷ $\epsilon_{\text{tot}}^{\text{break}} \sim 10\%$ for TMDs,¹⁵ and values in between for h-BN.⁷⁹

Although nanoindentation experiments represent the most used technique to study the mechanical properties of 2D-layered materials, they suffer for some drawbacks, among which the need to suspend the material under investigation on a pre-patterned holey substrate. This puts the investigated material in an environment quite different from that of a device structure, where the 2D layer is typically in contact with the substrate without suspension. Therefore, it may also be important to be able to directly map the mechanical properties of a 2D material deposited on a substrate. A possibility is provided by multi-frequency atomic force microscopy,^{420,421} an evolution of the conventional dynamic force microscopy in which the tip-sample system is not excited and detected at one single, fixed frequency, but by a combination of two or more frequencies, thus having access to complementary information on the tip-sample system going beyond the sample surface level [see sketch in Fig. 69(a)]. In particular, bi-modal atomic force microscopy has been successfully employed to measure the in-plane Young's modulus of a MoS₂ monolayer deposited on a Si/SiO₂ substrate,⁴⁰⁵ obtaining a value consistent with those obtained by standard indentation measurements (see Table XVII). In this case, the first and second flexural modes of an AFM cantilever have been used simultaneously to map the effective spring constant (k_*) between the tip and the sample and, by using contact mechanics and finite element analysis, the effect of the substrate stiffness has been accounted for in order to extract the mechanical properties of the deposited monolayer. In particular, the first cantilever mode (with spring constant k_1 , resonance frequency f_1 , amplitude A_1 , and phase ϕ_1) is driven in amplitude

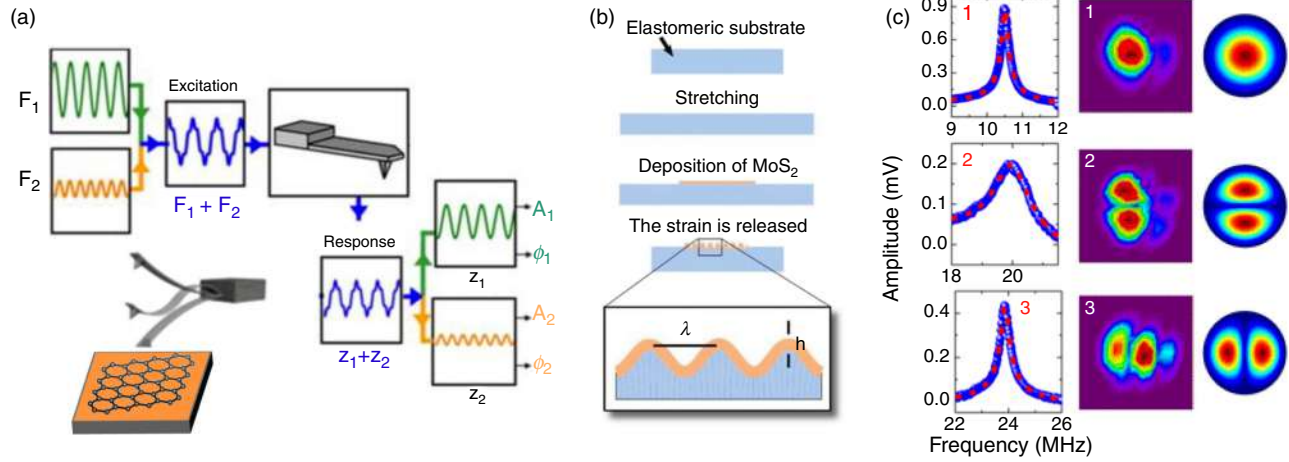


FIG. 69. (a) Diagram of the bimodal AFM technique. The amplitude of the first oscillation mode of the tip is used for topography imaging while the signal from the second mode gives access to different mechanical or electromagnetic properties. Adapted with permission from Garcia and Proksch, *Eur. Polym. J.* **49**, 1897 (2013). Copyright 2013 Elsevier.⁴²¹ (b) Sketch of the process employed in the buckling metrology technique. The flakes are transferred onto a stretched elastomeric substrate; when the stress of the substrate is released the flakes are subjected to uniaxial compressive strain that produces their buckling. Reprinted with permission from Iguñiz *et al.*, *Adv. Mater.* **31**, 1807150 (2019). Copyright 2019 Wiley-VCH Verlag GmbH & Co. KGaA, Weinheim.⁴⁰² (c) Resonator technique. Left: Multimode resonance measured in a BP membrane suspended over a circular cavity with size $10\ \mu\text{m}$, showing the first 3 modes within 9 and 26 MHz. Center: Spatially resolved flexural modes measured experimentally on the same circular device. The measurements were taken at the peak frequencies of the first 3 modes (10.51, 19.93, and 23.87 MHz). Right: Spatial distribution of the flexural modes simulated via finite element method (FEM) modeling. Adapted with permission from Wang *et al.*, *Nano Lett.* **16**, 5394 (2016). Copyright 2016 American Chemical Society.⁴¹⁵

modulation (AM) to track the sample topography and measure the tip-sample interaction stiffness, whilst the second cantilever mode (with spring constant k_2 , resonance frequency f_2 , amplitude A_2 , and fixed phase ϕ_2 of $\pi/2$) is driven in frequency modulation (FM) getting complementary information about the tip-sample interaction from its frequency shift (Δf_2). Such an experimental configuration, referred to as AM-FM mode, allows us to distinguish between changes in indentation depth (δ) and sample elastic modulus. Both these independent measurements can be used to obtain the effective spring constant of the tip-sample system,

$$k_* = \pi \sqrt{\frac{2}{3}} \left(\frac{k_1 A_1^0 \cos \phi_1}{Q_1 A_1} \right)^{-\frac{1}{2}} \left(\frac{2k_2 \Delta f_2}{f_2 + \Delta f_2} \right)^{\frac{3}{2}}, \quad (51)$$

where Q is the quality factor and A^0 is the amplitude of the tip resonance mode in air. The corresponding indentation depth during the scanning is given by

$$\delta = \frac{3}{4} \left(\frac{k_1 A_1^0 \cos \phi_1}{Q_1} \right) \left(\frac{2k_2 \Delta f_2}{f_2 + \Delta f_2} \right)^{-1}. \quad (52)$$

It is then possible to extract the Young's modulus of the sample (MoS_2 on Si/SiO_2) through the equation $k_* = 2R_{tip}E_*$, where R_{tip} is the tip radius, and the formula for the effective Young's modulus (E_*):

$$\frac{1}{E_*} = \frac{1 - \nu_t^2}{E_t} + \frac{1 - \nu_s^2}{E_s}, \quad (53)$$

where E_t , E_s , ν_t , and ν_s are Young's modulus and Poisson's ratio of the tip and the sample, respectively. At this point, the Young's modulus of the MoS_2 monolayer can be deduced by deconvolving the effect of the underlying (Si/SiO_2) substrate by FEM simulations and direct measurements of the substrate elastic constants.

Together with the mechanical testing techniques reviewed above, another powerful—and somehow simpler—technique employed in recent years to investigate the mechanical properties of very thin 2D materials is the so-called buckling-based metrology. This simple technique was first developed for rapidly determining the mechanical properties of thin polymer films and coatings by studying the buckling instability,⁴²² which arises when thin film is deposited onto a compliant substrate and it is subjected to a uniaxial compression [see Fig. 69(b)]. Very recently, the buckling metrology technique has also been applied to several TMDs^{402,407}—as well as to BP⁴¹⁴—obtaining values of Young's modulus in agreement with those obtained by most sophisticated testing methods (see Tables XVII and XVIII). In particular, the wavelength of the ripples that form on a thin 2D layer deposited on a stretched elastomeric substrate (i.e., PDMS or gel film) after the release of the substrate strain, is directly proportional to the Young's modulus of the 2D material. Indeed, the ripple pattern arises from the buckling instability resulting from the balance between the energy required to bend the stiff 2D material, the energy to elastically deform the soft underlying elastomeric substrate, and the adhesion energy between them. It can be demonstrated that, under specific conditions, the wavelength (λ) of these ripples is independent of the initial pre-stress of the elastomeric substrate and it only depends on the material properties of both flake and substrate through the formula⁴⁰²

$$\lambda = 2\pi t \left[\frac{(1 - \nu_s^2) E_f}{3(1 - \nu_s^2) E_s} \right]^{1/3}, \quad (54)$$

where t is the flake thickness, ν_s and ν_f are the Poisson's ratios of substrate and flake, and E_s and E_f are the Young's moduli of the substrate and flake, respectively. This equation is valid under a number of assumptions: (i) the flake should follow a sinusoidal rippling; (ii)

$E_f/E_s \gg 1$; (iii) the substrate should be much thicker than the flake; (iv) the amplitude of the ripples should be much smaller than their wavelength (thus shear forces are neglected); (v) the adhesion between the flake and substrate is strong enough to prevent slippage; and (vi) all the deformations are assumed to be elastic. Aside these limitations, the buckling-based metrology is a quite easy technique to be implemented and it returns reliable values of the Young's modulus, although the uncertainty on the estimated value is larger than that obtained with other techniques, partially due to the dependence of Eq. (54) on the flake thickness, which needs to be accurately determined by independent techniques.

The methods discussed so far have proven to be effective in quantifying the elastic parameters of atomically thin membranes. The knowledge of these parameters is particularly interesting within the context of sensing applications toward nano-electromechanical systems (NEMS). In fact, the ability to withstand high strains, the large Young's modulus, and the very low mass of 2D membranes make them near-ideal candidates for the realization of high-performance nanoresonators,^{423–425} extremely sensitive to—and, thus, well suited to detect—small displacements and mass/force variations. Indeed, the mass sensitivity of a resonator, δM , is proportional to its effective mass, M_{eff} .⁴²⁶ The displacement sensitivity, on the other hand, is equal to

$$S_z^{\frac{1}{2}} = \sqrt{\frac{4k_B T_{res} Q}{(2\pi f)^3 M_{eff}}}, \quad (55)$$

where f is the mode frequency, Q is the mode's quality factor, T_{res} is the resonating system temperature, and k_B is the Boltzmann constant. Given that $S_z^{\frac{1}{2}}$ improves (i.e., it gets smaller) for increasing mode frequency, it is interesting to note that the latter gets generally higher for smaller resonators; for circular suspended devices with diameter d , indeed, the frequency of the fundamental mode is^{78,423,427}

$$f_0 = \sqrt{\left(\frac{2.4048}{\pi d}\right)^2 \cdot \frac{T}{\rho t} + \left(\frac{10.21t}{\pi d^2}\right)^2 \cdot \frac{E_{2D}}{3\rho(1-\nu^2)}}, \quad (56)$$

where ρ is the mass density, T is the pre-tension, and t is the 2D-membrane-thickness.

Apart from making the dependence of the mode frequency on the resonator's diameter explicit, Eq. (56) presents many additional points of interest. First of all, this equation effectively captures the transition undergone by circular resonators as a function of their thickness, t . For relatively thick resonators, the system indeed behaves as a simply supported circular plate, with fundamental frequency $f_0 = \frac{10.21t}{\pi d^2} \sqrt{\frac{E_{2D}}{3\rho(1-\nu^2)}}$. In this limit, the dependence of f_0 on the elastic properties of the material (E_{2D} and ν) is apparent, and indeed Lee and coworkers could estimate a value of $E_{2D} \sim 80$ N/m (see Table XVII) for the Young's modulus of WTe_2 ,⁴⁰⁶ by comparing the results of Eq. (56) with the values of f_0 measured on a set of resonators of varying thickness and diameter (the Poisson's ratio ν was estimated from DFT simulations, see, e.g., Table III).

In the low-thickness regime, on the other hand, circular resonators reach the so-called *membrane limit*, for which f_0 tends to $\frac{2.4048}{\pi d} \sqrt{\frac{T}{\rho t}}$. In this regime, wherein all resonators based on single TMD monolayers naturally tend to fall, the device behavior is dominated by

the initial pre-tension, T , i.e., on the strain built in the membrane. As noted above, this observation dovetails nicely with the natural predisposition of 2D materials for strain engineering—which we extensively relayed throughout this review—and makes strained 2D materials (such as the nanodomains discussed in Refs. 112–114 and 134) ideally suited for the realization of high-frequency, high-performance nanoresonators, potentially interesting for NEMS-based sensing applications.^{428,429} In addition, with respect to graphene,⁴²⁸ TMD monolayers and BP are direct bandgap semiconductors, and they are thus very interesting for the fabrication of transducers based on the interplay between their mechanical and optical properties.

A nice example of a BP-based resonator is displayed in Fig. 69(c).⁴¹⁵ In that case, several multimode resonances were identified and spatially-mapped. Numerical calculations were employed to interpret the experiment and extract the Young's moduli in different directions, see Table XVIII.

Before concluding Sec. V, it is worth recalling that most of the above-mentioned techniques return averaged values on the whole sample, while in some cases, as for example in poly-crystalline membranes, the local values of Young's modulus and of the residual stress are desirable. In such cases, a spatial investigation of the membrane's elastic properties can be performed, for example, by micro-Brillouin light scattering.⁴³⁰ This technique is able to test the elastic properties of few nm-thick 2D membranes by probing the light frequency shift resulting from the inelastic light scattering on thermally populated acoustic waves. Alternatively, as reported in Fig. 69(c) for a suspended BP membrane,⁴¹⁵ it is also possible to map the individual flexural modes of a nanoresonator by scanning spectromicroscopy measurements, in which the readout laser is scanned across the device surface while recording the spatial variations of the signal amplitude at the frequency corresponding to a specific resonance mode.

VI. CONCLUSIONS AND PERSPECTIVES

In this review, we showed the great potential of strain to modify the properties of 2D materials and to induce therein fascinating effects. The methods themselves employed to mechanically-deform 2D crystals represent a very interesting experimental playground, where researchers have developed increasingly inventive approaches exploiting diverse growth techniques (either on deformed/patterned or dissimilar substrates), devices able to bend, bulge, stretch, or indent atomically thin membranes, or endogenous phenomena (such as gas trapping or hydrogen caging). These approaches are reviewed and are shown to be characterized by different strain configurations. In turn, the latter provide a precious tool to understand the mechanical and electronic properties of the investigated materials, as well as a means to deliberately modify those properties. Indeed, the bandgap energy and nature, the vibrational properties, and the linear and nonlinear optical characteristics can be modulated, down to the micro- and nanometer scale. Furthermore, great prospects have been envisioned regarding the quantum optical applications of strained 2D crystals as host of single-photon sources that can be made site-controlled, scalable, and integrable in photonic devices.

In this review, we presented a quantitative survey of the strain effects on various relevant quantities, such as the energy of the fundamental and higher-state excitons, the phonon frequencies, and vibration-related parameters (i.e., shift rates, Grüneisen parameters, splitting rates, and shear deformation potentials). Non-linear optical

effects, such as second and third harmonic generation, are also presented here, showing how their response to mechanical solicitations is of great relevance for the characterization of 2D materials, permitting to address their lattice symmetry properties and to probe higher energy states of the band structure. Apart from modifying the inherent optical and vibrational properties of 2D materials, strain can also be at the origin of intriguing effects, such as the fascinating creation of pseudo-magnetic fields thanks to strain gradients that directly act on the spin and valley degrees of freedom. To this regard, suitable strain patterns may lead to the insurgence of dissipation-less currents or to devices with improved transport and optical characteristics. Here, we discuss this opportunity, also addressing how strain can play a relevant role toward the utilization of layered materials in valleytronics and spintronics. Finally, the elasto-mechanical properties of vdW crystals can also be deduced by suitable applications of strain. In the concluding section of this work, we discuss possible methodologies to characterize the crystals, and we report a quantitative survey of the elastic parameters.

After a decade of studies, the effect of strain has been characterized by many different viewpoints, and this review shows how great knowledge has been achieved. Far from being exhausted, this research field still continues to progress and provide novel and exciting opportunities. Nonetheless, some obstacles still have to be faced. Indeed, the results we presented in the sections related to the optical and vibrational properties highlight how a large variability is found depending on the strain method. This suggests how the real strain configuration might be different from the nominal one, and further studies in this respect would be needed. In fact, the large variability observed prevents the utilization of noninvasive techniques such as Raman spectroscopy to quantitatively measure the strain.

In some cases, variations in the optical response or elastic response have also been reported by using a same setup and characterization technique. Also in this case, further studies could provide useful information to understand if these variations could be due to the exfoliation or growth technique, to the transfer processes, to the intrinsic presence of defects, or something else. This could possibly allow one to pinpoint the best fabrication techniques and methodologies.

While in most cases combined theoretical and experimental efforts permitted to achieve a clear picture of the effect of strain, in some other cases the picture is still hazy. The most striking example is that of single photon emitters, where both their origin and the real effect of strain are still unclear in most systems. Indeed, strain has been shown to favor the localization of quantum emitters, but it has not been allowed to gain a thorough knowledge of the emitters themselves, yet. Further studies could help to elucidate the still unclear aspects.

Finally, strain engineering has been predicted to give rise to exciting phenomena related to the strain coupling to the valley and spin degrees of freedom. Despite the great promise of this field, experimental evidence of many predicted effects is still lacking. Indeed, more experimental studies to complement the theoretical studies could show mesmerizing fundamental effects and pave the way for the realization of novel high-performance devices.

Indeed, this research field still presents some challenges and at the same time offers new opportunities.

Based on the widespread fundamental and practical applications of strain presented here, mechanically structuring certainly turns out

to be a most promising method to exploit and boost the enormous potential of 2D materials, either as a built-in source enhancing the properties of the material, or as an external perturbation that can be suitably engineered or variably tuned.

ACKNOWLEDGMENTS

The authors acknowledge C. Di Giorgio, F. Bobba, T. Yildirim, A. Surrente, P. Faria Jr., and Y. Lu for past and present collaborations. E.B., M.F., and A.P. are grateful for funding from the Regione Lazio programme “Progetti di Gruppi di ricerca” legge Regionale n. 13/2008 (SINFONIA project, prot. n. 85-2017-15200) via LazioInnova spa. A.P. acknowledges support by Sapienza Università di Roma under the grants Ricerche Ateneo.

DATA AVAILABILITY

The data that support the findings of this study are available from the corresponding author upon reasonable request.

REFERENCES

- ¹R. P. Feynman, “There’s plenty of room at the bottom,” *Eng. Sci.* **23**, 22 (1960).
- ²R. E. Peierls, “Quelques propriétés typiques des corps solides,” *Ann. I. H. Poincaré* **5**, 177 (1935).
- ³L. D. Landau, “Zur theorie der phasenumwandlungen II,” *Phys. Z. Sowjetunion* **11**, 26 (1937).
- ⁴L. D. Landau and E. M. Lifshitz, *Statistical Physics, Part I* (Pergamon, Oxford, 1980).
- ⁵N. D. Mermin, “Crystalline order in two dimensions,” *Phys. Rev.* **176**, 250 (1968).
- ⁶A. K. Geim and K. S. Novoselov, “The rise of graphene,” *Nat. Mater.* **6**, 183 (2007).
- ⁷R. F. Frindt, “Superconductivity in ultrathin NbSe₂ layers,” *Phys. Rev. Lett.* **28**, 299 (1972).
- ⁸R. F. Frindt, “Single crystals of MoS₂ several molecular layers thick,” *J. Appl. Phys.* **37**, 1928 (1966).
- ⁹K. S. Novoselov, A. K. Geim, S. V. Morozov, D. Jiang, Y. Zhang, S. V. Dubonos, I. V. Grigorieva, and A. A. Firsov, “Electric field effect in atomically thin carbon films,” *Science* **306**, 666 (2004).
- ¹⁰E. A. Abbott, *Flatland: A Romance of Many Dimensions* (Seeley & co, 1884).
- ¹¹P. Ajayan, P. Kim, and K. Banerjee, “Two-dimensional van der Waals materials,” *Phys. Today* **69**(9), 38 (2016).
- ¹²S. Z. Butler, S. M. Hollen, L. Cao, Y. Cui, J. A. Gupta, H. R. Gutiérrez, T. F. Heinz, S. S. Hong, J. Huang, A. F. Ismach, E. Johnston-Halperin, M. Kuno, V. V. Plashnitsa, R. D. Robinson, R. S. Ruoff, S. Salahuddin, J. Shan, L. Shi, M. G. Spencer, M. Terrones, W. Windl, and J. E. Goldberger, “Progress, challenges, and opportunities in two-dimensional materials beyond graphene,” *ACS Nano* **7**, 2898 (2013).
- ¹³A. Krishnan, E. Dujardin, T. W. Ebbesen, P. N. Yianilos, and M. M. J. Treacy, “Young’s modulus of single-walled nanotubes,” *Phys. Rev. B* **58**, 14013 (1998).
- ¹⁴M. K. Bles, A. W. Barnard, P. A. Rose, S. P. Roberts, K. L. McGill, P. Y. Huang, A. R. Ruyack, J. W. Kevek, B. Kobrin, D. A. Muller, and P. L. McEuen, “Graphene kirigami,” *Nature* **524**, 204 (2015).
- ¹⁵S. Bertolazzi, J. Brivio, and A. Kis, “Stretching and breaking of ultrathin MoS₂,” *ACS Nano* **5**, 9703 (2011).
- ¹⁶X. Li, L. Tao, Z. Chen, H. Fang, X. Li, X. Wang, J.-B. Xu, and H. Zhu, “Graphene and related two-dimensional materials: Structure-property relationships for electronics and optoelectronics,” *Appl. Phys. Rev.* **4**, 021306 (2017).
- ¹⁷N. Lu, H. Guo, L. Li, J. Dai, L. Wang, W.-N. Mei, X. Wu, and X. C. Zeng, “MoS₂/MX₂ heterobilayers: Bandgap engineering via tensile strain or external electrical field,” *Nanoscale* **6**, 2879 (2014).
- ¹⁸A. K. Geim and I. V. Grigorieva, “Van der Waals heterostructures,” *Appl. Phys. Rev.* **4**, 041101 (2013).

- ¹⁹B. Amorim, A. Cortijo, F. de Juan, A. Grushin, F. Guinea, A. Gutiérrez-Rubio, H. Ochoa, V. Parente, R. Roldán, P. San-Jose, J. Schiefele, M. Sturla, and M. Vozmediano, "Novel effects of strains in graphene and other two dimensional materials," *Phys. Rep.* **617**, 1–54 (2016).
- ²⁰C. Si, Z. Sun, and F. Liu, "Strain engineering of graphene: A review," *Nanoscale* **8**, 3207 (2016).
- ²¹R. Roldán, A. Castellanos-Gomez, E. Cappelluti, and F. Guinea, "Strain engineering in semiconducting two-dimensional crystals," *J. Phys.: Condens. Matter* **27**, 313201 (2015).
- ²²Z. Dai, L. Liu, and Z. Zhang, "Strain engineering of 2D materials: Issues and opportunities at the interface," *Adv. Mater.* **31**, 1805417 (2019).
- ²³S. Deng, A. V. Sumant, and V. Berry, "Strain engineering in two-dimensional nanomaterials beyond graphene," *Nano Today* **22**, 14–35 (2018).
- ²⁴D. A. Sanchez, Z. Dai, and N. Lu, "2D material bubbles: Fabrication, characterization, and applications," *Trends Chem.* **3**, 204–217 (2021).
- ²⁵H. Tomori, A. Kanda, H. Goto, Y. Ootuka, K. Tsukagoshi, S. Moriyama, E. Watanabe, and D. Tsuya, "Introducing nonuniform strain to graphene using dielectric nanopillars," *Appl. Phys. Express* **4**, 075102 (2011).
- ²⁶C. Palacios-Berraquero, D. M. Kara, A. R.-P. Montblanch, M. Barbone, P. Latawiec, D. Yoon, A. K. Ott, M. Loncar, A. C. Ferrari, and M. Atatüre, "Large-scale quantum-emitter arrays in atomically thin semiconductors," *Nat. Commun.* **8**, 15093 (2017).
- ²⁷H. Li, A. W. Contryman, X. Qian, S. M. Ardakani, Y. Gong, X. Wang, J. M. Weisse, C. H. Lee, J. Zhao, P. M. Ajayan, J. Li, H. C. Manoharan, and X. Zheng, "Optoelectronic crystal of artificial atoms in strain-textured molybdenum disulphide," *Nat. Commun.* **6**, 7381 (2015).
- ²⁸H. Moon, E. Bersin, C. Chakraborty, A.-Y. Lu, G. Grosso, J. Kong, and D. Englund, "Strain-correlated localized exciton energy in atomically thin semiconductors," *ACS Photonics* **7**, 1135 (2020).
- ²⁹A. Branny, S. Kumar, R. Proux, and B. D. Gerardot, "Deterministic strain-induced arrays of quantum emitters in a two-dimensional semiconductor," *Nat. Commun.* **8**, 15053 (2017).
- ³⁰B. Liu, Q. Liao, X. Zhang, J. Du, Y. Ou, J. Xiao, Z. Kang, Z. Zhang, and Y. Zhang, "Strain-engineered van der Waals interfaces of mixed-dimensional heterostructure arrays," *ACS Nano* **13**, 9057 (2019).
- ³¹H. Li, C. Tsai, A. L. Koh, L. Cai, A. W. Contryman, A. H. Fragapane, J. Zhao, H. S. Han, H. C. Manoharan, F. Abild-Pedersen, J. K. Nørskov, and X. Zheng, "Activating and optimizing MoS₂ basal planes for hydrogen evolution through the formation of strained sulphur vacancies," *Nat. Mater.* **15**, 48 (2016).
- ³²J. Chaste, A. Missaoui, S. Huang, H. Henck, Z. B. Aziza, L. Ferlazzo, C. Naylor, A. Balan, J. A. T. C. Johnson, R. Braive, and A. Ouerghi, "Intrinsic properties of suspended MoS₂ on SiO₂/Si pillar arrays for nanomechanics and optics," *ACS Nano* **12**, 3235 (2018).
- ³³D. Mazumder, J. Xie, Z. R. Kudrynskiy, X. Wang, O. Makarovskiy, M. A. Bhuiyan, H. Kim, T.-Y. Chang, D. L. Huffaker, Z. D. Kovalyuk, L. Zhang, and A. Patané, "Enhanced optical emission from 2D InSe bent onto Si-pillars," *Adv. Opt. Mater.* **8**, 2000828 (2020).
- ³⁴L. Sortino, M. Brooks, P. G. Zotev, A. Genco, J. Cambiasso, S. Mignuzzi, S. A. Maier, G. Burkard, R. Sapienza, and A. I. Tartakovskii, "Dielectric nanoantennas for strain engineering in atomically thin two-dimensional semiconductors," *ACS Photonics* **7**, 2413–2422 (2020).
- ³⁵Z. Dai, Y. Hou, D. A. Sanchez, G. Wang, C. J. Brennan, Z. Zhang, L. Liu, and N. Lu, "Interface-governed deformation of nanobubbles and nanotents formed by two-dimensional materials," *Phys. Rev. Lett.* **121**, 266101 (2018).
- ³⁶H. Li, M. Du, M. J. Mleczko, A. L. Koh, Y. Nishi, E. Pop, A. J. Bard, and X. Zheng, "Kinetic study of hydrogen evolution reaction over strained MoS₂ with sulfur vacancies using scanning electrochemical microscopy," *J. Am. Chem. Soc.* **138**, 5123 (2016).
- ³⁷S. Ren, Q. Tan, and J. Zhang, "Review on the quantum emitters in two-dimensional materials," *J. Semicond.* **40**, 071903 (2019).
- ³⁸M. Toth and I. Aharonovich, "Single photon sources in atomically thin materials," *Annu. Rev. Phys. Chem.* **70**, 123 (2019).
- ³⁹T. T. Tran, D. Wang, Z.-Q. Xu, A. Yang, M. Toth, T. W. Odom, and I. Aharonovich, "Deterministic coupling of quantum emitters in 2D materials to plasmonic nanocavity arrays," *Nano Lett.* **17**, 2634 (2017).
- ⁴⁰O. Iff, N. Lundt, S. Betzold, L. N. Tripathi, M. Emmerling, S. Tongay, Y. J. Lee, S.-H. Kwon, S. Höfling, and C. Schneider, "Deterministic coupling of quantum emitters in WSe₂ monolayers to plasmonic nanocavities," *Opt. Express* **26**, 25944 (2018).
- ⁴¹Y. Luo, G. D. Shepard, J. V. Ardelean, D. A. Rhodes, B. Kim, K. Barmak, J. C. Hone, and S. Strauf, "Deterministic coupling of site-controlled quantum emitters in monolayer WSe₂ to plasmonic nanocavities," *Nat. Nanotech.* **13**, 1137 (2018).
- ⁴²A. W. Schell, H. Takashima, T. T. Tran, I. Aharonovich, and S. Takeuchi, "Coupling quantum emitters in 2D materials with tapered fibers," *ACS Photonics* **4**, 761 (2017).
- ⁴³T. T. Tran, D. Wang, Z.-Q. Xu, A. Yang, M. Toth, T. W. Odom, and I. Aharonovich, "On-chip waveguide coupling of a layered semiconductor single photon source," *Nano Lett.* **17**, 5456 (2017).
- ⁴⁴L. C. Flatten, L. Weng, A. Branny, S. Johnson, P. R. Dolan, A. A. P. Trichet, B. D. Gerardot, and J. M. Smith, "Microcavity enhanced single photon emission from two-dimensional WSe₂," *Appl. Phys. Lett.* **112**, 191105 (2018).
- ⁴⁵C. Errando-Herranz, E. Schöll, R. Picard, M. Laini, S. Gyger, A. W. Elshaari, A. Branny, U. Wennberg, S. Barbat, T. Renaud, M. Brotons-Gisbert, C. Bonato, B. D. Gerardot, V. Zwiller, and K. D. Jöns, "Resonance fluorescence from waveguide-coupled strain-localized two-dimensional quantum emitters," [arXiv:2002.07657](https://arxiv.org/abs/2002.07657) (2020).
- ⁴⁶D. Bimberg, N. N. Ledentsov, and M. Grundmann, *Quantum Dot Heterostructures* (John Wiley & Sons, New York, 2001).
- ⁴⁷S.-W. Wang, H. Medina, K.-B. Hong, C.-C. Wu, Y. Qu, A. Manikandan, T.-Y. Su, P.-T. Lee, Z.-Q. Huang, Z. Wang, F.-C. Chuang, H.-C. Kuo, and Y.-L. Chueh, "Thermally strained band gap engineering of transition-metal dichalcogenide bilayers with enhanced light-matter interaction toward excellent photodetectors," *ACS Nano* **11**, 8768 (2017).
- ⁴⁸C. Martella, C. Mennucci, E. Cinquanta, A. Lamperti, E. Cappelluti, F. B. de Mongeot, and A. Molle, "Anisotropic MoS₂ nanosheets grown on self-organized nanopatterned substrates," *Adv. Mater.* **29**, 1605785 (2017).
- ⁴⁹S. Xie, L. Tu, Y. Han, L. Huang, K. Kang, K. U. Lao, P. Poddar, C. Park, D. A. Muller, R. A. DiStasio, Jr., and J. Park, "Coherent and atomically thin transition-metal dichalcogenide superlattices with engineered strain," *Science* **359**, 1131 (2018).
- ⁵⁰G. H. Ahn, M. Amani, H. Rasool, D.-H. Lien, J. P. Mastandrea, J. W. A. III, M. Dubey, D. C. Chrzan, A. M. Minor, and A. Javey, "Strain-engineered growth of two-dimensional materials," *Nat. Commun.* **8**, 608 (2017).
- ⁵¹C. R. Zhu, G. Wang, B. L. Liu, X. Marie, X. F. Qiao, X. Zhang, X. X. Wu, H. Fan, P. H. Tan, T. Amand, and B. Urbaszek, "Strain tuning of optical emission energy and polarization in monolayer and bilayer MoS₂," *Phys. Rev. B* **88**, 121301(R) (2013).
- ⁵²K. He, C. Poole, K. F. Mak, and J. Shan, "Experimental demonstration of continuous electronic structure tuning via strain in atomically thin MoS₂," *Nano Lett.* **13**, 2931 (2013).
- ⁵³S. B. Desai, G. Seol, J. S. Kang, H. Fang, C. Battaglia, R. Kapadia, J. W. Ager, J. Guo, and A. Javey, "Strain-induced indirect to direct bandgap transition in multilayer WSe₂," *Nano Lett.* **14**, 4592 (2014).
- ⁵⁴X. He, H. Li, Z. Zhu, Z. Dai, Y. Yang, P. Yang, Q. Zhang, P. Li, U. Schwingenschlög, and X. Zhang, "Strain engineering in monolayer WS₂, MoS₂, and the WS₂/MoS₂ heterostructure," *Appl. Phys. Lett.* **109**, 173105 (2016).
- ⁵⁵W. Wu, J. Wang, P. Ercius, N. C. Wright, D. M. Leppert-Simenauer, R. A. Burke, M. Dubey, A. M. Dogare, and M. T. Pettes, "Giant mechano-optoelectronic effect in an atomically thin semiconductor," *Nano Lett.* **18**, 2351 (2018).
- ⁵⁶S. Pak, J. Lee, Y.-W. Lee, A.-R. Jang, S. Ahn, K. Y. Ma, Y. Cho, J. Hong, S. Lee, H. Y. Jeong, H. Im, H. S. S. Shin, S. M. Morris, S. Cha, J. I. Sohn, and J. M. Kim, "Strain-mediated interlayer coupling effects on the excitonic behaviors in an epitaxially grown MoS₂/WS₂ van der Waals heterobilayer," *Nano Lett.* **17**, 5634 (2017).
- ⁵⁷C. Song, F. Fan, N. Xuan, S. Huang, G. Zhang, C. Wang, Z. Sun, H. Wu, and H. Yan, "Largely tunable band structures of few-layer InSe by uniaxial strain," *ACS Appl. Mater. Interfaces* **10**, 3994 (2018).
- ⁵⁸E. del Corro, L. Kavan, M. Kalbac, and O. Frank, "Strain assessment in graphene through the Raman 2D' mode," *J. Phys. Chem. C* **119**, 25651 (2015).
- ⁵⁹F. Wang, S. Li, M. A. Bissett, I. A. Kinloch, Z. Li, and R. J. Young, "Strain engineering in monolayer WS₂ and WS₂ nanocomposites," *2D Mater.* **7**, 045022 (2020).

- ⁶⁰Z. Zhang, L. Li, J. Horng, N. Z. Wang, F. Yang, Y. Yu, Y. Zhang, G. Chen, K. Watanabe, T. Taniguchi, X. H. Chen, F. Wang, and Y. Zhang, "Strain-modulated bandgap and piezo-resistive effect in black phosphorus field-effect transistors," *Nano Lett.* **17**, 6097 (2017).
- ⁶¹T. M. G. Mohiuddin, A. Lombardo, R. R. Nair, A. Bonetti, G. Savini, R. Jalil, N. Bonini, D. M. Basko, C. Galiotis, N. Marzari, K. S. Novoselov, A. K. Geim, and A. C. Ferrari, "Uniaxial strain in graphene by Raman spectroscopy: G peak splitting, Grüneisen parameters, and sample orientation," *Phys. Rev. B* **79**, 205433 (2009).
- ⁶²J.-U. Lee, S. Woo, J. Park, H. C. Park, Y.-W. Son, and H. Cheong, "Strain-shear coupling in bilayer MoS₂," *Nat. Commun.* **8**, 1370 (2017).
- ⁶³C. Androulidakis, E. Koukaras, J. Parthenios, G. Kalosakas, K. Papagelis, and C. Galiotis, "Graphene flakes under controlled biaxial deformation," *Sci. Rep.* **5**, 18219 (2016).
- ⁶⁴I. Niehues, R. Schmidt, M. Drüppel, P. Marauhn, D. Christiansen, M. Selig, G. Berghäuser, D. Wigger, R. Schneider, L. Braasch, R. Koch, A. Castellanos-Gomez, T. Kuhn, A. Knorr, E. Malic, M. Rohlfing, S. M. de Vasconcelos, and R. Bratschitsch, "Strain control of exciton-phonon coupling in atomically thin semiconductors," *Nano Lett.* **18**, 1751 (2018).
- ⁶⁵Z. Li, Y. Lv, L. Ren, J. Li, L. Kong, Y. Zeng, Q. Tao, R. Wu, H. Ma, B. Zhao, D. Wang, W. Dang, K. Chen, L. Liao, X. Duan, X. Duan, and Y. Liu, "Efficient strain modulation of 2D materials via polymer encapsulation," *Nat. Commun.* **11**, 1151 (2020).
- ⁶⁶H. J. Conley, B. Wang, J. I. Ziegler, R. F. Haglund, Jr., S. T. Pantelides, and K. I. Bolotin, "Bandgap engineering of strained monolayer and bilayer MoS₂," *Nano Lett.* **13**, 3626 (2013).
- ⁶⁷L. Wang, P. Makk, S. Zihlmann, A. Baumgartner, D. I. Indolese, K. Watanabe, T. Taniguchi, and C. Schönenberger, "Mobility enhancement in graphene by in situ reduction of random strain fluctuations," *Phys. Rev. Lett.* **124**, 157701 (2020).
- ⁶⁸D. Lloyd, X. Liu, J. W. Christopher, L. Cantley, A. Wadehra, B. L. Kim, B. B. Goldberg, A. K. Swan, and J. S. Bunch, "Band gap engineering with ultralarge biaxial strains in suspended monolayer MoS₂," *Nano Lett.* **16**, 5836 (2016).
- ⁶⁹D. Lloyd, X. Liu, N. Boddeti, L. Cantley, R. Long, M. L. Dunn, and J. S. Bunch, "Adhesion, stiffness, and instability in atomically thin MoS₂ bubbles," *Nano Lett.* **17**, 5329 (2017).
- ⁷⁰G. Wang, Z. Dai, Y. Wang, P. Tan, L. Liu, Z. Xu, Y. Wei, R. Huang, and Z. Zhang, "Measuring interlayer shear stress in bilayer graphene," *Phys. Rev. Lett.* **119**, 036101 (2017).
- ⁷¹J. S. Bunch, S. S. Verbridge, J. S. Alden, A. M. van der Zande, J. M. Parpia, H. G. Craighead, and P. L. McEuen, "Impermeable atomic membranes from graphene sheets," *Nano Lett.* **8**, 2458 (2008).
- ⁷²S. P. Koenig, L. Wang, J. Pellegrino, and J. S. Bunch, "Selective molecular sieving through porous graphene," *Nat. Nanotech.* **7**, 728 (2012).
- ⁷³S. Zhang, Y. Hou, S. Li, L. Liu, Z. Zhang, X.-Q. Feng, and Q. Li, "Tuning friction to a superlubric state via in-plane straining," *Proc. Natl. Acad. Sci. U. S. A.* **116**, 24452–24456 (2019).
- ⁷⁴S. Kovalchuk, M. G. Harats, G. López-Polín, J. N. Kirchhof, K. Höflich, and K. I. Bolotin, "Neutral and charged excitons interplay in non-uniformly strain-engineered WS₂," *2D Mater.* **7**, 035024 (2020).
- ⁷⁵R. Yang, J. Lee, S. Ghosh, H. Tang, R. M. Sankaran, C. A. Zorman, and P. X.-L. Feng, "Tuning optical signatures of single- and few-layer MoS₂ by blown-bubble bulge straining up to fracture," *Nano Lett.* **17**, 4568 (2017).
- ⁷⁶Y. Sun, J. Pan, Z. Zhang, K. Zhang, J. Liang, W. Wang, Z. Yuan, Y. Hao, B. Wang, J. Wang, Y. Wu, J. Zheng, L. Jiao, S. Zhou, K. Liu, C. Cheng, W. Duan, Y. Xu, Q. Yan, and K. Liu, "Elastic properties and fracture behaviors of biaxially deformed, polymorphic MoTe₂," *Nano Lett.* **19**, 761 (2019).
- ⁷⁷J. Tao, W. Shen, S. Wu, L. Liu, Z. Feng, C. Wang, C. Hu, P. Yao, H. Zhang, W. Pang, X. Duan, J. Liu, C. Zhou, and D. Zhang, "Mechanical and electrical anisotropy of few-layer black phosphorus," *ACS Nano* **9**, 11362 (2015).
- ⁷⁸A. Castellanos-Gomez, M. Poot, G. A. Steele, H. S. J. van der Zant, N. Agrait, and G. Rubio-Bollinger, "Elastic properties of freely suspended MoS₂ nano-sheets," *Adv. Mater.* **24**, 772 (2012).
- ⁷⁹A. Falin, Q. Cai, E. J. Santos, D. Scullion, D. Qian, R. Zhang, Z. Yang, S. Huang, K. Watanabe, T. Taniguchi, M. R. Barnett, Y. Chen, R. S. Ruoff, and L. H. Li, "Mechanical properties of atomically thin boron nitride and the role of interlayer interactions," *Nat. Commun.* **8**, 15815 (2017).
- ⁸⁰S. Manzeli, A. Allain, A. Ghadimi, and A. Kis, "Piezoresistivity and strain-induced band gap tuning in atomically thin MoS₂," *Nano Lett.* **15**, 5330 (2015).
- ⁸¹H. Moon, G. Grosso, C. Chakraborty, C. Peng, T. Taniguchi, K. Watanabe, and D. Englund, "Dynamic exciton funneling by local strain control in a monolayer semiconductor," *Nano Lett.* **20**, 6791 (2020).
- ⁸²F. A. Benimetskiy, V. A. Sharov, P. A. Alekseev, V. Kravtsov, K. B. Agapev, I. S. Sinev, I. S. Mukhin, A. Catanzaro, R. G. Polozkov, E. M. Alexeev, A. I. Tartakovskii, A. K. Samusev, M. S. Skolnick, D. N. Krizhanovskii, I. A. Shelykh, and I. V. Iorsh, "Measurement of local optomechanical properties of a direct bandgap 2D semiconductor," *APL Mater.* **7**, 101126 (2019).
- ⁸³M. R. Rosenberger, C. K. Dass, H.-J. Chuang, S. V. Sivaram, K. M. McCreary, J. R. Hendrickson, and B. T. Jonker, "Quantum calligraphy: Writing single-photon emitters in a two-dimensional materials platform," *ACS Nano* **13**, 904–912 (2019).
- ⁸⁴X. Liu, A. K. Sachan, S. T. Howell, A. Conde-Rubio, A. W. Knoll, G. Boero, R. Zenobi, and J. Brugger, "Thermomechanical nanostraining of two-dimensional materials," *Nano Lett.* **20**, 8250–8257 (2020).
- ⁸⁵N. Mendelson, M. Doherty, M. Toth, I. Aharonovich, and T. T. Tran, "Strain-induced modification of the optical characteristics of quantum emitters in hexagonal boron nitride," *Adv. Mater.* **32**, 1908316 (2020).
- ⁸⁶F. Ding, H. Ji, Y. Chen, A. Herklotz, K. Dörr, Y. Mei, A. Rastelli, and O. G. Schmidt, "Stretchable graphene: A close look at fundamental parameters through biaxial straining," *Nano Lett.* **10**, 3453 (2010).
- ⁸⁷Y. Y. Hui, X. Liu, W. Jie, N. Y. Chan, J. Hao, Y.-T. Hsu, L.-J. Li, W. Guo, and S. P. Lau, "Exceptional tunability of band energy in a compressively strained trilayer MoS₂ sheet," *ACS Nano* **7**, 7126 (2013).
- ⁸⁸O. Iff, D. Tedeschi, J. Martín-Sánchez, M. Moczala-Dusanowska, S. Tongay, K. Yumigeta, J. Taboada-Gutiérrez, M. Savaresi, A. Rastelli, P. Alonso-González, S. Höflich, R. Trotta, and C. Schneider, "Strain-tunable single photon sources in WSe₂ monolayers," *Nano Lett.* **19**, 6931 (2019).
- ⁸⁹T. Jiang, R. Huang, and Y. Zhu, "Interfacial sliding and buckling of monolayer graphene on a stretchable substrate," *Adv. Funct. Mater.* **24**, 396 (2014).
- ⁹⁰Q. Zhang, Z. Chang, G. Xu, Z. Wang, Y. Zhang, Z.-Q. Xu, S. Chen, Q. Bao, J. Z. Liu, Y.-W. Mai, W. Duan, M. S. Fuhrer, and C. Zheng, "Strain relaxation of monolayer WS₂ on plastic substrate," *Adv. Funct. Mater.* **26**, 8707 (2016).
- ⁹¹Z. Liu, M. Amani, S. Najmaei, Q. Xu, X. Zou, W. Zhou, T. Yu, C. Qiu, A. G. Birdwell, F. J. Crowne, R. Vajtai, B. I. Yakobson, Z. Xia, M. Dubey, P. M. Ajayan, and J. Lou, "Strain and structure heterogeneity in WS₂ atomic layers grown by chemical vapour deposition," *Nat. Commun.* **5**, 5246 (2014).
- ⁹²Y. K. Ryu, F. Carrascoso, R. López-Nebreda, N. Agrait, R. Frisenda, and A. Castellanos-Gomez, "Microheater actuators as a versatile platform for strain engineering in 2D materials," *Nano Lett.* **20**, 5339 (2020).
- ⁹³A. Castellanos-Gomez, R. Roldán, E. Cappelluti, M. Buscema, F. Guinea, H. S. J. van der Zant, and G. A. Steele, "Local strain engineering in atomically thin MoS₂," *Nano Lett.* **13**, 5361 (2013).
- ⁹⁴C. Rice, R. J. Young, R. Zan, U. Bangert, D. Wolverson, T. Georgiou, R. Jalil, and K. S. Novoselov, "Raman-scattering measurements and first-principles calculations of strain-induced phonon shifts in monolayer MoS₂," *Phys. Rev. B* **87**, 081307(R) (2013).
- ⁹⁵C. Androulidakis, E. N. Koukaras, M. Poss, K. Papageorgis, C. Galiotis, and S. Tawfik, "Strained hexagonal boron nitride: Phonon shift and Grüneisen parameter," *Phys. Rev. B* **97**, 241414(R) (2018).
- ⁹⁶A. P. John, A. Thenapparambil, and M. Thalakkulam, "Strain-engineering the Schottky barrier and electrical transport on MoS₂," *Nanotechnol.* **31**, 275703 (2020).
- ⁹⁷Y. Liu, X. Li, Y. Guo, T. Yang, K. Chen, C. Lin, J. Wei, Q. Liu, Y. Lu, L. Dong, and C. Shan, "Modulation on the electronic properties and band gap of layered ReSe₂ via strain engineering," *J. Alloys Compd.* **827**, 154364 (2020).
- ⁹⁸Y. Li, T. Wang, M. Wu, T. Cao, Y. Chen, R. Sankar, R. K. Ulaganathan, F. Chou, C. Wetzel, C.-Y. Xu, S. G. Louie, and S.-F. Shi, "Ultrasensitive tunability of the direct bandgap of 2D InSe flakes via strain engineering," *2D Mater.* **5**, 021002 (2018).
- ⁹⁹C. Song, F. Fan, N. Xuan, S. Huang, C. Wang, G. Zhang, F. Wang, Q. Xing, Y. Lei, Z. Sun, H. Wu, and H. Yan, "Drastic enhancement of the Raman intensity in few-layer InSe by uniaxial strain," *Phys. Rev. B* **99**, 195414 (2019).

- ¹⁰⁰J. Zhou, Y. Wu, H. Wang, Z. Wu, X. Li, W. Yang, C. Ke, S. Lu, C. Zhang, and J. Kang, "Strain manipulation of the polarized optical response in two-dimensional GaSe layers," *Nanoscale* **12**, 4069–4076 (2020).
- ¹⁰¹Y. Li, Z. Hu, S. Lin, S. K. Lai, W. Ji, and S. P. Lau, "Giant anisotropic Raman response of encapsulated ultrathin black phosphorus by uniaxial strain," *Adv. Funct. Mater.* **27**, 1600986 (2017).
- ¹⁰²G. Zhang, S. Huang, A. Chaves, C. Song, V. O. Özcelik, T. Low, and H. Yan, "Infrared fingerprints of few-layer black phosphorus," *Nat. Commun.* **8**, 14701 (2017).
- ¹⁰³J. Quereda, P. San-Jose, V. Parente, L. Vaquero-Garzon, A. J. Molina-Mendoza, N. Agrait, G. Rubio-Bollinger, F. Guinea, R. Roldán, and A. Castellanos-Gomez, "Strong modulation of optical properties in black phosphorus through strain-engineered rippling," *Nano Lett.* **16**, 2931–2937 (2016).
- ¹⁰⁴Q. Cai, D. Scullion, A. Falin, K. Watanabe, T. Taniguchi, Y. Chen, E. J. G. Santos, and L. H. Li, "Raman signature and phonon dispersion of atomically thin boron nitride," *Nanoscale* **9**, 3059 (2017).
- ¹⁰⁵Q. Zhao, T. Wang, R. Frisenda, and A. Castellanos-Gomez, "Giant piezoresistive effect and strong bandgap tunability in ultrathin InSe upon biaxial strain," *Adv. Sci.* **7**, 2001645 (2020).
- ¹⁰⁶S. Huang, G. Zhang, F. Fan, C. Song, F. Wang, Q. Xing, C. Wang, H. Wu, and H. Yan, "Strain-tunable van der Waals interactions in few-layer black phosphorus," *Nat. Commun.* **10**, 2447 (2019).
- ¹⁰⁷C. Lee, X. Wei, J. W. Kysar, and J. Hone, "Measurement of the elastic properties and intrinsic strength of monolayer graphene," *Science* **321**, 385 (2008).
- ¹⁰⁸H. Yan, C. Vajner, M. Kuhlman, L. Guo, L. Li, P. T. Araujo, and H.-T. Wang, "Elastic behavior of Bi₂Se₃ 2D nanosheets grown by van der Waals epitaxy," *Appl. Phys. Lett.* **109**, 032103 (2016).
- ¹⁰⁹L. Guo, H. Yan, Q. Moore, M. Buettner, J. Song, L. Li, P. T. Araujo, and H.-T. Wang, "Elastic properties of van der Waals epitaxy grown bismuth telluride 2D nanosheets," *Nanoscale* **7**, 11915 (2015).
- ¹¹⁰A. V. Tyurnina, D. A. Bandurin, E. Khestanova, V. G. Kravets, M. Koperski, F. Guinea, A. N. Grigorenko, A. K. Geim, and I. V. Grigorieva, "Strained bubbles in van der Waals heterostructures as local emitters of photoluminescence with adjustable wavelength," *ACS Photonics* **6**, 516–524 (2019).
- ¹¹¹H. Luo, X. Li, Y. Zhao, R. Yang, L. Bao, Y. Hao, Y.-n. Gao, N. N. Shi, Y. Guo, G. Liu, L. Zhao, Q. Wang, Z. Zhang, G. Zhang, J. Sun, Y. Huang, H. Gao, and X. Zhou, "Simultaneous generation of direct- and indirect-gap photoluminescence in multilayer MoS₂ bubbles," *Phys. Rev. Mater.* **4**, 074006 (2020).
- ¹¹²D. Tedeschi, E. Blundo, M. Felici, G. Pettinari, B. Liu, T. Yildirim, E. Petroni, C. Zhang, Y. Zhu, S. Sennato, Y. Lu, and A. Polimeni, "Controlled micro/nanodome formation in proton-irradiated bulk transition-metal dichalcogenides," *Adv. Mater.* **31**, 1903795 (2019).
- ¹¹³E. Blundo, C. Di Giorgio, G. Pettinari, T. Yildirim, M. Felici, Y. Lu, F. Bobba, and A. Polimeni, "Engineered creation of periodic giant, non-uniform strains in MoS₂ monolayers," *Adv. Mat. Interfaces* **7**, 2000621 (2020).
- ¹¹⁴C. Di Giorgio, E. Blundo, G. Pettinari, M. Felici, Y. Lu, A. M. Cucolo, A. Polimeni, and F. Bobba, "Nanoscale measurements of elastic properties and hydrostatic pressure in H₂-bulged MoS₂ membranes," *Adv. Mat. Interfaces* **7**, 2001024 (2020).
- ¹¹⁵N. Levy, S. A. Burke, K. L. Meaker, M. Panlasigui, A. Zettl, F. Guinea, A. H. C. Neto, and M. F. Crommie, "Strain-induced pseudo-magnetic fields greater than 300 Tesla in graphene nanobubbles," *Science* **329**, 544 (2010).
- ¹¹⁶F. Guinea, M. I. Katsnelson, and A. K. Geim, "Energy gaps and a zero-field quantum Hall effect in graphene by strain engineering," *Nat. Phys.* **6**, 30 (2010).
- ¹¹⁷H. Ochoa, R. Zarzuela, and Y. Tserkovnyak, "Emergent gauge fields from curvature in single layers of transition-metal dichalcogenides," *Phys. Rev. Lett.* **118**, 026801–026805 (2017).
- ¹¹⁸M. Settnes, S. R. Power, M. Brandbyge, and A.-P. Jauho, "Graphene nanobubbles as valley filters and beam splitters," *Phys. Rev. Lett.* **117**, 276801–276805 (2016).
- ¹¹⁹M. A. Cazalilla, H. Ochoa, and F. Guinea, "Quantum spin Hall effect in two-dimensional crystals of transition-metal dichalcogenides," *Phys. Rev. Lett.* **113**, 077201 (2014).
- ¹²⁰H. W. Kim, W. Ko, J. Ku, I. Jeon, D. Kim, H. Kwon, Y. Oh, S. Ryu, Y. Kuk, S. W. Hwang, and H. Suh, "Nanoscale control of phonon excitations in graphene," *Nat. Commun.* **6**, 7528 (2015).
- ¹²¹R. Larciprete, S. Colonna, F. Ronci, R. Flammini, P. Lacovig, N. Apostol, A. Politano, P. Feulner, D. Menzel, and S. Lizzit, "Self-assembly of graphene nanoblisters sealed to a bare metal surface," *Nano Lett.* **16**, 1808–1817 (2016).
- ¹²²G. D. Shepard, O. A. Ajayi, X. Li, X.-Y. Zhu, J. Hone, and S. Strauf, "Nanobubble induced formation of quantum emitters in monolayer semiconductors," *2D Mater.* **4**, 021019 (2017).
- ¹²³A. Srivastava, M. Sidler, A. V. Allain, D. S. Lembke, A. Kis, and A. Imamoglu, "Optically active quantum dots in monolayer WSe₂," *Nat. Nanotech.* **10**, 491–496 (2015).
- ¹²⁴M. Koperski, K. Nogajewski, A. Arora, V. Cherkov, P. Mallet, J. Y. Veuillen, J. Marcus, P. Kossacki, and M. Potemski, "Single photon emitters in exfoliated WSe₂ structures," *Nat. Nanotech.* **10**, 503–506 (2015).
- ¹²⁵C. M. Chow, H. Yu, A. M. Jones, J. Yan, D. G. Mandrus, T. Taniguchi, K. Watanabe, W. Yao, and X. Xu, "Unusual exciton-phonon interactions at van der Waals engineered interfaces," *Nano Lett.* **17**, 1194–1199 (2017).
- ¹²⁶S. Kumar, A. Kaczmarczyk, and B. D. Gerardot, "Strain-induced spatial and spectral isolation of quantum emitters in mono- and bilayer WSe₂," *Nano Lett.* **15**, 7567–7573 (2015).
- ¹²⁷L. Yu, M. Deng, J. L. Zhang, S. Borghardt, B. Kardynal, J. Vučković, and T. F. Heinz, "Site-controlled quantum emitters in monolayer MoSe₂," *Nano Lett.* **21**, 2376 (2021).
- ¹²⁸T. P. Darlington, C. Carmesin, M. Florian, E. Yanev, O. Ajayi, J. Ardelean, D. A. Rhodes, A. Ghiotto, A. Krayer, K. Watanabe, T. Taniguchi, J. W. Kysar, A. N. Pasupathy, J. C. Hone, F. Jahnke, N. J. Borys, and P. J. Schuck, "Imaging strain-localized excitons in nanoscale bubbles of monolayer WSe₂ at room temperature," *Nat. Nanotech.* **119**, 087401–087407 (2020).
- ¹²⁹J. Feng, X. Qian, C.-W. Huang, and J. Li, "Strain-engineered artificial atom as a broad-spectrum solar energy funnel," *Nat. Photon.* **6**, 866 (2012).
- ¹³⁰A. V. Kretinin, Y. Cao, J. S. Tu, G. L. Yu, R. Jalil, K. S. Novoselov, S. J. Haigh, A. Gholinia, A. Mishchenko, M. Lozada, T. Georgiou, C. R. Woods, F. Withers, P. Blake, G. Eda, A. Wirsig, C. Hucho, K. Watanabe, T. Taniguchi, A. K. Geim, and R. V. Gorbachev, "Electronic properties of graphene encapsulated with different two-dimensional atomic crystals," *Nano Lett.* **14**, 3270–3276 (2014).
- ¹³¹E. Khestanova, F. Guinea, L. Fumagalli, A. Geim, and I. Grigorieva, "Universal shape and pressure inside bubbles appearing in van der Waals heterostructures," *Nat. Commun.* **7**, 12587 (2016).
- ¹³²K. Yue, W. Gao, R. Huang, and K. M. Liechti, "Analytical methods for the mechanics of graphene bubbles," *J. Appl. Phys.* **112**, 083512 (2012).
- ¹³³Y. Huang, E. Sutter, N. N. Shi, J. Zheng, T. Yang, D. Englund, H.-J. Gao, and P. Sutter, "Reliable exfoliation of large-area high-quality flakes of graphene and other two-dimensional materials," *ACS Nano* **9**, 10612–10620 (2015).
- ¹³⁴E. Blundo, M. Felici, T. Yildirim, G. Pettinari, D. Tedeschi, A. Miriametro, B. Liu, W. Ma, Y. Lu, and A. Polimeni, "Evidence of the direct-to-indirect band gap transition in strained two-dimensional WS₂ and MoS₂," *Phys. Rev. Res.* **2**, 012024(R) (2020).
- ¹³⁵M. Seel and R. Pandey, "Proton and hydrogen transport through two-dimensional monolayers," *2D Mater.* **3**, 025004 (2016).
- ¹³⁶L. He, H. Wang, L. Chen, X. Wang, H. Xie, C. Jiang, C. Li, K. Elibol, J. Meyer, K. Watanabe, T. Taniguchi, Z. Wu, W. Wang, Z. Ni, X. Miao, C. Zhang, D. Zhang, H. Wang, and X. Xie, "Isolating hydrogen in hexagonal boron nitride bubbles by a plasma treatment," *Nat. Commun.* **10**, 2815 (2019).
- ¹³⁷D. C. Elias, R. R. Nair, T. M. G. Mohiuddin, S. V. Morozov, P. Blake, M. P. Halsall, A. C. Ferrari, D. W. Boukhvalov, M. I. Katsnelson, A. K. Geim, and K. S. Novoselov, "Control of graphene's properties by reversible hydrogenation: Evidence for graphane," *Science* **323**, 610 (2009).
- ¹³⁸M. M. S. Abdelnabi, E. Blundo, M. G. Betti, G. Cavoto, E. Placidi, A. Polimeni, A. Ruocco, K. Hu, Y. Ito, and C. Mariani, "Towards free-standing graphane: Atomic hydrogen and deuterium bonding to nano-porous graphene," *Nanotechnol.* **32**, 035707 (2021).
- ¹³⁹M. M. S. Abdelnabi, C. Izzo, E. Blundo, M. G. Betti, M. Sbroscia, G. Di Bella, G. Cavoto, A. Polimeni, I. García-Cortés, I. Rucandio, A. Moróño, K. Hu, Y. Ito, and C. Mariani, "Deuterium adsorption on free-standing graphene," *Nanomaterials* **11**, 130 (2021).
- ¹⁴⁰E. Stolyarova, D. Stolyarov, K. Bolotin, S. Ryu, L. Liu, K. T. Rim, M. Klima, M. Hybertsen, I. Pogorelsky, I. Pavlishin, K. Kusche, J. Hone, P. Kim, H. L.

- Stormer, V. Yakimenko, and G. Flynn, "Observation of graphene bubbles and effective mass transport under graphene films," *Nano Lett.* **9**, 332 (2009).
- ¹⁴¹P. Jia, W. Chen, J. Qiao, M. Zhang, X. Zheng, Z. Xue, R. Liang, C. Tian, L. He, Z. Di, and X. Wang, "Programmable graphene nanobubbles with three-fold symmetric pseudo-magnetic fields," *Nat. Commun.* **10**, 046801 (2019).
- ¹⁴²A. R. Goñi and K. Syassen, "Semiconductors and semimetals," in *Optical Properties of Semiconductors under Pressure*, 1st ed. (Academic Press, San Diego, 1998), Vol. 54, p. 247.
- ¹⁴³G. Pettinari, A. Polimeni, F. Masia, R. Trotta, M. Felici, M. Capizzi, T. Niebling, W. Stolz, and P. J. Klar, "Electron mass in dilute nitrides and its anomalous dependence on hydrostatic pressure," *Phys. Rev. Lett.* **98**, 146402 (2007).
- ¹⁴⁴B. Li, C. Ji, W. Yang, J. Wang, K. Yang, R. Xu, W. Liu, Z. Cai, J. Chen, and H. Kwang Mao, "Diamond anvil cell behavior up to 4 Mbar," *Proc. Natl. Acad. Sci. U. S. A.* **115**, 1713 (2018).
- ¹⁴⁵Q. Li, L. Sui, G. Niu, J. Jiang, Y. Zhang, G. Wu, M. Jin, and K. Yuan, "Pressure manipulation of interlayer interactions and ultrafast carrier dynamics in few-layer MoS₂," *J. Phys. Chem.* **124**, 11183 (2020).
- ¹⁴⁶A. P. Nayak, S. Bhattacharyya, J. Zhu, J. Liu, X. Wu, T. Pandey, C. Jin, A. K. Singh, D. Akinwande, and J.-F. Lin, "Pressure-induced semiconducting to metallic transition in multilayered molybdenum disulphide," *Nat. Commun.* **5**, 3731 (2014).
- ¹⁴⁷Z.-H. Chi, X.-M. Zhao, H. Zhang, A. F. Goncharov, S. S. Lobanov, T. Kagayama, M. Sakata, and X.-J. Chen, "Pressure-induced metallization of molybdenum disulfide," *Phys. Rev. Lett.* **113**, 036802 (2014).
- ¹⁴⁸Y. Zhuang, L. Dai, L. Wu, H. Li, H. Hu, K. Liu, L. Yang, and C. Pu, "Pressure-induced permanent metallization with reversible structural transition in molybdenum disulfide," *Appl. Phys. Lett.* **110**, 122103 (2017).
- ¹⁴⁹X. Wang, X. Chen, Y. Zhou, C. Park, C. An, Y. Zhou, R. Zhang, C. Gu, W. Yang, and Z. Yang, "Pressure-induced iso-structural phase transition and metallization in WSe₂," *Sci. Rep.* **7**, 46694 (2017).
- ¹⁵⁰L. Yang, L. Dai, H. Li, H. Hu, K. Liu, C. Pu, M. Hong, and P. Liu, "Pressure-induced metallization in MoSe₂ under different pressure condition," *RSC Adv.* **9**, 5794 (2019).
- ¹⁵¹U. Schwarz, D. Olguin, A. Cantarero, M. Hanfland, and K. Syassen, "Effect of pressure on the structural properties and electronic band structure of GaSe," *Phys. Status Solidi B* **244**, 244 (2007).
- ¹⁵²P. G. Naumov, M. A. ElGhazali, H. Mirhosseini, V. Süß, E. Morosan, C. Felser, and S. A. Medvedev, "Pressure-induced metallization in layered ReSe₂," *J. Phys.: Condens. Matter* **30**, 035401 (2018).
- ¹⁵³Y. Zhou, B. Zhang, X. Chen, C. Gu, C. An, Y. Zhou, Y. Y. K. Cai, C. Chen, H. Wu, R. Zhang, C. Park, Y. Xiong, X. Zhang, K. Wang, and Z. Yang, "Pressure-induced metallization and robust superconductivity in pristine 1T-SnSe₂," *Adv. Electron. Mater.* **4**, 1800155 (2018).
- ¹⁵⁴D. Errandonea, D. Martínez-García, A. Segura, A. Chevy, G. Tobias, E. Canadell, and P. Ordejón, "High-pressure, high-temperature phase diagram of InSe: A comprehensive study of the electronic and structural properties of the monoclinic phase of InSe under high pressure," *Phys. Rev. B* **73**, 235202 (2006).
- ¹⁵⁵A. Francisco-López, B. Han, D. Lagarde, X. Marie, B. Urbaszek, C. Robert, and A. R. Goñi, "On the impact of the stress situation on the optical properties of WSe₂ monolayers under high pressure," *Papers Phys.* **11**, 110005 (2019).
- ¹⁵⁶X. Cheng, Y. Li, J. Shang, C. Hu, Y. Ren, M. Liu, and Z. Qi, "Thickness-dependent phase transition and optical behavior of MoS₂ films under high pressure," *Nano Res.* **11**, 855 (2018).
- ¹⁵⁷X. Fu, F. Li, J.-F. Lin, Y. Gong, X. Huang, Y. Huang, B. Han, Q. Zhou, and T. Cui, "Pressure-dependent light emission of charged and neutral excitons in monolayer MoSe₂," *J. Phys. Chem. Lett.* **8**, 3556 (2017).
- ¹⁵⁸B. P. Nayak, T. Pandey, D. Voiry, J. Liu, S. T. Moran, A. Sharma, C. Tan, C.-H. Chen, L.-J. Li, M. Chhowalla, J.-F. Lin, A. K. Singh, and D. Akinwande, "Pressure-dependent optical and vibrational properties of monolayer molybdenum disulfide," *Nano Lett.* **15**, 346 (2015).
- ¹⁵⁹B. Han, F. Li, L. Li, X. Huang, Y. Gong, X. Fu, H. Gao, Q. Zhou, and T. Cui, "Correlatively dependent lattice and electronic structural evolutions in compressed monolayer tungsten disulfide," *J. Phys. Chem. Lett.* **8**, 941 (2017).
- ¹⁶⁰R. S. Alencar, K. D. A. Saboia, D. Machon, G. Montagnac, V. Meunier, O. P. Ferreira, A. SanMiguel, and A. G. S. Filho, "Atomic-layer MoS₂ under high pressure: Bimodal adhesion and biaxial strain effects," *Phys. Rev. Mater.* **1**, 024002 (2017).
- ¹⁶¹H. Jiang, L. Zheng, Z. Liu, and X. Wang, "Two-dimensional materials: From mechanical properties to flexible mechanical sensors," *InfoMat* **2**, 1077 (2020).
- ¹⁶²J.-S. Kim, R. Ahmad, T. Pandey, A. Rai, S. Feng, J. Yang, Z. Lin, M. Terrones, S. K. Banerjee, A. K. Singh, D. Akinwande, and J.-F. Lin, "Towards band structure and band offset engineering of monolayer Mo_{1-x}W_xS₂ via strain," *2D Mater.* **5**, 015008 (2018).
- ¹⁶³P. Chaikin and T. Lubensky, *Principles of Condensed Matter Physics* (Cambridge University Press, 1995).
- ¹⁶⁴S. Timoshenko and S. Woinowsky-Krieger, *Theory of Plates and Shells* (Mc Graw Hill, 2010).
- ¹⁶⁵P. Wang, W. Gao, Z. Cao, K. M. Liechti, and R. Huang, "Numerical analysis of circular graphene bubbles," *J. Appl. Mech.* **80**, 040905 (2013).
- ¹⁶⁶T. P. Darlington, A. Krayev, V. Venkatesh, R. Saxena, J. W. Kysar, N. J. Borys, D. Jariwala, and P. J. Schuck, "Facile and quantitative estimation of strain in nanobubbles with arbitrary symmetry in 2D semiconductors verified using hyperspectral nano-optical imaging," *J. Chem. Phys.* **153**, 024702 (2020).
- ¹⁶⁷S. K. Jain, V. Juričić, and G. T. Barkema, "Probing the shape of a graphene nanobubble," *Phys. Chem. Chem. Phys.* **19**, 7465 (2017).
- ¹⁶⁸H. Rostami, F. Guinea, M. Polini, and R. Roldán, "Piezoelectricity and valley Chern number in inhomogeneous hexagonal 2D crystals," *NPJ 2D Mater. Appl.* **2**, 51 (2018).
- ¹⁶⁹A. Jain, S. P. Ong, G. Hautier, W. Chen, W. D. Richards, S. Dacek, S. Cholia, D. Gunter, D. Skinner, G. Ceder, and K. A. Persson, "Commentary: The materials project: A materials genome approach to accelerating materials innovation," *APL Mater.* **1**, 011002 (2013).
- ¹⁷⁰M. de Jong, W. Chen, T. Angsten, A. Jain, R. Notestine, A. Gamst, M. Sluiter, C. K. Ande, S. van der Zwaag, J. J. Plata, C. Toher, S. Curtarolo, G. Ceder, K. A. Persson, and M. Asta, "Charting the complete elastic properties of inorganic crystalline compounds," *Sci. Data* **2**, 150009 (2015).
- ¹⁷¹M. M. Alyörük, Y. Aierken, D. Çakır, F. M. Peeters, and C. Sevik, "Promising piezoelectric performance of single layer transition metal dichalcogenides and dioxides," *J. Phys. Chem. C* **119**, 23231 (2015).
- ¹⁷²S. Appalakondaiah, G. Vaitheeswaran, A. Pradesh, S. Lebégue, N. E. Christensen, and A. Svane, "Effect of van der Waals interactions on the structural and elastic properties of black phosphorus," *Phys. Rev. B* **86**, 035105 (2012).
- ¹⁷³J.-W. Jiang and H. Park, "Negative poisson's ratio in single-layer black phosphorus," *Nat. Commun.* **5**, 4727 (2014).
- ¹⁷⁴W. B. Fichter, "Some solutions for the large deflections of uniformly loaded circular membranes," NASA Tech. Paper **3658**, 1 (1997).
- ¹⁷⁵P. Johari and V. B. Shenoy, "Tuning the electronic properties of semiconducting transition metal dichalcogenides by applying mechanical strains," *ACS Nano* **6**, 5449 (2012).
- ¹⁷⁶Y. Sun, S. E. Thomson, and T. Nishida, *Strain Effect in Semiconductors: Theory and Device Applications* (Springer, New York, 2010), Chap. 2.
- ¹⁷⁷P. Zhilyaev, E. Iakovlev, and I. Akhatov, "Liquid-gas phase transition of air inside graphene nanobubbles on the graphite substrate," *Nanotechnol.* **30**, 125701 (2019).
- ¹⁷⁸T. F. Aslyamov, E. S. Iakovlev, I. S. Akhatov, and P. A. Zhilyaev, "Model of graphene nanobubble: Combining classical density functional and elasticity theories," *J. Chem. Phys.* **152**, 054705 (2020).
- ¹⁷⁹F. Guinea, M. Katsnelson, and M. Vozmediano, "Midgap states and charge inhomogeneities in corrugated graphene," *Phys. Rev. B* **77**, 075422 (2008).
- ¹⁸⁰M. Vozmediano, M. Katsnelson, and F. Guinea, "Gauge fields in graphene," *Phys. Rep.* **496**, 109 (2010).
- ¹⁸¹We neglect here spin-orbit coupling and bandgap opening at the edges of finite-size systems.
- ¹⁸²A. Luican, G. Li, and E. Y. Andrei, "Quantized Landau level spectrum and its density dependence in graphene," *Phys. Rev. B* **83**, 041405 (2011).
- ¹⁸³K. S. Novoselov, A. K. Geim, S. V. Morozov, D. Jiang, M. I. Katsnelson, I. V. Grigorieva, S. V. Dubonos, and A. A. Firsov, "Two-dimensional gas of massless Dirac fermions in graphene," *Nature* **438**, 197 (2005).
- ¹⁸⁴A. H. Castro Neto, F. Guinea, N. M. R. Peres, K. S. Novoselov, and A. K. Geim, "The electronic properties of graphene," *Rev. Mod. Phys.* **81**, 109 (2009).

- ¹⁸⁵The opening of a gap at large uniaxial strain in some first-principle calculations was pointed out in Ref. ¹⁸⁹ to be not strictly connected to the merging of the K, K' point, but rather to the implicit breaking of the sublattice equivalency.
- ¹⁸⁶V. M. Pereira, A. H. Castro Neto, and N. M. R. Peres, "Tight-binding approach to uniaxial strain in graphene," *Phys. Rev. B* **80**, 045401 (2009).
- ¹⁸⁷R. M. Ribeiro, V. M. Pereira, N. M. R. Peres, P. R. Briddon, and A. H. C. Neto, "Strained graphene: Tight-binding and density functional calculations," *New J. Phys.* **11**, 115002 (2009).
- ¹⁸⁸S.-M. Choi, S.-H. Jhi, and Y.-W. Son, "Effects of strain on electronic properties of graphene," *Phys. Rev. B* **81**, 081407 (2010).
- ¹⁸⁹I. Y. Sahalianov, T. M. Radchenko, V. A. Tatarenko, G. Cuniberti, and Y. I. Prylutskyy, "Straintronics in graphene: Extra large electronic band gap induced by tensile and shear strains," *J. Appl. Phys.* **126**, 054302 (2019).
- ¹⁹⁰A. Sharma, V. Kotov, and A. Castro Neto, "Interacting anisotropic Dirac fermions in strained graphene and related systems," [arXiv:1206.5427](https://arxiv.org/abs/1206.5427) (2012).
- ¹⁹¹H. Rostami and R. Asgari, "Electronic ground-state properties of strained graphene," *Phys. Rev. B* **86**, 155435 (2012).
- ¹⁹²F. Liu, P. Ming, and J. Li, "Ab initio calculation of ideal strength and phonon instability of graphene under tension," *Phys. Rev. B* **76**, 064120 (2007).
- ¹⁹³E. V. Castro, K. S. Novoselov, S. V. Morozov, N. M. R. Peres, J. M. B. L. dos Santos, J. Nilsson, F. Guinea, A. K. Geim, and A. H. C. Neto, "Biased bilayer graphene: Semiconductor with a gap tunable by the electric field effect," *Phys. Rev. Lett.* **99**, 216802 (2007).
- ¹⁹⁴E. McCann and M. Koshino, "The electronic properties of bilayer graphene," *Rep. Prog. Phys.* **76**, 056503 (2013).
- ¹⁹⁵S.-M. Choi, S.-H. Jhi, and Y.-W. Son, "Controlling Energy Gap of Bilayer Graphene by Strain," *Nano Lett.* **10**, 3486–3489 (2010).
- ¹⁹⁶J. A. Crosse, "Strain-dependent conductivity in biased bilayer graphene," *Phys. Rev. B* **90**, 235403 (2014).
- ¹⁹⁷S. Lebègue and O. Eriksson, "Electronic structure of two-dimensional crystals from ab initio theory," *Phys. Rev. B* **79**, 115409 (2009).
- ¹⁹⁸K. F. Mak, C. Lee, J. Hone, J. Shan, and T. F. Heinz, "Atomically thin MoS_2 : A new direct-gap semiconductor," *Phys. Rev. Lett.* **105**, 136805 (2010).
- ¹⁹⁹A. Splendiani, L. Sun, Y. Zhang, T. Li, J. Kim, C.-Y. Chim, G. Galli, and F. Wang, "Emerging photoluminescence in monolayer MoS_2 ," *Nano Lett.* **10**, 1271 (2010).
- ²⁰⁰H. Yuan, Z. Liu, G. Xu, B. Zhou, S. Wu, D. Dumcenco, K. Yan, Y. Zhang, S.-K. Mo, P. Dudin, V. Kandyba, M. Yablonskikh, A. Barinov, Z. Shen, S. Zhang, Y. Huang, X. Xu, Z. Hussain, H. Y. Hwang, Y. Cui, and Y. Chen, "Evolution of the valley position in bulk transition-metal chalcogenides and their monolayer limit," *Nano Lett.* **16**, 4738 (2016).
- ²⁰¹A. Carvalho, R. M. Ribeiro, and A. H. Castro Neto, "Band nesting and the optical response of two-dimensional semiconducting transition metal dichalcogenides," *Phys. Rev. B* **88**, 115205 (2013).
- ²⁰²D. Kozawa, R. Kumar, A. Carvalho, K. Amara, W. Zhao, S. Wang, M. Toh, R. Ribeiro, A. Castro Neto, K. Matsuda, and G. Eda, "Photocarrier relaxation pathway in two-dimensional semiconducting transition metal dichalcogenides," *Nat. Commun.* **5**, 4543 (2014).
- ²⁰³M. Gibertini, F. M. D. Pellegrino, N. Marzari, and M. Polini, "Spin-resolved optical conductivity of two-dimensional group-VIB transition-metal dichalcogenides," *Phys. Rev. B* **90**, 245411 (2014).
- ²⁰⁴M. Bieniek, M. Korkusiński, L. Szulakowska, P. Potasz, I. Ozfidan, and P. Hawrylak, "Band nesting, massive Dirac fermions, and valley Landé and Zeeman effects in transition metal dichalcogenides: A tight-binding model," *Phys. Rev. B* **97**, 085153 (2018).
- ²⁰⁵L. Mennel, V. Smejkal, L. Linhart, J. Burgdörfer, F. Libisch, and T. Mueller, "Band nesting in two-dimensional crystals: An exceptionally sensitive probe of strain," *Nano Lett.* **20**, 4242 (2020).
- ²⁰⁶E. Cappelluti, R. Roldán, J. A. Silva-Guillén, P. Ordejón, and F. Guinea, "Tight-binding model and direct-gap/indirect-gap transition in single-layer and multilayer MoS_2 ," *Phys. Rev. B* **88**, 075409 (2013).
- ²⁰⁷E. Scalise, M. Houssa, G. Pourtois, V. Afanasév, and A. Stesmans, "First-principles study of strained 2D MoS_2 ," *Phys. E: Low-dimensional Syst. Nanostructures* **56**, 416–421 (2014).
- ²⁰⁸W. S. Yun, S. W. Han, S. C. Hong, I. G. Kim, and J. D. Lee, "Thickness and strain effects on electronic structures of transition metal dichalcogenides: 2H- MX_2 semiconductors ($M = \text{Mo}, \text{W}; X = \text{S}, \text{Se}, \text{Te}$)," *Phys. Rev. B* **85**, 033305 (2012).
- ²⁰⁹H. Pan and Y.-W. Zhang, "Tuning the electronic and magnetic properties of MoS_2 nanoribbons by strain engineering," *J. Phys. Chem. C* **116**, 11752–11757 (2012).
- ²¹⁰Q. Zhang, Y. Cheng, L.-Y. Gan, and U. Schwingenschlögl, "Giant valley drifts in uniaxially strained monolayer MoS_2 ," *Phys. Rev. B* **88**, 245447 (2013).
- ²¹¹M. Ghorbani-Asl, S. Borini, A. Kuc, and T. Heine, "Strain-dependent modulation of conductivity in single-layer transition-metal dichalcogenides," *Phys. Rev. B* **87**, 235434 (2013).
- ²¹²H. Shi, H. Pan, Y.-W. Zhang, and B. I. Yakobson, "Quasiparticle band structures and optical properties of strained monolayer MoS_2 and WS_2 ," *Phys. Rev. B* **87**, 155304 (2013).
- ²¹³C.-H. Chang, X. Fan, S.-H. Lin, and J.-L. Kuo, "Orbital analysis of electronic structure and phonon dispersion in MoS_2 , MoSe_2 , WS_2 , and WSe_2 monolayers under strain," *Phys. Rev. B* **88**, 195420 (2013).
- ²¹⁴S. Horzum, H. Sahin, S. Cahangirov, P. Cudazzo, A. Rubio, T. Serin, and F. M. Peeters, "Phonon softening and direct to indirect band gap crossover in strained single-layer MoSe_2 ," *Phys. Rev. B* **87**, 125415 (2013).
- ²¹⁵D. M. Guzman and A. Strachan, "Role of strain on electronic and mechanical response of semiconducting transition-metal dichalcogenide monolayers: An ab-initio study," *J. Appl. Phys.* **115**, 243701 (2014).
- ²¹⁶S. Bhattacharyya, T. Pandey, and A. Singh, "Effect of strain on electronic and thermoelectric properties of few layers to bulk MoS_2 ," *Nanotechnol.* **25**, 465701 (2014).
- ²¹⁷M. Hosseini, M. Elahi, M. Pourfath, and D. Esseni, "Strain induced mobility modulation in single-layer MoS_2 ," *J. Phys. D: Appl. Phys.* **48**, 375104 (2015).
- ²¹⁸B. G. Shin, G. H. Han, S. J. Yun, H. M. Oh, J. J. Bae, Y. J. Song, C. Park, and Y. H. Lee, "Indirect bandgap puddles in monolayer MoS_2 by substrate-induced local strain," *Adv. Mater.* **28**, 9378–9384 (2016).
- ²¹⁹D. J. Trainer, Y. Zhang, F. Bobba, X. Xi, S.-W. Hla, and M. Iavarone, "The effects of atomic-scale strain relaxation on the electronic properties of monolayer MoS_2 ," *ACS Nano* **13**, 8284–8291 (2019).
- ²²⁰C. Zhang, M.-Y. Li, J. Tersoff, Y. Han, Y. Su, L.-J. Li, D. A. Muller, and C.-K. Shih, "Strain distributions and their influence on electronic structures of WSe_2 - MoS_2 laterally strained heterojunctions," *Nat. Nanotech.* **13**, 152–158 (2018).
- ²²¹M. Precner, T. Polaković, Q. Qiao, D. J. Trainer, A. V. Putilov, C. Di Giorgio, I. Cone, Y. Zhu, X. X. Xi, M. Iavarone, and G. Karapetrov, "Evolution of metastable defects and its effect on the electronic properties of MoS_2 films," *Sci. Rep.* **8**, 6724 (2018).
- ²²²Y. L. Fu, Y. Wan, N. Tang, Y. min Ding, J. Gao, J. Yu, H. Guan, K. Zhang, W. Wang, C. Zhang, J. jie Shi, X. Wu, S.-F. Shi, W. Ge, L. Dai, and B. Shen, "K-A crossover transition in the conduction band of monolayer MoS_2 under hydrostatic pressure," *Nanoscale* **8**, 10843 (2016).
- ²²³K. Zollner, P. E. F. Junior, and J. Fabian, "Strain-tunable orbital, spin-orbit, and optical properties of monolayer transition-metal dichalcogenides," *Phys. Rev. B* **100**, 195126 (2019).
- ²²⁴W.-T. Hsu, L.-S. Lu, D. Wang, J.-K. Huang, M.-Y. Li, T.-R. Chang, Y.-C. Chou, Z.-Y. Juang, H.-T. Jeng, L.-J. Li, and W.-H. Chang, "Evidence of indirect gap in monolayer WSe_2 ," *Nat. Commun.* **8**, 929 (2017).
- ²²⁵M. Peña Álvarez, E. del Corro, A. Morales-García, L. Kavan, M. Kalbac, and O. Frank, "Single layer molybdenum disulfide under direct out-of-plane compression: Low-stress band-gap engineering," *Nano Lett.* **15**, 3139–3146 (2015).
- ²²⁶L. Ortenzi, L. Pietronero, and E. Cappelluti, "Zero-point motion and direct-indirect band-gap crossover in layered transition-metal dichalcogenides," *Phys. Rev. B* **98**, 195313 (2018).
- ²²⁷H. Peelaers and C. G. Van de Walle, "Effects of strain on band structure and effective masses in MoS_2 ," *Phys. Rev. B* **86**, 241401 (2012).
- ²²⁸Y. Ge, W. Wan, W. Feng, D. Xiao, and Y. Yao, "Effect of doping and strain modulations on electron transport in monolayer MoS_2 ," *Phys. Rev. B* **90**, 035414 (2014).
- ²²⁹L. Wang, A. Kutana, and B. I. Yakobson, "Many-body and spin-orbit effects on direct-indirect band gap transition of strained monolayer MoS_2 and WS_2 ," *Annalen der Phys.* **526**, L7–L12 (2014).

- ²³⁰H. Rostami, R. Roldán, E. Cappelluti, R. Asgari, and F. Guinea, "Theory of strain in single-layer transition metal dichalcogenides," *Phys. Rev. B* **92**, 195402 (2015).
- ²³¹A. Zilli, M. De Luca, D. Tedeschi, H. A. Fonseca, A. Miriametro, H. H. Tan, C. Jagadish, M. Capizzi, and A. Polimeni, "Temperature dependence of interband transitions in wurtzite InP nanowires," *ACS Nano* **9**, 4277–4287 (2015).
- ²³²M. De Luca, A. Zilli, H. A. Fonseca, S. Mokkapat, A. Miriametro, H. H. Tan, L. M. Smith, C. Jagadish, M. Capizzi, and A. Polimeni, "Polarized light absorption in wurtzite InP nanowire ensembles," *Nano Lett.* **15**, 998–1005 (2015).
- ²³³D. Tedeschi, H. A. Fonseca, E. Blundo, A. Granados del Águila, Y. Guo, H. H. Tan, P. C. M. Christianen, C. Jagadish, A. Polimeni, and M. De Luca, "Hole and electron effective masses in single InP nanowires with a wurtzite-zincblende homojunction," *ACS Nano* **14**, 11613–11622 (2020).
- ²³⁴M. De Luca and A. Polimeni, "Electronic properties of wurtzite-phase InP nanowires determined by optical and magneto-optical spectroscopy," *Appl. Phys. Rev.* **4**, 041102 (2017).
- ²³⁵D. Tedeschi, M. De Luca, A. G. del Águila, Q. Gao, G. Ambrosio, M. Capizzi, H. H. Tan, P. C. M. Christianen, C. Jagadish, and A. Polimeni, "Value and anisotropy of the electron and hole mass in pure wurtzite InP nanowires," *Nano Lett.* **16**, 6213 (2016).
- ²³⁶Z. Jiang, Z. Liu, Y. Li, and W. Duan, "Scaling universality between band gap and binding energy of two-dimensional semiconductors," *Phys. Rev. Lett.* **118**, 266401 (2017).
- ²³⁷G. Wang, A. Chernikov, M. M. Glazov, T. F. Heinz, X. Marie, T. Amand, and B. Urbaszek, "Colloquium: Excitons in atomically thin transition metal dichalcogenides," *Rev. Mod. Phys.* **90**, 021001 (2018).
- ²³⁸J. Dean and D. G. Thomas, "Intrinsic absorption-edge spectrum of gallium phosphide," *Phys. Rev.* **150**, 690 (1966).
- ²³⁹M. Baranowski, P. Plochocka, R. Su, L. Legrand, T. Barisien, F. Bernardot, Q. Xiong, C. Testelin, and M. Chamorro, "Exciton binding energy and effective mass of CsPbCl₃: A magneto-optical study," *Photonics Res.* **8**, A50–55 (2020).
- ²⁴⁰L. Waldecker, A. Raja, M. Rösner, C. Steinke, A. Bostwick, R. J. Koch, C. Jozwiak, T. Taniguchi, K. Watanabe, E. Rotenberg, T. O. Wehling, and T. F. Heinz, "Rigid band shifts in two-dimensional semiconductors through external dielectric screening," *Phys. Rev. Lett.* **123**, 206403 (2019).
- ²⁴¹M. Feierabend, Z. Khatibi, G. Berghäuser, and E. Malic, "Dark exciton based strain sensing in tungsten-based transition metal dichalcogenides," *Phys. Rev. B* **99**, 195454 (2019).
- ²⁴²R. Beams, L. G. Cançado, A. Jorio, A. N. Vamivakas, and L. Novotny, "Tip-enhanced Raman mapping of local strain in graphene," *Nanotechnol.* **26**, 175702 (2015).
- ²⁴³J. Lee, S. J. Yun, C. Seo, K. Cho, T. S. Kim, G. H. An, K. Kang, H. S. Lee, and J. Kim, "Switchable, tunable, and directable exciton funneling in periodically wrinkled WS₂," *Nano Lett.* **21**, 43 (2021).
- ²⁴⁴K. Elibol, B. Bayer, S. Hummel, J. Kotakoski, G. Argentero, and J. Meyer, "Visualising the strain distribution in suspended two-dimensional materials under local deformation," *Sci. Rep.* **6**, 28485 (2016).
- ²⁴⁵K.-D. Park, O. Khatib, V. Kravtsov, G. Clark, X. Xu, and M. B. Raschke, "Hybrid tip-enhanced nanospectroscopy and nanoimaging of monolayer WSe₂ with local strain control," *Nano Lett.* **16**, 2621–2627 (2016).
- ²⁴⁶A. Smiri, T. Amand, and S. Jaziri, "Optical properties of excitons in two-dimensional transition metal dichalcogenide nanobubbles," *J. Chem. Phys.* **154**, 084110 (2021).
- ²⁴⁷P. San-Jose, V. Parente, F. Guinea, R. Roldán, and E. Prada, "Inverse funnel effect of excitons in strained black phosphorus," *Phys. Rev. X* **6**, 031046 (2016).
- ²⁴⁸J. Kern, I. Niehues, P. Tonndorf, R. Schmidt, D. Wigger, R. Schneider, T. Stiehm, S. M. de Vasconcellos, D. E. Reiter, T. Kuhn, and R. Bratschkitsch, "Nanoscale positioning of single-photon emitters in atomically thin WSe₂," *Adv. Mater.* **28**, 7101 (2016).
- ²⁴⁹K. P. Dhakal, S. Roy, H. Jang, X. Chen, W. S. Yun, H. Kim, J. Lee, J. Kim, and J.-H. Ahn, "Local strain induced band gap modulation and photoluminescence enhancement of multilayer transition metal dichalcogenides," *Chem. Mater.* **29**, 5124–5133 (2017).
- ²⁵⁰L. Mennel, M. M. Furchi, S. Wachter, M. Paur, D. K. Polyushkin, and T. Mueller, "Optical imaging of strain in two-dimensional crystals," *Nat. Commun.* **9**, 516 (2018).
- ²⁵¹J. S. Ross, S. Wu, H. Yu, N. J. Ghimire, A. M. Jones, G. Aivazian, J. Yan, D. G. Mandrus, D. Xiao, W. Yao, and X. Xu, "Electrical control of neutral and charged excitons in a monolayer semiconductor," *Nat. Commun.* **4**, 1474 (2013).
- ²⁵²L. Chirrolli, E. Prada, F. Guinea, R. Roldán, and P. San-Jose, "Strain-induced bound states in transition-metal dichalcogenide bubbles," *2D Mater.* **6**, 025010 (2019).
- ²⁵³C. Carmesin, M. Lorke, M. Florian, D. Erben, A. Schulz, T. O. Wehling, and F. Jahnke, "Quantum-dot-like states in molybdenum disulfide nanostructures due to the interplay of local surface wrinkling, strain, and dielectric confinement," *Nano Lett.* **19**, 3182–3186 (2019).
- ²⁵⁴Y. Xu, Z. Shi, X. Shi, K. Zhang, and H. Zhang, "Recent progress in black phosphorus and black-phosphorus-analogue materials: Properties, synthesis and applications," *Nanoscale* **11**, 14491–14527 (2019).
- ²⁵⁵X. Mu, J. Wang, and M. Sun, "Two-dimensional black phosphorus: Physical properties and applications," *Mater. Today Phys.* **8**, 92–111 (2019).
- ²⁵⁶A. Morita, "Semiconducting black phosphorus," *Appl. Phys. A* **39**, 227 (1986).
- ²⁵⁷H. Liu, A. T. Neal, Z. Zhu, Z. Luo, X. Xu, D. Tománek, and P. D. Ye, "Phosphorene: An Unexplored 2D Semiconductor with a High Hole Mobility," *ACS Nano* **8**, 4033–4041 (2014).
- ²⁵⁸L. Liang, J. Wang, W. Lin, B. G. Sumpter, V. Meunier, and M. Pan, "Electronic Bandgap and Edge Reconstruction in Phosphorene Materials," *Nano Lett.* **14**, 6400–6406 (2014).
- ²⁵⁹L. Li, J. Kim, C. Jin, G. Ye, D. Qiu, F. da Jornada, Z. Shi, L. Chen, Z. Zhang, F. Yang, K. Watanabe, T. Taniguchi, W. Ren, S. Louie, X. Chen, Y. Zhang, and F. Wang, "Direct observation of the layer-dependent electronic structure in phosphorene," *Nat. Nanotech.* **12**, 21 (2017).
- ²⁶⁰Y. Cai, Q. Ke, G. Zhang, Y. P. Feng, V. B. Shenoy, and Y.-W. Zhang, "Giant phononic anisotropy and unusual anharmonicity of phosphorene: Interlayer coupling and strain engineering," *Adv. Funct. Mater.* **25**, 2230–2236 (2015).
- ²⁶¹Y. Cai, G. Zhang, and Y.-W. Zhang, "Layer-dependent band alignment and work function of few-layer phosphorene," *Sci. Rep.* **4**, 6677 (2014).
- ²⁶²It should be noticed that different approximations within the framework of first-principle calculations can result in quite different band structures. In spite of this uncertainty, the qualitative trends are very well reproduced independently of the kind of approximation, making *ab-initio* techniques a valid support in investigation.
- ²⁶³V. Tran, R. Soklaski, Y. Liang, and L. Yang, "Layer-controlled band gap and anisotropic excitons in few-layer black phosphorus," *Phys. Rev. B* **89**, 235319 (2014).
- ²⁶⁴A. N. Rudenko and M. I. Katsnelson, "Quasiparticle band structure and tight-binding model for single- and bilayer black phosphorus," *Phys. Rev. B* **89**, 201408 (2014).
- ²⁶⁵S.-i. Narita, S.-i. Terada, S. Mori, K. Muro, Y. Akahama, and S. Endo, "Far-infrared cyclotron resonance absorptions in black phosphorus single crystals," *J. Phys. Soc. Jpn.* **52**, 3544–3553 (1983).
- ²⁶⁶F. Xia, H. Wang, and Y. Jia, "Rediscovering black phosphorus: A unique anisotropic 2D material for optoelectronics and electronics," *Nat. Commun.* **5**, 4458 (2014).
- ²⁶⁷A. S. Rodin, A. Carvalho, and A. H. Castro Neto, "Strain-induced gap modification in black phosphorus," *Phys. Rev. Lett.* **112**, 176801 (2014).
- ²⁶⁸T. Low, A. S. Rodin, A. Carvalho, Y. Jiang, H. Wang, F. Xia, and A. H. Castro Neto, "Tunable optical properties of multilayer black phosphorus thin films," *Phys. Rev. B* **90**, 075434 (2014).
- ²⁶⁹X. Peng, Q. Wei, and A. Copple, "Strain-engineered direct-indirect band gap transition and its mechanism in two-dimensional phosphorene," *Phys. Rev. B* **90**, 085402 (2014).
- ²⁷⁰G. Qin, Q.-B. Yan, Z. Qin, S.-Y. Yue, H.-J. Cui, Q.-R. Zheng, and G. Su, "Hinge-like structure induced unusual properties of black phosphorus and new strategies to improve the thermoelectric performance," *Sci. Rep.* **4**, 6946 (2014).
- ²⁷¹J.-W. Jiang and H. S. Park, "Analytic study of strain engineering of the electronic bandgap in single-layer black phosphorus," *Phys. Rev. B* **91**, 235118 (2015).
- ²⁷²H. Duan, M. Yang, and R. Wang, "Electronic structure and optic absorption of phosphorene under strain," *Phys. E: Low-dimensional Syst. Nanostructures* **81**, 177–181 (2016).

- ²⁷³C. Liao, Y. Zhao, and G. Ouyang, "Strain-modulated band engineering in two-dimensional Black Phosphorus/MoS₂ van der Waals heterojunction," *ACS Omega* **3**, 14641 (2018).
- ²⁷⁴Y. Xu, J. Wang, G. Liu, G. Zhao, Y. Tian, and J. Yang, "Properties of monolayer black phosphorus affected by uniaxial strain," *Phys. E: Low-dimensional Syst. Nanostructures* **117**, 113834 (2020).
- ²⁷⁵C. Robert, D. Lagarde, F. Cadiz, G. Wang, B. Lassagne, T. Amand, A. Balocchi, P. Renucci, S. Tongay, B. Urbaszek, and X. Marie, "Exciton radiative lifetime in transition metal dichalcogenide monolayers," *Phys. Rev. B* **93**, 205423 (2016).
- ²⁷⁶H. Liu, T. Wang, C. Wang, D. Liu, and J. Luo, "Exciton radiative recombination dynamics and nonradiative energy transfer in two-dimensional transition-metal dichalcogenides," *J. Phys. Chem. C* **123**, 10087 (2019).
- ²⁷⁷F. Li, Y. Yan, B. Han, L. Li, X. Huang, M. Yao, Y. Gong, X. Jin, B. Liu, C. Zhu, Q. Zhou, and T. Cui, "Pressure confinement effect in MoS₂ monolayers," *Nanoscale* **7**, 9075 (2015).
- ²⁷⁸Y. Ye, X. Dou, K. Ding, D. Jiang, F. Yang, and B. Sun, "Pressure-induced K-A crossing in monolayer WSe₂," *Nanoscale* **8**, 10843 (2016).
- ²⁷⁹X. Fan, C.-H. Chang, W. T. Zheng, J.-L. Kuo, and D. J. Singh, "The electronic properties of single-layer and multilayer MoS₂ under high pressure," *J. Phys. Chem. C* **119**, 10189 (2015).
- ²⁸⁰X. Dou, K. Ding, D. Jiang, and B. Sun, "Tuning and identification of inter-band transitions in monolayer and bilayer molybdenum disulfide using hydrostatic pressure," *ACS Nano* **8**, 7458 (2014).
- ²⁸¹D. A. Bandurin, A. V. Tyurnina, G. L. Yu, A. Mishchenko, V. Zólyomi, S. V. Morozov, R. K. Kumar, R. V. Gorbachev, Z. R. Kudrynskiy, S. Pezzini, Z. D. Kovalyuk, U. Zeitler, K. S. Novoselov, A. Patané, L. Eaves, I. V. Grigorieva, V. I. Fal'ko, A. K. Geim, and Y. Cao, "High electron mobility, quantum hall effect and anomalous optical response in atomically thin InSe," *Nat. Nanotech.* **12**, 223–227 (2017).
- ²⁸²J. Felton, E. Blundo, S. Ling, J. Glover, Z. R. Kudrynskiy, O. Makarovskiy, Z. D. Kovalyuk, E. Besley, G. Walker, A. Polimeni, and A. Patané, "The interaction of hydrogen with the van der Waals crystal γ -InSe," *Molecules* **25**, 2526 (2020).
- ²⁸³G. W. Mudd, M. R. Molas, X. Chen, V. Zólyomi, K. Nogajewski, Z. R. Kudrynskiy, Z. D. Kovalyuk, G. Yusa, O. Makarovskiy, L. Eaves, M. Potemski, V. I. Falko, and A. Patané, "The direct-to-indirect band gap crossover in two-dimensional van der Waals Indium Selenide crystals," *Sci. Rep.* **6**, 39619 (2016).
- ²⁸⁴D. J. Terry, V. Zólyomi, M. Hamer, A. V. Tyurnina, D. G. Hopkinson, A. M. Rakowski, S. J. Magorrian, N. Clark, Y. M. Andreev, O. Kazakova, K. Novoselov, S. J. Haigh, V. I. Fal'ko, and R. Gorbachev, "Infrared-to-violet tunable optical activity in atomic films of GaSe, InSe, and their heterostructures," *2D Mater.* **5**, 041009 (2018).
- ²⁸⁵Y. Wang, C. Cong, W. Yang, J. Shang, N. Peimyo, Y. Chen, J. Kang, J. Wang, W. Huang, and T. Yu, "Strain-induced direct-indirect bandgap transition and phonon modulation in monolayer WS₂," *Nano Res.* **8**, 2562 (2015).
- ²⁸⁶L. Mennel, M. Paur, and T. Mueller, "Second harmonic generation in strained transition metal dichalcogenide monolayers: MoS₂, MoSe₂, WS₂, and WSe₂," *APL Photonics* **4**, 034404 (2019).
- ²⁸⁷J. Liang, J. Wang, Z. Zhang, Y. Su, Y. Guo, R. Qiao, P. Song, P. Gao, Y. Zhao, Q. Jiao, S. Wu, Z. Sun, D. Yu, and K. Liu, "Universal imaging of full strain tensor in 2D crystals with third-harmonic generation," *Adv. Mater.* **31**, 1808160 (2019).
- ²⁸⁸F. Carrascoso, H. Li, R. Frisenda, and A. Castellanos-Gomez, "Strain engineering in single-, bi- and tri-layer MoS₂, MoSe₂, WS₂ and WSe₂," *Nano Res.* **14**, 1698–1703 (2021).
- ²⁸⁹R. Frisenda, M. Druppel, R. Schmidt, S. M. de Vasconcellos, D. P. de Lara, R. Bratschitsch, M. Rohlfling, and A. Castellanos-Gomez, "Biaxial strain tuning of the optical properties of single-layer transition metal dichalcogenides," *2D Mater. Appl.* **1**, 10 (2017).
- ²⁹⁰R. Schmidt, I. Niehues, R. Schneider, M. Druppel, T. Deilmann, M. Rohlfling, S. M. de Vasconcellos, A. Castellanos-Gomez, and R. Bratschitsch, "Reversible uniaxial strain tuning in atomically thin WSe₂," *2D Mater.* **3**, 021011 (2016).
- ²⁹¹I. Niehues, A. Blob, T. Stiehm, R. Schmidt, V. Jadrisko, B. Radatović, D. Capeta, M. Kralj, S. M. de Vasconcellos, and R. Bratschitsch, "Strain transfer across grain boundaries in MoS₂ monolayers grown by chemical vapor deposition," *2D Mater.* **5**, 031003 (2018).
- ²⁹²J. Liang, J. Zhang, Z. Li, H. Hong, J. Wang, Z. Zhang, X. Zhou, R. Qiao, J. Xu, P. Gao, Z. Liu, Z. Liu, Z. Sun, S. Meng, K. Liu, and D. Yu, "Monitoring local strain vector in atomic-layered MoSe₂ by second-harmonic generation," *Nano Lett.* **17**, 7539 (2017).
- ²⁹³J. D. Caldwell, I. Aharonovich, G. Cassabois, J. H. Edgar, B. Gil, and D. N. Basov, "Photonics with hexagonal boron nitride," *Nat. Rev. Mat.* **4**, 552–567 (2019).
- ²⁹⁴Y.-M. He, G. Clark, J. R. Schaibley, Y. He, M.-C. Chen, Y.-J. Wei, Q. Z. Xing Ding, W. Yao, X. Xu, C.-Y. Lu, and J.-W. Pan, "Single quantum emitters in monolayer semiconductors," *Nat. Nanotech.* **10**, 497 (2015).
- ²⁹⁵C. Chakraborty, L. Kinnischtzke, K. M. Goodfellow, R. Beams, and A. N. Vamivakas, "Voltage-controlled quantum light from an atomically thin semiconductor," *Nat. Nanotech.* **10**, 507 (2015).
- ²⁹⁶P. Michler, A. Kiraz, C. Becher, W. V. Schoenfeld, P. M. Petroff, L. D. Zhang, E. Hu, and A. Imamoglu, "A quantum dot single-photon turnstile device," *Science* **290**, 2282–2285 (2000).
- ²⁹⁷Y.-M. He, O. Iff, N. Lundt, V. Baumann, M. Davanco, K. Srinivasan, S. Höfling, and C. Schneider, "Cascaded emission of single photons from the biexciton in monolayered WSe₂," *Nat. Commun.* **7**, 13409 (2016).
- ²⁹⁸R. M. Stevenson, R. J. Young, P. Atkinson, K. Cooper, D. A. Ritchie, and A. J. Shields, "A semiconductor source of triggered entangled photon pairs," *Nature* **439**, 179–182 (2006).
- ²⁹⁹C. Palacios-Berraquero, M. Barbone, D. M. Kara, X. Chen, I. Goykhman, D. Yoon, A. K. Ott, J. Beitner, K. Watanabe, T. Taniguchi, A. C. Ferrari, and M. Atatüre, "Atomically thin quantum light-emitting diodes," *Nat. Commun.* **7**, 12978 (2016).
- ³⁰⁰T. T. Tran, K. Bray, M. J. Ford, M. Toth, and I. Aharonovich, "Quantum emission from hexagonal boron nitride monolayers," *Nat. Nanotech.* **11**, 37–41 (2016).
- ³⁰¹N. Mendelson, D. Chugh, J. R. Reimers, T. S. Cheng, A. Gottscholl, H. Long, C. J. Mellor, A. Zettl, V. Dyakonov, P. H. Beton, S. V. Novikov, C. Jagadish, H. H. Tan, M. J. Ford, M. Toth, C. Bradac, and I. Aharonovich, "Identifying carbon as the source of visible single-photon emission from hexagonal boron nitride," *Nat. Mater.* **20**, 321 (2021).
- ³⁰²J. Klein, M. Lorke, M. Florian, F. Sigger, L. Sigl, S. Rey, J. Wierzbowski, J. Cerne, K. Müller, E. Mitterreiter, P. Zimmermann, T. Taniguchi, K. Watanabe, U. Würstbauer, M. Knap, R. Schmidt, J. J. Finley, and A. W. Holleitner, "Site-selectively generated photon emitters in monolayer MoS₂ via local helium ion irradiation," *Nat. Commun.* **10**, 2755 (2019).
- ³⁰³O. Benson, C. Santori, M. Pelton, and Y. Yamamoto, "Regulated and entangled photons from a single quantum dot," *Phys. Rev. Lett.* **84**, 2513–2516 (2000).
- ³⁰⁴R. Trotta, J. Martín-Sánchez, J. S. Wildmann, G. Piredda, M. Reindl, C. Schimpf, E. Zallo, S. Stroj, J. Edlinger, and A. Rastelli, "Wavelength-tunable sources of entangled photons interfaced with atomic vapours," *Nat. Commun.* **7**, 10375 (2016); Y. Chen, J. Zhang, M. Zopf, K. Jung, Y. Zhang, R. Keil, F. Ding, and O. G. Schmidt, "Wavelength-tunable entangled photons from silicon-integrated III-V quantum dots," *Nat. Commun.* **7**, 10387 (2016).
- ³⁰⁵C. Chakraborty, N. R. Jungwirth, G. D. Fuchs, and A. N. Vamivakas, "Electrical manipulation of the fine-structure splitting of WSe₂ quantum emitters," *Phys. Rev. B* **99**, 045308 (2019).
- ³⁰⁶P. Rivera, J. R. Schaibley, A. M. Jones, J. S. Ross, S. Wu, G. Aivazian, P. Klement, K. Seyler, G. Clark, N. J. Ghimire, J. Yan, D. Mandrus, W. Yao, and X. Xu, "Observation of long-lived interlayer excitons in monolayer MoSe₂-WSe₂ heterostructures," *Nat. Commun.* **6**, 6242 (2015).
- ³⁰⁷M. Kremser, M. Brotons-Gisbert, J. Knörzer, J. Gückelhorn, M. Meyer, M. Barbone, A. V. Stier, B. D. Gerardot, K. Müller, and J. J. Finley, "Discrete interactions between a few interlayer excitons trapped at a MoSe₂-WSe₂ heterointerface," *NPJ 2D Mater. Appl.* **4**, 8 (2020).
- ³⁰⁸H. Yu, G.-B. Liu, J. Tang, X. Xu, and W. Yao, "Moiré excitons: From programmable quantum emitter arrays to spin-orbit-coupled artificial lattices," *Sci. Adv.* **3**, e1701696 (2017).

- ³⁰⁹N. Zhang, A. Surrente, M. Baranowski, D. K. Maude, P. Gant, A. Castellanos-Gomez, and P. Plochocka, "Moiré intralayer excitons in a MoSe₂/MoS₂ Heterostructure," *Nano Lett.* **18**, 7651–7657 (2018).
- ³¹⁰K. Tran, G. Moody, F. Wu, X. Lu, J. Choi, K. Kim, A. Rai, D. A. Sanchez, J. Quan, A. Singh, J. Embley, A. Zepeda, M. Campbell, T. Autry, T. Taniguchi, K. Watanabe, N. Lu, S. K. Banerjee, K. L. Silverman, S. Kim, E. Tutuc, L. Yang, A. H. MacDonald, and X. Li, "Evidence for moiré excitons in van der Waals heterostructures," *Nature* **567**, 71–75 (2019).
- ³¹¹H. Baek, M. Brotons-Gisbert, Z. X. Koong, A. Campbell, M. Rambach, K. Watanabe, T. Taniguchi, and B. D. Gerardot, "Highly energy-tunable quantum light from Moiré-trapped excitons," *Sci. Adv.* **6**, eaba8526 (2020).
- ³¹²J. S. O. Evans, T. A. Mary, T. Vogt, M. A. Subramanian, and A. W. Sleight, "Negative thermal expansion in ZrW₂O₈ and HfW₂O₈," *Chem. Mater.* **8**, 2809–2823 (1996).
- ³¹³K. Wang and R. R. Reeber, "Mode Grüneisen parameters and negative thermal expansion of cubic ZrW₂O₈ and ZrMo₂O₈," *Appl. Phys. Lett.* **76**, 2203–2204 (2000).
- ³¹⁴V. Gava, A. L. Martinotto, and C. A. Perottoni, "First-principles mode Grüneisen parameters and negative thermal expansion in α -ZrW₂O₈," *Phys. Rev. Lett.* **109**, 195503 (2012).
- ³¹⁵N. Mounet and N. Marzari, "First-principles determination of the structural, vibrational and thermodynamic properties of diamond, graphite, and derivatives," *Phys. Rev. B* **71**, 205214 (2005).
- ³¹⁶L. M. Malard, M. A. Pimenta, G. Dresselhaus, and M. S. Dresselhaus, "Raman spectroscopy in graphene," *Phys. Rep.* **473**, 51 (2009).
- ³¹⁷N. Ferralis, "Probing mechanical properties of graphene with Raman spectroscopy," *J. Mater. Sci.* **45**, 5135 (2010).
- ³¹⁸A. Molina-Sánchez, K. Hummer, and L. Wirtz, "Vibrational and optical properties of MoS₂: From monolayer to bulk," *Surf. Sci. Rep.* **70**, 554–586 (2015).
- ³¹⁹X. Zhang, X.-F. Qiao, W. Shi, J.-B. Wu, D.-S. Jiang, and P.-H. Tan, "Phonon and Raman scattering of two-dimensional transition metal dichalcogenides from monolayer, multilayer to bulk material," *Chem. Soc. Rev.* **44**, 2757–2785 (2015).
- ³²⁰M. Krečmarová, D. Andres-Penaes, L. Fekete, P. Ashcheulov, A. Molina-Sánchez, R. Canet-Albiach, I. Gregora, V. Mortet, J. P. Martínez-Pastor, and J. F. Sánchez-Royo, "Optical contrast and Raman spectroscopy techniques applied to few-layer 2D hexagonal boron nitride," *Nanomaterials* **9**, 1047 (2019).
- ³²¹R. Loudon, "The raman effect in crystals," *Adv. Phys.* **50**, 813–864 (2001).
- ³²²J. A. Steele, P. Puech, and R. A. Lewis, "Polarized Raman backscattering selection rules for (*hhl*)-oriented diamond- and zinblende-type crystals," *J. Appl. Phys.* **120**, 055701 (2016).
- ³²³E. Blundo, "Proton-induced straining of two-dimensional crystals," *Il Nuovo Cimento C* **43**, 112 (2020).
- ³²⁴Y. Wang, C. Cong, C. Qiu, and T. Yu, "Raman spectroscopy study of lattice vibration and crystallographic orientation of monolayer MoS₂ under uniaxial strain," *Small* **9**, 2857 (2013).
- ³²⁵A. M. Dadgar, D. Scullion, K. Kang, D. Esposito, E.-H. Yang, I. P. Herman, M. A. Pimenta, E.-J. G. Santos, and A. N. Pasupathy, "Achieving large, tunable strain in monolayer transition-metal dichalcogenides," *Chem. Mater.* **30**, 5148 (2018).
- ³²⁶F. Wang, I. A. Kinloch, D. Wolfson, R. Tenne, A. Zak, E. O'Connell, U. Bangert, and R. J. Young, "Strain-induced phonon shifts in tungsten disulfide nanoplatelets and nanotubes," *2D Mater.* **4**, 015007 (2017).
- ³²⁷B. Karki, B. Freelon, M. Rajapakse, R. Musa, S. M. S. Riyadh, B. Morris, U. Abu, M. Yu, G. Sumanasekera, and J. B. Jasinski, "Strain-induced vibrational properties of few layer black phosphorus and MoTe₂ via Raman spectroscopy," *Nanotechnol.* **31**, 425707 (2020).
- ³²⁸G. Wang, Z. Zhang, Y. Wang, E. Gao, X. Jia, Z. Dai, C. Weng, L. Liu, Y. Zhang, and Z. Zhang, "Out-of-plane deformations determined mechanics of vanadium disulfide (VS₂) sheets," *ACS Appl. Mater. Interfaces* **13**, 3040 (2021).
- ³²⁹D. Doratotaj, J. R. Simpson, and J.-A. Yan, "Probing the uniaxial strains in MoS₂ using polarized Raman spectroscopy: A first-principles study," *Phys. Rev. B* **93**, 075401 (2016).
- ³³⁰H. Kim, H. K. S. M. Kim, and H. Rho, "Polarization-dependent anisotropic Raman response of CVD-grown vertically stacked MoS₂ layers," *J. Raman Spectrosc.* **51**, 774 (2020).
- ³³¹F. Tuinstra and J. L. Koenig, "Raman spectrum of graphite," *J. Chem. Phys.* **53**, 1126 (1970).
- ³³²D. Kochan, S. Irmer, and J. Fabian, "Model spin-orbit coupling hamiltonians for graphene systems," *Phys. Rev. B* **95**, 165415 (2017).
- ³³³J. Ribeiro-Souares, R. M. Almeida, E. B. Barros, P. T. Araujo, M. S. Dresselhaus, L. G. Cançado, and A. Jorio, "Group theory analysis of phonons in two-dimensional transition metal dichalcogenides," *Phys. Rev. B* **90**, 115438 (2014).
- ³³⁴S. J. Magorrian, *Theory of Electronic and Optical Properties of Atomically Thin Films of Indium Selenide* (Springer, Cham, 2019) pp. 1–11.
- ³³⁵S. Jandl and C. Carlone, "Raman spectrum of crystalline InSe," *Solid State Commun.* **25**, 5–8 (1978).
- ³³⁶M. R. Molas, A. V. Tyurnina, V. Zólyomi, A. K. Ott, D. J. Terry, M. J. Hamer, C. Yelgel, A. Babiński, A. G. Nasibulin, A. C. Ferrari, V. I. Fal'ko, and R. Gorbachev, "Raman spectroscopy of GaSe and InSe post-transition metal chalcogenides layers," *Faraday Discuss.* **227**, 163–170 (2021).
- ³³⁷H. B. Ribeiro, M. A. Pimenta, and C. J. de Matos, "Raman spectroscopy in black phosphorus," *J. Raman Spectrosc.* **49**, 76–90 (2018).
- ³³⁸Y. Zhu, W. Zheng, W. Wang, S. Zhu, L. Li, L. Cheng, M. Jin, Y. Ding, and F. Huang, "Raman tensor of layered black phosphorus," *PhotonIX* **1**, 17 (2020).
- ³³⁹C. Thomsen, S. Reich, and P. Ordejón, "Ab initio determination of the phonon deformation potentials of graphene," *Phys. Rev. B* **65**, 073403 (2002).
- ³⁴⁰M. Huang, H. Yan, C. Chen, D. Song, T. F. Heinz, and J. Hone, "Phonon softening and crystallographic orientation of strained graphene studied by Raman spectroscopy," *Proc. Natl. Acad. Sci. U. S. A.* **106**, 7304–7308 (2009).
- ³⁴¹M. Huang, H. Yan, T. F. Heinz, and J. Hone, "Probing strain-induced electronic structure change in graphene by Raman spectroscopy," *Nano Lett.* **10**, 4074–4079 (2010).
- ³⁴²C. Metzger, S. Rémi, M. Liu, S. V. Kusminskiy, A. H. Castro Neto, A. K. Swan, and B. B. Goldberg, "Biaxial strain in graphene adhered to shallow depressions," *Nano Lett.* **10**, 6–10 (2010).
- ³⁴³Z. H. Ni, T. Yu, Y. H. Lu, Y. Y. Wang, Y. P. Feng, and Z. X. Shen, "Uniaxial strain on graphene: Raman spectroscopy study and band-gap opening," *ACS Nano* **2**, 2301–2305 (2008).
- ³⁴⁴L. Gong, R. J. Young, I. A. Kinloch, I. Riaz, R. Jalil, and K. S. Novoselov, "Optimizing the reinforcement of polymer-based nanocomposites by graphene," *ACS Nano* **6**, 2086–2095 (2012).
- ³⁴⁵J. Zabel, R. R. Nair, A. Ott, T. Georgiou, A. K. Geim, K. S. Novoselov, and C. Casiraghi, "Raman spectroscopy of graphene and bilayer under biaxial strain: Bubbles and balloons," *Nano Lett.* **12**, 617 (2012).
- ³⁴⁶M. Yagmurcukardes, C. Bacaksiz, E. Unsal, B. Akbali, R. T. Senger, and H. Sahin, "Strain mapping in single-layer two-dimensional crystals via Raman activity," *Phys. Rev. B* **97**, 115427 (2018).
- ³⁴⁷K. Androulidakis, E. N. Koukaras, J. Rahova, K. Sampathkumar, J. Parthenios, K. Papageorgis, O. Frank, and C. Galiotis, "Wrinkled few-layer graphene as highly efficient load bearer," *ACS Appl. Mater. Interfaces* **9**, 26593–26601 (2017).
- ³⁴⁸A. C. Ferrari, J. C. Meyer, V. Scardaci, C. Casiraghi, M. Lazzeri, F. Mauri, S. Piscanec, D. Jiang, K. S. Novoselov, S. Roth, and A. K. Geim, "Raman spectrum of graphene and graphene layers," *Phys. Rev. Lett.* **97**, 187401 (2006).
- ³⁴⁹J. Lee, G. Ahn, J. Shim, Y. Lee, and S. Ryu, "Optical separation of mechanical strain from charge doping in graphene," *Nat. Commun.* **3**, 1024 (2012).
- ³⁵⁰M. Mohr, J. Maultzsch, and C. Thomsen, "Splitting of the Raman 2D band of graphene subjected to strain," *Phys. Rev. B* **82**, 201409 (2010).
- ³⁵¹R. Geick, C. H. Perry, and G. Rupperecht, "Normal modes in hexagonal boron nitride," *Phys. Rev.* **146**, 543–547 (1966).
- ³⁵²I. Stenger, L. Schué, M. Boukhicha, B. Berini, B. Plaçais, A. Loiseau, and J. Barjon, "Low frequency Raman spectroscopy of few-atomic-layer thick hBN crystals," *2D Mater.* **4**, 031003 (2017).
- ³⁵³Y. Du, J. Maassen, W. Wu, Z. Luo, X. Xu, and P. D. Ye, "Auxetic black phosphorus: A 2D material with negative Poisson's ratio," *Nano Lett.* **16**, 6701–6708 (2016).
- ³⁵⁴S. Liang, M. N. Hasan, and J.-H. Seo, "Direct observation of Raman spectra in black phosphorus under uniaxial strain conditions," *Nanomaterials* **9**, 566 (2019).
- ³⁵⁵P. Campagnola, "Second harmonic generation imaging microscopy: Applications to diseases diagnostics," *Anal. Chem.* **83**, 3224 (2011).

- ³⁵⁶A. R. Khan, B. Liu, W. Ma, L. Zhang, A. Sharma, Y. Zhu, T. Lü, and Y. Lu, "Direct measurement of folding angle and strain vector in atomically thin WS₂ using second harmonic generation," *ACS Nano* **14**, 15806–15815 (2020).
- ³⁵⁷K. Beach, M. C. Lucking, and H. Terrones, "Strain dependence of second harmonic generation in transition metal dichalcogenide monolayers and the fine structure of the C exciton," *Phys. Rev. B* **101**, 155431 (2020).
- ³⁵⁸Y. Kikuchi, Y. Miyauchi, R. Takaeoka, T. Suzuki, M. Tanaka, and S. Ohno, "Multiple-peak resonance of optical second harmonic generation arising from band nesting in monolayer transition metal dichalcogenides TX₂ on SiO₂/Si(001) substrates (T = Mo, W; X = S, Se)," *Phys. Rev. B* **100**, 075301 (2019).
- ³⁵⁹F. Guinea, A. K. Geim, M. I. Katsnelson, and K. S. Novoselov, "Generating quantizing pseudomagnetic fields by bending graphene ribbons," *Phys. Rev. B* **81**, 035408 (2010).
- ³⁶⁰H. Rostami and R. Asgari, "Electronic structure and layer-resolved transmission of bilayer graphene nanoribbon in the presence of vertical fields," *Phys. Rev. B* **88**, 035404 (2013).
- ³⁶¹E. Andrade, R. Carrillo-Bastos, and G. G. Naumis, "Valley engineering by strain in Kekulé-distorted graphene," *Phys. Rev. B* **99**, 035411 (2019).
- ³⁶²A. Kormányos, G. Burkard, M. Gmitra, J. Fabian, V. Zólyomi, N. D. Drummond, and V. Fal'ko, "k-p theory for two-dimensional transition metal dichalcogenide semiconductors," *2D Mater.* **2**, 022001 (2015).
- ³⁶³W. Wu, L. Wang, Y. Li, F. Zhang, L. Lin, S. Niu, D. Chenet, X. Zhang, Y. Hao, T. F. Heinz, J. Hone, and Z. L. Wang, "Piezoelectricity of single-atomic-layer MoS₂ for energy conversion and piezotronics," *Nature* **514**, 470 (2014).
- ³⁶⁴H. Zhu, Y. Wang, J. Xiao, M. Liu, S. Xiong, Z. J. Wong, Z. Ye, Y. Ye, X. Yin, and X. Zhang, "Observation of piezoelectricity in free-standing monolayer MoS₂," *Nat. Nanotech.* **10**, 151 (2015).
- ³⁶⁵O. Bistoni, P. Barone, E. Cappelluti, L. Benfatto, and F. Mauri, "Giant effective charges and piezoelectricity in gapped graphene," *2D Mater.* **6**, 045015 (2019).
- ³⁶⁶S. Tarasenko and E. Ivchenko, "Pure spin photocurrents in low-dimensional structures," *Jetp Lett.* **81**, 231 (2005).
- ³⁶⁷A. Rycerz, J. Tworzydło, and C. Beenakker, "Valley filter and valley valve in graphene," *Nat. Phys.* **3**, 172 (2007).
- ³⁶⁸T. Ando, Y. Zheng, and H. Suzuura, "Dynamical conductivity and zero-mode anomaly in honeycomb lattices," *J. Phys. Soc. Jpn.* **71**, 1318–1324 (2002).
- ³⁶⁹D. Xiao, W. Yao, and Q. Niu, "Valley-contrasting physics in graphene: Magnetic moment and topological transport," *Phys. Rev. Lett.* **99**, 236809 (2007).
- ³⁷⁰D. Xiao, M.-C. Chang, and Q. Niu, "Berry phase effects on electronic properties," *Rev. Mod. Phys.* **82**, 1959–2007 (2010).
- ³⁷¹T. Ando, "Theory of valley Hall conductivity in graphene with gap," *J. Phys. Soc. Jpn.* **84**, 114705 (2015).
- ³⁷²L. E. Golub, S. A. Tarasenko, M. V. Entin, and L. I. Magarill, "Valley separation in graphene by polarized light," *Phys. Rev. B* **84**, 195408 (2011).
- ³⁷³T. L. Linnik, "Photoinduced valley currents in strained graphene," *Phys. Rev. B* **90**, 075406 (2014).
- ³⁷⁴R. Battilomo, N. Scopigno, and C. Ortix, "Berry curvature dipole in strained graphene: A Fermi surface warping effect," *Phys. Rev. Lett.* **123**, 196403 (2019).
- ³⁷⁵T. Fujita, M. B. A. Jalil, and S. G. Tan, "Valley filter in strain engineered graphene," *Appl. Phys. Lett.* **97**, 043508 (2010).
- ³⁷⁶F. Zhai and L. Yang, "Strain-tunable spin transport in ferromagnetic graphene junctions," *Appl. Phys. Lett.* **98**, 062101 (2011).
- ³⁷⁷Z. Niu, "Spin and valley dependent electronic transport in strain engineered graphene," *J. Appl. Phys.* **111**, 103712 (2012).
- ³⁷⁸Z. Khatibi, H. Rostami, and R. Asgari, "Valley polarized transport in a strained graphene based corbino disc," *Phys. Rev. B* **88**, 195426 (2013).
- ³⁷⁹S. Zhu, J. A. Stroschio, and T. Li, "Programmable extreme pseudomagnetic fields in graphene by a uniaxial stretch," *Phys. Rev. Lett.* **115**, 245501 (2015).
- ³⁸⁰R. Carrillo-Bastos, C. León, D. Faria, A. Latgé, E. Y. Andrei, and N. Sandler, "Strained fold-assisted transport in graphene systems," *Phys. Rev. B* **94**, 125422 (2016).
- ³⁸¹S. P. Milovanović and F. M. Peeters, "Strain controlled valley filtering in multi-terminal graphene structures," *Appl. Phys. Lett.* **109**, 203108 (2016).
- ³⁸²M. Settnes, J. H. Garcia, and S. Roche, "Valley-polarized quantum transport generated by gauge fields in graphene," *2D Mater.* **4**, 031006 (2017).
- ³⁸³Y.-T. Zhang and F. Zhai, "Strain enhanced spin polarization in graphene with Rashba spin-orbit coupling and exchange effects," *J. Appl. Phys.* **111**, 033705 (2012).
- ³⁸⁴M. M. Grujić, M. Ž. Tadić, and F. M. Peeters, "Spin-valley filtering in strained graphene structures with artificially induced carrier mass and spin-orbit coupling," *Phys. Rev. Lett.* **113**, 046601 (2014).
- ³⁸⁵Q.-P. Wu, Z.-F. Liu, A.-X. Chen, X.-B. Xiao, and Z.-M. Liu, "Full valley and spin polarizations in strained graphene with Rashba spin orbit coupling and magnetic barrier," *Sci. Rep.* **6**, 21590 (2016).
- ³⁸⁶T. Cao, G. Wang, W. Han, H. Ye, C. Zhu, J. Shi, Q. Niu, P. Tan, E. Wang, B. Liu, and J. Feng, "Valley-selective circular dichroism of monolayer molybdenum disulfide," *Nat. Commun.* **3**, 887 (2012).
- ³⁸⁷A. Jones, H. Yu, N. Ghimire, S. Wu, G. Aivazian, J. Ross, B. Zhao, J. Yan, D. Mandrus, D. Xiao, W. Yao, and X. Xu, "Optical generation of excitonic valley coherence in monolayer WSe₂," *Nat. Nanotech.* **8**, 634 (2013).
- ³⁸⁸X. Xu, W. Yao, D. Xiao, and T. Heinz, "Spin and pseudospins in layered transition metal dichalcogenides," *Nat. Phys.* **10**, 343 (2014).
- ³⁸⁹D. Xiao, G.-B. Liu, W. Feng, X. Xu, and W. Yao, "Coupled spin and valley physics in monolayers of MoS₂ and other group-VI dichalcogenides," *Phys. Rev. Lett.* **108**, 196802 (2012).
- ³⁹⁰G. Sallen, L. Bouet, X. Marie, G. Wang, C. R. Zhu, W. P. Han, Y. Lu, P. H. Tan, T. Amand, B. L. Liu, and B. Urbaszek, "Robust optical emission polarization in MoS₂ monolayers through selective valley excitation," *Phys. Rev. B* **86**, 081301 (2012).
- ³⁹¹H. Zeng, J. Dai, W. Yao, D. Xiao, and X. Cui, "Valley polarization in MoS₂ monolayers by optical pumping," *Nat. Nanotech.* **7**, 490 (2012).
- ³⁹²A. Srivastava, M. Silder, A. Allain, D. Lembke, A. Kis, and A. Imamoglu, "Valley Zeeman effect in elementary optical excitations of monolayer WSe₂," *Nat. Phys.* **11**, 141 (2015).
- ³⁹³S. Wu, J. Ross, G.-B. Liu, G. Aivazian, A. Jones, Z. Fei, W. Zhu, D. Xiao, W. Yao, D. Cobden, and X. Xu, "Electrical tuning of valley magnetic moment through symmetry control in bilayer MoS₂," *Nat. Phys.* **9**, 149 (2013).
- ³⁹⁴I. Sodemann and L. Fu, "Quantum nonlinear Hall effect induced by Berry curvature dipole in time-reversal invariant materials," *Phys. Rev. Lett.* **115**, 216806 (2015).
- ³⁹⁵J.-S. You, S. Fang, S.-Y. Xu, E. Kaxiras, and T. Low, "Berry curvature dipole current in the transition metal dichalcogenides family," *Phys. Rev. B* **98**, 121109 (2018).
- ³⁹⁶J. Lee, Z. Wang, H. Xie, K. Mak, and J. Shan, "Valley magnetoelectricity in single-layer MoS₂," *Nat. Mater.* **16**, 887 (2017).
- ³⁹⁷J. Son, K.-H. Kim, Y. H. Ahn, H.-W. Lee, and J. Lee, "Strain engineering of the Berry curvature dipole and valley magnetization in monolayer MoS₂," *Phys. Rev. Lett.* **123**, 036806 (2019).
- ³⁹⁸I. W. Frank, D. M. Tanenbaum, A. M. van der Zande, and P. L. McEuen, "Mechanical properties of suspended graphene sheets," *J. Vacuum Sci. Technol. B: Microelectron. Nanometer Struct. Process., Meas., Phenom.* **25**, 2558 (2007).
- ³⁹⁹G. Wang, Z. Dai, J. Xiao, S. Feng, C. Weng, L. Liu, Z. Xu, R. Huang, and Z. Zhang, "Bending of multilayer van der Waals materials," *Phys. Rev. Lett.* **123**, 116101 (2019).
- ⁴⁰⁰K. Liu, Q. Yan, M. Chen, W. Fan, Y. Sun, J. Suh, D. Fu, S. Lee, J. Zhou, S. Tongay, J. Ji, J. B. Neaton, and J. Wu, "Elastic properties of chemical-vapor-deposited monolayer MoS₂, WS₂, and their bilayer heterostructures," *Nano Lett.* **14**, 5097–5103 (2014).
- ⁴⁰¹R. C. Cooper, C. Lee, C. A. Marianetti, X. Wei, J. Hone, and J. W. Kysar, "Nonlinear elastic behavior of two-dimensional molybdenum disulfide," *Phys. Rev. B* **87**, 035423 (2013).
- ⁴⁰²N. Iguíñiz, R. Frisenda, R. Bratschitsch, and A. Castellanos-Gomez, "Revisiting the buckling metrology method to determine the Young's modulus of 2D materials," *Adv. Mater.* **31**, 1807150 (2019).
- ⁴⁰³Y. Li, C. Yu, Y. Gan, P. Jiang, J. Yu, Y. Ou, D.-F. Zou, C. Huang, J. Wang, T. Jia, Q. Luo, X.-F. Yu, H. Zhao, C.-F. Gao, and J. Li, "Mapping the elastic properties of two-dimensional MoS₂ via bimodal atomic force microscopy and finite element simulation," *npj Comput. Mater.* **4**, 49 (2018).
- ⁴⁰⁴Y. Yang, X. Li, M. Wen, E. Hacıoğlu, W. Chen, Y. Gong, J. Zhang, B. Li, W. Zhou, P. M. Ajayan, Q. Chen, T. Zhu, and J. Lou, "Brittle fracture of 2D MoSe₂," *Adv. Mater.* **29**, 1604201 (2017).

- ⁴⁰⁵R. Zhang, V. Koutsos, and R. Cheung, "Elastic properties of suspended multi-layer WSe₂," *Appl. Phys. Lett.* **108**, 042104 (2016).
- ⁴⁰⁶J. Lee, F. Ye, Z. Wang, R. Yang, J. Hu, Z. Mao, J. Wei, and P. X.-L. Feng, "Single- and few-layer WTe₂ and their suspended nanostructures: Raman signatures and nanomechanical resonances," *Nanoscale* **8**, 7854–7860 (2016).
- ⁴⁰⁷Q. Zhao, R. Frisenda, T. Wang, and A. Castellanos-Gomez, "InSe: A two-dimensional semiconductor with superior flexibility," *Nanoscale* **11**, 9845–9850 (2019).
- ⁴⁰⁸Y. Li, C. Yu, Y. Gan, Y. Kong, P. Jiang, D.-F. Zou, P. Li, X.-F. Yu, R. Wu, H. Zhao, C.-F. Gao, and J. Li, "Elastic properties and intrinsic strength of two-dimensional InSe flakes," *Nanotechnol.* **30**, 335703 (2019).
- ⁴⁰⁹B. Chitara and A. Ya'akovovitz, "Elastic properties and breaking strengths of GaS, GaSe and GaTe nanosheets," *Nanoscale* **10**, 13022–13027 (2018).
- ⁴¹⁰A. Castellanos-Gomez, M. Poot, A. Amor-Amorós, G. A. Steele, H. S. J. van der Zant, N. Agrait, and G. Rubio-Bollinger, "Mechanical properties of freely suspended atomically thin dielectric layers of mica," *Nano Res.* **5**, 550–557 (2012).
- ⁴¹¹H. Wang, E. J. Sandoz-Rosado, S. H. Tsang, J. Lin, M. Zhu, G. Mallick, Z. Liu, and E. H. T. Teo, "Elastic properties of 2D ultrathin tungsten nitride crystals grown by chemical vapor deposition," *Adv. Funct. Mater.* **29**, 1902663 (2019).
- ⁴¹²A. Lipatov, H. Lu, M. Alhabeb, B. Anasori, A. Gruverman, Y. Gogotsi, and A. Sinitskii, "Elastic properties of 2D Ti₃C₂T_x MXene monolayers and bilayers," *Sci. Adv.* **4**, eaat0491 (2018).
- ⁴¹³H. Chen, P. Huang, D. Guo, and G. Xie, "Anisotropic mechanical properties of black phosphorus nanoribbons," *J. Phys. Chem. C* **120**, 29491–29497 (2016).
- ⁴¹⁴L. Vaquero-Garzon, R. Frisenda, and A. Castellanos-Gomez, "Anisotropic buckling of few-layer black phosphorus," *Nanoscale* **11**, 12080–12086 (2019).
- ⁴¹⁵Z. Wang, H. Jia, X.-Q. Zheng, R. Yang, G. J. Ye, X. H. Chen, and P. X.-L. Feng, "Resolving and tuning mechanical anisotropy in black phosphorus via nano-mechanical multimode resonance spectromicroscopy," *Nano Lett.* **16**, 5394 (2016).
- ⁴¹⁶M. Moreno-Moreno, G. Lopez-Polin, A. Castellanos-Gomez, C. Gomez-Navarro, and J. Castellanos-Herrero, "Environmental effects in mechanical properties of few-layer black phosphorus," *2D Mater.* **3**, 031007 (2016).
- ⁴¹⁷J.-Y. Wang, Y. Li, Z.-Y. Zhan, T. Li, L. Zhen, and C.-Y. Xu, "Elastic properties of suspended black phosphorus nanosheet," *Appl. Phys. Lett.* **108**, 013104 (2016).
- ⁴¹⁸L. D. Landau and E. M. Lifshitz, "Theoretical physics," in *Theory Elasticity*, 2nd revised ed. (Pergamon Press, Course, 1970), Vol. 7.
- ⁴¹⁹D. Vella and B. Davidovitch, "Indentation metrology of clamped, ultra-thin elastic sheets," *Soft Matter* **13**, 2264–2278 (2017).
- ⁴²⁰R. Garcia and E. T. Herruzo, "The emergence of multifrequency force microscopy," *Nat. Nanotech.* **7**, 217–226 (2012).
- ⁴²¹R. Garcia and R. Prokschb, "Nanomechanical mapping of soft matter by bimodal force microscopy," *Eur. Polym. J.* **49**, 1897–1906 (2013).
- ⁴²²C. M. Stafford, C. Harrison, K. L. Beers, A. Karim, E. J. Amis, M. R. VanLandingham, H.-C. Kim, W. Volksen, R. D. Miller, and E. E. Simonyi, "A buckling-based metrology for measuring the elastic moduli of polymeric thin films," *Nat. Mater.* **3**, 545–550 (2004).
- ⁴²³A. Castellanos-Gomez, R. van Leeuwen, M. Buscema, H. S. J. van der Zant, G. A. Steele, and W. J. Venstra, "Single-layer MoS₂ mechanical resonators," *Adv. Mater.* **25**, 6719–6723 (2013).
- ⁴²⁴J. Lee, Z. Wang, K. He, J. Shan, and P. X.-L. Feng, "High frequency MoS₂ nanomechanical resonators," *ACS Nano* **7**, 6086–6091 (2013).
- ⁴²⁵N. Morell, A. Reserbat-Plantey, I. Tsioutsios, K. G. Schädler, F. Dubin, F. H. L. Koppens, and A. Bachtold, "High quality factor mechanical resonators based on WSe₂ monolayers," *Nano Lett.* **16**, 5102–5108 (2016).
- ⁴²⁶K. L. Ekinci, Y. T. Yang, and M. L. Roukes, "Ultimate limits to inertial mass sensing based upon nanoelectromechanical systems," *J. Appl. Phys.* **95**, 2682–2689 (2004).
- ⁴²⁷T. Wah, "Vibration of circular plates," *J. Acoust. Soc. Am* **34**, 275–281 (1962).
- ⁴²⁸J. S. Bunch, A. M. van der Zande, S. S. Verbridge, I. W. Frank, D. M. Tanenbaum, J. M. Parpia, H. G. Craighead, and P. L. McEuen, "Electromechanical resonators from graphene sheets," *Science* **315**, 490–493 (2007).
- ⁴²⁹T. Yildirim, L. Zhang, G. P. Neupane, S. Chen, J. Zhang, H. Yan, M. M. Hasan, G. Yoshikawa, and Y. Lu, "Towards future physics and applications via two-dimensional material NEMS resonators," *Nanoscale* **12**, 22366–22385 (2020).
- ⁴³⁰B. Graczykowski, M. Sledzinska, M. Placidi, D. Saleta Reig, M. Kasprzak, F. Alzina, and C. M. Sotomayor Torres, "Elastic properties of few nanometers thick polycrystalline MoS₂," *Nano Lett* **17**, 7647–7651 (2017).
- ⁴³¹Z. Y. Zhu, Y. C. Cheng, and U. Schwingenschlögl, "Giant spin-orbit induced spin splitting in two-dimensional transition-metal dichalcogenide semiconductors," *Phys. Rev. B* **84**, 153402 (2011).